

Institute for Energy Research (IEF)  
Plasma Physics (IEF-4)

# **Three-dimensional plasma transport in open chaotic magnetic fields: A computational assessment for tokamak edge layers**

*Frerichs, Heinke Gerd*



# Three-dimensional plasma transport in open chaotic magnetic fields: A computational assessment for tokamak edge layers

Von der Fakultät für Mathematik, Informatik und Naturwissenschaften  
der RWTH Aachen University zur Erlangung des akademischen Grades  
eines Doktors der Naturwissenschaften genehmigte Dissertation

vorgelegt von

**Dipl.-Phys. Heinke Gerd Frerichs**

aus Jülich

Berichter:	Univ.-Prof. Dr.rer.nat. Hans-Jörg Kull
	Univ.-Prof. Dr.rer.nat. Detlev Reiter
Tag der mündlichen Prüfung:	24.02.2010

Diese Dissertation ist auf den Internetseiten der Hochschulbibliothek online verfügbar.



The major part of this thesis was carried out as member of the German Research School for Simulation Sciences, a joint venture of RWTH Aachen University and Forschungszentrum Jülich.



**Three-dimensional plasma transport  
in open chaotic magnetic fields:  
A computational assessment for  
tokamak edge layers**

*Frerichs, Heinke Gerd*

Berichte des Forschungszentrums Jülich; 432 1  
ISSN 0944-2952  
Institut für Energieforschung (IEF)  
Plasma Physics (IEF-4)  
Jül-432 1

D 82 (Diss., RWTH Aachen, Univ., 2010)

Vollständig frei verfügbar im Internet auf dem Jülicher Open Access Server (JUWEL)  
unter <http://www.fz-juelich.de/zb/juwel>

Zu beziehen durch: Forschungszentrum Jülich GmbH · Zentralbibliothek, Verlag  
D-52425 Jülich · Bundesrepublik Deutschland  
☎ 02461 61-5220 · Telefax: 02461 61-6103 · e-mail: [zb-publikation@fz-juelich.de](mailto:zb-publikation@fz-juelich.de)

---

# Abstract

The development of nuclear fusion as an alternative energy source requires the research on magnetically confined, high temperature plasmas. In particular, the quantification of plasma flows in the domain near exposed material surfaces of the plasma container by computer simulations is of key importance, both for guiding interpretation of present fusion experiments and for aiding the ongoing design activities for large future devices such as ITER, W7-X or the DEMO reactor. There is a large number of computational issues related to the physics of hot, fully ionized and magnetized plasmas near surfaces of the vacuum chamber. This thesis is dedicated to one particular such challenge, namely the numerical quantification of self-consistent kinetic neutral gas and plasma fluid flows in very complex 3D (partially chaotic) magnetic fields, in the absence of any common symmetries for plasma and neutral gas dynamics.

In high-confinement (H-mode) plasmas, which are presently envisaged for ITER, an instability occurs naturally at the plasma edge, leading to high transient heat and particle loads to the first wall and the divertor targets. Extrapolations to ITER relevant power levels indicate that this instability, the so called *edge localized mode* (ELM), will lead to a significant reduction of the ITER wall lifetime and additional impurity production reducing the plasma performance. A promising technique to control ELMs is the application of *resonant magnetic perturbations* (RMPs) at the plasma edge, as successfully demonstrated at the DIII-D and JET tokamaks and recently under consideration for ELM mitigation in ITER. Modeling of the perturbed magnetic field structure and comparison to experimental observations suggests the formation of an open chaotic system at the plasma edge with remnant magnetic island chains, chaotic domains and short magnetic flux tubes. However, quantifying the impact of such a complex magnetic field structure on the edge plasma is still the subject of ongoing research. This is the topic of the present thesis - and it requires at least 3D numerical transport models.

Distinct from conventional Eulerian 2D fluid solvers, applied routinely to magnetic fusion edge plasma studies, complex 3D magnetic topologies are currently treated by the geometrically more flexible Lagrangian schemes, supplemented by Monte Carlo procedures for higher order derivatives (dissipative terms due to diffusion processes) and sources. These particle based algorithms are combined with a field line reconstruction technique for dealing with partially chaotic magnetic fields, involving field aligned grids. A generalization from regular-structured to block-structured grids is carried out in this thesis, which greatly enhances the applicability range of present 3D fusion plasma edge codes, in particular also to poloidally magnetic diverted configurations, such as DIII-D and ITER.

The EMC3-EIRENE code is such a 3D edge plasma and neutral particle transport code and is applied in this thesis to two distinct configurations of open chaotic magnetic edge layers: at the TEXTOR and DIII-D tokamaks. The DIII-D tokamak has been chosen because of its recent progress in ELM mitigation by application of RMPs. The

---

advancements of the code presented in this thesis have allowed for the first time 3D self-consistent plasma and neutral gas transport simulations for RMP scenarios at DIII-D with ITER similar plasma shape. A strong 3D effect of RMPs on the edge plasma is found and analyzed in detail. It is found that a pronounced striation pattern of target particle and heat fluxes at DIII-D can only be obtained up to a certain upper limiting level of anomalous cross-field transport. Hence, in comparison to experimental data, these findings allow to narrow down the range of this model parameter. This constraint to cross field transport levels is more stringent in DIII-D than for TEXTOR simulations, because of the shorter wall-to-wall connection length of magnetic field lines (and hence already geometrically reduced role of cross field diffusion) in the latter. Furthermore, improvements of the edge transport model, such as the implementation of an edge transport barrier, are carried out and discussed in order to allow realistic simulations of H-mode plasmas.

Of particular interest is also the reduction of steady state heat fluxes, even in absence of the transient ones caused by ELMs. A favorable regime is the so called *detached* divertor operation, in which plasma exhausts (particle and heat fluxes towards the divertor target) are extinguished in a neutral gas cloud, resulting in low plasma power and ion fluxes to the material surfaces bounding the system. At TEXTOR, the achievement of a similar favorable regime with a 3D perturbed boundary is studied in the RMP induced helical divertor configuration. It is shown in this thesis that plasma states, which are both consistent with the limited experimental data and show transition to reduced particle and heat fluxes, can indeed be observed in numerical simulations of the TEXTOR helical divertor. This is, however, at the expense of also reduced upstream temperatures, which might not be consistent with an advanced tokamak operation (in which the hottest possible confined plasma periphery should be combined with the coldest possible plasma-wall contact zone). The mechanism for the observed behavior is found to be a combination of strong cross-field diffusion and consequently a damping of parallel counter-flows and a sudden increase in momentum losses due to charge exchange with atomic hydrogen. These findings are similar to results from simulations for the W7-AS stellarator. The presence of impurities in the plasma (released wall material due to plasma-wall interaction) is found to have a significant impact on the plasma edge. They introduce an additional cooling of electrons by line radiation, which affects plasma-neutral particle interaction as well and eventually results in a strong reduction of the target ion flux.

The presented improvements of the EMC3-EIRENE code and the subsequent plasma transport studies at TEXTOR and DIII-D allow future extrapolations to ITER relevant scales. In particular the ongoing development of high-performance computers facilitates the direct application of the EMC3-EIRENE code to RMP ELM-control scenarios at ITER in the near future, at least from a point of view of the magnetic configuration capabilities of the code and edge transport model, including transport barrier descriptions. One critical remaining computational challenge is, however, the wall-clock time of present supercomputers, when scaling CPU performance of the code from present applications up to ITER size configurations. This may require structural modifications of the EMC3 part of the code.

# Contents

<b>1</b>	<b>Introduction</b>	<b>1</b>
<b>2</b>	<b>Chaotic magnetic edge layers in tokamaks</b>	<b>5</b>
2.1	The concepts of magnetic confinement and plasma exhaust . . . . .	5
2.1.1	The limiter configuration . . . . .	7
2.1.2	The poloidal divertor configuration . . . . .	8
2.1.3	Chaotic magnetic edge layers . . . . .	9
2.2	Experimental setup of resonant magnetic perturbations . . . . .	10
2.2.1	The DIII-D tokamak . . . . .	10
2.2.2	The TEXTOR tokamak . . . . .	11
2.3	Modeling of the magnetic field structure . . . . .	12
2.3.1	Magnetic field in vacuum approach . . . . .	13
2.3.2	Field line tracing . . . . .	14
2.4	Visualization of the magnetic field structure . . . . .	19
2.4.1	Poincaré plots . . . . .	19
2.4.2	Connection length plots . . . . .	20
<b>3</b>	<b>A 3D model for plasma edge transport</b>	<b>23</b>
3.1	Fluid dynamics . . . . .	23
3.2	Magnetized and collisional plasmas . . . . .	25
3.2.1	Approximation of higher order moments . . . . .	26
3.2.2	Anomalous cross-field transport . . . . .	26
3.2.3	Kinetic corrections . . . . .	27
3.2.4	Collision integrals for charged particles . . . . .	28
3.3	The EMC3-model . . . . .	30
3.3.1	Main plasma . . . . .	30
3.3.2	Impurities of small concentration . . . . .	32
<b>4</b>	<b>Numerical simulation of the plasma edge</b>	<b>35</b>
4.1	A Lagrangian solver for Fokker-Planck type equations . . . . .	35
4.1.1	The Fokker-Planck equation and its relation to stochastic processes	37
4.1.2	Discrete time approximation of sample paths . . . . .	38
4.1.3	Spatially inhomogeneous transport coefficients . . . . .	39
4.2	Fast reconstruction of magnetic field lines . . . . .	41
4.2.1	Generation of a field aligned grid . . . . .	42
4.2.2	Interpolation of field lines . . . . .	45

4.2.3	Mapping of field line coordinates . . . . .	46
4.3	The EMC3-EIRENE code package . . . . .	49
4.3.1	Boundary conditions and input parameters . . . . .	51
4.3.2	Parallelization and scalability . . . . .	53
4.3.3	Execution time of simulations . . . . .	55
4.3.4	Convergence study . . . . .	57
<b>5</b>	<b>Plasma transport in poloidally diverted RMP discharges at DIII-D</b>	<b>63</b>
5.1	Magnetic field structure . . . . .	64
5.2	Parallel profiles in the axisymmetric SOL . . . . .	66
5.3	3D effects on the edge plasma . . . . .	70
5.3.1	Particle and heat flux pattern on the divertor target . . . . .	70
5.3.2	3D structure of the edge plasma . . . . .	73
5.4	Edge transport modeling for H-mode plasmas . . . . .	81
5.4.1	Ad hoc modeling of an edge transport barrier . . . . .	81
5.4.2	Modeling of axisymmetric H-mode plasmas . . . . .	83
5.4.3	Modeling of RMP H-mode plasmas . . . . .	87
<b>6</b>	<b>Plasma transport in the helical divertor at TEXTOR</b>	<b>89</b>
6.1	Brief summary of plasma detachment . . . . .	90
6.2	Characteristics of the TEXTOR helical divertor . . . . .	91
6.2.1	Structure of the magnetic field . . . . .	91
6.2.2	Structure of the edge plasma . . . . .	94
6.3	Averaged transport analysis . . . . .	95
6.3.1	Integrated particle flux . . . . .	95
6.3.2	Integrated heat flux . . . . .	97
6.4	Detailed transport analysis . . . . .	98
6.4.1	Analysis of selected strike points . . . . .	98
6.4.2	Distribution of hydrogen radiation and ionization sources . . . . .	102
6.4.3	Field line profiles . . . . .	104
6.4.4	Conclusions of the detailed transport analysis . . . . .	108
6.5	Impact of impurity radiation . . . . .	109
<b>7</b>	<b>Conclusions</b>	<b>113</b>
<b>A</b>	<b>Random numbers and related issues</b>	<b>117</b>
A.1	Random number generators . . . . .	118
A.2	Generation of non-uniformly distributed random numbers . . . . .	118
A.3	Application in the EMC3-EIRENE code . . . . .	119
A.4	Relaxation of noisy iterations . . . . .	121
<b>B</b>	<b>Verification of the generalized EMC3-EIRENE code</b>	<b>125</b>
B.1	Block-structured grid decomposition . . . . .	125
B.1.1	Comparison to established simulations . . . . .	126

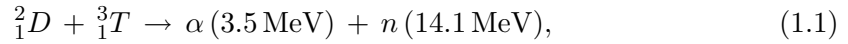
B.1.2	Application to poloidal divertor tokamaks . . . . .	127
B.2	Spatially varying coefficients for cross-field transport . . . . .	133
<b>C</b>	<b>Visualization of the magnetic field and plasma structures in the TEXTOR helical divertor</b>	<b>137</b>
<b>D</b>	<b>Impurity transport</b>	<b>141</b>
D.1	Distribution of carbon ions . . . . .	141
D.2	Boundary conditions . . . . .	142
D.3	Reaction Rates . . . . .	147
D.4	Parameter studies of separatrix density and input power . . . . .	148
D.5	Impurity sources . . . . .	149
<b>E</b>	<b>Trilinear hexahedral elements and their application in toroidal configurations</b>	<b>151</b>
E.1	Bilinear quadrilateral . . . . .	152
E.2	Trilinear, cylindrical hexahedra . . . . .	153
E.3	Data interpolation . . . . .	156
E.4	Example: Simulation of camera pictures . . . . .	158
	<b>References</b>	<b>161</b>
	<b>Symbols and Acronyms</b>	<b>173</b>
	<b>Index</b>	<b>175</b>
	<b>Curriculum vitae</b>	<b>177</b>
	<b>Acknowledgments</b>	<b>179</b>





# 1 Introduction

Controlled thermonuclear fusion is considered as an alternative to present sources for the generation of base load electricity [1]. The idea is based on the physical processes providing the source of thermal energy in the sun and the stars: the fusion of hydrogen nuclei and thereby releasing the difference in binding energy in form of kinetic energy. The easiest process to exploit in a fusion reactor on earth is the fusion of nuclei of the two hydrogen isotopes deuterium and tritium:



which results in the production of an  $\alpha$  particle (helium nucleus), an additional neutron and the release of 17.6 MeV kinetic energy. The advantage of this process is its relatively high reaction rate compared to other fusion processes, with a maximum at temperatures of 10–30 keV. At these temperatures the hydrogen fuel is fully ionized, i.e. in the plasma state. However, Coulomb collisions between charged particles have a much larger cross-section than the reaction (1.1) and lead to particle and power losses. Therefore a good confinement of this hot plasma is necessary for an efficient fusion reactor.

While confinement of the plasma is naturally given in the sun by its own gravitational force, an artificial confinement has to be generated in the laboratory. The most promising technique to achieve controlled thermonuclear fusion on earth is the magnetic confinement in toroidal devices. Here, roughly speaking, electrons and ions are bound to magnetic field lines by the Lorentz force. Presently, two concepts for magnetic confinement of fusion plasmas are applied: tokamaks [2, 3] and stellarators [4]. The basic difference between these two concepts is the method of generating the magnetic confinement field. In stellarators, the complete confinement field is produced by external coils, while in tokamaks a part of the confinement field is produced by an induced plasma current. The quality of plasma confinement is measured by the so called *fusion* or *triple product*  $n \cdot T \cdot \tau_E$  of density  $n$ , temperature  $T$  and energy confinement time  $\tau_E$ . Presently, the tokamak concept is more advanced than the stellarator concept, and allows confinement times of up to  $\tau_E \approx 1$  s. For the next step fusion device ITER [5, 6] it is planned to achieve  $\tau_E = 4 - 5$  s with a power gain of  $Q = P_{\text{fusion}}/P_{\text{heat}} = 10$ .  $Q$  is the ratio of the usable fusion power  $P_{\text{fusion}}$  and the supplied heating power  $P_{\text{heat}}$ .

One of the critical issues in fusion devices is the exhaust of particles and energy, which essentially determine the level of negative surface effects such as material erosion, fuel implantation, dust formation etc. on plasma exposed surfaces. Concepts to establish

these necessary exhausts are so called *limiter* configurations and *poloidal divertor* configurations, which are well-known in the field of plasma-boundary physics [7]. Advancing from the conceptionally simpler limiter configuration to the poloidal divertor configuration allowed the access to steep temperature gradients between confined plasma and the plasma-wall contact zone, and, furthermore a high confinement regime, the so called H-mode [8, 9], however, at the expense of introducing an additional instability, the so called *Edge Localized Mode* (ELM) [10, 11]. These ELMs lead to high transient heat and particle loads onto the first wall and the divertor targets. Extrapolations to ITER relevant power levels indicate that this could lead to a significant reduction of the ITER wall lifetime [12, 13].

An alternative configuration to the poloidal divertor is based on the concept of *ergodic divertors* [14, 15], where external *resonant magnetic perturbations* (RMPs) are applied at the plasma edge to improve the control of particle and energy exhausts as well as to reduce the impurity content in the core plasma. Following earlier experiments, as for example TEXT (USA) [16], CSTN-III [17], JIPP T-IIU (both Japan) [18] and Tore-Supra (France) [19, 20], over the last several years RMP coils have also been installed in various other tokamaks such as TEXTOR and DIII-D. An unexpected experimental finding was that the application of RMPs provides a promising tool for suppression of ELMs (at DIII-D [21, 22]) or mitigation (at DIII-D and JET [23]), the latter meaning reduced size and increased frequency of ELMs. Recently, RMPs are under consideration for ELM mitigation in ITER [24, 25] as well. The application of RMPs leads to formation of an open chaotic magnetic field system at the plasma edge, turning plasma transport within this system into a complex 3D problem. In particular magnetic surfaces are destroyed at the plasma edge and the corresponding toroidal and poloidal symmetry is broken. However, the various processes contributing to plasma transport are still not fully understood and demand (in addition to experimental investigations) for extensive 3D numerical simulations for their quantification. The rapid progress in computational resources over the last few years now allows to include 3D effects in calculations, therefore extending previous research which was based on reduced (averaged) 2D and 1D transport models [26, 27, 28, 29].

Because of the inherent 3D nature of the problem, the conventionally applied 2D plasma flow and plasma surface interaction models in tokamak configurations (B2-EIRENE [30, 31, 32], EDGE2D-NIMBUS [33, 34], SOLDOR/NEUT2D [35, 36]) are not applicable in the presence of RMPs. 3D effects are naturally present in stellarators, for which a computational edge plasma transport model already exist: the EMC3-EIRENE code. This is a coupled version of the 3D macroscopic fluid plasma transport solver EMC3 [37, 38, 39] and the 6D (in phase space) microscopic neutral gas transport solver EIRENE [31], both are Monte Carlo codes. The EMC3-EIRENE code is routinely applied to conditions at the W7-AS [40, 41], W7-X [42] and LHD [43, 44] stellarators (the latter, however, without the divertor region, partly due to issues with the particular field line reconstruction method discussed below) and has been adapted to conditions at the TEXTOR tokamak [45, 46, 47] and the ITER plasma-startup limiter configuration [48].

The motivation for this present thesis is to quantify 3D effects of resonant magnetic perturbations (RMPs) on the edge plasma in circular, limiter plasmas as well as in strongly

---

shaped poloidal divertor plasmas by means of numerical simulations. Confronting the numerical tool with observations from present fusion devices with RMP fields is a necessary step to establish a reliable “bookkeeping” tool also for predictions for future fusion devices. This is of particular importance for the understanding of ELM mitigation by RMPs in ITER. However, for the simulations of ITER relevant RMP scenarios with the EMC3-EIRENE code, it was necessary to significantly advance and verify the code also for H-mode plasmas in poloidal divertor configurations. These steps have been carried out in the present thesis.

In all transport models mentioned above, the magnetic field  $\mathbf{B}$  is externally prescribed and kept fixed during the entire calculation. The extremely strong anisotropy of parallel to perpendicular (to  $\mathbf{B}$ ) plasma transport does, however, require a precise knowledge of  $\mathbf{B}$  at any point and time in the simulation. To keep these two distinct physical processes also separated in the simulation, a local, field aligned coordinate system (with one coordinate line parallel to  $\mathbf{B}$ ) is used. The EMC3-EIRENE code package profits from a very flexible representation of the magnetic field structure, which has already enabled applications to such distinct configurations like the W7-AS stellarator and the ITER plasma-startup limiter edge. A field line reconstruction technique is used, based upon a computational grid with regular structured toroidal blocks, and combined with a *reversible field line mapping* technique (RFLM) [49] at block boundaries. Such a regular decomposition in the poloidal and radial coordinate, however, is not efficiently applicable to poloidal divertor tokamaks, such as JET, DIII-D, ASDEX-U and ultimately ITER, nor in the complete plasma edge of the LHD stellarator (i.e. including the divertor region). This is because of the remoteness of the divertor plates from the inner edge plasma boundary and the corresponding strong poloidal non-uniformity of the radial width of the simulation domain. For poloidal divertor tokamaks, a uniform discretization would either lead to issues related to the spatial resolution in different regions of the computational domain (divertor region vs. upstream region) or, when extending the simulation domain to a uniform radial width, largely waste computational resources.

In current 2D edge codes these issues are dealt with by using multiple connected grids in a poloidal plane. The extensions of the EMC3-EIRENE code carried out in this thesis address the same problem, however within the existing 3D field line reconstruction approach in a field aligned grid. The RFLM concept is supplemented with a cell surface mapping technique, which can be implemented in the EMC3-EIRENE code. This advancement allows an arbitrary - but for convenience still kept block-structured - decomposition of the simulation domain. It is shown that a combination of (a) field line mapping between toroidal blocks and (b) cell surface mapping including the transformation of the local coordinate system at some poloidal or radial cuts allows both accurate magnetic field representations as well as plasma fluid and neutral gas kinetic transport simulations. This thesis is organized as follows:

- Chapter 2 will briefly outline the general aspects of magnetic confinement of fusion plasmas in tokamaks and introduce the concepts for particle and energy exhaust. In particular the experimental setup used for the creation of chaotic magnetic edge layers by RMPs at the TEXTOR and DIII-D tokamak will be described. Also the model for the magnetic field and its numerical implementation is described

and visualization methods for the resulting field structure are presented. These methods involve tracing of magnetic field lines, which are - from a mathematically point of view - solutions of an ordinary differential equation. The performance and accuracy of several numerical integration methods are investigated and compared.

- To investigate the 3D effects of chaotic magnetic edge layers on the edge plasma, the transport model implemented in the EMC3-EIRENE code will be reviewed in chapter 3. It is a steady state fluid model for the edge plasma in the presence of trace impurities, including interactions with neutral particles. This model is formulated as a set of coupled, strongly anisotropic, highly non-linear partial differential equations of Fokker-Planck type.
- Chapter 4 provides a numerical scheme for a self-consistent solver for these equations. This scheme is then supplemented by a fast field line reconstruction method, which is necessary even with present high performance computers. This transport solver and the field line reconstruction method are both implemented in the 3D transport code EMC3-EIRENE. In particular the advancement of the code to block-structured grids is described here, which was necessary for simulations of poloidal divertor configurations. In the last part of this chapter boundary conditions and input parameters of the code as well as parallelization, execution time and convergence of simulation runs are discussed.
- The advancements of the EMC3-EIRENE code allow for the first time the application to ITER similar shape plasmas, as e.g. produced at the DIII-D tokamak. This tokamak has been chosen because of its recent progress in ELM mitigation by application of RMPs. Studies of RMP scenarios at DIII-D are presented in chapter 5. These include the investigation of striation patterns in particle and heat target loads, the impact of short magnetic flux tubes and helical magnetic lobes. It will be shown that the structure of the magnetic field is very well represented in the plasma structure as well, resulting in a strong 3D spatial modulation of plasma density and temperature. The EMC3-model for cross-field transport is extended in order to simulate the effects of an edge transport barrier in H-mode plasmas.
- Of particular interest is a specific plasma state called *detachment*, with reduced plasma particle and heat fluxes to the material surfaces bounding the system despite intense upstream conditions. In chapter 6 it is studied whether a similar state can be achieved at the TEXTOR tokamak in the helical divertor configuration, a configuration where a 3D chaotic magnetic edge layer is created by the application of RMPs. It will be shown that the 3D magnetic field configuration does not allow to speak of phenomena such as high-recycling or detachment in the sense of poloidal divertor upstream-downstream balances ("2-point models"). It will also be shown that the level of cross-field transport and the presence of impurities can have a significant impact on the plasma state.

The main results will be summarized in the conclusions. An outlook to future research motivated by this thesis will be given as well, in particular with regard to the application to ITER.

## 2 Chaotic magnetic edge layers in tokamaks

Presently, the tokamak configuration is the most advanced one and is currently investigated for the first prototype fusion reactors. Both devices investigated in this thesis (DIII-D and TEXTOR) are tokamaks which apply RMPs to control plasma exhausts. The basic idea is to enhance cross-field losses and hence, the plasma exposed surface area. However, the detailed impact on the edge plasma is not fully understood so far and still the subject of ongoing research. In particular the impact on the pressure gradient in the edge transport barrier in H-mode plasmas is of great interest, because this is correlated with the stabilization of so called peeling-ballooning MHD modes (see e.g. [50, 51]) considered as the cause of ELMs [52]. The application of RMPs results in the formation of an open chaotic magnetic field system at the plasma edge, i.e. magnetic surfaces are destroyed and the corresponding toroidal and poloidal symmetry is broken. Fusion plasmas are strongly coupled to the magnetic field, therefore this chapter gives an introduction to the magnetic configuration of these edge layers before later chapters review the plasma transport model and its numerical implementation.

The first section will give a brief overview of the general concepts for establishing plasma exhausts, starting with an illustration of the magnetic confinement scheme in tokamaks. Section 2.2 will introduce the TEXTOR and DIII-D tokamaks, which both apply RMPs to create open chaotic magnetic edge layers. The plasma exposed surface area in TEXTOR is essentially determined by this, resulting in a magnetic field structure referred to as helical divertor - or more precisely helical ergodic divertor - configuration. On the other hand, the chaotic edge layer at DIII-D introduces a significant modification of the plasma boundary and exposed surface area, but does not completely determine the latter. Therefore this configuration is not regarded as an ergodic divertor but rather an *ergodized* poloidal divertor. The groundwork for modeling chaotic magnetic edge layers is described in section 2.3, starting with the ansatz for the perturbed magnetic field and then analyzing numerical methods for field line integration. Visualization methods for the resulting magnetic field structure are then reviewed in section 2.4.

### 2.1 The concepts of magnetic confinement and plasma exhaust

A tokamak is a toroidal device in which the plasma itself is used to produce an essential part of the magnetic confinement field. The concept is extensively described in many textbooks, e.g. in [2, 3], therefore only a brief introduction is given here to introduce the relevant parameters for this thesis. The magnetic confinement is achieved by a

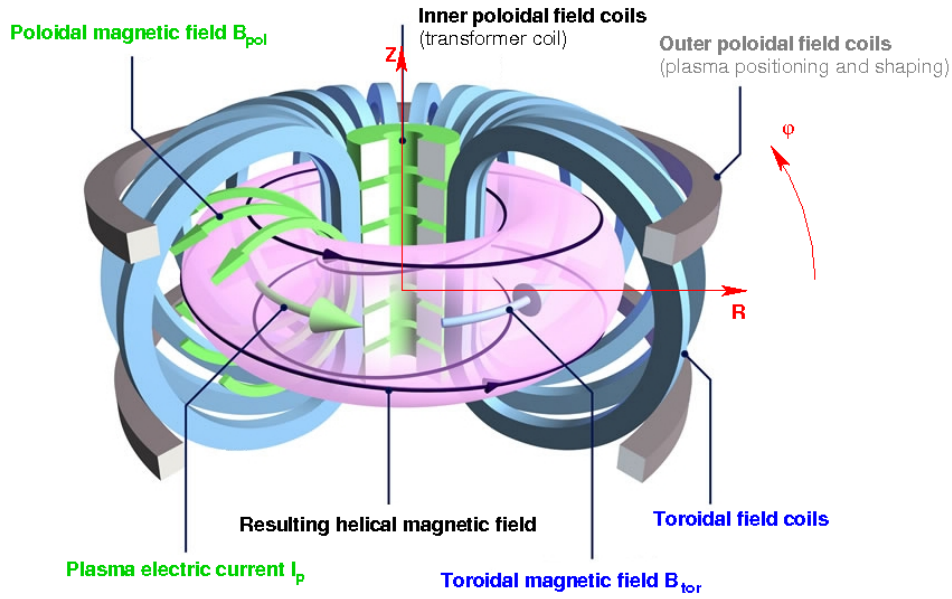


Figure 2.1: Schematic view of a tokamak [53], demonstrating the setup for the superposition of toroidal (blue) and poloidal (green) field components, and the orientation of the cylindrical coordinate system (red) which is used throughout this thesis.

superposition of a toroidal and poloidal magnetic field, which is illustrated by a schematic view of the tokamak configuration in figure 2.1. The toroidal magnetic field  $\mathbf{B}_{\text{tor}}$  is created by a set of field coils distributed around the torus (blue). The poloidal magnetic field  $\mathbf{B}_{\text{pol}}$  on the other hand, is created by a toroidal plasma current  $I_p$  (green). This plasma current is induced by a transformer coil at the center. The outer poloidal field coils (gray) are used for position and shape control of the plasma with a suitable choice of parameters. The resulting helical magnetic field

$$\mathbf{B}_{\text{equi}} = \mathbf{B}_{\text{tor}} + \mathbf{B}_{\text{pol}} \quad (2.1)$$

allows a stable plasma equilibrium and therefore the magnetic confinement of the plasma. The plasma equilibrium in tokamaks is described by the axisymmetric Grad-Shafranov equation [54] in the framework of ideal magnetohydrodynamics (MHD), i.e. an ideally conducting fluid. The equilibrium consists of nested *magnetic surfaces* in the form of tori which are each made up of helical field lines [55]. Field lines can either close in themselves after a finite number of revolutions, or completely fill a magnetic surface (Note that this is sometimes referred to as ergodic, distinct to the behavior of field lines in ergodic divertors which fill a finite volume, see section 2.1.3 and 2.4). The helical winding of a field line on such a magnetic surface is characterized by the *safety factor*  $q$ , which is the toroidal distance  $\Delta\varphi$  that is required to perform one poloidal revolution

( $\Delta\vartheta = 2\pi$ , where  $\vartheta$  is the poloidal angle, see figure 2.10):

$$q = \frac{\Delta\varphi}{2\pi}. \quad (2.2)$$

An alternative formulation is  $q = m/n$ , where  $m$  and  $n$  are the numbers of toroidal and poloidal revolutions until the field line closes in itself.  $q$  depends on the magnetic field components  $\mathbf{B}_{\text{tor}}$  and  $\mathbf{B}_{\text{pol}}$ , and is essentially a function of some radial coordinate for a magnetic surface, e.g. the minor radius in case of a circular plasma. The name *safety factor* is due to its important role in plasma stability.

The control of particle and energy exhaust from a burning fusion plasma is a key issue for the establishment of nuclear fusion as an alternative energy source. Certain requirements for the plasma boundary turn this into a challenging field of research:

- Wall components must not be damaged by overheating. This imposes a limit on the heat flux to plasma exposed surfaces which is given by current knowledge of materials. E.g. a steady state heat flux of  $q = 10 \text{ MW m}^{-2}$  is expected for ITER [56] (and even more during transient events such as ELMs). This is of the same order of magnitude as the peak heat fluxes encountered during the atmospheric re-entry of space crafts [7].
- Helium as the final product of hydrogen fusion can dilute the plasma and must therefore be efficiently pumped out of the system (but before its kinetic energy can be used for plasma heating). This is possible only by a certain level of plasma-wall contact, therefore erosion and migration of wall material is unavoidable.
- On the other hand, efficient re-fueling with a high energy confinement is required to maintain a steady-state burning fusion plasma.

Several mechanisms to control plasma exhausts are briefly reviewed below, starting with the well-known limiter and poloidal divertor configurations [7]. Afterwards, the more advanced concept of chaotic magnetic edge layers is introduced.

### 2.1.1 The limiter configuration

The concept of limiter tokamaks is rather simple: A limiting object is mounted in the plasma chamber, which separates the plasma volume into two regions: a confined region with closed magnetic surfaces and the so called *Scrape-Off Layer* (SOL), where field lines have a short wall-to-wall connection length  $L_c \approx 10 - 100 \text{ m}$  (depending on the machine size). This allows controlled particle and heat fluxes to the limiting wall. However, these particle and heat fluxes are restricted to a small area, which may exceed the limitations of the wall material. Also, released impurities and recycled neutrals (ions and electrons recombined at the wall) may directly enter the main plasma.

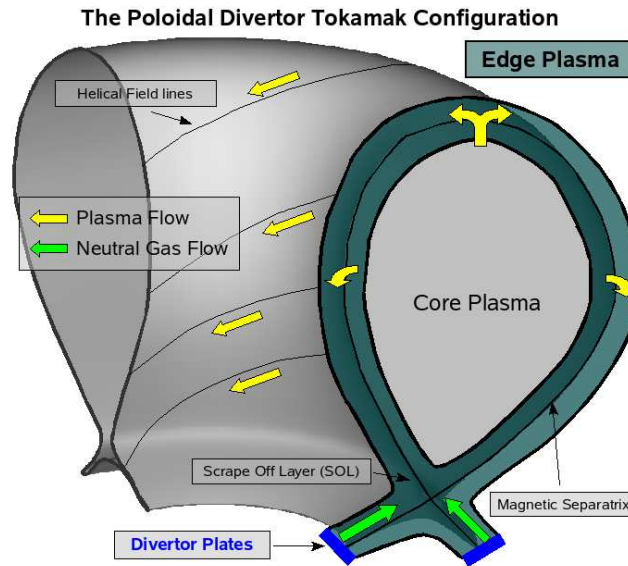


Figure 2.2: Schematic view of the poloidal divertor tokamak configuration. Directions of plasma and neutral gas flow in the edge plasma region (highlighted in green) are indicated by colored arrows.

### 2.1.2 The poloidal divertor configuration

A second configuration is the so called *poloidal divertor*, where field lines in the SOL are magnetically diverted to the *divertor target or plates*. The concept of this configuration is sketched in figure 2.2, where the magnetic separatrix as a boundary for the confined plasma is highlighted. In this configuration the plasma-surface interaction areas (the divertor plates) are far away from the core plasma. The two advantages of this configuration are:

- Improved pumping capability for neutral particles and therefore a better control of particle exhausts.
- Access to a high-confinement regime, the so called H-mode [8, 9], which is considered as standard scenario for ITER.

The plasma-wetted area, however, is still relatively small in poloidal divertors, which results in high localized particle and energy fluxes. Furthermore, the H-mode introduces an additional instability, the so called *edge localized mode* (ELM) [10, 11]. These ELMs flush the plasma from impurities (and helium ash), but also result in high transient heat loads onto the first wall (of the surrounding plasma chamber) and the divertor targets. Extrapolations to ITER relevant power levels indicate that this will lead to a significant reduction of the ITER wall lifetime [12].



### 2.1.3 Chaotic magnetic edge layers

An advanced technique to control particle and energy exhausts is the application of resonant magnetic perturbations in order to create an open chaotic magnetic edge layer. The idea is based on the concept of ergodic divertors [14, 15] but is meanwhile applied to supplement other configurations as well. RMPs are of particular interest as they have been found to be a promising tool to control ELMs in ITER.

In a helical magnetic field system such as a tokamak, magnetic perturbations are resonant to the helicity of particular magnetic field lines. As  $q$  in (2.2) is essentially a function of the minor radius, the resonances can be restricted to the plasma edge (so that the core plasma remains unaffected). Whenever  $q = m/n$  is a rational number, magnetic perturbations can lead to the formation of magnetic island chains. The width of these islands depends on the perturbation strength and its spectrum. If the perturbation strength is increased so that two neighboring island chains overlap, then domains with chaotic field line behavior occur. These field lines can fill the complete volume of overlap between island chains and are therefore often called *ergodic* field lines. These kind of systems are extensively investigated in the theory of nonlinear systems and chaotic dynamics (see e.g. [57, 58, 59] or [60] for a qualitative introduction to this topic) and it is well-known that so called *regions of stochasticity* can occur. However, *stochastic trajectories* are a direct consequence of the non-integrability of a non-linear system, which is still deterministic and does not contain ad hoc stochastic forces [59].

A characteristic parameter to study the level of stochasticity is the well-established Chirikov-parameter [61, 26, 62]

$$\sigma_{\text{Chir}} = \frac{\delta(m, n) + \delta(m + 1, n)}{\Delta(m, n)}, \quad (2.3)$$

which relates the distance  $\Delta(m, n)$  between two neighboring resonant magnetic surfaces  $(m, n)$  and  $(m + 1, n)$  to the respective island widths  $\delta(m, n)$  and  $\delta(m + 1, n)$ .  $\sigma_{\text{Chir}} > 1$  is the necessary condition for island overlap, and hence also for stochasticity. Another commonly used parameter is the so called Kolmogorov-length [62]

$$L_K = \pi q R_0 \left( \frac{\pi \sigma_{\text{Chir}}}{2} \right)^{-4/3}, \quad (2.4)$$

the correlation length between two initially neighboring field lines and  $R_0$  the major radius of the torus center (see figures 2.3 and 2.4). These parameters allow a first analysis of the magnetic field structure induced by RMPs. However, in this thesis more detailed methods are applied to resolve in detail the spatial structure. These methods are introduced in section 2.4.

Often the chaotic edge layer is synonymously called *stochastic boundary*. However, this notation is not used in this thesis to avoid confusion with the stochastic method to

solve plasma transport in chapter 4. The general effect of RMPs is to introduce an intermediate volume with enhanced cross-field losses between the confined plasma (with closed magnetic surfaces) and the regular SOL. The experimental setup of two such configurations are introduced in the following section. Plasma transport studies within these configurations are performed in chapters 6 and 5, respectively.

Yet another concept is the *island divertor* where the resonance effect is used to create large magnetic islands at the plasma edge. The position of these islands is chosen so that the inner island boundary forms the magnetic separatrix while the outer boundary is intersected by divertor plates. Such a concept is e.g. applied in the W7-AS and W7-X stellarators.

## 2.2 Experimental setup of resonant magnetic perturbations

This section briefly describes the experimental setup of the DIII-D and TEXTOR tokamaks. In particular the setup of the coils to generate resonant magnetic perturbations is presented. Modeling and visualization of the resulting magnetic field structure is discussed in sections 2.3 and 2.4, respectively.

### 2.2.1 The DIII-D tokamak

The DIII-D tokamak [63] (figure 2.3 (a)) is located at General Atomics in San Diego, USA. DIII-D is a poloidal divertor machine for D-shaped plasmas with major radius  $R_{\text{maj}} = 1.66$  m, minor radius  $r_{\text{min}} = 0.67$  m at the midplane and vertical elongation of  $\kappa \approx 1.8$ . The toroidal field of up to  $\mathbf{B}_{\text{tor}} = 2.2$  T can be generated with plasma currents of up to  $I_p = 3$  MA. The maximum heating power is  $P_{\text{heat}} = 16$  MW for  $\Delta T = 5$  s by neutral beam injection with an additional 6 MW by ion cyclotron heating and 4 MW by electron cyclotron heating.

The DIII-D tokamak is equipped with a set of  $2 \times 6$  frame-like coils at the Low Field Side (LFS) (i.e. the outboard side with smaller magnetic field strength), the so called I-coils, for resonant magnetic perturbation of the edge plasma. The I-coils can be wired in even parity, as e.g. shown in figure 2.3 (b), or in odd parity, where each pair of upper and lower coil is powered by opposite directed currents. The configuration presented in figure 2.3 (b) creates a perturbation field with toroidal symmetry number  $n = 3$  (i.e.  $\Delta\varphi = 120$  deg), other configuration allow  $n = 1$  and  $n = 2$  fields as well. Typical currents are of the order  $I_{\text{I-coils}} = 3 - 6$  kA. In the present thesis only the perturbation field of the I-coils is considered, while error fields due to coil misalignments and error field correction by additional coils, the so called C-coils, are neglected. This is to study an “ideal” perturbation with toroidal symmetry  $n = 3$  (i.e.  $\Delta\varphi = 120$  deg).

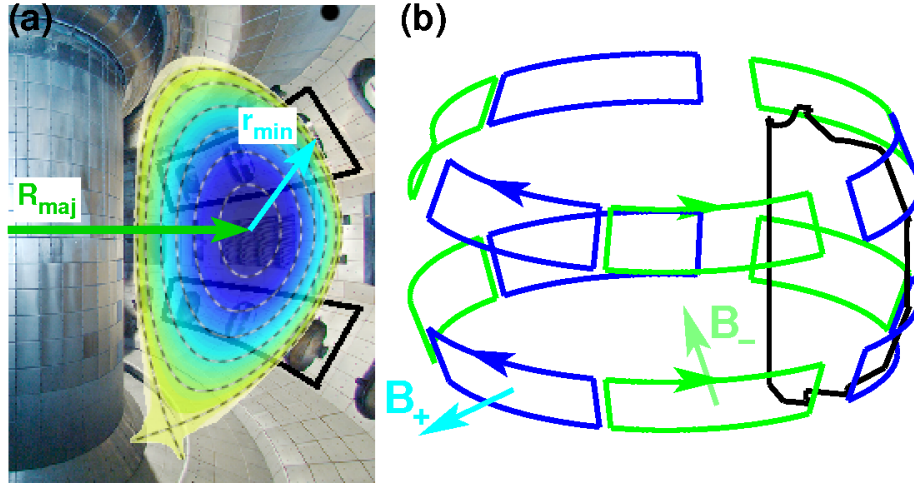


Figure 2.3: (a) Inside view of the DIII-D tokamak, the position of the I-coils is sketched in black. (b) Wire-frame model of the I-coils, powered by positive (blue) and negative (green) currents.

### 2.2.2 The TEXTOR tokamak

The TEXTOR tokamak (Tokamak Experiment for Technology Oriented Research) [64] is located at the Research Centre Jülich, Germany at the Institute for Energy Research - Plasma Physics. TEXTOR is a medium-sized tokamak with major plasma radius  $R_{maj} = 1.75$  m (figure 2.4) and circular plasma cross section. The plasma is limited either by the DED target (blue) on the High Field Side (HFS) (i.e. the inboard side) at  $r_{min} = 0.477$  m or by the movable ALT-II target (red) on the Low Field Side at  $r_{min} = 0.45 - 0.47$  m. The toroidal field of up to  $B_{tor} = 3$  T at the plasma center can be generated and plasma currents of up to  $I_p = 800$  kA can be induced with a pulse length of up to  $\Delta T = 10$  s. The maximum heating power is  $P_{heat} = 9$  MW.

The TEXTOR tokamak has been extended by a set of 16 helical coils [65], located on the HFS at  $r_{min} = 0.532$  m. Each coil performs one toroidal turn and covers a poloidal angle of  $\Delta\vartheta \approx 72$  deg (see figure 2.4 (a)). The coils are covered by graphite plates for protection during plasma discharges. These plates form the DED target which is indicated in blue in figure 2.4 (b).

This coil-set allows a perturbation of the magnetic field which is resonant at the plasma edge around the  $q = 3$  - surface (at  $r_{min} \approx 0.43$  m). The wiring of the coils presented in figure 2.4 (a) creates a perturbation field with poloidal base mode number  $m = 6$  and toroidal base mode number  $n = 2$ , referred to as the  $m/n = 6/2$  - configuration. Other current distributions can be applied to create perturbation fields in 3/1 or 12/4 configuration (see e.g. [66]). The coil current in each configuration is limited to  $I_{12/4} = 15$  kA,  $I_{6/2} = 7.5$  kA and  $I_{3/1} = 3.75$  kA.

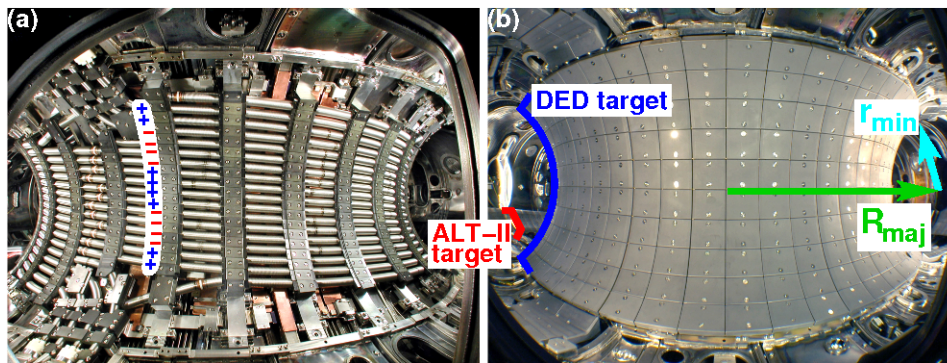


Figure 2.4: Inside view of the TEXTOR tokamak with the DED coils mounted on the High Field Side (a), which are covered by graphite tiles for protection during plasma discharges (b).

Coil currents can be either static or dynamic with frequencies of  $1 - 10$  kHz which led to the name Dynamic Ergodic Divertor (DED). However, in this thesis only static operation is considered. As the plasma exposed surface area is completely determined by the helical pattern of the magnetic field structure (see section 6.2), this scenario is also referred to as *helical divertor*.

## 2.3 Modeling of the magnetic field structure

The magnetic field structure at the plasma edge is considered within the so called *vacuum approach*, presented in section 2.3.1. In this ansatz the vacuum perturbation field is superimposed to an (axisymmetric) equilibrium field, while the modification of the magnetic perturbation field due to a plasma response is neglected. The validity of this approach is related to the issue of penetration of the RMP field into the plasma. This is still the subject of ongoing research [67, 68, 69, 70, 71], studying the effects of field amplification or shielding due to plasma rotation or diamagnetic effects, which may be important at the pedestal in H-mode plasmas. However, a good agreement between calculated magnetic field structure employing this vacuum approximation and experimentally observed plasma edge structure has been found at the TEXTOR tokamak [72, 73]. The latter reference includes an analysis of the screening of the perturbation field by plasma rotation, which is found to be weak at the very plasma edge. However, the validity of the vacuum approach still needs to be established for DIII-D H-mode plasmas. Simulations of particle and heat transport in comparison to experimental observations as carried out in this present thesis can help to address this issue.

The resulting very complex magnetic field structure at the plasma edge is visualized by two methods: so called *Poincaré plots* or *Connection Length plots* (defined in sections 2.4.1 and 2.4.2). These methods are both based on field line tracing (i.e. integration),

which is discussed in section 2.3.2. In this thesis the GOURDON code is used, which applies an Adams-Bashforth method for numerical integration. The accuracy and performance of this method will be compared to that of other integration methods such as the Euler and Runge-Kutta method.

An alternative to numerical field line integration is the application of a so called *symplectic mapping* method [74, 75, 76, 66]. This method is based on the Hamiltonian representation of the field line equation. The advantage over numerical field line integration is the intrinsic conservation of magnetic flux, but the disadvantage is the indirect and only approximate treatment of the perturbation field by its Fourier components which essentially depend on the underlying plasma equilibrium. This method is not used throughout this thesis and is therefore not regarded any further.

### 2.3.1 Magnetic field in vacuum approach

The magnetic field  $\mathbf{B}_{\text{vac}}$  in the vacuum approach is given by the unperturbed, axisymmetric MHD equilibrium  $\mathbf{B}_{\text{equi}}$  and the vacuum perturbation field  $\mathbf{B}_{\text{pert}}$ , where the equilibrium field in (2.1) is made up of a poloidal and toroidal component  $\mathbf{B}_{\text{pol}}$  and  $\mathbf{B}_{\text{tor}}$ , respectively:

$$\mathbf{B}_{\text{vac}} = \mathbf{B}_{\text{tor}} + \mathbf{B}_{\text{pol}} + \mathbf{B}_{\text{pert}}. \quad (2.5)$$

Presently, field line ripple effects resulting from a toroidally discrete set of magnetic field coils are neglected (e.g. for TEXTOR the field line ripple, measured as maximum deviation from toroidally symmetric magnetic surfaces, is less than 3 mm at  $r_{\text{min}} = 47.7$  cm [77]). Therefore a toroidally symmetric radial dependence

$$\mathbf{B}_{\text{tor}}(R) = B_0 \frac{R_0}{R} \mathbf{e}_\varphi \quad (2.6)$$

for the toroidal magnetic field  $\mathbf{B}_{\text{tor}}$  can be assumed. The cylindrical coordinate system has been introduced in figure 2.1 with  $R = R_{\text{maj}}$ .  $B_0$  is a reference value of the toroidal field strength at the radial position  $R_0$ , e.g. at the magnetic axis of the corresponding MHD equilibrium. The poloidal field component  $\mathbf{B}_{\text{pol}} = \nabla \times \mathbf{A}_{\text{pol}}$  is related to the poloidal magnetic flux  $\Psi_{\text{pol}}$  by the vector potential  $\mathbf{A}_{\text{pol}} = \frac{1}{2\pi} \Psi_{\text{pol}} \nabla \varphi$ :

$$\mathbf{B}_{\text{pol}}(R, Z) = -\frac{1}{2\pi R} \frac{\partial \Psi_{\text{pol}}}{\partial Z} \mathbf{e}_R + \frac{1}{2\pi R} \frac{\partial \Psi_{\text{pol}}}{\partial R} \mathbf{e}_Z. \quad (2.7)$$

The MHD equilibrium is determined by the Grad-Shafranov equation [54] for which analytical solutions are known only in special cases [78, 79]. In the present studies  $\Psi_{\text{pol}}$  is provided from the MHD equilibrium code DIVA [80] for TEXTOR calculations or from the MHD reconstruction code EFIT [81, 82] for DIII-D calculations. In both cases

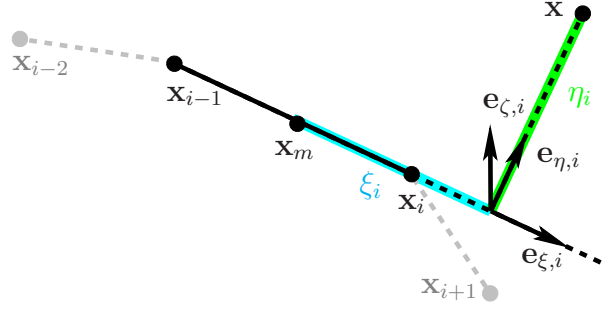


Figure 2.5: Segment of a polygon defined by the nodes  $\mathbf{x}_{i-1}, \mathbf{x}_i$ . The magnetic field at  $\mathbf{x}$  produced by a current  $I_{\text{poly}}$  through this segment is related to the distances  $\xi_i, \eta_i$  and is directed along  $\mathbf{e}_{\zeta,i} = \mathbf{e}_{\xi,i} \times \mathbf{e}_{\eta,i}$ .

$\Psi_{\text{pol}}$  is given as a 2D set of data values  $\Psi_{ij} = \Psi_{\text{pol}}(R_i, Z_j)$  which are then used in a 5th order B-spline interpolation to obtain  $\Psi_{\text{pol}}(R, Z)$  (see e.g. [83, 84]).

$\mathbf{B}_{\text{pert}}$  is obtained by Biot-Savart law from a set of polygons that describe the shape of the perturbation coils (i.e. the DED coils at TEXTOR or the I-coils at DIII-D). The contribution to  $\mathbf{B}_{\text{pert}}$  from a polygon with  $N_{\text{poly}}$  straight segments defined by the nodes  $\mathbf{x}_i, i = 0, \dots, N_{\text{poly}}$  is given in [47, p. 50]:

$$\mathbf{B}_{\text{poly}}(\mathbf{x}) = -\frac{\mu_0}{4\pi} \sum_{i=1}^{N_{\text{poly}}} \frac{I_{\text{poly}}}{\eta_i} \left[ \frac{\xi_i - \frac{L_i}{2}}{\sqrt{\left(\xi_i - \frac{L_i}{2}\right)^2 + \eta_i^2}} - \frac{\xi_i + \frac{L_i}{2}}{\sqrt{\left(\xi_i + \frac{L_i}{2}\right)^2 + \eta_i^2}} \right] \mathbf{e}_{\zeta,i} \quad (2.8)$$

$L_i$  is the length of segment  $i$  and  $\mathbf{x}_m = \frac{1}{2}(\mathbf{x}_{i-1} + \mathbf{x}_i)$ , while the distances  $\xi_i, \eta_i$  and the local, orthogonal coordinate system with  $\mathbf{e}_{\zeta,i} = \mathbf{e}_{\xi,i} \times \mathbf{e}_{\eta,i}$  are defined in figure 2.5. The current  $I_{\text{poly}}$  is set to the current in the respective perturbation coils.

The polygon representation of the DED coils at the TEXTOR tokamak is shown in figure 2.6, where each polygon is composed of  $N_p \approx 600$  segments. (2.8) is applied for each of the 16 polygons that make up the set of DED coils.

### 2.3.2 Field line tracing

Magnetic field lines, as a visualization of  $\mathbf{B}$ , are solutions of the ordinary differential equation (ODE)

$$\frac{d\mathbf{x}}{dl} = \mathbf{b}, \quad \mathbf{b} = |\mathbf{B}|^{-1} \mathbf{B}. \quad (2.9)$$

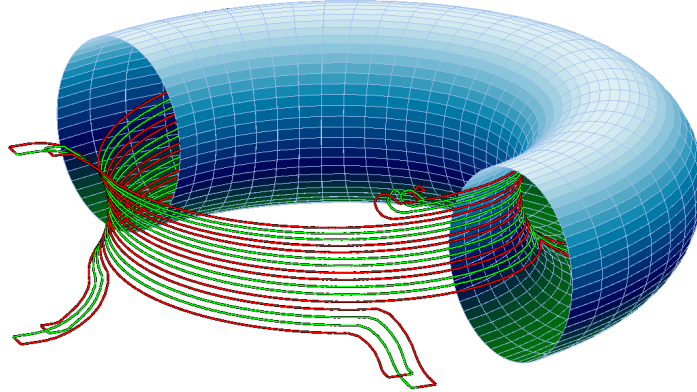


Figure 2.6: Wire-frame model of the DED coils at the TEXTOR tokamak. Each of the 16 coils is represented by a polygon, powered by the current  $I_{\text{poly}}$ . The combination of positive (green) and negative (red) currents (from top to bottom) shown here corresponds to a  $m/n = 12/4$  configuration.

Due to the complicated nature of the perturbation field (2.8), an analytic integration of (2.9) is not possible. Therefore (2.9) needs to be integrated numerically. The integration of chaotic trajectories requires high accuracy, therefore a 5th order Adams-Bashforth method is applied here. This method is described below and afterwards compared to lower order methods.

Starting from a given initial point  $\mathbf{x}_0$ , the recursive integration scheme with stepsize  $\Delta$  reads:

$$\mathbf{x}_{n+1} = \mathbf{x}_n + \Delta \left[ \mathbf{b}_n + \frac{1}{2} \nabla_n^{(1)} + \frac{5}{12} \nabla_n^{(2)} + \frac{3}{8} \nabla_n^{(3)} + \frac{251}{720} \nabla_n^{(4)} \right], \quad (2.10)$$

where  $\nabla_n^{(k)}$  are the backward differences

$$\nabla_n^{(k)} \equiv \sum_{m=0}^k (-1)^m \binom{k}{m} \mathbf{b}_{n-m}, \quad \mathbf{b}_i \equiv \mathbf{b}(\mathbf{x}_i). \quad (2.11)$$

The advantage of Adams-Bashforth methods over Runge-Kutta methods (of the same order) is that  $\mathbf{b}$  needs to be evaluated only once per integration step, while  $\mathbf{b}$  at previous positions can be stored and re-used. This is an important numerical issue, because the evaluation of  $\mathbf{B}_{\text{pert}}$  is numerically quite expensive. However, initial values have to be obtained at the starting point  $\mathbf{x}_0$ . For this 4 Runge-Kutta-Gills backward steps

$$\mathbf{x}_{i-1} = \mathbf{x}_i - \frac{\Delta}{6} \left[ k_1 + (2 - \sqrt{2}) k_2 + (2 + \sqrt{2}) k_3 + k_4 \right], \quad (2.12)$$

are used, where  $k_j = \mathbf{b}(\mathbf{x}_{ij})$  with  $\mathbf{x}_{ij}$  from the table below:

$j$	$\mathbf{x}_{ij}$
1	$\mathbf{x}_i$
2	$\mathbf{x}_i + \frac{1}{2} k_1$
3	$\mathbf{x}_i + \frac{1}{2} (-1 + \sqrt{2}) k_1 + (1 - \frac{1}{2}\sqrt{2}) k_2$
4	$\mathbf{x}_i - \frac{1}{2}\sqrt{2} k_2 + (1 + \frac{1}{2}\sqrt{2}) k_3$

The magnetic field representation (2.5) described in the previous section with its components (2.6), (2.7) and (2.8) and the integration method described here are implemented in the GOURDON code, which is later used for visualization of the magnetic field structure. For this, integration is stopped when a field line intersects the limiting wall or after some termination condition.

### Analysis of integration methods

The long-term accuracy of field-line integration is assessed in figure 2.7 by comparing the Adams-Bashforth algorithm to other integration algorithms, starting with the simplest algorithm, the Euler method (1st order in  $\Delta$ ), but also the Heun method (2nd order in  $\Delta$ , forward Euler method as predictor and trapezoidal method as corrector) and the classical 4th order Runge-Kutta method. A DIII-D configuration with perturbation field of toroidal mode number  $n = 3$  is chosen for the magnetic setup and a field line on a closed, but perturbed magnetic surface at ( $R_0 = 118.8$  cm,  $Z_0 = 0$  cm,  $\varphi_0 = 0$  deg) is selected. The integration step is set to  $\Delta_0 = 1$  cm, which corresponds to an average toroidal step of  $\Delta\varphi = 0.33$  deg (with  $\bar{R} = 175$  cm). The long-term accuracy of the integration methods is measured by the cross-field deviation of the field line

$$\Delta x_n = \sqrt{\Delta R_n^2 + \Delta Z_n^2} \quad (2.13)$$

in the poloidal plane  $\varphi_0$  from its *exact* path after  $n$  toroidal turns. As the exact path of the field line is not known analytically, it is approximated by field line tracing, also with the Adams-Bashforth method but with trace step  $\Delta_3 = 10^{-3}$  cm. The run times of various algorithms on a 2.66 GHz Intel CPU system for tracing the selected field lines for  $N = 1000$  toroidal turns are summarized in the following table:



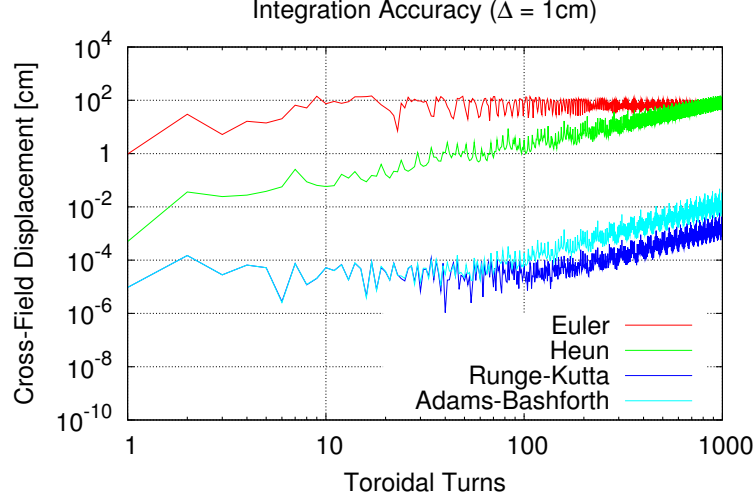


Figure 2.7: Long-term accuracy of several integration methods: Euler (red), Heun (green), Runge-Kutta (blue), Adams-Bashforth (light blue). The accuracy is measured by the cross-field displacement  $\Delta_n$  after  $n$  toroidal turns for a selected field line in a DIII-D like configuration.

Run times	$\Delta_0 = 1$ cm	$\Delta_1 = 0.1$ cm	$\Delta_2 = 0.01$ cm
Euler (E1)	56 s	539 s	$5.5 \cdot 10^3$ s
Heun (H2)	100 s	1033 s	$1.0 \cdot 10^4$ s
Runge-Kutta (RK4)	215 s	1995 s	$2.0 \cdot 10^4$ s
Adams-Bashforth (AB5)	52 s	527 s	$5.2 \cdot 10^3$ s

As can be seen in figure 2.7 the displacement introduced by the Euler method is already  $\Delta_{E1}^{(0)} \approx 1$  cm after one toroidal turn, while it is only  $\Delta_{H2}^{(0)} \approx 5 \cdot 10^{-4}$  cm with the Heun method and  $\Delta_{RK4}^{(0)} \approx \Delta_{AB5}^{(0)} \approx 10^{-5}$  cm with the Runge-Kutta or Adams-Bashforth methods. Using the Euler method, it takes only a couple of toroidal turns for the displacement to increase to the order  $10^2$  cm, which corresponds to the plasma cross-section. Hence, with trace steps of  $\Delta_0 = 1$  cm the Euler method is inadequate for the present problem. Ultimately, the magnetic field structure is related to the plasma structure and the long-term accuracy can be compared to characteristic plasma scales. At low collisionalities, particles can have mean free paths of up to 100 toroidal turns, therefore the Heun method is also not sufficient, because  $\Delta_{H2}^{(0)} \gtrsim 1$  cm after about 30 toroidal turns. Only the Runge-Kutta and Adams-Bashforth methods yield  $\Delta_{RK4}^{(0)}, \Delta_{AB5}^{(0)} \lesssim 10^{-3}$  cm for about 200 toroidal turns, where the Runge-Kutta method is slightly more accurate than the Adams-Bashforth method, but runs a factor of 4 slower.

In figure 2.8 (a) and (b) the integration step is subsequently reduced to  $\Delta_1 = 0.1$  cm and  $\Delta_2 = 0.01$  cm. The initial error after one toroidal turn (which is already about 1000

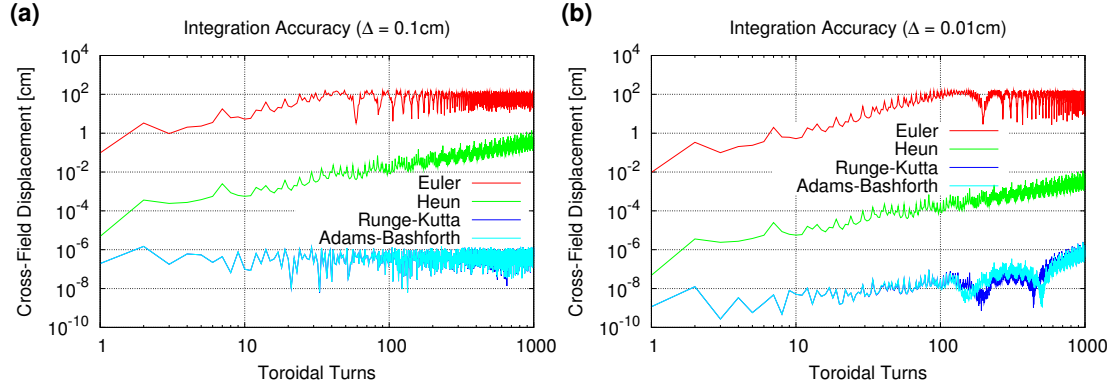


Figure 2.8: Long-term accuracy for a field line on a perturbed, but closed magnetic surface. Smaller integration steps than in figure 2.7 are used here: (a)  $\Delta_a = 0.1$  cm, (b)  $\Delta_b = 0.01$  cm.

trace steps of  $\Delta_0$ ) of the Euler method decreases to  $\Delta_{E1}^{(1)} \approx 0.1$  cm and  $\Delta_{E1}^{(2)} \approx 0.01$  cm, respectively. This stepwise decrease of the error by one order of magnitude each can be expected from a 1st order method like the Euler method. The initial error of the Heun method decreases from  $\Delta_{H2}^{(0)} \approx 5 \cdot 10^{-2}$  cm to  $\Delta_{H2}^{(1)} \approx 5 \cdot 10^{-4}$  cm and to  $\Delta_{H2}^{(2)} \approx 5 \cdot 10^{-6}$  cm, which is expected from a 2nd order method like the Heun method. The initial errors of the Runge-Kutta and Adams-Bashforth methods, however, decrease from  $\Delta_{RK4}^{(0)}, \Delta_{AB5}^{(0)} \approx 10^{-5}$  cm to  $\Delta_{RK4}^{(1)}, \Delta_{AB5}^{(1)} \approx 2 \cdot 10^{-7}$  cm and to  $\Delta_{RK4}^{(2)}, \Delta_{AB5}^{(2)} \approx 10^{-9}$  cm, which is not according to their respective 4th and 5th order scaling. This is probably because at this low level of integration error, additional numerical (round off) errors may become important, e.g. for the calculation of the intersection of the field line with the reference plane at  $\varphi_0$ .

The Euler integration methods introduces a long-term deviation of the order  $10^2$  cm, even for much smaller integration steps. Hence, the Euler method is inadequate for all tested levels of trace steps. The Heun method may be applied to the problem at hand, however, only with small enough integration steps. But this significantly increases the run-time of field line integration and is therefore not recommended. Runge-Kutta and Adams-Bashforth methods yield much better long-term accuracies, even with larger integration steps. As the Adams-Bashforth method is by a factor of 4 faster than the Runge-Kutta method, it is the most suitable method for field line integration.

Applied to a field line with chaotic trajectory (figure 2.9) one can see that even with the Adams-Bashforth method it is not possible to obtain a good long-term accuracy for more than 100 toroidal turns. However, with a sufficiently low step size it is still possible to use this method in simulations of transport processes in collisionless plasmas. The plasma simulations in this thesis are for collisional plasmas (i.e. mean free paths are much smaller), therefore the step size of  $\Delta = 1$  cm is still adequate.

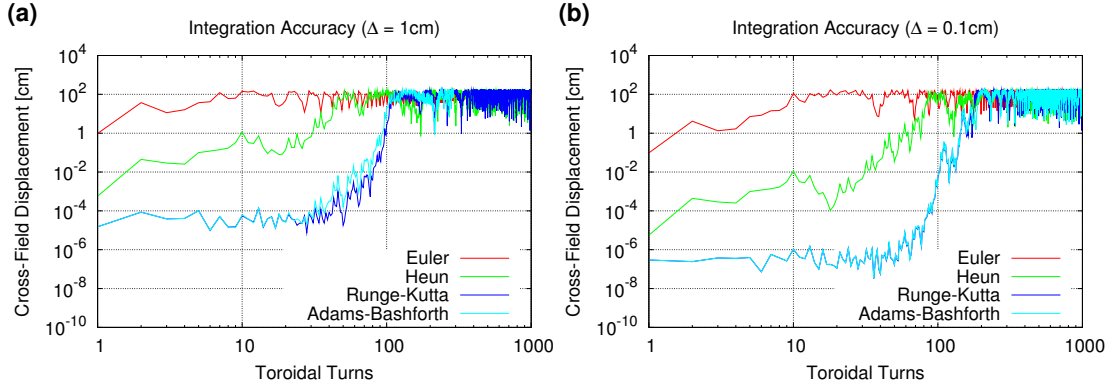


Figure 2.9: Long-term accuracy for a field line with chaotic trajectory. Integration steps of  $\Delta_a = 1.0$  cm (a) and  $\Delta_b = 0.1$  cm (b) are used.

## 2.4 Visualization of the magnetic field structure

The visualization methods for the magnetic field structure discussed below involve tracing of magnetic field lines. That is, integrating the ODE (2.9) for the magnetic field (2.5) with the contributions from (2.6)-(2.8). As described in the previous section, this is done numerically using the 5th order Adams-Bashforth algorithm (2.10). Two different methods for the visualization of the information obtained by field line tracing are described in the following.

### 2.4.1 Poincaré plots

The concept of Poincaré plots originates from Henri Poincaré's studies of dynamical systems, in particular of the three-body problem applied to celestial mechanics [85]. Meanwhile, Poincaré plots have become a wide-spread method in modern studies of nonlinear systems and chaos [57, 60, 58, 59], not only for recent research on the three-body problem [86]. The basic idea is to study periodic orbits of an  $n$  - dimensional continuous dynamical system by its intersections with an  $n-1$  - dimensional hypersurface  $\Sigma$ , the so called Poincaré section. Applied to magnetically confined plasmas in toroidal devices, this means studying the intersections of magnetic field lines with a poloidal reference plane  $\varphi_0$ . The *first return* or Poincaré map  $P$  is defined on  $\Sigma$ , which maps the point  $p \in \Sigma$  to the first return of the corresponding trajectory to  $\Sigma$ . For magnetic field lines, which can be parameterized by the toroidal angle  $\varphi$ , this is

$$P : (R(\varphi_0), Z(\varphi_0)) \mapsto (R(\varphi_0 + 2\pi), Z(\varphi_0 + 2\pi)). \quad (2.14)$$

This introduces a discrete dynamical system of dimension 2. Then the Poincaré plot can be regarded as visualization of the orbits of this system. The orbit for a given starting

point  $(R_0, Z_0)$  is defined by the iterative application of (2.14), which is obtained by field line integration. Let  $P^n, n \geq 1$  denote the  $n$ -th iterate of  $P$  and  $P^0 \equiv (R_0, Z_0)$ , then the corresponding orbit is given by the collection of points  $\{P^n, n \geq 0\}$ . For the generation of Poincaré plots a set of starting points  $(R_m, Z_m), m = 0, \dots, M$  is selected, while the iteration of  $P$  is stopped at some  $n = N_{\max}$  or when field lines intersect the wall. The latter condition is the essential difference between an open and a closed dynamical system.

Figure 2.10 shows Poincaré plots for an RMP scenario at the TEXTOR tokamak with  $m/n = 6/2$  poloidal and toroidal base mode number. Start points are distributed at the inner midplane ( $Z = 0$ ) from  $R_1 = 128$  cm to  $R_2 = 143$  cm in equidistant steps of  $\Delta R = 0.25$  cm and from  $R_2$  to  $R_3 = 158$  cm in steps of  $\Delta R = 1.0$  cm. Field line tracing is stopped at  $N_{\max} = 2000$ . The  $R, Z$  coordinate system in the selected  $\varphi_0$  - plane in figure 2.10 (a) is converted to a  $\vartheta, \psi^*$  coordinate system in figure 2.10 (b), where  $\vartheta$  is the poloidal angle and

$$\psi^* = \frac{\Psi_{\text{pol}} - \Psi_{\text{pol}}^{(\text{axis})}}{\Psi_{\text{pol}}^{(\text{sepx})} - \Psi_{\text{pol}}^{(\text{axis})}} \quad (2.15)$$

the normalized poloidal magnetic flux (which can be regarded as a radial coordinate similar to  $r_{\min}$ ).  $\Psi_{\text{pol}}^{(\text{axis})}$  is the poloidal flux at the magnetic axis (in the plasma center) and  $\Psi_{\text{pol}}^{(\text{sepx})}$  the poloidal flux at the unperturbed separatrix. This coordinate transformation allows to focus on the edge plasma region. It can be seen that in the center region ( $\psi^* \lesssim 0.7$ ), where RMPs are weak, closed but perturbed magnetic surfaces prevail. Without perturbations, magnetic surfaces would appear as horizontal lines in figure 2.10 (b), therefore the choice of  $\psi^*$  as radial coordinate. For  $\psi^* \lesssim 0.8$  magnetic island chains are present [57, 59], most pronounced at the lower order resonances  $m/n = 4/2$  and  $5/2$ . From  $\psi^* \approx 0.8$  outwards a domain of chaotic field line behavior exists, which can be seen by the scattered black dots in figure 2.10. This region is often also called (partially) *ergodic domain*, because field lines fill the complete region (or some part of it). These field lines are called *ergodic field lines*. A detailed analysis of the magnetic field structure induced by RMPs at TEXTOR can be found in [87, 88, 89, 66]. While Poincaré plots are a very useful technique to investigate the long-term behavior of magnetic field lines on perturbed flux surfaces, in island chains and in chaotic domains, it is not very conclusive in regions where field lines intersect the wall after only a few toroidal turns. Hence, the study of an open chaotic system requires an additional visualization method.

## 2.4.2 Connection length plots

Such an alternative visualization method for the magnetic field structure is based on the wall-to-wall connection length  $L_c$  of magnetic field lines. For this, a number of starting points  $(\xi_i, \eta_i), i = 0, \dots, N-1$  is distributed on a selected surface, e.g. the same poloidal plane used for Poincaré plots. Then, field lines are traced from these starting points

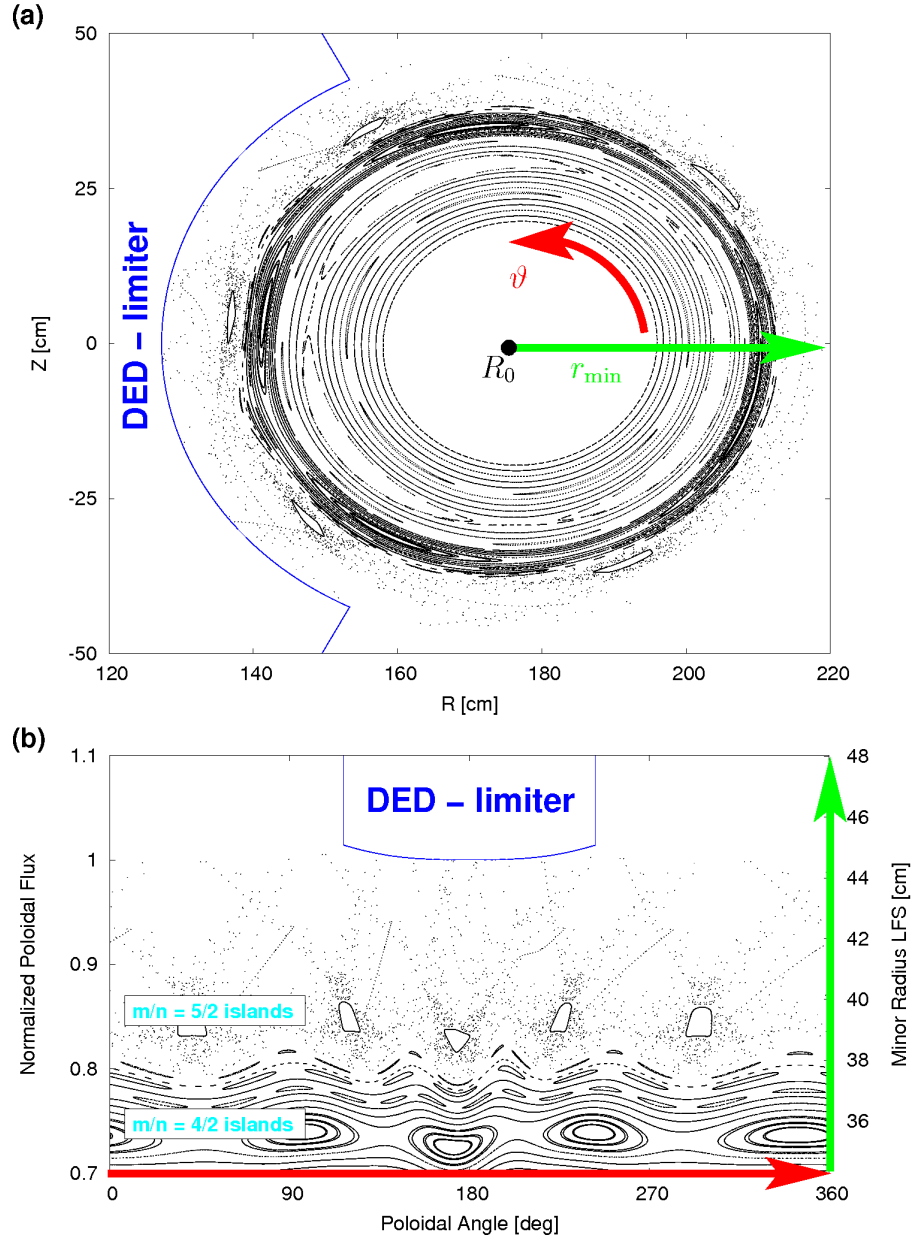


Figure 2.10: Poincaré plots in (a)  $R, Z$ -coordinates and (b) transformed to  $\vartheta, \psi^*$ -coordinates, which allows to focus on the edge region. The corresponding minor radius  $r_{\min}$  at the LFS is given by the right vertical axis.

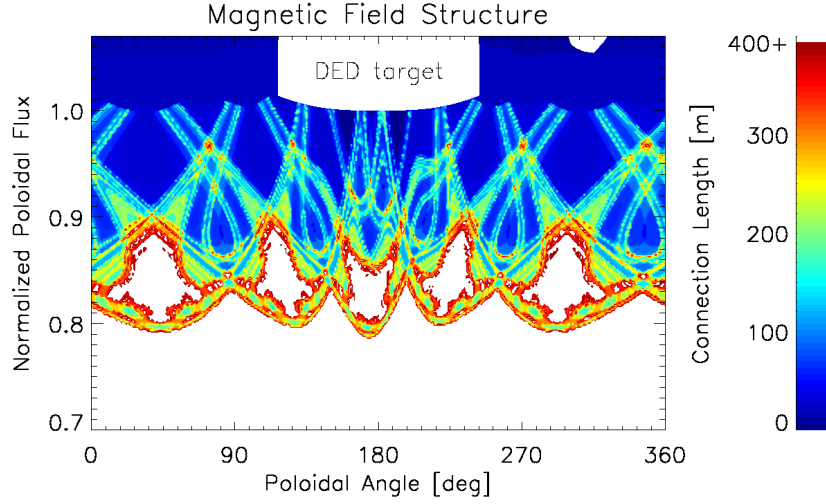


Figure 2.11: Connection length plot at the same reference plane as the Poincaré plot in figure 2.10.

in both directions until they intersect the wall or until some cut-off length  $L_{c,\max}$  is reached. This yields the connection length in positive and negative direction  $L_c^+$  and  $L_c^-$ , respectively, which is combined to the total wall-to-wall connection length

$$L_c = L_c^+ + L_c^- \leq 2 L_{c,\max}. \quad (2.16)$$

Such a connection length plot is shown in figure 2.11 for the same RMP scenario used above, where field line tracing is stopped at  $L_{c,\max} = 200$  m in each direction. Starting points for field line tracing are distributed with a poloidal and radial resolution of  $n_{\text{pol}} = 361$  and  $n_{\text{rad}} = 181$ , respectively. This connection length plot shows the presence of short magnetic flux tubes of  $L_c \approx 50$  m (blue), alternating in poloidal direction with finger-like structure with ergodic field lines of  $L_c \approx 200$  m (green), the so called *ergodic fingers*. It can be seen that this region with *open* field lines has a complex structure which is barely observable in the Poincaré plot 2.10. As both visualization methods give complementary information about the magnetic field structure, a superposition of both plot types is usually applied (see e.g. figure 6.1 (a)).

Connection length plots are also used to visualize the so called *magnetic footprints*, that is the area where field lines intersect the wall. These magnetic footprints are of interest, because they give a first indication of how the plasma surface interaction area is influenced by RMPs. To generate such plots, starting points for field line tracing are distributed on the limiting wall, e.g. the DED-target in figure 6.1 (b). This analysis of the magnetic field structure already suggests that plasma transport is a complex 3D problem.

## 3 A 3D model for plasma edge transport

The plasma edge in fusion devices is a region of high physical diversity. It is the contact region of the hot hydrogen plasma and a solid wall, which results in plasma recycling (i.e. recombination of ions and electrons to neutral particles at the wall), but also leads to erosion of wall material. The interaction between re-emitted neutrals and the plasma can determine the state of the plasma edge [7, Chap. 4.8] (high-recycling, detachment, see chapter 6), which is an important issue for the lifetime of wall components and for the production of plasma impurities. Impurities, both by plasma-wall interaction and by deliberate injection, can radiate a considerable amount of the power entering the plasma edge and therefore can in turn impact the main plasma. Hence, a realistic plasma edge model must include not only main (i.e. hydrogen) plasma transport, but also the production and transport of neutrals as well as plasma impurities.

In this chapter the plasma edge model used for the simulations later in this thesis is presented: a steady state model for a plasma with small impurity concentration in a given magnetic field structure, including interactions with neutral particles. This model is necessarily three dimensional, because of the inherent 3D magnetic field structure in the presence of RMPs (see chapter 2). The present model is based on a fluid approach for the plasma part, while neutral particles are considered within a kinetic description. Balance equations for density  $n$ , mean velocity  $\mathbf{u}$  and temperature  $T$  are derived in section 3.1. These balance equations contain transport coefficients given by higher order moments of the distribution function, and can be closed by appropriate assumptions for these coefficients. Such coefficients are given by Braginskii in [90] for the case of collisional and magnetized plasmas, such as the edge plasma in fusion devices. Details are presented in section 3.2. The EMC3-model for a steady state plasma with small impurity concentration ( $Z_a n_a \ll n_i$  for some impurity species  $a$  and main ion species  $i$ ) is then derived in section 3.3.

### 3.1 Fluid dynamics

The fluid model is based on a kinetic description of the plasma state by a set of local one-particle distribution functions  $f_a = f_a(\mathbf{x}, \mathbf{v}, t)$  for particle species  $a$ . The time evolution is given by the Boltzmann equation

$$\frac{\partial f_a}{\partial t} + \mathbf{v} \cdot \frac{\partial f_a}{\partial \mathbf{x}} + \frac{\mathbf{F}_a}{m_a} \cdot \frac{\partial f_a}{\partial \mathbf{v}} = C_a, \quad (3.1)$$

the solution of which describes the statistical distribution in phase space  $(\mathbf{x}, \mathbf{v})$  of one particle.  $\mathbf{F}_a$  is the macroscopic force field acting on particles of species  $a$  and  $m_a$  the corresponding particle mass. Microscopic properties due to collisions between particles are included in the collision term  $C_a$ . In fusion plasmas the gravitational force can be neglected and only the most dominant Lorentz force is considered:

$$\mathbf{F}_a = q_a \left[ \mathbf{E} + \frac{1}{c} (\mathbf{v} \times \mathbf{B}) \right]. \quad (3.2)$$

$\mathbf{E}$  and  $\mathbf{B}$  are the electric and magnetic fields, respectively,  $c$  is the speed of light and  $q_a$  is the electric charge of a particle from species  $a$ . Macroscopic plasma quantities for species  $a$  are defined by moments of  $f_a$  with regard to the particle velocity  $\mathbf{v}$ :

$$\text{Particle density (0th moment):} \quad n_a = \int d^3v f_a \quad (3.3)$$

$$\text{Fluid velocity (1st moment):} \quad n_a \mathbf{u}_a = \int d^3v \mathbf{v} f_a \quad (3.4)$$

$$\text{Temperature (2nd moment):} \quad \frac{3}{2} n_a T_a = \int d^3v \frac{m_a}{2} (\mathbf{v} - \mathbf{u}_a)^2 f_a \quad (3.5)$$

Rather than solving (3.1), the fluid approach involves balance equations for  $n_a$ ,  $\mathbf{u}_a$  and  $T_a$ . These balance equations can be derived in a similar way to (3.3)-(3.5) by integration of (3.1) with the same respective weighting and (3.2) for  $\mathbf{F}_a$ :

**Particle balance**

$$\frac{\partial n_a}{\partial t} + \frac{\partial}{\partial \mathbf{x}} \cdot (n_a \mathbf{u}_a) = \int d^3v C_a \quad (3.6)$$

**Momentum balance**

$$\begin{aligned} \frac{\partial}{\partial t} (m_a n_a \mathbf{u}_a) + \frac{\partial}{\partial \mathbf{x}} \cdot (m_a n_a \langle \mathbf{v} \mathbf{v} \rangle) - q_a n_a \left[ \mathbf{E} + \frac{1}{c} (\mathbf{u}_a \times \mathbf{B}) \right] \\ = \int d^3v C_a m_a \mathbf{v} \end{aligned} \quad (3.7)$$

**Energy balance**

$$\begin{aligned} \frac{\partial}{\partial t} \left( \frac{3}{2} n_a T_a + \frac{1}{2} m_a n_a u_a^2 \right) + \frac{\partial}{\partial \mathbf{x}} \cdot \left( \frac{m_a n_a}{2} \langle \mathbf{v} v^2 \rangle \right) - q_a n_a \mathbf{E} \cdot \mathbf{u}_a \\ = \int d^3v C_a \frac{m_a v^2}{2} \end{aligned} \quad (3.8)$$



These balance equations still contain the higher order moments  $\langle \mathbf{v} \mathbf{v} \rangle$  and  $\langle \mathbf{v} v^2 \rangle$ , where  $\langle \dots \rangle \equiv \frac{1}{n_a} \int d^3v \dots f_a$  and  $\mathbf{v} \mathbf{v}$  is the dyadic product of  $\mathbf{v}$  with itself. Introducing definitions for the quantities scalar pressure  $p_a$ , viscosity tensor  $\underline{\pi}_a$  and conductive heat flux vector  $\mathbf{h}_a$

$$p_a = n_a T_a \quad (3.9)$$

$$\underline{\pi}_a = m_a n_a \left\langle \mathbf{w} \mathbf{w} - \frac{w^2}{3} \underline{\mathbf{I}} \right\rangle \quad (3.10)$$

$$\mathbf{h}_a = \frac{m_a n_a}{2} \langle \mathbf{w} w^2 \rangle \quad (3.11)$$

with the random velocity  $\mathbf{w} \equiv \mathbf{v} - \mathbf{u}_a$ ,  $\langle \mathbf{w} \rangle = 0$  and unit tensor  $\underline{\mathbf{I}}$  allows to write the higher order moments in the following form:

$$m_a n_a \langle \mathbf{v} \mathbf{v} \rangle = \underline{\pi}_a + p_a \underline{\mathbf{I}} + m_a n_a \mathbf{u}_a \mathbf{u}_a \quad (3.12)$$

$$\frac{m_a n_a}{2} \langle \mathbf{v} v^2 \rangle = \mathbf{h}_a + \mathbf{u}_a \cdot \underline{\pi}_a + \frac{5}{2} n_a T_a \mathbf{u}_a + \frac{m_a n_a}{2} u_a^2 \mathbf{u}_a \quad (3.13)$$

It is exactly the treatment of these higher order moments which makes the difference between conventional fluid dynamics and plasma fluid dynamics. The specific treatment for magnetized and collisional plasmas is presented in the following section. Here the approach by Braginskii [90] is followed, where  $\underline{\pi}_a$  and  $\mathbf{h}_a$  are related to the gradients of lower order moments. Other approaches include balance equations for  $\underline{\pi}_a$  and  $\mathbf{h}_a$  as well (see e.g. [91] for a treatment of transport processes in a multicomponent plasma by Grad's method, i.e. an expansion of the distribution function in Hermite polynomials), however at the price of including even higher order moments to be accounted for. Eventually one has to stop the expansion for practical reasons and approximate higher order moments to close the system of equations.

## 3.2 Magnetized and collisional plasmas

Before the balance equations (3.6) - (3.8) can be applied, this system of equations needs to be closed, i.e. appropriate assumptions have to be made for  $\underline{\pi}_a$  in (3.10) and  $\mathbf{h}_a$  in (3.11). Also the integrals of the collision term on the right hand side (r.h.s.) of (3.6) - (3.8) need to be evaluated. The approach described by Braginskii is based on the Chapman-Enskog method [92] applied to collisional and magnetized plasmas ( $\omega \tau \gg 1$ )<sup>1</sup>. Then the distribution function  $f_a \approx f_a^0 + f_a^1$  can be approximated by a Maxwellian  $f_a^0$

<sup>1</sup>For typical conditions at the plasma edge  $n \approx 5 \cdot 10^{18} \text{ m}^{-3}$ ,  $T \approx 50 \text{ eV}$  and  $B \approx 2 \text{ T}$ :  $\omega_e \tau_e \approx 6 \cdot 10^5$  and  $\omega_i \tau_i \approx 2 \cdot 10^4$ , where  $\omega_e$  and  $\omega_i$  are the electron and ion gyro frequencies and  $\tau_e$  and  $\tau_i$  the respective collision times, see e.g. [90] or [93].

with a small perturbation  $f_a^1 \ll f_a^0$ . This allows to derive expressions for  $\mathbf{h}_a$ ,  $\underline{\pi}_a$  as well as for the collision integrals.

### 3.2.1 Approximation of higher order moments

$\mathbf{h}_a$  in (3.11) can be identified as a heat flux which is assumed to be conductive, i.e. due to the presence of a temperature gradient resulting in a small perturbation of the Maxwellian distribution function. Under this assumption,  $\mathbf{h}_a$  can be written in the form:

$$\mathbf{h}_a = -\kappa_{a\parallel} \nabla_{\parallel} T_a - \kappa_{a\perp} \nabla_{\perp} T_a - \kappa_{a\wedge} \mathbf{e}_{\parallel} \times \nabla T_a, \quad (3.14)$$

where  $\nabla_{\parallel} = \mathbf{e}_{\parallel} \mathbf{e}_{\parallel} \cdot \frac{\partial}{\partial \mathbf{x}}$  and  $\nabla_{\perp} = (\mathbf{I} - \mathbf{e}_{\parallel} \mathbf{e}_{\parallel}) \cdot \frac{\partial}{\partial \mathbf{x}}$  are the gradients parallel and perpendicular to the direction  $\mathbf{e}_{\parallel}$  of the magnetic field.  $\kappa_{a\parallel}$ ,  $\kappa_{a\perp}$  and  $\kappa_{a\wedge}$  are so-called transport coefficients, which can be given separately for parallel and cross-field transport processes. A similar ansatz is made for the viscous momentum transport which is caused by the gradient of the fluid velocity. E.g. for the parallel component:

$$\mathbf{e}_{\parallel} \cdot \underline{\pi}_a \cdot \mathbf{e}_{\parallel} = -\eta_{a\parallel} \mathbf{e}_{\parallel} \cdot \nabla_{\parallel} u_{a\parallel}, \quad (3.15)$$

where  $\eta_{a\parallel}$  is again a transport coefficient. The calculation of transport coefficients is the subject of kinetic transport theory and beyond the scope of this thesis. Results within the classical transport theory by Braginskii [90] considering Coulomb collisions, but neglecting the influence of micro turbulence, have been found to be a good approximation for parallel transport processes. Transport coefficients for electrons (index  $e$ ) and ions (index  $i$ ) are given by

$$\kappa_{e\parallel} = 3.16 \frac{n_e T_e \tau_e}{m_e} \quad \kappa_{i\parallel} = 3.9 \frac{n_i T_i \tau_i}{m_i} \quad (3.16)$$

$$\eta_{e\parallel} = 0.73 n_e T_e \tau_e \quad \eta_{i\parallel} = 0.96 n_i T_i \tau_i. \quad (3.17)$$

Cross-field transport processes, however, are found to be much larger than predicted by the classical transport theory (and also by the neo-classical theory which accounts for drifts in inhomogeneous  $B$ -fields) and are not fully understood so far. These are discussed in the following section.

### 3.2.2 Anomalous cross-field transport

An extensive review of several theories for this *anomalous* cross-field transport is given in [94], but without concluding in a single model. Hence, the cross-field counterparts of (3.16)-(3.17) remain unknown at this point. In the present model the ansatz

$$\mathbf{h}_{e,i\perp} = -\kappa_{e,i\perp}^* \nabla_{\perp} T_{e,i}, \quad \kappa_{e,i\perp}^* = n_{e,i} \chi_{e,i} \quad (3.18)$$

for anomalous transport is used, where  $\chi_{e,i}$  are free model parameters. The cross-field viscosity is related to the cross-field particle transport, which is also anomalous and accounted for by a diffusion ansatz, e.g. for ions:

$$\mathbf{\Gamma}_{i\perp} = n_i \mathbf{u}_{i\perp} = -D_{\perp} \nabla_{\perp} n_i, \quad (3.19)$$

where  $D_{\perp}$  is the anomalous diffusion coefficient, also a free model parameter. Cross-field viscosity of parallel momentum is then given by

$$(\underline{\pi}_a \cdot \mathbf{e}_{\parallel})_{\perp} = -\eta_{a\perp}^* \nabla_{\perp} u_{a\parallel}, \quad \eta_{a\perp}^* = m_a n_a D_{\perp}. \quad (3.20)$$

Although cross-field transport is much larger than expected, it is still much slower than parallel transport, and hence, a strong anisotropy remains: typically  $\kappa_{\parallel}/\kappa_{\perp} \sim 10^6$ .

### 3.2.3 Kinetic corrections

Also parallel transport processes may not be sufficiently described by (3.16) and (3.17) which is suggested by 2D modeling benchmarks [95] and comparisons between 3D modeling and experimental observations [96, 97]. Kinetic corrections to this fluid description are e.g. suggested in [7] by limits of the parallel heat flux and viscosity. The *free streaming* limit for the electron heat flux is given by

$$q_{e\parallel\text{limit}} = \alpha_e n_e v_{th} T_e, \quad v_{th} = \sqrt{\frac{2T_e}{m_e}}, \quad (3.21)$$

while it is stated in [98] that the ion viscosity modulus can never exceed  $\frac{4}{7}n_i T_i$ . The common way to include such limits in the transport model is to introduce an effective heat flux

$$q_{e\parallel\text{eff}} = \left[ \frac{1}{q_{e\parallel\text{classic}}} + \frac{1}{q_{e\parallel\text{limit}}} \right]^{-1} \quad (3.22)$$

to replace the classical heat flux  $q_{e\parallel\text{classic}}$  from (3.14). An analog expression is also introduced for the parallel ion viscosity, whereas electron viscosity is usually neglected as  $m_e \ll m_i$ . The coefficient  $\alpha_e$  in (3.21) is a numerical factor of order 1 and needs to be determined by kinetic calculations. In [7]  $\alpha_e$  is approximated to  $\alpha_e = 0.15$ , however other approaches [28] suggest values of  $\alpha_e = 0.03 \dots 0.1$ . In any case, the ansatz (3.21) remains *ad hoc* and introduces an additional free model parameter.

### 3.2.4 Collision integrals for charged particles

The collision term  $C_a$  on the right hand side of (3.1) is the rate of change of  $f_a$  due to collisions between particles. It can be split in a part due to elastic collisions (Coulomb collisions) and a second part due to inelastic collisions (e.g. due to ionization, recombination or charge exchange):

$$C_a = C_a^{(E)} + C_a^{(I)} = \sum_b C_{ab}(f_a, f_b) + C_a^{(I)} \quad (3.23)$$

Here the Coulomb collision term has been split further to resolve the contribution  $C_{ab}(f_a, f_b)$  from each particle species  $b$ .

#### Particle transfer

Elastic collisions do not result in particle transformations, hence the r.h.s. in (3.6) is given by ionization, recombination and charge exchange rates alone.

$$\int d^3v C_a = \sum_b \underbrace{\int d^3v C_{ab}}_{=0} + \underbrace{\int d^3v C_a^{(I)}}_{\equiv S_a^{(p)}} = S_a^{(p)} \quad (3.24)$$

#### Momentum transfer

Momentum transfer between particle species is due to elastic and inelastic collisions. Using (3.23) for the r.h.s. in (3.7) gives

$$\int d^3v C_a m_a \mathbf{v} = \sum_b \underbrace{\int d^3v C_{ab} m_a \mathbf{v}}_{\equiv \mathbf{R}_{ab}} + \underbrace{\int d^3v C_a^{(I)} m_a \mathbf{v}}_{\equiv \mathbf{S}_a^{(m)}} = \mathbf{R}_{ab} + \mathbf{S}_a^{(m)}. \quad (3.25)$$

The transfer of momentum due to Coulomb collisions  $\mathbf{R}_{ab} = \mathbf{R}_{ab}^u + \mathbf{R}_{ab}^T$  given in [90] is made up of two parts: a friction force  $\mathbf{R}_{ab}^u$  due to a relative velocity  $\Delta \mathbf{u}_{ab} = \mathbf{u}_b - \mathbf{u}_a$  and a thermal force  $\mathbf{R}_{ab}^T$  due to the presence of temperature gradients. Under the assumption of a weakly perturbed Maxwellian distribution  $f_a = f_a^0 + f_a^1$ , the friction force is given by (omitting the indices  $a, b$ )  $\mathbf{R}^u = \mathbf{R}_0^u + \mathbf{R}_1^u$  and the thermal force by  $\mathbf{R}^T = \mathbf{R}_1^T$ . The parallel component of the leading order term in  $\mathbf{R}^u$  is (see appendix B in [99] for a derivation):

$$\mathbf{R}_{ab\parallel}^u = \mu_{ab} n_a \tau_{ab}^{-1} (\mathbf{u}_b - \mathbf{u}_a)_\parallel. \quad (3.26)$$

This expression includes the reduced mass  $\mu_{ab} = \frac{m_a m_b}{m_a + m_b}$  and the collision time  $\tau_{ab}$  for particles of species  $a$  and  $b$ :

$$\tau_{ab}^{-1} = \frac{4\sqrt{2\pi}}{3} \frac{\ln \Lambda n_b q_a^2 q_b^2}{\sqrt{\mu_{ab}} T_a^{3/2}}, \quad (3.27)$$

which is in turn dependent on the Coulomb logarithm  $\ln \Lambda$ . The latter results from a cut-off of the Coulomb potential and is given in [90] by

$$\ln \Lambda = \begin{cases} 23.4 - 1.15 \log_{10} n[cm^{-3}] + 3.45 \log_{10} T[eV], & T < 50 \text{ eV} \\ 25.3 - 1.15 \log_{10} n[cm^{-3}] + 2.3 \log_{10} T[eV], & T > 50 \text{ eV} \end{cases} \quad (3.28)$$

with a weak dependence on temperature and density, but often  $\ln \Lambda \approx 15$  is assumed. Including the first order correction  $\mathbf{R}_1^u$  results in a correction factor of  $\alpha_0 = 0.51$  for  $\mathbf{R}^u$  in (3.26) [90].

Thermal forces  $\mathbf{R}_{ab}^T$  are due to the presence of temperature gradients. The contribution parallel to the magnetic field is given by

$$\mathbf{R}_{ab\parallel}^T = n_a \alpha_{ab} \nabla_{\parallel} T_b, \quad (3.29)$$

where the coefficient  $\alpha_{ab}$  is given in [90] for collisions between ions and electron by

$$\alpha_{ie} = 0.71 Z_i^2, \quad (3.30)$$

while for ion-ion collisions in plasmas with a dominant ion species  $i$  ( $n_a \ll n_i$ ) it is given in [100] by

$$\alpha_{ai} = \frac{3 (\mu + 5\sqrt{2}(Z_a/Z_i)^2 (1.1\mu^{5/2} - 0.35\mu^{3/2}) - 1)}{2.6 - 2\mu + 5.4\mu^2}, \quad \mu = \frac{m_a}{m_a + m_i}. \quad (3.31)$$

### Energy transfer

Energy transfer between different particle species is treated in a similar way:

$$\begin{aligned} \int d^3v C_a \frac{m_a v^2}{2} &= \sum_b \underbrace{\int d^3v C_{ab} \frac{m_a v^2}{2}}_{\equiv \mathbf{u}_a \cdot \mathbf{R}_{ab} + Q_{ab}} + \underbrace{\int d^3v C_a^{(I)} \frac{m_a v^2}{2}}_{\equiv S_a^{(e)}} \\ &= \mathbf{u}_a \cdot \mathbf{R}_{ab} + Q_{ab} + S_a^{(e)}. \end{aligned} \quad (3.32)$$

$\mathbf{R}_{ab}$  is the momentum transfer from (3.25) while  $Q_{ab}$  is the heat generated in species  $a$  due to collisions with particles of the species  $b$ :

$$Q_{ab} = 3n_a \frac{\mu_{ab}}{m_a + m_b} \tau_{ab}^{-1} (T_b - T_a) \quad (3.33)$$

### 3.3 The EMC3-model

The fluid equations (3.6)-(3.8) combined with the magnetized and collisional plasma approximations presented in the last section allow a multi-species description of the edge plasma with 3 balance equations per species (and cross-field transport is determined by (3.18)-(3.20)). Typically, fusion plasmas are hydrogen plasmas with some impurities (such as e.g. carbon) of much lower densities. The model presented in this section is a steady-state ( $\frac{\partial}{\partial t} = 0$ ) transport model for a hydrogen plasma with small impurity concentration ( $Z_a n_a \ll n_i$ , where  $i$  denotes the main ions species and  $a$  is some impurity species with ion charge number  $Z_a$ ). The assumption of small impurity concentrations allows to treat impurity transport in a separate approach from the main plasma. The only effect of impurities on the main plasma in this approximation is an additional energy sink  $\mathcal{S}_{e,\text{cool}}$  due to inelastic collisions between electrons and impurity ions (i.e. excitation, ionization). In section 3.3.1 model equations for the main plasma are derived. Then, in section 3.3.2 the model for impurities is derived.

#### 3.3.1 Main plasma

The main plasma in the trace impurity approximation is a two component plasma of electrons (e) and hydrogen ions (i) and hence, is described by a set of 6 balance equations. This set can be reduced to 4 balance equations for  $n_i, u_{i\parallel}, T_e$  and  $T_i$  under the assumption of quasi-neutrality and locally ambipolar flow

$$n_e \approx n_i, \quad \mathbf{u}_e \approx \mathbf{u}_i. \quad (3.34)$$

#### Particle transport

The particle balance for the main plasma ions is given by (3.6), the ansatz for anomalous cross-field transport (3.19) and collision term (3.24):

##### Particle transport (EMC3)

$$\nabla \cdot \left[ n_i u_{i\parallel} \mathbf{e}_{\parallel} - D_{\perp} \mathbf{I}_{\perp} \cdot \nabla n_i \right] = S_p \quad (3.35)$$

with  $\underline{\mathbf{I}}_{\perp} = \underline{\mathbf{I}} - \mathbf{e}_{\parallel} \mathbf{e}_{\parallel}$ .  $S_p$  is a source due to the ionization of neutral hydrogen.

### Momentum transport

The model equation for parallel momentum is derived by the sum of (3.7) for electrons and main ions, using the parallel viscosity from (3.15) and the collision term (3.25). Applying (3.34) allows to neglect all terms with  $m_e$  in the resulting equation ( $m_e \ll m_i$ ), because similar terms with  $m_i$  are present. The contributions from the electric field in the ion and electron momentum equations cancel each other ( $q_e = -q_i$ ) and also friction and thermal forces  $\mathbf{R}_{ei} = -\mathbf{R}_{ie}$ . The anomalous cross-field viscosity for ions  $\eta_{\perp} = m_i n_i D_{\perp}$  is taken from (3.20), leading to the model equation for parallel momentum:

#### Momentum transport (EMC3)

$$\nabla \cdot \mathbf{e}_{\parallel} \left[ m_i n_i u_{i\parallel}^2 - \eta \mathbf{e}_{\parallel} \cdot \nabla u_{i\parallel} \right] - \nabla \cdot \underline{\mathbf{I}}_{\perp} \cdot D_{\perp} \nabla (m_i n_i u_{i\parallel}) = -\mathbf{e}_{\parallel} \cdot \nabla p + S_m \quad (3.36)$$

where  $S_m$  is a source due to ionization of or charge exchange with with neutral particles.

### Energy transport

The model equations for electron and ion temperatures are derived from (3.8) with the parallel heat flux (3.14) and the cross-field heat flux (3.18), while contributions due to a finite viscosity are neglected. The *adiabatic cooling* term  $\frac{m_a n_a}{2} u_a^2 \mathbf{u}_a$  is also neglected with respect to  $\frac{5}{2} n_a T_a \mathbf{u}_a$  (because it does not fit easily in the applied numerical scheme) for sub- or near sonic flows  $u_a \leq c_s$ :

$$\frac{m_a n_a}{2} u_a^2 \leq \frac{m_a n_a}{2} c_s^2 = \frac{m_a n_a}{2} \frac{T_e + T_i}{m_i} \approx \frac{m_a}{m_i} n_a T_a < \frac{5}{2} n_a T_a. \quad (3.37)$$

This is a good approximation for electrons ( $m_e \ll m_i$ ), but for ions near the target plates ( $u_i \approx c_s$ , Bohm condition with  $c_s$  from (4.48)) this term results in an increase of heat convection by 40 %. Recently it has been implemented in the model and its impact is discussed in [47]. In addition, the term  $q_a n_a \mathbf{u}_a \cdot \mathbf{E}$  can be neglected as well, using Ohm's law in the *small larmor radius approximation* [101]

$$\mathbf{E} + \mathbf{u}_i \times \mathbf{B} = \eta_r \mathbf{j} \quad (3.38)$$

with electric resistivity  $\eta_r$  and electric current density  $\mathbf{j}$ . Using the quasi-neutrality and ambipolarity (3.34) conditions yields

$$\mathbf{j} = q_i n_i \mathbf{u}_i + q_e n_e \mathbf{u}_e \approx 0, \quad (3.39)$$

and multiplying (3.38) with  $q_a n_a \mathbf{u}_a$  gives

$$q_a n_a \mathbf{u}_a \cdot \mathbf{E} \approx 0, \quad a = e, i. \quad (3.40)$$

The resulting model equations for electron and ion energy transport are

**Electron energy transport (EMC3)**

$$\begin{aligned} \nabla \cdot \mathbf{e}_{\parallel} \left[ \frac{5}{2} T_e n_i u_{i\parallel} - \kappa_e \mathbf{e}_{\parallel} \cdot \nabla T_e \right] - \nabla \cdot \mathbf{I}_{\perp} \cdot \left[ \chi_e n_i \nabla T_e + \frac{5}{2} T_e D_{\perp} \nabla n_i \right] \\ = -\frac{3m_e}{m_i} \frac{n_e}{\tau_{ei}} (T_e - T_i) + S_{ee} - \mathcal{S}_{e,\text{cool}} \end{aligned} \quad (3.41)$$

**Ion energy transport (EMC3)**

$$\begin{aligned} \nabla \cdot \mathbf{e}_{\parallel} \left[ \frac{5}{2} T_i n_i u_{i\parallel} - \kappa_i \mathbf{e}_{\parallel} \cdot \nabla T_i \right] - \nabla \cdot \mathbf{I}_{\perp} \cdot \left[ \chi_i n_i \nabla T_i + \frac{5}{2} T_i D_{\perp} \nabla n_i \right] \\ = +\frac{3m_e}{m_i} \frac{n_e}{\tau_{ei}} (T_e - T_i) + S_{ei} \end{aligned} \quad (3.42)$$

where  $S_{ee}$  and  $S_{ei}$  are energy sources due interactions with neutral particles, while  $\mathcal{S}_{e,\text{cool}}$  is an energy sink due to excitation and ionization of impurities. The details of  $\mathcal{S}_{e,\text{cool}}$  will be discussed in the next section.

### 3.3.2 Impurities of small concentration

The transport model for trace impurities is reduced to one balance equation. Due to the similar masses of impurity and main plasma ions (with respect to the electron mass  $m_e$ ), a common temperature  $T_a \approx T_i$  is assumed for all ion species. Parallel momentum is determined by the force balance

$$0 = F_p + F_E + F_{fr} + F_{th,e} + F_{th,i} \quad (3.43)$$

between



$$\text{Pressure gradient:} \quad F_p = -\nabla_{\parallel} p_a \quad (3.44)$$

$$\text{Electrical force:} \quad F_E = Z_a n_a e E_{\parallel} \quad (3.45)$$

$$\text{Frictional force:} \quad F_{fr} = \frac{\mu_{ai} n_a (u_{i\parallel} - u_{a\parallel})}{\tau_{ai}} \quad (3.46)$$

$$\text{Electron thermal force:} \quad F_{th,e} = \alpha_{ae} n_a \nabla_{\parallel} T_e \quad (3.47)$$

$$\text{Ion thermal force:} \quad F_{th,i} = \alpha_{ai} n_a \nabla_{\parallel} T_i \quad (3.48)$$

with  $\alpha_{ae}$  from (3.30) and  $\alpha_{ai}$  from (3.31). This force balance is consistent with a fluid momentum balance equation (3.7) when inertial and viscous contributions are neglected. This assumption significantly changes the quality of this equation: the partial differential equation is reduced to an algebraic equation, which can be directly solved for  $u_{a\parallel}$ . The electrical field in (3.45) is determined by the electron momentum balance by neglecting all terms containing the electron mass:

$$e E_{\parallel} = -\frac{1}{n_e} \nabla_{\parallel} p_e - \alpha_{ie} \nabla_{\parallel} T_e, \quad (3.49)$$

which is consistent with the approach for the momentum balance of the main ions plasma in (3.36). Now the explicit expression for  $u_{a\parallel}$  is:

$$\begin{aligned} u_{a\parallel} &= u_{i\parallel} + \frac{\tau_{ai}}{\mu_{ai}} \left[ c_e Z_a (Z_a - 1) \nabla_{\parallel} T_e + (\alpha_{ai} - 1) \nabla_{\parallel} T_i - \frac{Z_a}{n_e} \nabla_{\parallel} p_e \right] \\ &\quad - \frac{\tau_{ai}}{\mu_{ai} n_a} T_i \nabla_{\parallel} n_a \end{aligned} \quad (3.50)$$

$$= \mathcal{V}_{a\parallel} - \frac{D_{a\parallel}}{n_a} \nabla_{\parallel} n_a, \quad D_{a\parallel} = \frac{\tau_{ai} T_i}{\mu_{ai}} \quad (3.51)$$

This expression for  $u_{a\parallel}$  is then used in the impurity particle balance equation

**Impurity transport (EMC3)**

$$\nabla \cdot [n_a \mathcal{V}_{a\parallel} \mathbf{e}_{\parallel} - D_{a\parallel} \mathbf{e}_{\parallel} \mathbf{e}_{\parallel} \cdot \nabla n_a - D_{a\perp} \mathbf{I}_{\perp} \cdot \nabla n_a] = S_a^{(p)}. \quad (3.52)$$

The sources  $S_a^{(p)}$  on the r.h.s of (3.52) are given by ionization and recombination rates (incl. charge exchange) for impurity ions  $a$  of charge  $Z_a$  and their adjacent charge stages:

$$S_a^{(p)} = R_{Z_a-1 \rightarrow Z_a}^{(\text{ion})} + R_{Z_a+1 \rightarrow Z_a}^{(\text{rec})} - R_{Z_a \rightarrow Z_a+1}^{(\text{ion})} - R_{Z_a \rightarrow Z_a-1}^{(\text{rec})}. \quad (3.53)$$

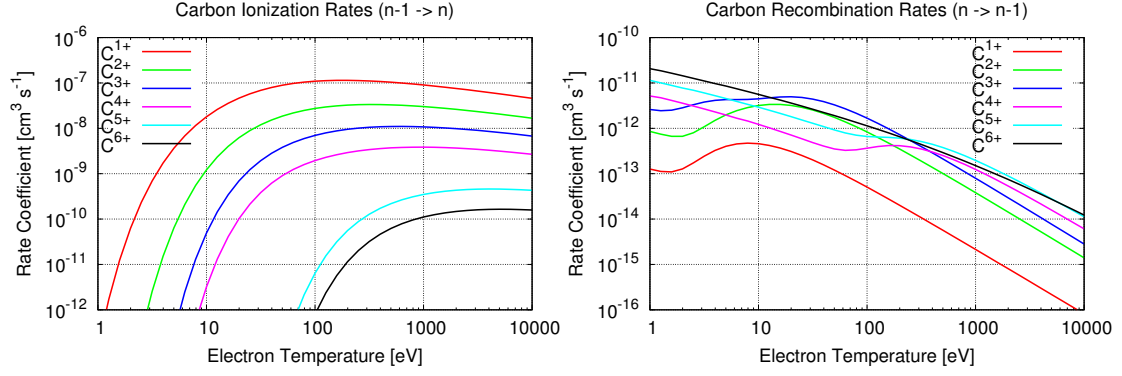


Figure 3.1: Rate coefficients for ionization and recombination of carbon, taken from a Corona model.

The feedback on the main plasma is given by a sink  $\mathcal{S}_{e,\text{cool}}$  in the electron energy equation (3.41) which includes energy losses due to ionization and radiation:

$$\mathcal{S}_{e,\text{cool}} = \sum_{n=0}^{Z_{\text{max}}-1} P_n^{(\text{rad})} + \sum_{n=0}^{Z_{\text{max}}-1} E_n R_{n \rightarrow n+1}^{(\text{ion})}, \quad (3.54)$$

where  $E_n$  is the ionization energy for ions of charge  $n$ .

### Reaction rates

The reaction rates  $P$  and  $R$  in (3.53) and (3.54) are of the generic form

$$X_{ab} = n_a n_b r_{ab} \quad (3.55)$$

where  $r_{ab}$  is the rate coefficient for the specific process between particles of species  $a$  and  $b$ . Rate coefficients for ionization and recombination obtained from a Corona model are presented in figure 3.1 for carbon. The Corona model is valid for an optically thin plasma at low densities such as in the Corona of the sun. In this case excitation and ionization is due to collisions with electrons only (and only from the ground electronic stat), while relaxation and recombination is due to radiative transitions only. The Corona model has been used for the description of impurities in fusion plasmas for many years, e.g. the reaction rates in figure 3.1 are taken from the impurity transport code STRAHL [102] and have also been used in previous transport studies with the EMC3-EIRENE code. Recently, the EMC3-EIRENE code has been advanced to use data from a generalized collisional radiative model [103] for  $R$  and  $P$  provided by the ADAS project [104]. A comparison of the two models and their impact on impurity transport has been investigated in [99].

## 4 Numerical simulation of the plasma edge

The model equations derived in chapter 3 are of a Fokker-Planck similar type. Analytical solutions of the Fokker-Planck equation (FPE) are known only for some special cases [105], and in particular no analytical solution is known for the present 3D case with local, non-linear transport coefficients. Hence, a numerical treatment is necessary. In this chapter the numerical framework of the EMC3-EIRENE code is presented with a focus on the plasma transport part (EMC3).

In section 4.1 a stochastic simulation (Monte Carlo) method for solving linearized FPEs is presented (see e.g. [106] for an introduction to stochastic simulations). The presented method naturally accounts for the strong anisotropy of parallel and cross-field transport processes, because of its formulation within a local, field aligned coordinate system:

$$\mathbf{e}_1 = -\frac{(\mathbf{e}_\parallel \cdot \nabla)\mathbf{e}_\parallel}{|(\mathbf{e}_\parallel \cdot \nabla)\mathbf{e}_\parallel|}, \quad \mathbf{e}_2 = \mathbf{e}_\parallel \times \mathbf{e}_1, \quad \mathbf{e}_3 = \mathbf{e}_\parallel. \quad (4.1)$$

This coordinate system is reconstructed from a field aligned grid which has to be generated in a pre-processing step. The particular field line reconstruction method is described in section 4.2, where the original method implemented in EMC3 is generalized to block-structured grids to allow more flexible configurations. In particular, this generalization has allowed for the first time the application of the 3D edge transport model in chapter 3 to ITER similar plasma scenarios, such as that investigated at the DIII-D tokamak (see chapter 5). A summary of that generalization is given in [107]. In section 4.3 the EMC3-EIRENE code is introduced, presenting the boundary conditions and input parameters for the code. A self-consistent, non-linear solution of the model equations is obtained by an iterative application of the code to the linearized problem. Furthermore, simulation runs on high performance computers are discussed, including convergence criteria for the final solution.

### 4.1 A Lagrangian solver for Fokker-Planck type equations

The model equations for particles (3.35), parallel momentum (3.36) and energy transport (3.41),(3.42) are of the generic type

$$\nabla \cdot [\mathcal{V}_{\text{pl}} \mathcal{F} - \mathcal{D}_{\text{pl}} \cdot \nabla \mathcal{F}] = \mathcal{S}, \quad (4.2)$$

for some plasma quantity  $\mathcal{F}$ , such as ion density  $n_i$ , parallel fluid velocity  $u_{i\parallel}$  or ion and electron temperature  $T_i$  and  $T_e$ , respectively. Continuity equations for impurity transport are of the same type as well. The structure of  $\mathcal{F}$  is determined by a scalar source  $\mathcal{S}$ , convection vector  $\mathcal{V}_{\text{pl}}$  and diffusion tensor  $\mathcal{D}_{\text{pl}}$ . The fast parallel transport processes can be separated from the much slower cross-field ones by considering the special form of  $\mathcal{D}_{\text{pl}}$  in (4.2):

$$\mathcal{D}_{\text{pl}} = \mathcal{D}_{\parallel} \mathbf{e}_{\parallel} \mathbf{e}_{\parallel} + \mathcal{D}_{\perp} (1 - \mathbf{e}_{\parallel} \mathbf{e}_{\parallel}). \quad (4.3)$$

(4.2) can be transformed into a steady state Fokker-Planck type equation

$$\nabla \cdot [\mathcal{V}_{\text{fp}} \mathcal{F} - \nabla \cdot \mathcal{D}_{\text{fp}} \mathcal{F}] = \mathcal{S}, \quad (4.4)$$

with corresponding Fokker-Planck drift and diffusion coefficients  $\mathcal{V}_{\text{fp}}$  and  $\mathcal{D}_{\text{fp}}$ , respectively:

$$\mathcal{V}_{\text{fp}} = \mathcal{V}_{\text{pl}} + \underbrace{\nabla \cdot \mathcal{D}_{\text{pl}}}_{=\mathcal{V}_{\mathcal{D}}}, \quad \mathcal{D}_{\text{fp}} = \mathcal{D}_{\text{pl}}. \quad (4.5)$$

This results in the additional drift  $\mathcal{V}_{\mathcal{D}}$  given by

$$\mathcal{V}_{\mathcal{D}} = \nabla \mathcal{D}_{\perp} + \mathbf{e}_{\parallel} \mathbf{e}_{\parallel} \cdot \nabla (\mathcal{D}_{\parallel} - \mathcal{D}_{\perp}) + \mathbf{e}_{\parallel} (\mathcal{D}_{\parallel} - \mathcal{D}_{\perp}) \nabla \cdot \mathbf{e}_{\parallel} + (\mathcal{D}_{\parallel} - \mathcal{D}_{\perp}) (\mathbf{e}_{\parallel} \cdot \nabla) \mathbf{e}_{\parallel}. \quad (4.6)$$

As mentioned in the introduction, analytical solutions of the Fokker-Planck equation (4.4) are known for some special cases [105], but not for the present case of an extremely anisotropic, highly non-linear, three dimensional set of partial differential equations. Common numerical techniques for solving partial differential equations are finite volume or finite element methods (see e.g. [108, 109, 110]) which belong in the class of Eulerian solvers. Lagrangian schemes provide another class of solvers which are more flexible with regard to the geometry of the problem. For the present problem, the geometry is essentially given by the magnetic field structure, because of the strong anisotropy of parallel and cross-field transport processes. The Lagrangian scheme presented in the following section provides a solver for the linearized version of (4.4). The concept of this technique has been presented in [39] and is only briefly reviewed here. It is based on the relation between the Fokker-Planck equation and a specific Ito stochastic process (see [111]) and involves the simulation of *fluid parcels*  $\Delta \mathcal{F}$ , i.e. weighted trajectories of the stochastic process, with initial distribution determined by  $\mathcal{S}$  and dedicated transition probability  $p = p(\mathbf{x}, t; \mathbf{x}', t + \tau)$  for their dynamics.

### 4.1.1 The Fokker-Planck equation and its relation to stochastic processes

Originally, the Fokker-Planck equation (FPE) was used to describe the Brownian motion of test particles in a fluid [105]. It describes the time evolution of the probability density function for the particle position. However, it can also be applied to the general case of the distribution functions  $\mathcal{F}$ , which is dependent on  $N$  macroscopic variables  $x_i, i = 1, \dots, N$ . The FPE then reads

$$\frac{\partial \mathcal{F}(\mathbf{x}, t)}{\partial t} = \left[ - \sum_{i=1}^N \frac{\partial}{\partial x_i} D_i^{(1)}(\mathbf{x}) + \sum_{i,j=1}^N \frac{\partial^2}{\partial x_i \partial x_j} D_{ij}^{(2)}(\mathbf{x}) \right] \mathcal{F}(\mathbf{x}, t), \quad (4.7)$$

where  $D^{(1)}$  is the drift vector and  $D^{(2)}$  the diffusion tensor. The formulation of a partial differential equation for  $W$  such as (4.7) implies that  $W(\mathbf{x}, t_0 + \tau)$  at some later time  $t_0 + \tau$  is completely determined by  $W(\mathbf{x}, t_0)$ . This feature is closely related to a *Markov process*, which is a stochastic process describing the random evolution of a memoryless system. In the present case (differential equation) one speaks of a continuous Markov process, whereas for neutral particles, when the transitions are described by a (Boltzmann) collision integral, the Markov process is discontinuous (jump process).

Consider a Markov process (in  $N = 3$  dimensions) with transition probability  $p(\mathbf{x}, s | \mathbf{y}, t)$ , then the distribution function  $\mathcal{F}$  fulfills:

$$\mathcal{F}(\mathbf{x}, s) = \int d^3y \, p(\mathbf{x}, s | \mathbf{y}, t) \mathcal{F}(\mathbf{y}, t). \quad (4.8)$$

One can show (see [111]) that for (4.8) to correspond to the FPE (4.7) the following conditions are required for  $p$ :

$$\lim_{t \downarrow s} \frac{1}{t - s} \int_{|\mathbf{y} - \mathbf{x}| > \varepsilon} d^3y \, p(\mathbf{x}, s | \mathbf{y}, t) = 0 \quad (4.9)$$

$$\lim_{t \downarrow s} \frac{1}{t - s} \int_{|\mathbf{y} - \mathbf{x}| < \varepsilon} d^3y \, (\mathbf{y} - \mathbf{x}) p(\mathbf{x}, s | \mathbf{y}, t) = \mathbf{D}^{(1)}(\mathbf{x}, s) \quad (4.10)$$

$$\lim_{t \downarrow s} \frac{1}{t - s} \int_{|\mathbf{y} - \mathbf{x}| < \varepsilon} d^3y \, \frac{1}{2} (\mathbf{y} - \mathbf{x}) (\mathbf{y} - \mathbf{x}) p(\mathbf{x}, s | \mathbf{y}, t) = \underline{\mathbf{D}}^{(2)}(\mathbf{x}, s) \quad (4.11)$$

with  $\varepsilon > 0$ . It can be shown [111, p. 108] that individual sample paths of the stochastic process determined by  $p$  can be described by the Ito stochastic differential equation (SDE)

$$d\mathbf{X}_t = \mathbf{a}(\mathbf{X}_t) dt + \sum_{i=1}^k \mathbf{b}_i(\mathbf{X}_t) dW_t^i, \quad (4.12)$$

for a  $k$ -dimensional Wiener process  $W_t = (W_t^1, \dots, W_t^k)$  and drift and diffusion coefficients  $\mathbf{a}(\mathbf{X}_t)$  and  $\mathbf{b}_i(\mathbf{X}_t)$ , respectively, which fulfill:

$$\mathbf{D}^{(1)} = \mathbf{a}, \quad \underline{\mathbf{D}}^{(2)} = \frac{1}{2} \sum_{i=1}^k \mathbf{b}_i \mathbf{b}_i. \quad (4.13)$$

An approximate solution for the inhomogeneous FPE (4.4) can be obtained by simulating an ensemble of sample paths, i.e. histories of the stochastic process (4.12), with initial distribution and weight determined by  $\mathcal{S}$ . An elaborate review of the relation between the probability density and trajectory point of view is e.g. given in [112].

#### 4.1.2 Discrete time approximation of sample paths

Before turning to a discrete time approximation, parallel and cross-field transport processes in (4.12) are separated in a field aligned coordinate system (4.1) using (4.5) in (4.13) and for  $k = 3$ :

$$\mathbf{a} = \mathcal{V}_{\text{fp}} = a_{\parallel} \mathbf{e}_{\parallel} + \sum_{i=1}^2 a_i \mathbf{e}_i \quad (4.14)$$

$$\mathbf{b}_{1,2} = \underbrace{\sqrt{2 \mathcal{D}_{\perp}}}_{b_{1,2}} \mathbf{e}_{1,2}, \quad \mathbf{b}_3 = \underbrace{\sqrt{2 \mathcal{D}_{\parallel}}}_{b_{\parallel}} \mathbf{e}_{\parallel}. \quad (4.15)$$

Starting from the integral expression of (4.12) for a small, but finite time step  $\tau$  with  $\mathbf{X}_n = \mathbf{X}_{t_n}, t_n = n \tau$  and  $\mathbf{X}_0$  sampled from  $\mathcal{S}$ :

$$\mathbf{X}_{n+1} = \mathbf{X}_n + \sum_{i=1}^2 \int_{t_n}^{t_{n+1}} dt a_i \mathbf{e}_i + \int_{t_n}^{t_{n+1}} dt a_{\parallel} \mathbf{e}_{\parallel} + \sum_{i=1}^2 \int_{t_n}^{t_{n+1}} dW_t^i b_i \mathbf{e}_i + \int_{t_n}^{t_{n+1}} dW_t^{\parallel} b_{\parallel} \mathbf{e}_{\parallel} \quad (4.16)$$

and following the reasoning in [39] and [41] for the parallel transport processes, one obtains that the contribution from  $\mathcal{D}_{\parallel} \mathbf{e}_{\parallel} \mathbf{e}_{\parallel}$  in (4.3) results only (up to a 2nd order expansion of a field line) in a displacement along the field line. All parallel transport processes combined result in the displacement  $\Delta L_n$  along the field line with

$$\Delta L_n = \mathcal{V}_{\text{pl}}^{\parallel} \tau + (\nabla \cdot \mathcal{D}_{\parallel} \mathbf{e}_{\parallel}) \tau + \sqrt{2 \mathcal{D}_{\parallel}} \tau \xi_n, \quad (4.17)$$

where  $\xi_n$  is a Gaussian distributed random variable. The remaining cross-field transport is approximated by:

$$\Delta \mathbf{X}_n^\perp = (a_1 \mathbf{e}_1 + a_2 \mathbf{e}_2) \tau + \sqrt{4 \mathcal{D}_\perp} \tau \mathbf{b}_\perp \quad (4.18)$$

$$a_1 = \mathbf{e}_1 \cdot (\mathcal{V}_{\text{pl}} + \nabla \mathcal{D}_\perp) \quad (4.19)$$

$$a_2 = \mathbf{e}_2 \cdot (\mathcal{V}_{\text{pl}} + \nabla \mathcal{D}_\perp) - \mathcal{D}_\perp |(\mathbf{e}_\parallel \cdot \nabla) \mathbf{e}_\parallel| \quad (4.20)$$

$$\mathbf{b}_\perp = \cos(2\pi\eta_n) \mathbf{e}_1 + \sin(2\pi\eta_n) \mathbf{e}_2, \quad (4.21)$$

where  $\eta_n$  is a uniformly distributed random variable. The choice of cross-field trajectories on a circle reflects a) that the two cross-field unit vectors  $\mathbf{e}_1$  and  $\mathbf{e}_2$  can be selected arbitrarily and b) the isotropic property of cross-field transport. This first order in  $\tau$  approximation of the stochastic integral in (4.16) is known as the Euler-Maruyama approximation for SDEs [113], in analogy to the Euler approximation for ordinary differential equations.

Single trajectories  $j$  of the stochastic process represent *sample fluid parcels*, which are assigned a weight  $w_j$  according to the source distribution  $\mathcal{S}$  (dimension: quantity of  $\mathcal{S} \cdot$  volume). Because of the application of random numbers, this Lagrangian scheme is often also referred to as Monte Carlo (MC) method, while sample fluid parcels are referred to as MC particles (see also appendix A for a discussion of random numbers and their generation in computer simulations). Sampling many such trajectories then allows to approximate the distribution function  $\mathcal{F}$ . E.g. a so called *track length estimator* can be applied in a computational grid with  $N_{\text{cell}}$  cells (see e.g. figure 4.1 and 4.3)

$$\mathcal{F}_i = \frac{1}{V_i} \sum_{j=1}^{N_{\text{MC}}(i)} w_j \tau_{ji}, \quad i = 1, \dots, N_{\text{cell}}, \quad (4.22)$$

$$s_{\mathcal{F},i}^2 = \frac{1}{V_i^2 (N_{\text{MC}}(i) - 1)} \left[ N_{\text{MC}}(i) \sum_{j=1}^{N_{\text{MC}}(i)} (w_j \tau_{ji})^2 - \left( \sum_{j=1}^{N_{\text{MC}}(i)} w_j \tau_{ji} \right)^2 \right] \quad (4.23)$$

to provide an estimate  $\mathcal{F}_i$  of  $\mathcal{F}$  in grid cell  $i$  with standard deviation  $s_{\mathcal{F},i}$ . Here  $V_i$  is the volume of cell  $i$ ,  $w_j$  the weight of MC particle  $j$ ,  $\tau_{ji}$  the time it spend in cell  $i$  and  $N_{\text{MC}}(i)$  the number of MC particles that actually visited cell  $i$ . This terminology results from the case that  $\mathcal{F}$  is a particle flux  $n \cdot v$ , hence  $w_j \sim v$  (velocity of the particle), and hence,  $w_j \cdot \tau_{ji} \sim l$  (length of track in cell  $i$ ).

### 4.1.3 Spatially inhomogeneous transport coefficients

Generally, the representative diffusivity  $\mathcal{D}_{\text{pl}}$  in (4.2) is not constant in space, even in the case where the transport coefficients in their original meaning might be spatially constant, like for the cross-field energy transport where the effective conductivity  $n\chi$  varies in space despite a constant  $\chi$ . The following *two-step* method is used in the

EMC3 code to account for a  $\nabla_{\perp} n$  contribution in the energy balance equation. Its implementation in the code has been advanced in this thesis to include effects of spatially varying  $\chi_e$ ,  $\chi_i$  and  $D_{\perp}$  as well.

Transforming the plasma transport equations of type (4.2) into Fokker-Planck type equations (4.4) introduces the additional drift term  $\mathcal{V}_D = \nabla \mathcal{D}$  in (4.5). E.g. in case of  $\mathcal{D}_{\perp} = \mathcal{D}_{\perp}(\mathbf{x})$ , the explicit calculation of the cross-field derivative in the jump step  $\Delta \mathbf{X}_d = \mathcal{V}_D \tau$  in (4.18) can be avoided by introducing the correction step  $\Delta \mathbf{X}_c$  to the regular diffusion jump step  $\Delta \mathbf{X}_D = \mathbf{b}_{\perp} \sqrt{4\mathcal{D}(\mathbf{X}_n)\tau}$  in (4.18).  $\Delta \mathbf{X}_c$  is determined by the difference of  $\mathcal{D}$  evaluated at  $\mathbf{X}_n$  and  $\mathbf{X}_n + \Delta \mathbf{X}_D$ :

$$\Delta \mathbf{X}_c = \Delta \mathbf{X}_D(\mathbf{X}_n + \Delta \mathbf{X}_D) - \Delta \mathbf{X}_D \quad (4.24)$$

$$= \mathbf{b}_{\perp} \left( \sqrt{4\mathcal{D}(\mathbf{X}_n + \Delta \mathbf{X}_D)\tau} - \sqrt{4\mathcal{D}(\mathbf{X}_n)\tau} \right) \quad (4.25)$$

The equivalence of  $\Delta \mathbf{X}_c$  and  $\Delta \mathbf{X}_d$  (at least on average) for small jumps  $\Delta \mathbf{X}_D$  is seen from the expansion

$$\sqrt{\mathcal{D}(\mathbf{X}_n + \Delta \mathbf{X}_D)} = \sqrt{\mathcal{D}(\mathbf{X}_n)} + \frac{\Delta \mathbf{X}_D \cdot \nabla \mathcal{D}(\mathbf{X}_n)}{2\sqrt{\mathcal{D}(\mathbf{X}_n)}} + O(\Delta \mathbf{X}_D^2). \quad (4.26)$$

Neglecting the higher order terms results in

$$\Delta \mathbf{X}_c = \mathbf{b}_{\perp} \sqrt{4\tau} \frac{1}{2\sqrt{\mathcal{D}(\mathbf{X}_n)}} \Delta \mathbf{X}_D \cdot \nabla \mathcal{D}(\mathbf{X}_n) \quad (4.27)$$

$$= 2 \mathbf{b}_{\perp} \mathbf{b}_{\perp} \cdot \nabla \mathcal{D}(\mathbf{X}_n) \tau. \quad (4.28)$$

Remember  $\mathbf{b}_{\perp}$  from (4.21) which has the property

$$\begin{aligned} \langle 2 \mathbf{b}_{\perp} \mathbf{b}_{\perp} \rangle &= \langle 2 \cos^2(2\pi\eta) \rangle \mathbf{e}_1 \mathbf{e}_1 + \langle 2 \sin^2(2\pi\eta) \rangle \mathbf{e}_2 \mathbf{e}_2 \\ &\quad + \langle 2 \cos(2\pi\eta) \sin(2\pi\eta) \rangle [\mathbf{e}_1 \mathbf{e}_2 + \mathbf{e}_2 \mathbf{e}_1] \end{aligned} \quad (4.29)$$

$$= \mathbf{e}_1 \mathbf{e}_1 + \mathbf{e}_2 \mathbf{e}_2 = \mathbf{I}_{\perp} \quad (4.30)$$

and so on average  $\langle \Delta \mathbf{X}_c \rangle = \Delta \mathbf{X}_d$ . Hence, using  $\Delta \mathbf{X}_c$  from (4.24) rather than  $\Delta \mathbf{X}_d$  therefore allows to avoid the explicit calculation of cross-field derivatives. Spatially varying transport coefficients are e.g. expected in the edge transport barrier region in H-mode plasmas and this procedure is used in section 5.4 for simulations of such plasmas. Several tests have been performed to verify the correct implementation in the EMC3-EIRENE code (see appendix B.2). The nature of this two-step method is consistent with a Stratanovich interpretation of the SDE (4.12) which is equivalent to (4.2) if the unmodified transport coefficients  $\mathcal{V}_{pl}$  and  $\mathcal{D}_{pl}$  are used in (4.13).



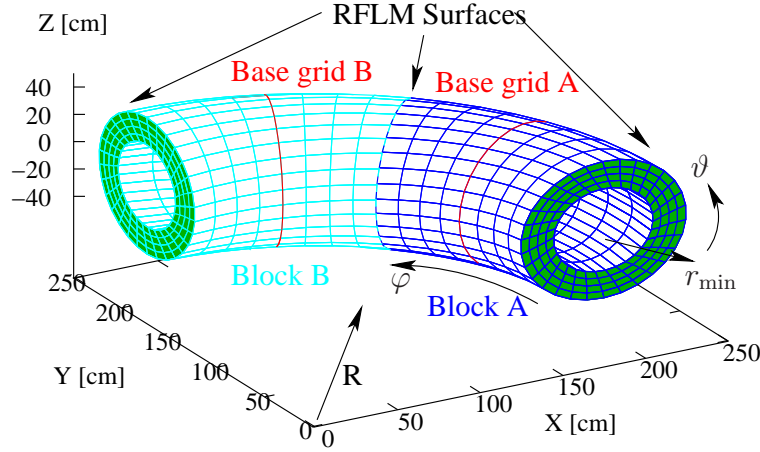


Figure 4.1: Field aligned grid with 2 toroidal blocks of  $\Delta\varphi = 45$  deg each. This kind of grid is e.g. used for simulations of the edge plasma at the TEXTOR tokamak in the presence of an RMP field with 4-fold toroidal symmetry.

## 4.2 Fast reconstruction of magnetic field lines

The application of the numerical method presented in the previous section requires jump steps along and perpendicular to magnetic field lines. Although it is in principle possible to use one of the integration methods for field lines which were discussed in section 2.3.2, a field line reconstruction method can be used to speed up plasma transport calculations.

The field line reconstruction method described below is based on a computational grid (see figure 4.1) which is constructed from a set of pre-calculated field lines. This procedure allows a speed-up of 3-4 orders of magnitude with respect to full field line integration “on the fly” at the position of fluid parcels. The generation process for such a magnetic field aligned grid is described in section 4.2.1. Magnetic field lines can be reconstructed from this grid by interpolation, this is described in section 4.2.2. The computational grid is divided into several blocks in toroidal direction (e.g. blocks A and B in figure 4.1, hereafter referred to as toroidal blocks) to prevent strong grid deformations in ergodic regions. For this, a field line mapping between adjacent blocks is introduced in section 4.2.3. A similar *multiple local magnetic coordinate system approach* is e.g. used in the 3D heat transport code for edge plasmas E3D [114]. Contrary to the cubic spline interpolation scheme used there, the method used here applies a simpler, (tri-) linear interpolation scheme, which is regarded as sufficiently accurate but still simple enough to allow calculations of plasma fluid transport (in magnetic coordinates) as well as kinetic neutral particle transport (in Cartesian coordinates) within one single geometry module.

### 4.2.1 Generation of a field aligned grid

Each toroidal block  $m$  ( $= A, B$  in figure 4.1) of the 3D magnetic field aligned grid is generated by tracing field lines starting from a 2D base grid at a fixed toroidal position  $\varphi = \Phi_m$ . For the purpose of field line interpolation (see section 4.2.2) the base grid is made up of quadrilaterals. The generation process of the 3D grid can be divided into the following steps:

1. Determine toroidal range for the simulation domain according to the symmetry of the selected plasma scenario (e.g.  $\Delta\varphi_{\text{sim}} = 180$  deg for an  $m/n = 6/2$  RMP scenario at TEXTOR (see section 2.2 or chapter 6) or  $\Delta\varphi_{\text{sim}} = 120$  deg for an  $n = 3$  RMP scenario at DIII-D (see chapter 5).
2. Divide the simulation domain into  $n_Z$  toroidal blocks of size  $\Delta\varphi_{\text{block}} = \Delta\varphi_{\text{sim}}/n_Z$ . For TEXTOR simulations a value of  $\Delta\varphi_{\text{block}} = 45$  deg is typically used [45] (i.e. 2 blocks for the  $m/n = 12/4$  configuration or 4 blocks for the  $m/n = 6/2$  configuration), while for DIII-D simulations a value of  $\Delta\varphi_{\text{block}} = 40$  deg is chosen, which is close to the TEXTOR value but reflects the different toroidal symmetry at DIII-D.
3. To prepare the base grid, at first the inner and outer simulation boundary is generated for each toroidal block. A closed magnetic surface is taken as inner simulation boundary, which is marked green in figure 4.2 for an example of a poloidal divertor configuration. It is obtained by the Poincaré method described in section 2.4.1. At the outer plasma edge no such magnetic surface exists in the presence of RMPs. In this case the reference scenario without RMPs is considered to obtain the  $R, Z$ -contours of field lines on the unperturbed magnetic surface. For poloidal divertor configurations two separate field lines are taken to identify the outer SOL boundary and the lower boundary of the private flux region, respectively (both marked light blue in figure 4.2).
4. Make a quadrilateral decomposition to provide a 2D base grid for each toroidal block. For TEXTOR simulations it is sufficient to perform a regular structured decomposition in the radial and poloidal coordinate, such as in figure 4.1. This is, however, not appropriate for simulations of poloidal divertor configurations such as DIII-D, because of the remoteness of the divertor plates from the inner edge plasma boundary and the corresponding strong poloidal non-uniformity of the radial width of the simulation domain (compare figure 4.2 and 2.2). For poloidal divertor tokamaks, a uniform discretization would either lead to issues related to the spatial resolution in different regions of the computational domain (divertor region vs. upstream region) or, when extending the simulation domain to a uniform radial width, largely waste computational resources. Therefore, a block-structured decomposition is more appropriate.

The block-structured decomposition into quadrilaterals is guided by the unperturbed separatrix (red line in figure 4.2). Each block has its own radial and poloidal resolution  $n_r, n_p$ , only  $n_p^{(2)} = n_p^{(1)} + n_p^{(3)}$  is required for a continuous transition be-

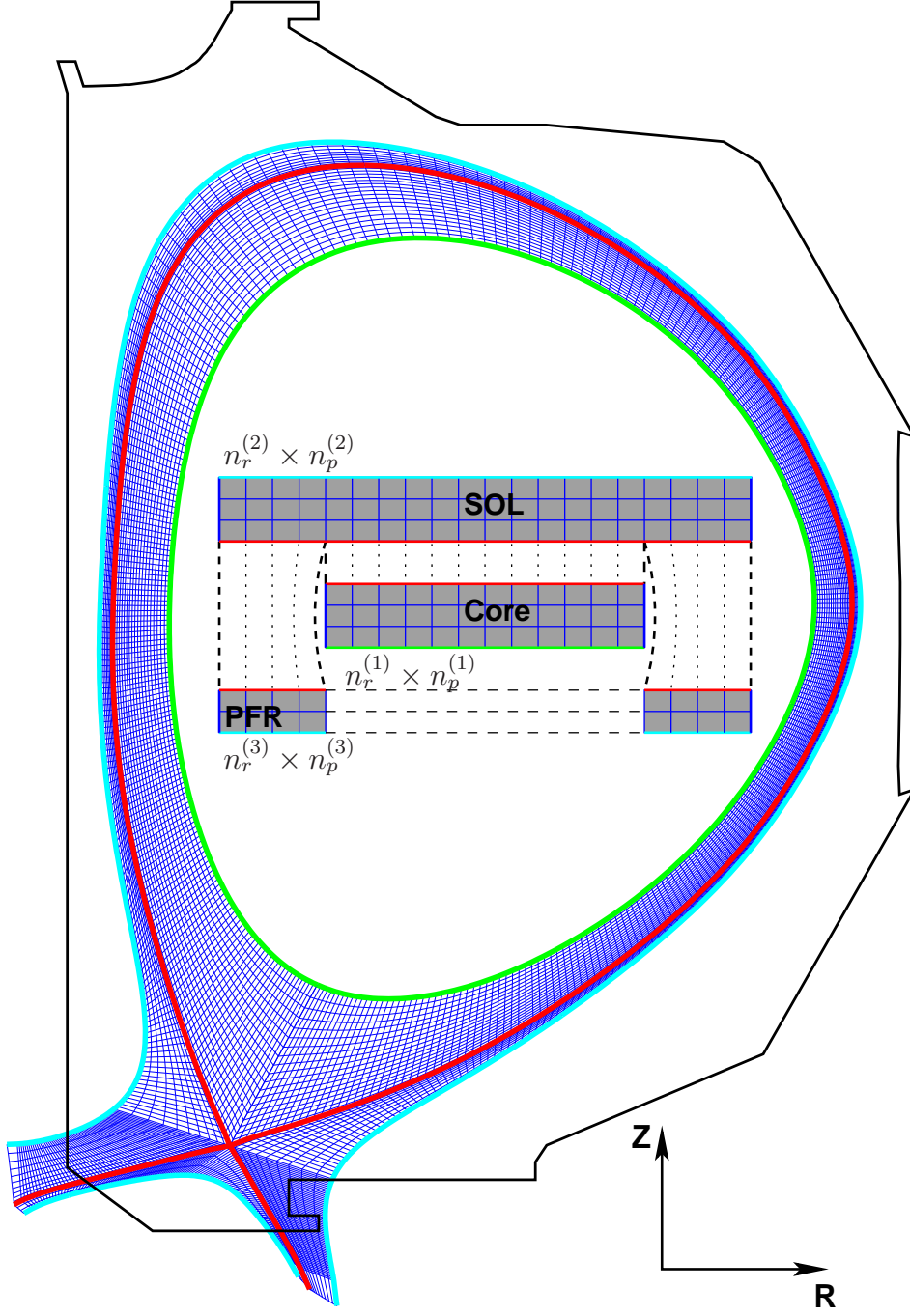


Figure 4.2: Example of a base grid for a poloidal divertor configuration. The simulation domain is bounded on the inside by a closed magnetic flux surface (green) and on the outside by  $R, Z$ -contours of unperturbed field lines in the SOL and in the private flux region (light blue). The decomposition into quadrilaterals is guided by the unperturbed separatrix (red):  $\psi^* = 1$ , eq. (2.15).

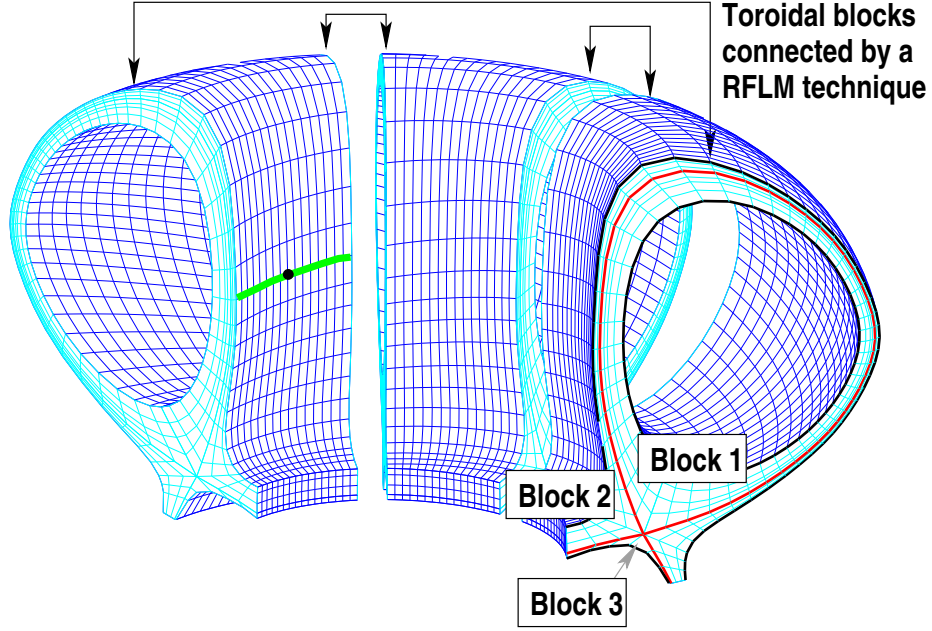


Figure 4.3: 3D field aligned grid for a poloidal divertor configuration with 3 toroidal blocks, where each toroidal block is made up of 3 sub-blocks. The toroidal blocks are continuous in real space, but shifted apart in this figure to highlight the grid structure.

tween blocks. A topological view of this kind of decomposition is given in the inset in figure 4.2. The following grid resolution is used for the simulations in chapter 5:

	$n_r$	$n_p$
Core (Block 1)	48	720
SOL (Block 2)	32	864
PFR (Block 3)	6	144

However, a lower resolution is chosen for the example in figure 4.2 for the purpose of visualization. Grid points of the base grid in toroidal block  $m$  at  $\varphi = \Phi_m$  are labeled

$$\begin{aligned}
 \mathbf{x}_{\mathbf{i}}^{(\text{base})} &= (R_{\mathbf{i}}, Z_{\mathbf{i}}), & \mathbf{i} &= {}_{ij}^{(lm)}, & m &= 1, \dots, n_Z & (4.31) \\
 & & & & l &= 1, 2, 3 \\
 & & & & i &= 0, \dots, n_r^{(l,m)} \\
 & & & & j &= 0, \dots, n_p^{(l,m)}.
 \end{aligned}$$

5. The 3D grid is created by tracing field lines  $\mathbf{x}_i(\varphi)$  (such as the green line in figure 4.2), starting from  $\mathbf{x}_i^{(\text{base})}$  (black dot) in steps of  $\Delta\varphi = \Delta\varphi_{\text{block}}/n_t$  in forward and backward direction, where  $n_t$  is the toroidal resolution. This provide the grid points

$$\mathbf{x}_{i,k} = \mathbf{x}_i(\varphi_k^m), \quad \varphi_k^m = \Phi_m + \frac{k - n_t/2}{n_t} \Delta\varphi_{\text{block}}, \quad k = 0, \dots, n_t. \quad (4.32)$$

Later, field lines are approximated by these grid points by

$$\mathbf{x}_i^*(\varphi) = (1 - \varphi^*) \mathbf{x}_{i,k} + \varphi^* \mathbf{x}_{i,k+1} \quad (4.33)$$

$$\varphi^* = \frac{\varphi - \varphi_k^m}{\varphi_{k+1}^m - \varphi_k^m}, \quad \varphi \in [\varphi_k^m, \varphi_{k+1}^m]. \quad (4.34)$$

An example of such a 3D grid is shown in figure 4.3, where toroidal blocks are shifted apart to highlight the grid structure.

#### 4.2.2 Interpolation of field lines

Any magnetic field line can now easily be reconstructed within each toroidal block by a bilinear interpolation

$$\mathbf{x}(\xi, \eta, \varphi) = \sum_{n=1}^4 \mathbf{x}_{i_n}^*(\varphi) N_n(\xi, \eta), \quad \xi, \eta \in [-1, 1], \quad (4.35)$$

where  $\{\mathbf{i}_n; n = 1, \dots, 4\}$  denotes the set of the 4 surrounding field lines from (4.33).  $N_n(\xi, \eta)$  are the shape functions of a 4-node (bilinear) quadrilateral which are well-known in finite element methods (see e.g. [108]):

$$N_n(\xi, \eta) = \frac{1}{4} (1 + \xi_n \xi) (1 + \eta_n \eta) \quad (4.36)$$

and

$n$	1	2	3	4
$\xi_n$	-1	1	1	-1
$\eta_n$	-1	-1	1	1

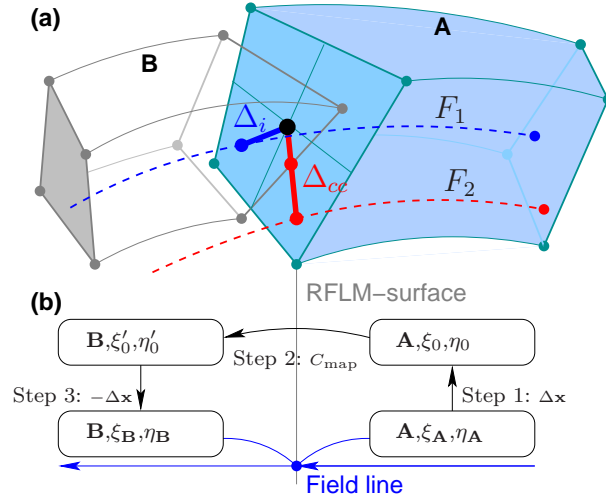


Figure 4.4: (a) Two hexahedral grid cells at the interface between toroidal blocks. (b) Schematic view of the numerical realization of the reversible field line mapping technique.

This setup defines a local, field aligned coordinate system, where coordinate lines given by  $(\xi, \eta) = (\xi_0, \eta_0)$  are field line representations, i.e. a field line is parameterized by the toroidal angle  $\varphi$  with its corresponding  $(R, Z)$  coordinates given by (4.35). This provides a simple and fast method to reconstruct field lines within a toroidal block. For a complete field line reconstruction, however, this method has to be combined with a field line mapping between adjacent blocks, which is described in the following section.

### 4.2.3 Mapping of field line coordinates

The field line coordinates  $\xi, \eta$  have to be mapped from one toroidal block to the adjacent one at their mutual interface, while the real space position  $\mathbf{x}_{\text{real}}$  is fixed. Such a procedure has been described in [49] for the application in 3D plasma edge modeling codes. This section provides the details of an efficient numerical implementation, which has been advanced in this thesis to allow block-structured decompositions.

The continuity condition for a field line at the interface plane  $\varphi_{\text{int}}$  between toroidal block A and B (figure 4.4 (a)) reads

$$\mathbf{x}_A(\xi_A, \eta_A, \varphi_{\text{int}}) = \mathbf{x}_{\text{real}} = \mathbf{x}_B(\xi_B, \eta_B, \varphi_{\text{int}}), \quad \mathbf{A} = \begin{pmatrix} l_A A \\ i_A, j_A \end{pmatrix}, \mathbf{B} = \begin{pmatrix} l_B B \\ i_B, j_B \end{pmatrix} \quad (4.37)$$

where  $\mathbf{x}_A, \mathbf{x}_B$  are given by (4.35) evaluated in the respective grid cells denoted by  $\mathbf{A}, \mathbf{B}$ . For (4.37) to be a reversible mapping, it is necessary that the quadrilateral faces at the interface are convex [115]. This ensures the invertability of (4.35).

The tricky part of (4.37) is that while the cell number  $\mathbf{A}$  in toroidal block  $A$  is known (assuming the field line needs to be traced from block  $A$  to  $B$ ), the cell number  $\mathbf{B}$  in the adjacent toroidal block  $B$  is not a priori known. This is because of the discontinuous cell interface between toroidal blocks (see figure 4.4 (a)). Finding the correct cell number  $\mathbf{B}$  and accordingly the field line coordinates  $(\xi_{\mathbf{B}}, \eta_{\mathbf{B}})$  is necessary to obtain the field line representation in toroidal block  $B$ . However, this task can be numerically quite expensive for a given point  $\mathbf{x}$  in a large grid, which is usually the case when accurate field line reconstruction is required. To minimize the computational effort, the following *reference-field-line* method can be applied instead.

A coarse cell mapping  $C_{\text{map}}$  is defined in a pre-processing step, only once for each magnetic configuration. This mapping is defined for one reference field line  $(\xi_0, \eta_0)$  in each cell at a toroidal block boundary, e.g. for  $\xi_0, \eta_0 = 0$  (black dot in figure 4.4.a), and returns the corresponding position  $(\xi'_0, \eta'_0)$  in block  $B$ :

$$C_{\text{map}} : \mathbf{A} \rightarrow (\mathbf{B}, \xi'_0, \eta'_0). \quad (4.38)$$

Once this mapping is set up, it can be used to speed up the procedure for solving (4.37) for any point  $(\xi_{\mathbf{A}}, \eta_{\mathbf{A}})$  (see schematic view of this procedure is given in figure 4.4 (b)):

1. Calculate the displacement  $\Delta \mathbf{x}$  between the current and the reference field line

$$\Delta \mathbf{x} \equiv \mathbf{x}^{(\mathbf{A})}(\xi_0, \eta_0) - \mathbf{x}^{(\mathbf{A})}(\xi_{\mathbf{A}}, \eta_{\mathbf{A}}), \quad (4.39)$$

whenever a field line defined by  $(\mathbf{A}, \xi_{\mathbf{A}}, \eta_{\mathbf{A}})$  at a toroidal block boundary needs to be mapped to the adjacent toroidal block.

2. Carry out the precomputed mapping  $C_{\text{map}}$  for the reference point  $(\xi_0, \eta_0)$  in cell  $\mathbf{A}$  to find the intermediate coordinates  $(\mathbf{B}, \xi'_0, \eta'_0) = C_{\text{map}}(\mathbf{A})$ .
- 3a. Use (4.35) to relate  $\Delta \mathbf{x}$  from (4.39) to the corresponding displacement  $(\Delta \xi_{\mathbf{B}}, \Delta \eta_{\mathbf{B}})$  in the new field line coordinates. If  $(\Delta \xi_{\mathbf{B}}, \Delta \eta_{\mathbf{B}})$  remains within cell  $\mathbf{B}$  (such as for the blue displacement  $\Delta_i$  in figure 4.4 (a)), then

$$(\mathbf{B}, \xi_{\mathbf{B}}, \eta_{\mathbf{B}}) = C(\mathbf{A}) - (0, \Delta \xi_{\mathbf{B}}, \Delta \eta_{\mathbf{B}}), \quad (4.40)$$

are the new field line coordinates in block  $B$ . These are the exact coordinates of the field line.

- 3b. However, in case of cell crossing displacements like  $\Delta_{cc}$  (red displacement in figure 4.4.a) the step  $\Delta_{cc}$  is segmented into two parts, while the cell number  $\mathbf{B}$  is updated at the cell boundary. Also, the local field line coordinates need to be transformed between adjacent cells. The details of this procedure depend on the grid topology.

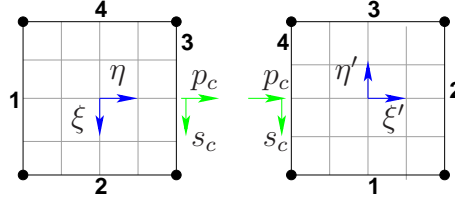


Figure 4.5: Orientation of the local coordinate systems, i.e. cell surfaces  $i_{\text{surf}}$ ,  $i'_{\text{surf}}$  between adjacent cells. Example:  $\eta = 1$  - surface ( $i_{\text{surf}} = 3$ ) meets  $\xi' = -1$  - surface ( $i'_{\text{surf}} = 4$ ). Local coordinates can be related to a surface coordinate  $s_c$  and a perpendicular coordinate  $p_c$  at the cell interface.

### Structured grids

In structured grids with radial, poloidal and toroidal cell indices  $i_r = 0, \dots, n_r - 1$ ;  $i_p = 0, \dots, n_p - 1$ ;  $i_t = 0, \dots, n_t - 1$ , the updated cell number and the corresponding coordinate transformation are given by the simple relation:

$$i'_p = (i_p \pm 1) \mod n_p, \quad \xi' = \xi, \quad \eta' = \mp 1 \quad (4.41)$$

$$\text{or } i'_r = i_r \pm 1, \quad \xi' = \mp 1, \quad \eta' = \eta \quad (4.42)$$

at poloidal (4.41) or radial (4.42) cell surfaces, respectively. The advantage of structured grids is that (4.41) and (4.42) are rather simple to compute, however, the disadvantage is that structured grids have only a very limited flexibility regarding the shape of the simulation domain. In particular, as stated above, the simulation of a poloidal diver-tor configuration requires at least a block-structured decomposition of the simulation domain, which is a special case of an unstructured decomposition.

### Unstructured grids

The field line reconstruction method described above is still applicable in unstructured grids, only (4.41) and (4.42) need to be generalized. In unstructured grids, the grid connectivity is defined by a neighbor relation  $M_{\text{neigh}}$  between adjacent cells  $\mathbf{A}$ ,  $\mathbf{B}$  (see figure 4.5 for the numbering convention of cell surfaces  $i_{\text{surf}}$ ,  $i'_{\text{surf}}$ ):

$$M_{\text{neigh}} : (\mathbf{A}, i_{\text{surf}}) \leftrightarrow (\mathbf{B}, i'_{\text{surf}}). \quad (4.43)$$

Because of the particular field line reconstruction method, the local field line coordinates need to be transformed as well (figure 4.5). For this an additional transformation matrix  $\underline{\mathbf{M}}_{\xi\eta}$  needs to be defined:



$$(\xi', \eta') = \underline{\mathbf{M}}_{\xi\eta} \cdot (\xi, \eta), \quad (4.44)$$

where  $\varphi$  is fixed in the special case when the structure in toroidal direction remains. This transformation matrix depends on the relative orientation of the surfaces  $i_{\text{surf}}, i'_{\text{surf}}$  (for details see appendix B.1):

$$\underline{\mathbf{M}}_{\xi\eta}(i_{\text{surf}}, i'_{\text{surf}}) = (-1)^k \cdot \underline{\mathbf{M}}_j \quad (4.45)$$

with

$$\underline{\mathbf{M}}_0 = \begin{pmatrix} 1 & 0 \\ 0 & -1 \end{pmatrix}, \quad \underline{\mathbf{M}}_1 = \begin{pmatrix} 0 & 1 \\ 1 & 0 \end{pmatrix} \quad (4.46)$$

and integer valued indices  $k, j$ :

$$k = \lfloor (i_{\text{surf}} + i'_{\text{surf}})/2 \rfloor, \quad j = (i_{\text{surf}} + i'_{\text{surf}}) \bmod 2.$$

As was already shown in figures 4.2 and 4.3, not a fully unstructured grid, but a block-structured decomposition is sufficient for the edge plasma simulations at DIII-D in chapter 5. Grid cells at block boundaries are connected by  $(M_{\text{neigh}}, \underline{\mathbf{M}}_{\xi\eta})$  from (4.43) and (4.45), while a regular structure remains within each block. This allows the application of (4.41) and (4.42) inside each block. While the decomposition guided by the unperturbed separatrix seems natural from a magnetic configurational point of view, the method described above is flexible enough to allow for different kind of decompositions as well.

This generalized field line reconstruction method has been implemented in the 3D plasma and neutral gas transport code EMC3-EIRENE within the scope of this thesis. The numerically correct implementation is analyzed in appendix B.1.

### 4.3 The EMC3-EIRENE code package

The Lagrangian method for solving Fokker-Planck equations from section 4.1 is combined with the field line reconstruction method from section 4.2 and implemented in the 3D edge plasma transport code EMC3. Interaction of the edge plasma with - and transport of - neutral gas are treated by the EIRENE code. The details of neutral particle production and transport in the EIRENE code are beyond the scope of this thesis and can be found in references [116, 31]. Both codes, EMC3 and EIRENE, are iteratively coupled to obtain a self-consistent solution of the edge plasma in interaction with neutral particles (see figure 4.6). The EMC3 code is divided into three modules for the calculation of individual plasma parameter.

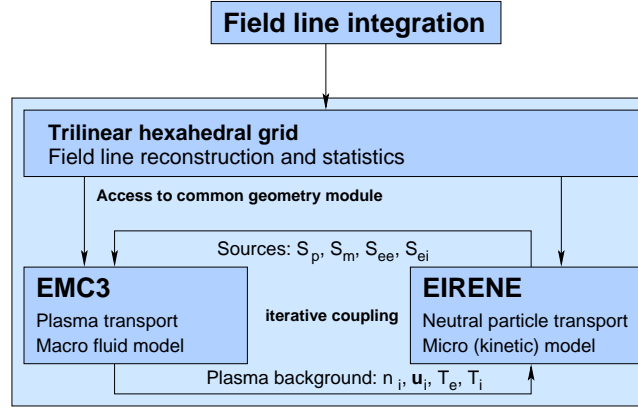


Figure 4.6: Schematic view of the EMC3-EIRENE code package.

The STREAMING module combines the calculation of main plasma density  $n_i$  and parallel flow  $u_{i\parallel}$ , the ENERGY module combines the calculation of electron and ion temperatures  $T_e$  and  $T_i$ , and the IMPURITY module combines the calculation of the densities  $n_a, a = 0, \dots, Z$  for an impurity species with nuclear charge  $Z$  (e.g.  $Z = 6$  for carbon). In summary:

Plasma parameter	Module in the EMC3-code
$T_e, T_i$	ENERGY
$n_i, u_{i\parallel}$	STREAMING
$n_a, a = 0, \dots, Z$	IMPURITY

Plasma parameters are evaluated on a computational grid by (4.22), which is the sum of the individual contributions of the simulated fluid parcels. In the following, this grid is referred to as *plasma grid*, because the plasma parameter are defined on it. It is not necessarily the same as the grid used for field line reconstruction (the latter being referred to as *magnetic grid*), as counting sample paths is independent from the magnetic field structure. However, for convenience the plasma grid is based on the magnetic grid. Firstly, the limiting surfaces such as walls or divertor targets are approximated in the plasma grid by “cutting-out” all cells in which the center point is located behind this surfaces (from the plasma point of view). This is demonstrated by the dashed areas in figure 4.7. Boundary conditions for the plasma are then defined on these approximated surfaces (see below). However, plasma conditions are mapped to the real surface for the coupling to the neutral transport code EIRENE (see [77]). Close to the wall the same resolution is used for the plasma grid and for the magnetic grid, because in this region typically large parallel gradients occur. Further inside, several magnetic grid cells in toroidal direction are combined to one plasma grid cell.

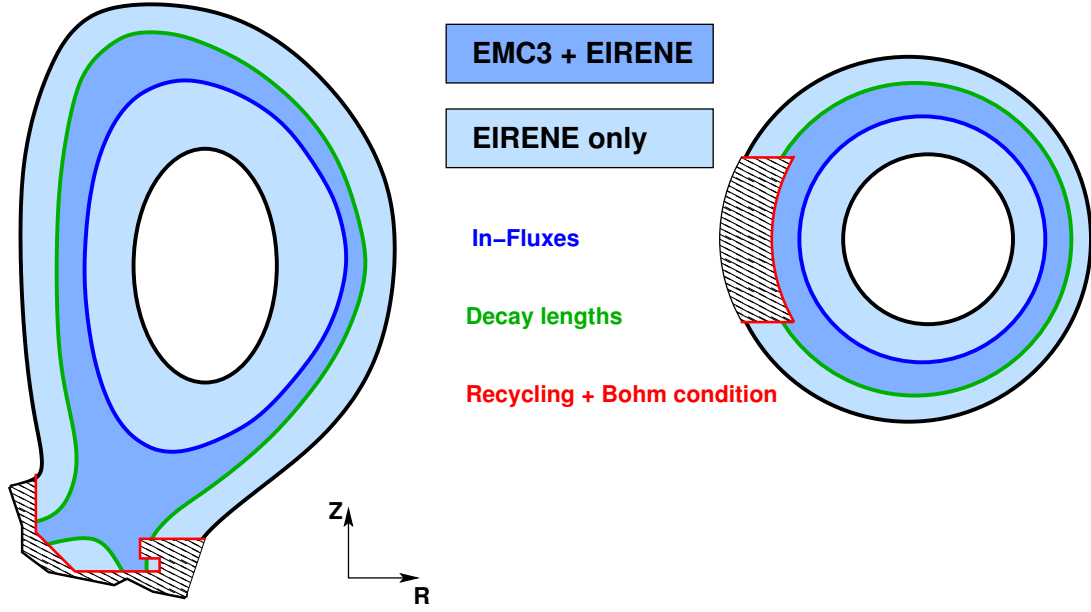


Figure 4.7: Schematic view of the simulation domain and the type of local boundary conditions applied in the EMC3-EIRENE code: for the DIII-D tokamak (left) and the TEXTOR tokamak (right).

#### 4.3.1 Boundary conditions and input parameters

Boundary conditions are necessary for solving partial differential equations such as the plasma transport equations (3.35), (3.36), (3.41) and (3.42). Different kinds of boundary conditions are applied in the EMC3-EIRENE code (see figure 4.7).

- **Inner simulation boundary:** (marked dark blue in figure 4.7) The boundary conditions at the inner simulation domain are prescribed total fluxes across that surface.

$\Gamma_{\text{in}}^{(p)}$	Particle in-flux (main plasma)
$\Gamma_{\text{in}}^{(m)}$	Parallel momentum in-flux
$\Gamma_{\text{in}}^{(e,i)}$	Energy in-flux (power) for electrons and ions
$\Gamma_{\text{in}}^{(imp,a)}$	In-flux for impurity species $a$

To obtain the particle in-flux  $\Gamma_{\text{in}}^{(p)}$  for the core plasma, the simulation domain for EIRENE is extended further inside to the core plasma. All neutrals which are ionized in this region are considered to contribute to  $\Gamma_{\text{in}}^{(p)}$  in steady state. No cross-field transport of parallel momentum is assumed at the inner simulation boundary, i.e.  $\Gamma_{\text{in}}^{(m)} = 0$ . The energy in-flux is  $\Gamma_{\text{in}}^{(e,i)}$  is set to the effective heating power  $P_{\text{in}} = P_{\text{heat}} - P_{\text{rad}}^{(\text{core})}$  taken from experimental observations, where  $P_{\text{heat}}$  is the total heating power and  $P_{\text{rad}}^{(\text{core})}$  the radiated power in the core plasma.  $P_{\text{in}}$  is

distributed in equal parts to electrons and ions, hence  $\Gamma_{\text{in}}^{(e)} = \Gamma_{\text{in}}^{(i)} = \frac{1}{2} P_{\text{in}}$ . No mass accumulation in the core is assumed for impurities with atomic number  $Z$  in steady state:

$$\sum_{a=0}^Z \Gamma_{\text{in}}^{(imp,a)} = 0. \quad (4.47)$$

The distribution to individual charge stages is left as a free parameter, which is analyzed in section D.2. In addition to these fluxes, the plasma density  $n_{\text{in}}$  at the inner simulation boundary is prescribed. This is realized iteratively by scaling the total target particle flux  $\Gamma_{\text{target}}$  accordingly.

- **Outer simulation boundary:** (marked green in figure 4.7) At the outer simulation boundary and for purely diffusive cross-field transport, an exponential decay is expected for each plasma parameter. This decay is characterized by e-folding lengths  $\lambda_p, \lambda_m, \lambda_{ee}, \lambda_{ei}, \lambda_{imp,Z}$ . If, however, the simulation domain extends far enough outward into the SOL, then these parameters are of no significance in the simulations [117]. Decay lengths are related to absorption / reflection probabilities for the realization within a Monte Carlo scheme.

The outer simulation boundary for EIRENE, i.e. for neutral gas transport, is extended further outside to include the complete divertor region. This is necessary, because neutral particles are not bound to the magnetic field and can propagate freely also in regions with no plasma. At these outer- and innermost surfaces for EIRENE (black boundaries in figure 4.7) reflection and thermal re-emission of neutral particles is assumed.

- **Target surfaces:** (marked red in figure 4.7) At target surfaces 100 % recycling of the plasma is assumed. That is plasma ions and electrons recombine to neutral particles. Hence, the target particle flux distribution  $\Gamma_{\text{target}}$  provides the source for neutral particles. The Bohm condition [101, 7] of sonic flow  $u_{i\parallel} = c_s$  with the local ion sound velocity  $c_s$  provides the boundary condition for parallel momentum, while the electron and ion heat flux is related to the particle flux by sheath heat transmission coefficients  $\gamma_e = 2.5$  and  $\gamma_i = 4.5$ , respectively:

$$q_{\text{target}}^{(e)} = \gamma_e T_e \Gamma_{\text{target}}, \quad q_{\text{target}}^{(i)} = \gamma_i T_i \Gamma_{\text{target}}, \quad c_s = \sqrt{\frac{T_e + T_i}{m_i}}. \quad (4.48)$$

In addition to these boundary conditions, coefficients for anomalous cross-field transport  $D_{\perp}, \chi_e, \chi_i$  have to be specified as input parameters in order to fully determine the transport problem to be solved. A spatial distribution of  $D_{\perp}, \chi_e, \chi_i$  can be described as well, e.g. for the analysis of H-mode plasmas in section 5.4. The implementation in the code is based on the procedure described in section 4.1.3.

### 4.3.2 Parallelization and scalability

The numerical implementation of the Lagrangian algorithm presented in section 4.1 is ideally suited for parallelization on multi-processor computing architectures. Each calculation of the plasma parameter, i.e. each iteration step, can be divided into the following steps:

- Calculate transport coefficients  $\mathcal{V}_{\text{fp}}$  and  $\mathcal{D}_{\text{fp}}$
- Sample trajectories of fluid parcels
- Collect contributions from each fluid parcel in each grid cell and calculate plasma quantities according to (4.22)

Here the major numerical effort is to generate the trajectories. The calculation of transport coefficients is independent from cell to cell and therefore can be easily distributed to  $N_{\text{CPU}}$  computing cores. Also fluid parcels are independent from each other and can therefore be distributed to several computing cores as well. The code is parallelized with the MPI (Message Passing Interface) library [118]: Transport coefficients are broadcasted to all  $N_{\text{CPU}}$  processes and then trajectories of fluid parcels are sampled on each process separately. Finally, results from each computing core are gathered and stored for the next iteration step.

This parallelization scheme allows to run the EMC3-EIRENE code on several high performance computers. The simulations presented in this thesis have been performed on the following systems:

- **JUMP** (Jülich Multi Processor) [119], an IBM Power6 575 cluster of 14 nodes with 32 processors each.
- **JuRoPA/HPC-FF** (Jülich Research on Petaflop Architectures) [120], a cluster of 2208+1080 nodes of 2 Intel Xeon X5570 (Nehalem-EP) quad-core processors each.
- **VIP** [121], another IBM Power6 575 cluster, located at Rechenzentrum Garching, 205 nodes with 32 processors each.

Performance tests have been carried out for the STREAMING module ( $n_i, u_{i\parallel}$  calculation) and for the ENERGY module ( $T_e, T_i$  calculation). These tests have been performed on the VIP system at Rechenzentrum Garching with simulations of an RMP scenario at TEXTOR. The performance is measured by the speedup

$$S(N_{\text{CPU}}) = \frac{T(N_{\text{CPU}})}{T(1)} \quad (4.49)$$

which is the ratio between the run times  $T$  on  $N_{\text{CPU}}$  processors and on one processor, where the total number of MC particles  $N_{\text{MC}} = N_{\text{CPU}} \times N_{\text{MC}} / \text{CPU}$  is kept constant. The speedup of the EMC3-EIRENE code is shown in figure 4.8. It can be seen that

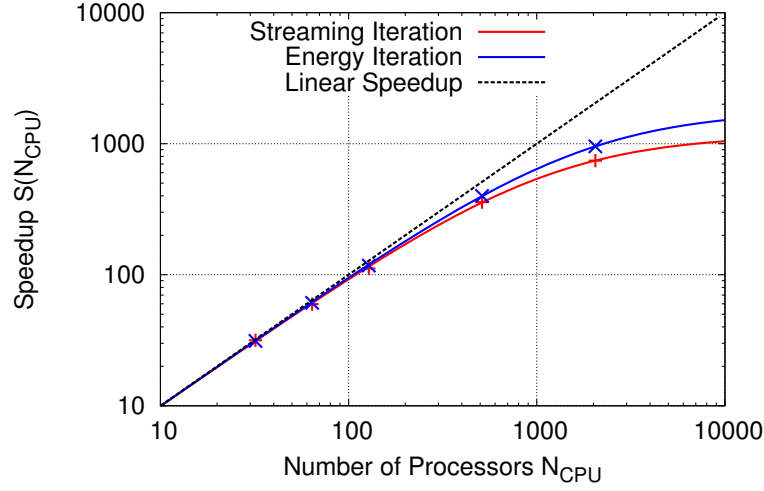


Figure 4.8: Speedup of the STREAMING ( $n_i$ ,  $u_{i\parallel}$  calculation) and ENERGY ( $T_e$ ,  $T_i$  calculation) modules of the EMC3-EIRENE code. The test case is an RMP scenario at the TEXTOR tokamak.

the speedup for the given  $N_{MC}$  and the selected TEXTOR configuration is almost linear up to  $N_{CPU} = 512$  processors, for both the STREAMING and ENERGY subroutines. Following Amdahl's [122] law for the speedup of a parallelized program

$$S(N_{CPU}) = \frac{1}{r_s + \frac{r_p}{N_{CPU}}} \quad r_s + r_p = 1, \quad (4.50)$$

allows to estimate the fraction  $r_s$  of the program that remains sequential. A fit of (4.50) to the data in figure 4.8 using GNUPLLOT [123] yields

$$r_s(\text{STREAMING}) = (0.86 \pm 0.02) \cdot 10^{-3}, \quad r_s(\text{ENERGY}) = (0.56 \pm 0.01) \cdot 10^{-3} \quad (4.51)$$

for the sequential parts of the STREAMING and ENERGY module, respectively. Note that these results strongly depend on the value of  $N_{MC}$  and the selected plasma scenario (magnetic field configuration, boundary conditions, transport coefficients). The sequential part  $r_s$  limits the maximum number of CPUs that can be used for an efficient speedup. Certainly, this limit will shift upwards when more MC particles have to be traced for better statistics required in specific problems. Thus, a hard CPU limit does not exist for the EMC3-EIRENE code in this sense.

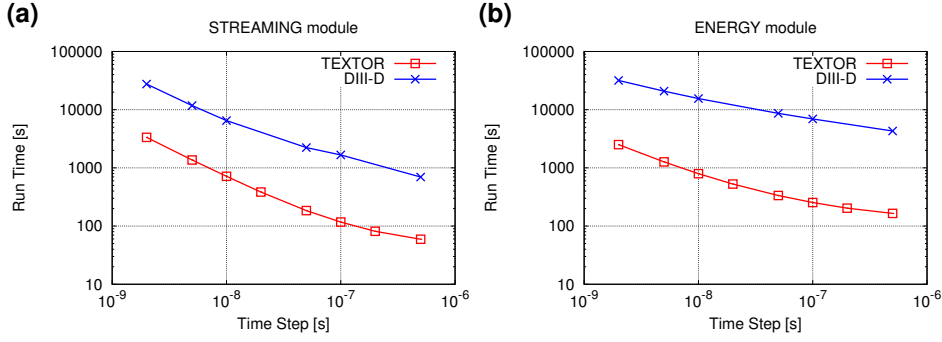


Figure 4.9: Scaling of the execution times  $T_{\text{STR}}$  and  $T_{\text{ENE}}$  of the STREAMING and ENERGY modules with the time step  $\tau$  for a TEXTOR and DIII-D simulation.

### 4.3.3 Execution time of simulations

The execution time  $T$  of a single iteration step significantly depends on the scenario at hand. Clearly, it depends on the magnetic field structure of the plasma edge, or in detail on the combination of short and long open field lines and their intermixture. But it is also strongly dependent on the physical model parameters such as the radial width of the simulation domain and on the level of parallel and cross-field transport. And thirdly, it also depends on the time step  $\tau$  in the discrete time approximation (4.17) and (4.18) of the trajectories of the stochastic process (4.12) associated with the corresponding plasma transport equation (4.2) as well as on the particular source and sink treatment strategies in the code (which are not discussed here). Hence, a simple scaling of  $T$  with certain parameters cannot be expected. Nevertheless, the impact of  $\tau$  and  $D_{\perp}$  on  $T$  is investigated below.

The scaling of the execution times  $T_{\text{STR}}$  and  $T_{\text{ENE}}$  of the STREAMING and ENERGY modules, respectively, with the time step  $\tau$  is shown in figure 4.9 for RMP scenarios at TEXTOR and DIII-D, where  $N_{\text{MC}} / \text{CPU} = 10^4$  MC particles on 32 CPUs are used. Cross-field transport coefficients are set to a level which is typical for the simulations in chapters 6 and 5. It can be seen that  $T_{\text{STR}}$  (DIII-D) and  $T_{\text{ENE}}$  (DIII-D) are one order of magnitude larger than the respective values for the TEXTOR simulation. This is because the simulation volume, in particular the radial extent, for the edge plasma in DIII-D is much larger than for TEXTOR. An extrapolation to ITER, which is again much larger than DIII-D, indicates that one might run into problems with the wall clock time limit  $T_{\text{wall}}$  (the maximum run-time for a program), which is set to 12 – 24 h on the supercomputers mentioned in the previous section. Therefore, one should consider a further investigation of the source and sink treatment strategies in the code and, related to that, restrict the life-time of a MC-particle (e.g. by introducing artificial sources and sinks). This has to be left to subsequent work and cannot be performed within the scope of this thesis.

Other parameters that impact the execution time are the coefficients for anomalous

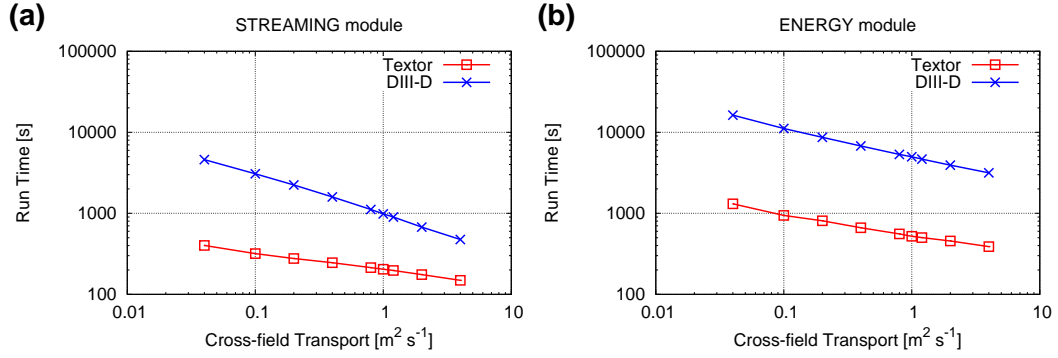


Figure 4.10: Execution times  $T_{\text{STR}}$  and  $T_{\text{ENE}}$  of the STREAMING and ENERGY modules in dependence of cross-field transport  $D_{\perp}$ .

cross-field transport  $D_{\perp}$ ,  $\chi_e$  and  $\chi_i$ .  $T_{\text{STR}}(D_{\perp})$  and  $T_{\text{ENE}}(D_{\perp})$  are shown in figure 4.10, where  $\chi_{\perp} = 3 D_{\perp}$  in all cases. From the type of the cross-field jump of a MC particle in (4.18) one might expect  $T \sim \mathcal{D}_{\perp}^{-1/2}$  scaling, if cross-field transport alone is relevant to connect sources and sinks. However, this is not necessarily the case, because  $T$  depends on many coupled parameters as mentioned above. Nevertheless, a certain scaling can be observed for the selected scenarios, which can be analyzed by the ansatz

$$T(D_{\perp}) = T_0 \left( \frac{D_{\perp}}{D_0} \right)^{\alpha}. \quad (4.52)$$

The data in figure 4.10 can be used to fit the coefficient  $\alpha$ , which yields for the TEXTOR scenario:

$$\alpha_{\text{STR}} = -0.209 \pm 0.004, \quad \alpha_{\text{ENE}} = -0.275 \pm 0.009. \quad (4.53)$$

It can be seen that the impact of  $D_{\perp}$  on the execution times of the DIII-D RMP scenario is stronger, which is reflected in the coefficients

$$\alpha_{\text{STR}} = -0.486 \pm 0.009, \quad \alpha_{\text{ENE}} = -0.353 \pm 0.003. \quad (4.54)$$

This difference can be explained qualitatively by the following reasoning: In figure 6.2 (c) it can be seen that there is a strong parallel plasma flow throughout the plasma edge in the TEXTOR RMP scenario, while the parallel plasma flow is much weaker in the DIII-D scenario presented in figure 5.7 (c). Hence, in the DIII-D scenario cross-field transport is relatively more important, and therefore has a stronger impact on  $T$ .



#### 4.3.4 Convergence study

The plasma transport equations (3.35), (3.36), (3.41) and (3.42) are non-linearly coupled. Therefore the transport coefficients  $\mathcal{V}_{\text{fp}}$  and  $\mathcal{D}_{\text{fp}}$  in (4.4) depend on the solutions  $\mathcal{F}$  for all plasma parameters  $n_i$ ,  $u_{i\parallel}$ ,  $T_e$  and  $T_i$ . Hence, the self-consistent simulation of the plasma edge requires an iterative application of the transport code EMC3-EIRENE. In an abstract form, the numerical implementation of the solver for the linearized version of (4.4) can be written as a  $N_{\text{cell}}$ -dimensional function  $\phi$ :

$$\phi : \mathbb{R}^{N_{\text{cell}}} \rightarrow \mathbb{R}^{N_{\text{cell}}}, \mathcal{F}_{\text{in}} \mapsto \mathcal{F}_{\text{out}}, \quad (4.55)$$

where  $\mathcal{V}_{\text{fp}} = \mathcal{V}_{\text{fp}}(\mathcal{F}_{\text{in}})$ ,  $\mathcal{D}_{\text{fp}} = \mathcal{D}_{\text{fp}}(\mathcal{F}_{\text{in}})$  are non-linear functions of  $\mathcal{F}_{\text{in}}$ . Then a self-consistent solution  $\mathcal{F}$  is necessarily a fixed point  $\mathcal{F}^* = \phi(\mathcal{F}^*)$  of the mapping  $\phi$ , which can be obtained numerically by a fixed point iteration

$$\mathcal{F}^{(n+1)} = \phi(\mathcal{F}^{(n)}) \quad (4.56)$$

for some initial value  $\mathcal{F}^{(0)}$ . However, the issue of convergence of noisy fixed point iterations is still open. For the present studies the measure of convergence for simulation runs is taken to be the relative change  $\Delta\mathcal{F}$  between iterations:

$$\Delta\mathcal{F}^2 = \frac{4 \sum_{j=1}^{N_{\text{cell}}} w_j \left( \frac{\mathcal{F}^{(n-1)} - \mathcal{F}^{(n)}}{\mathcal{F}^{(n-1)} + \mathcal{F}^{(n)}} \right)^2}{\sum_{j=1}^{N_{\text{cell}}} w_j}, \quad w_j = p_j V_j, \quad (4.57)$$

where each grid cell is weighted with its volume  $V_j$  and the local pressure  $p_j$  (the hot and dense plasma region is of higher interest than the near vacuum region at the far edge). Relaxation is essential for obtaining a rapid convergence in solving a non-linear, coupled system of equations. For the present calculations the relaxation scheme

$$\mathcal{F}_j^{(n,\text{relax})} = \alpha_{\text{relax}} \mathcal{F}_j^{(n-1)} + (1 - \alpha_{\text{relax}}) \mathcal{F}_j^{(n)} \quad (4.58)$$

is applied after each iteration step. An approximate convergence is reached, when  $\Delta\mathcal{F}$  is reduced to a low, but finite level  $\Delta\mathcal{F}_0$ . This finite  $\Delta\mathcal{F}_0$  is not related to machine precision, but instead to the noise level  $s_{\mathcal{F},i}$  in (4.23) which is naturally present in Monte Carlo procedures. How quickly this saturation level is reached for a given number of MC particles depends on the detailed transport characteristics of the system at hand, on the choice of under-relaxation factors  $\alpha_{\text{relax}}$ , smoothing by averaging, etc...

While for fixed transport coefficients (i.e. fixed  $\mathcal{F}_{\text{in}}$  in (4.55)) the fluctuations  $s_{\mathcal{F},i}$  of  $\mathcal{F}_{\text{out}}$  scale according to the central limit theorem ( $s_{\mathcal{F},i} \sim N_{\text{MC}}^{-1/2}$ ), this can in general not be expected for the relative changes  $\Delta n_e$ ,  $\Delta T_e$ ,  $\Delta T_i$  in the full non-linear problem.

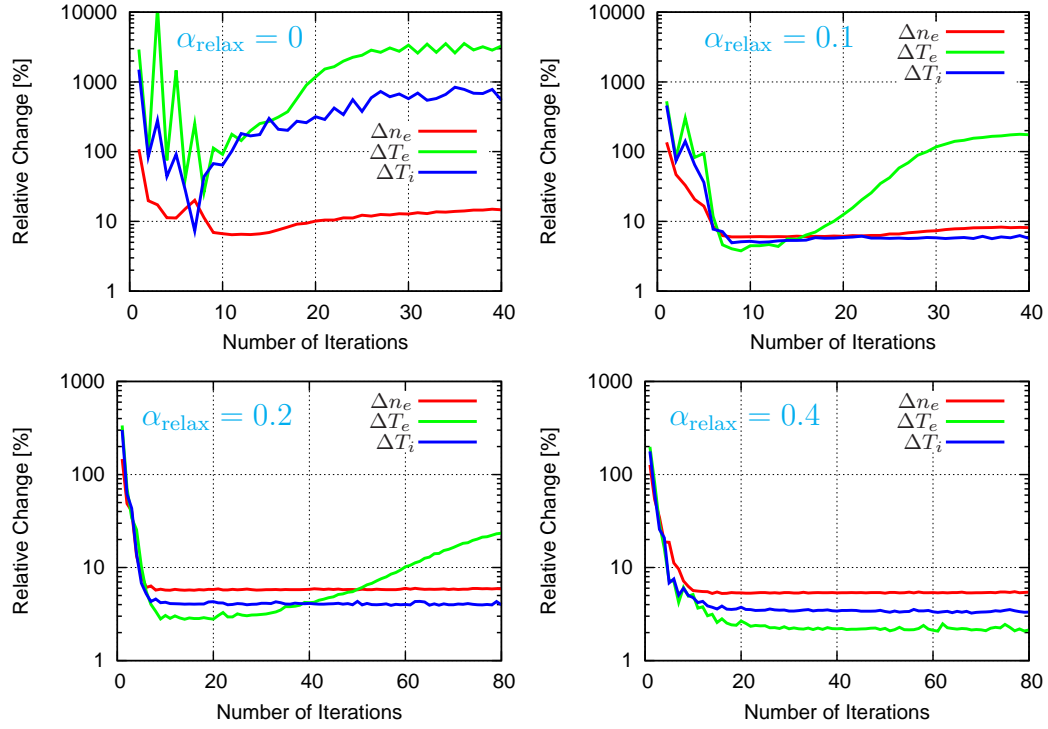


Figure 4.11: Convergence study for relaxation factors  $\alpha_{\text{relax}} = 0, 0.1, 0.2$  and  $0.4$ . All simulations are performed with  $N_{\text{MC}} = 64 \text{ k}$  MC particles.

These relative changes are not statistically independent from each other, because the plasma transport equations (3.35), (3.36), (3.41) and (3.42) are strongly coupled: i.e. also the transport coefficients themselves in the corresponding SDE (4.12) are updated after each calculation, because they depend non-linearly on the iterated plasma state. Therefore, e.g.

$$\Delta T_e^{(n)} = \Delta T_e(n_e^{(n-1)}, u_{i\parallel}^{(n-1)}, T_e^{(n-1)}, T_i^{(n-1)}, \alpha_{\text{relax}}, N_{\text{MC}}) \quad (4.59)$$

depends non-linearly on the previous solutions of all plasma parameters, the relaxation factor  $\alpha_{\text{relax}}$  as well as on the number of MC particles. Hence, a simple  $\Delta \mathcal{F}_0 \sim N_{\text{MC}}^{-1/2}$  scaling cannot be expected for the iterated, non-linear system.

The approximate convergence is now investigated for a TEXTOR scenario. The relative changes  $\Delta n_e$ ,  $\Delta T_e$  and  $\Delta T_i$  after each iteration step are displayed in figure 4.11 for various relaxation factors, where all simulations are performed with  $N_{\text{MC}} = 64 \text{ k}$  MC particles. For  $\alpha_{\text{relax}} = 0$ , the relative change of the density is reduced to  $\Delta n_e = 7\%$  after the 9th iteration and stays on that level for a few iterations. The relative changes of the electron and ion temperature, however, reach a minimum of  $\Delta T_e = 26\%$  after the

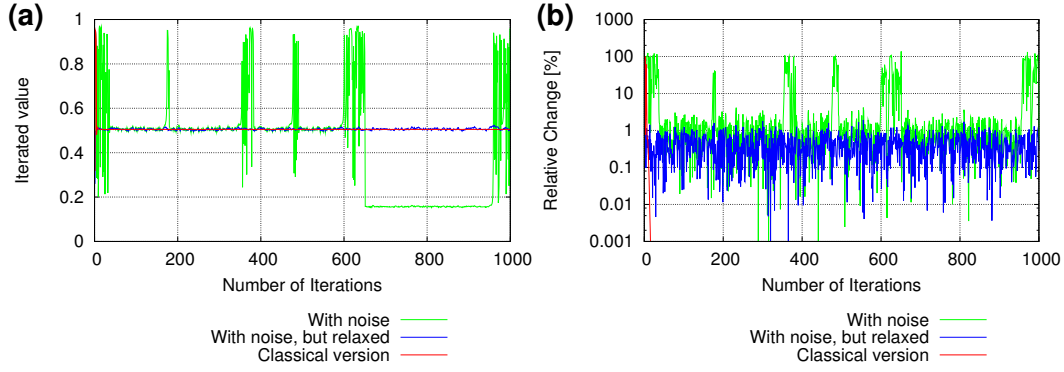


Figure 4.12: Convergence study for the triple iterated logistic map using  $r = 3.83$ : (a)  $y_n$  and (b)  $\Delta y_n$ .

8th and  $\Delta T_i = 7\%$  after the 7th iteration, respectively, but immediately increase again. No stable solution for  $T_e$  and  $T_i$  is reached and then also  $\Delta n_e$  increases again.

Although a stable fixed point iteration is required for the application in plasma transport simulations, this can not necessarily be expected from a non-linear, multi-dimensional function such as (4.55). In particular, even the very simple, well-known logistic map introduced in [124] (see also [58, 125] for a discussion)

$$x_{n+1} = r x_n (1 - x_n) \quad (4.60)$$

exhibits chaotic behavior for  $3.57 \lesssim r \leq 4$  with small intervals of non-chaotic behavior in between. One such *island of stability* is located in the region of  $r = 1 + \sqrt{8}$ , where the sequence (4.60) oscillates between 3 values, i.e. the sequence  $y_n = x_{3n}, n \in \mathbb{N}$  converges (see red line figure 4.12 (a)). Convergence to machine precision is reached after 50, where the convergence in figure 4.12 (b) is measured by the relative change

$$\Delta y_n = \left| 2 \frac{y_n - y_{n-1}}{y_n + y_{n-1}} \right|. \quad (4.61)$$

Now an additional noise term  $s_n = 0.01 y_n \xi$  with normal distributed random variable  $\xi$  is introduced into the triple iterated logistic map  $y_n$ :

$$y_n^* = y_n + s_n = (1 + 0.01 \xi) y_n. \quad (4.62)$$

As can be seen in figure 4.12, even a relatively small noise of 1% can result in a sudden chaotic behavior of the noisy sequence. At first, it takes about 40 iterations for the sequence to be attracted to the unperturbed fixed point. But then, after about 180 iterations, the sequence is suddenly attracted to one of the other two fixed points of  $y_n$  but returns after a few iterations, while after 650 iterations it suddenly jumps to the

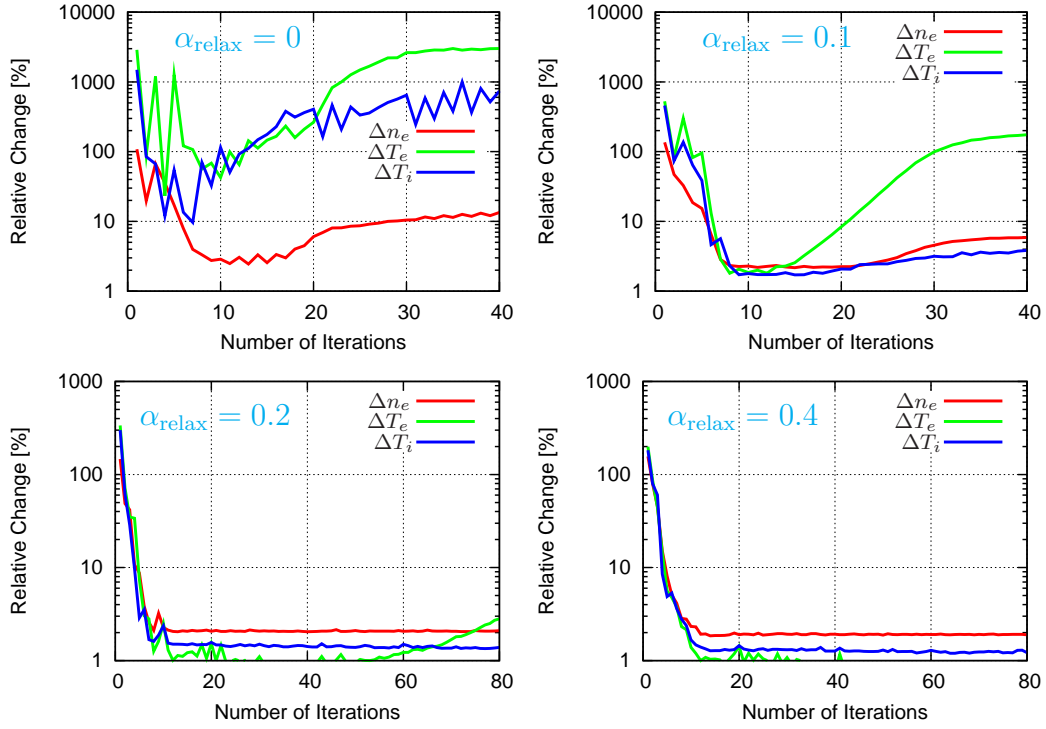


Figure 4.13: Convergence study for relaxation factors  $\alpha_{\text{relax}} = 0, 0.1, 0.2$  and  $0.4$ . All simulations are performed with  $N_{\text{MC}} = 512\text{k}$  MC particles.

third fixed point and stays there for 300 iterations. Hence, the stability of an iterated, non-linear sequence can be significantly affected by noise. This is reflected in plasma transport calculations by the divergence of the iterated  $T_e$  and  $T_i$  in figure (4.11) for  $\alpha_{\text{relax}} = 0$ . Introducing a relaxation factor  $\alpha_{\text{relax}}$ , such as in (4.58) for the plasma transport simulations, allows to stabilize the iterated map  $y_n^*$  (at least for the first 1000 iterations shown in figure 4.12).

Such a stabilization can also be observed in the plasma transport simulations in figure 4.11, however the level of stabilization depends on the value of  $\alpha_{\text{relax}}$ . For  $\alpha_{\text{relax}} = 0.1$ , the relative changes are reduced to  $\Delta n_e = 6\%$ ,  $\Delta T_e = 4\%$  and  $\Delta T_i = 5\%$  after 8 iterations. However, this is stable only for a few further iterations. Then fluctuations related to the non-linear transport characteristics of electron heat conductivity provoke an instability in  $T_e$ . Increasing the relaxation factor to  $\alpha_{\text{relax}} = 0.2$ , results in a slightly lower  $\Delta n_e = 5.8\%$  after the 8th iteration, as well as  $\Delta T_e = 3.4$ ,  $\Delta T_i = 4.6$ . This is then stable for about 25 iterations, but afterwards an instability in the  $T_e$  calculation arises as well. An even higher relaxation factor of  $\alpha_{\text{relax}} = 0.4$  results in  $\Delta n_e = 5.4\%$ ,  $\Delta T_e = 2.2\%$  and  $\Delta T_i = 3.5\%$ , which is stable at least for up to 80 iterations. Also note, that with  $\alpha_{\text{relax}} = 0.4$  the intrinsic noise level  $\Delta\mathcal{F}_0$  is reached later than with  $\alpha_{\text{relax}} = 0.2$  (e.g. after about 16 iteration for  $T_e$ ).

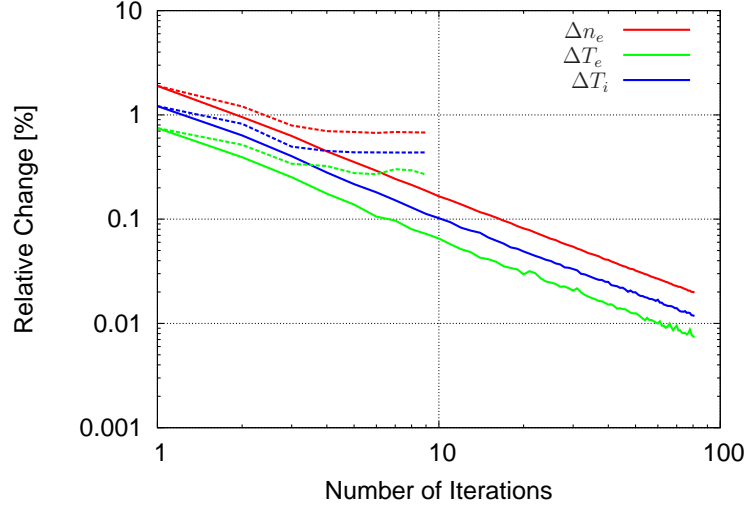


Figure 4.14: Solid lines: relative changes  $\Delta n_e$ ,  $\Delta T_e$  and  $\Delta T_i$  for increasing  $\alpha_{\text{relax}}$  according to (4.63), starting from a “converged” solution with  $\alpha_{\text{relax}} = 0.4$  and  $N_{\text{MC}} = 512\text{ k}$ . Dashed lines: relative changes for  $\alpha_{\text{relax}} = 0.4$  and  $N_{\text{MC}} = 4096\text{ k}$ .

Increasing the number of MC particles reduces the intrinsic error level  $\Delta\mathcal{F}_0$ . Whether this is sufficient to stop the divergence of  $T_e^{(n)}$  is investigated now. The simulations from figure 4.11 have been repeated with  $N_{\text{MC}} = 512\text{ k}$  MC particles. The relative changes between plasma transport iterations are presented in figure 4.13. Indeed  $\Delta n_e$ ,  $\Delta T_e$  and  $\Delta T_i$  are reduced with respect to figure 4.11: For  $\alpha_{\text{relax}} = 0$ , the initial (after 8 iterations) noise level of  $n_e$  is reduced to  $\Delta n_e \approx 3\%$ , however,  $T_e^{(n)}$  still diverges with higher  $N_{\text{MC}}$ . The initial noise level for  $\alpha_{\text{relax}} = 0.1$  is reduced as well, after 10 iterations:  $\Delta n_e = 2.3\%$ ,  $\Delta T_e = 1.9\%$  and  $\Delta T_i = 1.7\%$ , but  $T_e^{(n)}$  starts to diverge a few iterations afterwards. Even for  $\alpha_{\text{relax}} = 0.2$ , where  $\Delta T_e$  is reduced to  $1\%$ ,  $T_e^{(n)}$  is only stable up to the 60th iteration. The relative changes  $\Delta n_e = 2.1\%$  and  $\Delta T_i = 1.5\%$  are stable at least up to the 80th iteration. Only  $\alpha_{\text{relax}} = 0.4$  is sufficient to keep  $\Delta T_e$  below  $1\%$  for at least 80 iterations, where  $\Delta n_e = 1.9\%$  and  $\Delta T_i = 1.3\%$ .

Instead of increasing  $N_{\text{MC}}$  to reduce the noise level  $\Delta\mathcal{F}_0$  once a stable solution has been reached, one can also subsequently increase  $\alpha_{\text{relax}}$ . Starting from a “converged” solution, e.g. for  $\alpha_{\text{relax}} = 0.4$  and  $N_{\text{MC}} = 512\text{ k}$  (now iteration number  $n = 1$ ), the relaxation factor  $\alpha_{\text{relax}}(n)$ ,  $n \geq 2$  is given for subsequent iterations with the same  $N_{\text{MC}}$  by

$$\alpha_{\text{relax}}(n) = \frac{n-1}{n}. \quad (4.63)$$

This corresponds to a weight of  $1/n$  for the new iteration with respect to the integrated (over iterations) number of MC particles  $n \cdot N_{\text{MC}}$ . The relative changes  $\Delta n_e$ ,  $\Delta T_e$  and

$\Delta T_i$  from such a procedure are displayed in figure 4.14. As can be seen there, all relative changes obey an  $n^{-1}$  scaling, as can be expected (see appendix A.4). This scaling is much stronger than what one can achieve with the same computational effort by simply increasing  $N_{\text{MC}}$  (dashed lines in figure 4.14). Increasing  $N_{\text{MC}}$  by a factor of 8 to  $N_{\text{MC}} = 4096 \text{ k}$  leads to a reduction of relative changes by about  $\sqrt{8}$ , but which takes about 4 iterations. This corresponds to the computational effort of 32 iterations with  $N_{\text{MC}} = 512 \text{ k}$ , where the relative changes are already reduced to  $\frac{1}{32}$  when following the relaxation scheme in (4.63). Hence, the procedure of increasing  $\alpha_{\text{relax}}$  according to (4.63) is very effective and more adequate to increase the accuracy of the simulation results than by simply increasing  $N_{\text{MC}}$ .

## 5 Plasma transport in poloidally diverted RMP discharges at DIII-D

Presently, the most promising application of RMP induced chaotic magnetic edge layers is the control of Edge Localized Modes (ELMs) in ITER relevant plasma scenarios, such as under investigation at the DIII-D tokamak (see chapters 1 and 2 for references). ELMs are naturally present in H-mode plasmas, and result in high transient heat loads onto the first wall and the divertor target. As mentioned in the introduction, extrapolations to ITER relevant power levels indicate that this could lead to a significant reduction of the ITER wall lifetime. Because of its recent success in ELM control at DIII-D and JET, RMPs are now under consideration for ITER as well. However, the detailed impact on the edge plasma is not fully understood so far and still the subject of ongoing research. In particular, the impact on the pressure gradient in the edge transport barrier in H-mode plasmas is of great interest, because this is correlated with the stabilization of so called peeling-ballooning MHD modes considered as the cause of ELMs.

In this chapter the resulting 3D effects on an ITER similar shape plasma at DIII-D are analyzed which are introduced by RMPs with toroidal mode number  $n = 3$ . With the generalization of the magnetic field line representation technique and grid connectivity carried out in section 4.2.3, the EMC3-EIRENE code has become a flexible tool to analyze these 3D effects in detail for the first time for poloidal divertor configurations. The subsequent sections are organized as follows: at first, an overview of the magnetic field structure in DIII-D is given in section 5.1. This is followed by a brief analysis of plasma profiles along an axisymmetric SOL field line in section 5.2. It will be shown that high-recycling features of the SOL can be found in simulations for poloidal divertor tokamaks with the EMC3-EIRENE code. Then, in section 5.3, the resulting 3D effects on the edge plasma in the presence of RMPs are analyzed. In particular, the patterns of particle and heat flux on the divertor target and their dependence on the level of anomalous cross-field transport are investigated. Furthermore, 3D volumetric effects are analyzed, namely the impact of helical magnetic lobes and short magnetic flux tubes. Realistic simulations of H-mode plasmas require an advancement of the cross-field transport model in the EMC3-EIRENE code in order to include the effects of an edge transport barrier. No concluding model has yet been found for anomalous cross-field transport, and hence, only an ‘ad hoc’ ansatz can be made here. Several approaches are investigated in section 5.4. In addition, the impact of hydrogen pumping and re-fueling is investigated as well. This last section motivates more detailed studies, which, however, have to be left for the future.

## 5.1 Magnetic field structure

In the following sections an ITER similar shape plasma scenario at DIII-D is considered, which is based on discharge #132731 with the characteristic values:

$\mathbf{B}_{\text{tor}}(R = 175 \text{ cm})$	$= 1.85 \text{ T}$
$I_p$	$= 1.52 \text{ MA}$
$q(\psi^* = 0.95)$	$= 3.6$

The shape of the plasma is characterized by the elongation  $\kappa$  and triangularity  $\bar{\delta}$ :

$$\kappa = \frac{h}{w}, \quad \bar{\delta} = \frac{d_u + d_l}{w}, \quad (5.1)$$

where  $w, h, d_u$  and  $d_l$  are defined by the shape of the separatrix (see figure 5.1 (a)). For the present case:  $\kappa = 1.9$  and  $\bar{\delta} = 0.51$ . The magnetic separatrix divides the confined plasma region from the outer scrape-off layer plasma region where field lines intersect divertor targets within relatively short distance (see figure 2.2). In terms of nonlinear dynamics, the separatrix associated with the hyperbolic fixed point  $\mathbf{x}_0$  (with regard to the Poincaré map  $P$  in (2.14)) - more frequently called the X-point - is given by two invariant manifolds: the stable and unstable manifolds  $W^s$  and  $W^u$ , respectively [57]. These manifolds are defined by field lines  $\mathbf{x}_{\mathbf{p}}(l)$  that enter or leave the X-point (where  $l$  is the length along the field line defined by  $\mathbf{x}_{\mathbf{p}}(0) = \mathbf{p}$ ):

$$W^s = \{\mathbf{p} | \mathbf{x}_{\mathbf{p}}(l) \rightarrow \mathbf{x}_0 \text{ as } t \rightarrow \infty\} \quad (5.2)$$

$$W^u = \{\mathbf{p} | \mathbf{x}_{\mathbf{p}}(l) \rightarrow \mathbf{x}_0 \text{ as } t \rightarrow -\infty\}. \quad (5.3)$$

In the unperturbed case both stable  $W^s$  and unstable  $W^u$  manifolds coincide and form the separatrix as shown in figure 5.1 (a). However, in the presence of resonant magnetic perturbations the two separatrix manifolds  $W^s$  and  $W^u$  no longer coincide, but still provide a boundary for the plasma as no field lines can intersect them. When these manifolds approach the X-point in the unstable direction they start to oscillate wildly and intersect each other (but not themselves) as illustrated in figure 5.1 (b). These so called *homoclinic tangles* are well known in perturbed nonlinear dynamical systems [57, p. 222] and have been investigated as well in poloidally diverted tokamaks, e.g. in [126].

The RMP field in the present case is generated by the I-coils only (figure 2.3), which are powered by a current of  $I_c = 4 \text{ kA}$  in the present case. The error field due to coil misalignments and the empirically determined error field correction by the C-coils are neglected. This approach has been chosen to study the physics of the intentionally applied perturbations. In a future analysis this should be compared to the more realistic case. The resulting magnetic field structure in the vacuum approach (see section 2.3) is visualized in figure 5.3. The wall-to-wall connection length  $L_c$  of magnetic field lines is



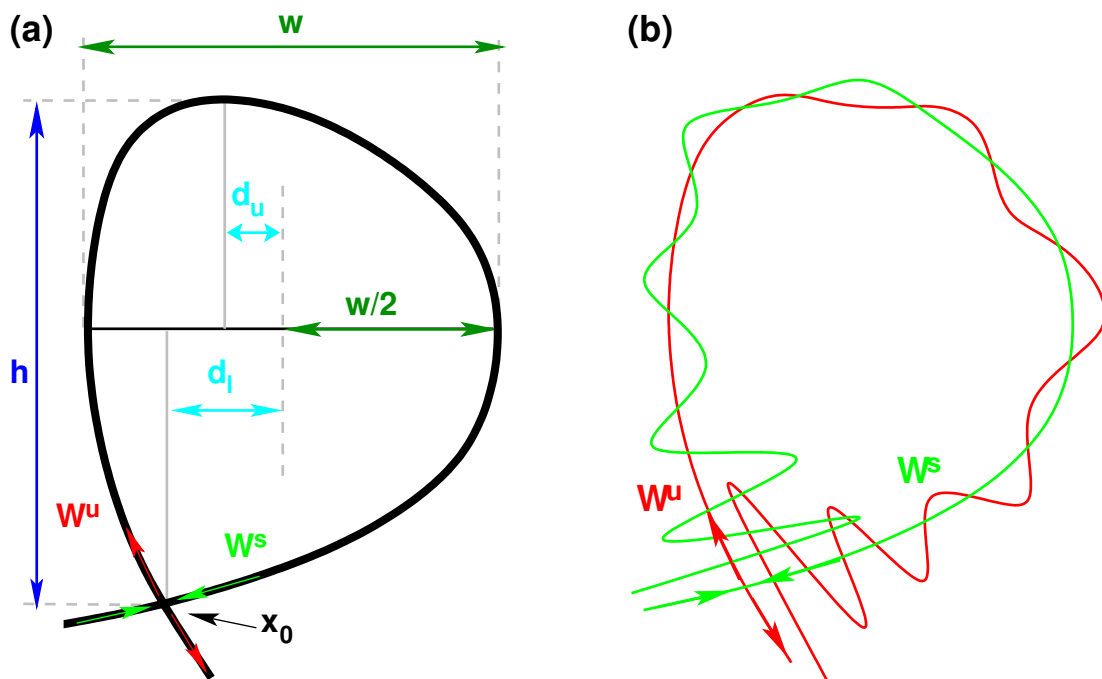


Figure 5.1: (a) The unperturbed separatrix associated with the hyperbolic fixed point  $x_0$  is defined by the stable and unstable manifolds  $W^s$  and  $W^u$ , respectively. The shape can be characterized by the elongation  $\kappa$  and triangularity  $\delta$  which are related to the height  $h$ , width  $w$  and the radial displacements  $d_u$  and  $d_l$  of the uppermost and lowermost positions. (b) stable and unstable manifolds for the perturbed system.

displayed in color in combination with a Poincaré plot. The complex field structure has been the topic of recent research [127, 128, 129] and includes:

- magnetic island chains (visualized by the Poincaré plot),
- partially ergodic domains (yellow, red and white regions with scattered black dots from the Poincaré plot),
- short magnetic flux tubes ( $L_c \approx 100$  m, blue regions) and
- helical magnetic lobes ( $L_c \approx 400$  m, green regions), guiding field lines from inside the former separatrix (i.e. without RMPs, normalized poloidal flux  $\psi^* = 1$ ) to the divertor targets, and thereby creating a helical striation pattern on the targets (see figure 5.2) .

These helical lobes are formed by the separatrix manifolds and extend into the regular *scrape-off layer* (SOL). They introduce an intermediate layer between the confined region and the regular SOL. Stable and unstable manifolds may intersect each other (but not themselves) [57]. As a result, inward loops of these manifolds exclude certain regions (the

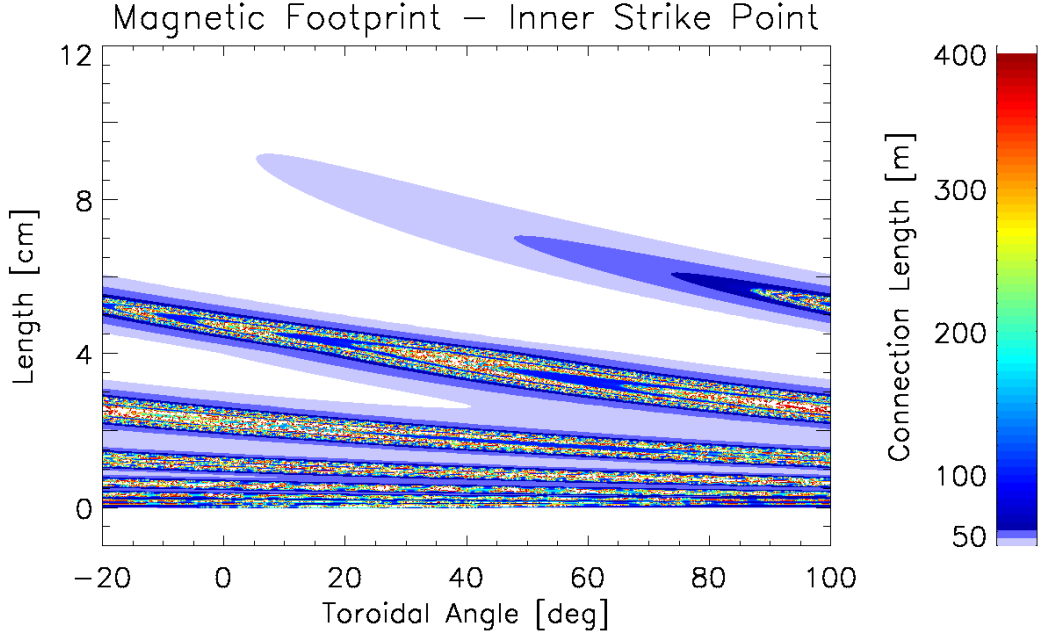


Figure 5.2: Magnetic footprint on the divertor target at the inner strike point (ISP).

short magnetic flux tubes) from this intermediate layer. A detailed discussion can be found in [130]. This mesh of short flux tubes is suspected to act as an additional 3D SOL and hence, as a sink for the plasma [131]. This functionality is motivated by modeling and experimental observations at the TEXTOR tokamak [132, 72, 97]. In the following the effects of such a magnetic field structure on the edge plasma are investigated.

## 5.2 Parallel profiles in the axisymmetric SOL

Before turning to the full 3D calculations, a brief confirmation is given in this section that the code at least reproduces robust 2D edge plasma features. Here: establishment of the well characterized “high recycling regime” with re-ionization of recycling neutrals dominantly occurring in the divertor itself. For this the DIII-D configuration described above is used, but with RMPs turned off. Plasma profiles along a flux tube slightly outside the unperturbed separatrix (figure 5.1 (a)) are discussed. For these the frequently employed so called 2-point models [7] are known to be applicable.

Parallel profiles of  $n_e$  and  $T_e$  in the SOL at  $\psi^* = 1.01$ , i.e. slightly outside the separatrix, are shown in figure 5.4 (for details on the input parameters  $n_{in}$ ,  $P_{in}$ , as well as the transport coefficients  $D_{\perp}$ ,  $\chi_{\perp}$  see section 5.4). Clear features of a high-recycling SOL are found: large parallel temperature gradients, resulting in predominantly conductive heat transport to the target (i.e. conduction limited regime), and large densities in front

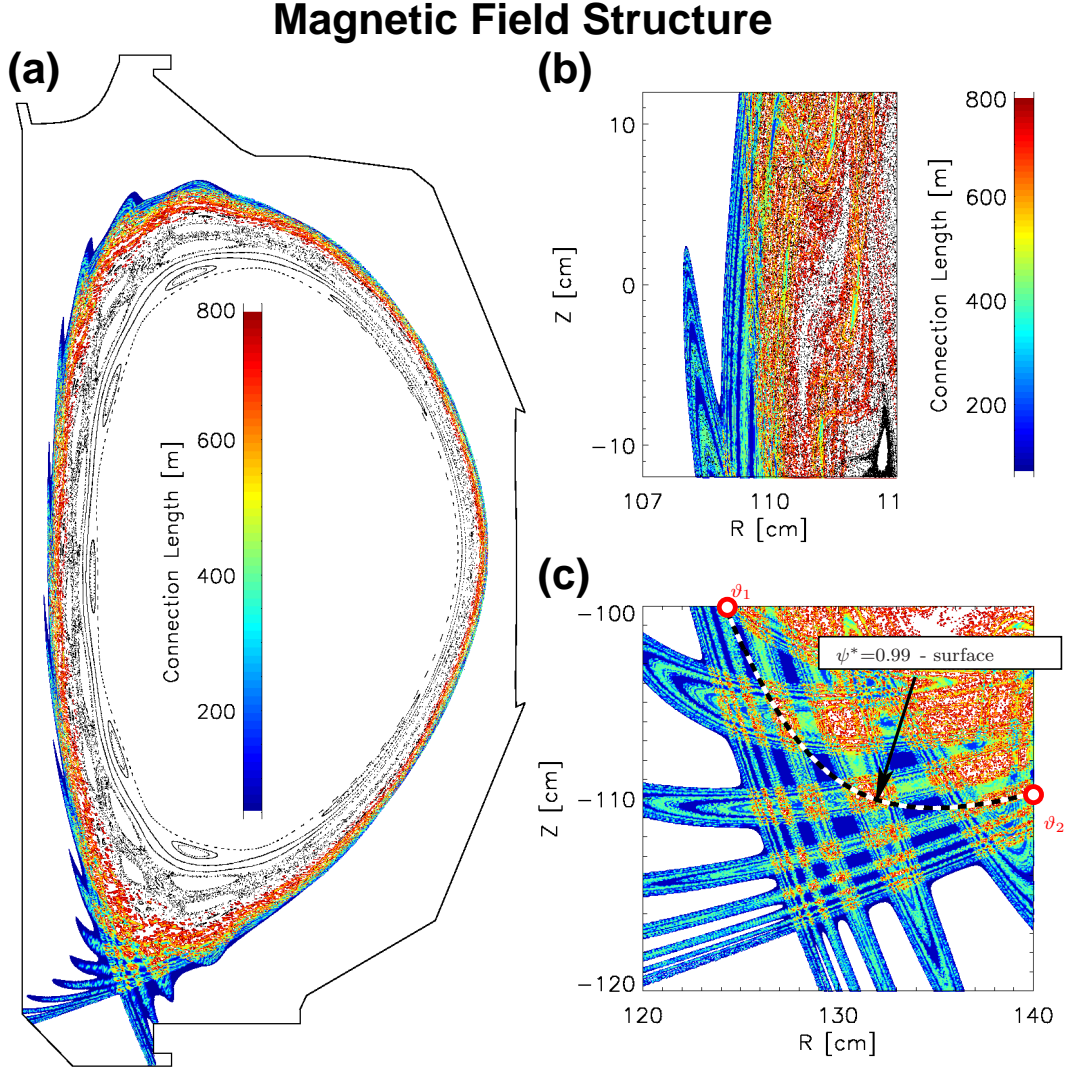


Figure 5.3: Magnetic field structure of a typical DIII-D plasma with ITER similar shape in the presence of an  $n = 3$  RMP field. The wall-to-wall connection length  $L_c$  of magnetic field lines is indicated by color in addition to a Poincaré plot, i.e. intersection points of field lines with a reference plane. (a) full cross-section at  $\varphi = 0$  deg, (b) zoom of the HFS midplane region, (c) zoom of the X-point region. The position of the unperturbed (and axisymmetric)  $\psi^* = 0.99$ -surface is marked by a white-black dashed line with the end points corresponding to poloidal angles of  $\vartheta_1 = 197.4$  deg and  $\vartheta_2 = 206.5$  deg, respectively.

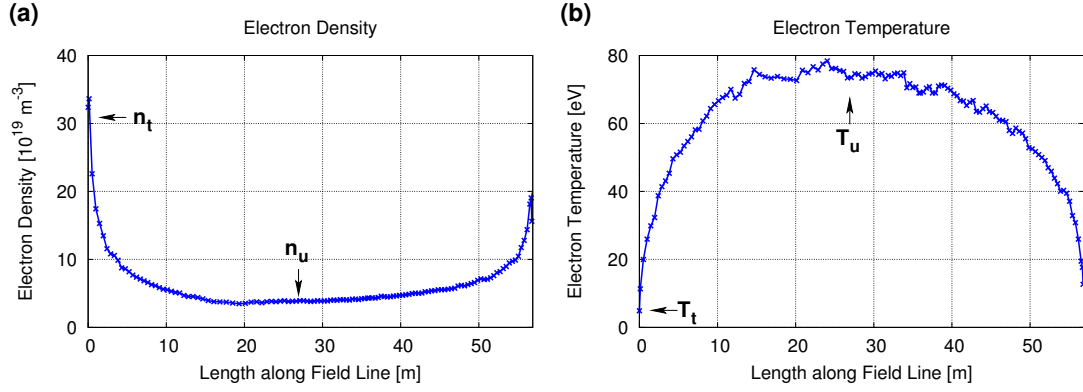


Figure 5.4: Parallel profiles of (a) electron density  $n_e$  and (b) electron temperature  $T_e$  at  $\psi^* = 1.01$  (i.e. just outside the separatrix  $\psi^* = 1$ , see also figure 5.1 (a)).

of the divertor target. The density increases from an upstream value  $n_u \approx 4.0 \cdot 10^{19} \text{ m}^{-3}$  at the stagnation point to  $n_t \geq 30.0 \cdot 10^{19} \text{ m}^{-3}$  at the target at the outer strike point ( $L = 0 \text{ m}$ ). The temperature, on the other hand, drops from  $T_u \approx 75 \text{ eV}$  to  $T_t \approx 5 \text{ eV}$ . Such a behavior can indeed be expected for the given collisionalities [7]:

$$\nu_{\text{SOL}}^* = 10^{-16} \cdot n_u [\text{m}^{-3}] \cdot L_c [\text{m}] / 2 \cdot (T_u [\text{eV}])^{-2} \approx 20 \quad (5.4)$$

with  $L_c = 57 \text{ m}$  for the selected SOL field line in figure 5.4. Following the simple SOL model for the conduction limited case in [7] allows to relate the temperature gradient factor  $f_T \equiv T_u/T_t$  to the SOL collisionality (see equation 4.109 in [7]):

$$\nu_{\text{SOL}}^* \approx C f_T^{1/2} \left( 1 - f_T^{-7/2} \right), \quad C = \frac{4}{7} \frac{\kappa_0}{(\gamma_e + \gamma_i) e c_{st}} 10^{-16}. \quad (5.5)$$

With  $\kappa_0 \approx 2068$  and  $c_{st} \approx 3.36 \cdot 10^4 \frac{\text{m}}{\text{s}}$  obtained from local temperatures at the target, one can estimate the temperature gradient factor to  $f_T \approx 42$ . This is significantly larger than the value of  $f_T \approx 15$  observed in the simulations, but can be explained by the following extensions to the highly idealized “Basic 2-Point Model” (see section 5.4 in [7]):

- Volumetric power losses due to radiation and charge exchange losses are accounted for by the power loss factor  $f_{\text{power}}$ :

$$f_{\text{power}} \equiv \frac{P_{\text{vol}}}{P_{\text{vol}} + P_{\text{target}}} \quad (5.6)$$

where  $P_{\text{vol}}$  are the total volumetric power losses and  $P_{\text{target}}$  the total power losses at the target plates.

- Momentum losses due to frictional collisions with neutrals are accounted for by the momentum loss factor  $f_{\text{mom}}$ , which is defined by the simple pressure balance equation

$$2 n_t T_t = f_{\text{mom}} n_u T_u. \quad (5.7)$$

- Heat convection is included by the conduction factor  $f_{\text{cond}}$ :

$$f_{\text{cond}} = \frac{q_{\parallel \text{cond}}}{q_{\parallel \text{cond}} + q_{\parallel \text{conv}}}, \quad (5.8)$$

which accounts for the tendency of heat convection to reduce temperature gradients.

Using the simulations results one finds that  $f_{\text{power}} \approx 0.01$  (EMC3-EIRENE output in (5.6),  $f_{\text{mom}} \approx 1$  (from (5.7) and  $n_t, T_t, n_u, T_u$  from figure 5.4) and  $f_{\text{cond}} \approx 0.26$  (from (5.8) evaluated at the target):

$$q_{\text{cond}} = \kappa_0 (T_t [\text{eV}])^{5/2} \frac{\partial T_t}{\partial L} [\text{eV m}^{-1}], \quad q_{\text{conv}} = \frac{5}{2} n_t T_t c_{st}. \quad (5.9)$$

Hence, heat convection still plays a significant role in the present scenario. These extensions allow to estimate the effect on  $f_T$  (see equation 5.27 in [7]):

$$f_T \Big|_{\text{Extended Model}} = f_T \frac{f_{\text{cond}}^{6/7} f_{\text{mom}}^2}{(1 - f_{\text{power}})^2} \approx 13.5. \quad (5.10)$$

This is much closer to the value  $f_T \approx 15$  observed in the simulations. Another, more global and less quantitative parameter typically used to characterize “high recycling conditions” is the SOL flux amplification factor  $R$  ( $R > 1$  for “high recycling”) with  $R = \Gamma_{\text{target}} / \Gamma_{\text{into SOL}}$ .  $\Gamma_{\text{into SOL}}$  is not a direct output of the code, but  $\Gamma_{\text{into edge}} = \Gamma_{\text{in}}^{(p)}$  is (see section 4.3.1). Using this latter parameter to calculate  $R$  results in a different absolute value, which depends on the radial width of the simulation domain. However, in comparison to typical TEXTOR simulations, this approach gives for the present “high recycling” case at DIII-D a value which is by more than one order of magnitude larger.

Recently, a “high-recycling regime” was predicted also for the W7-X stellarator by simulations with the EMC3-EIRENE code [133], which has not been observed in all prior simulations for W7-AS and LHD. Therefore, together with the present finding this demonstrates that the EMC3-EIRENE code is indeed applicable to high-recycling scenarios in tokamaks. A detailed benchmark with a 2D transport code is beyond the scope of this thesis and can be found in [134].

### 5.3 3D effects on the edge plasma

The transport model presented in chapter 3 accounts for anomalous cross-field transport by free model parameters  $D_{\perp}$ ,  $\chi_{e,\perp}$  and  $\chi_{i,\perp}$ , where  $\chi_{\perp} = \chi_{e,\perp} = \chi_{i,\perp}$  is assumed throughout this chapter. Particle and heat fluxes to the wall - although guided by the underlying magnetic topology - depend on the transport characteristics in the very complex 3D plasma edge and in particular on the level of cross-field transport. Experimentally, the patterns of target particle and heat fluxes are the clearest indication for 3D effects induced by RMPs. Therefore section 5.3.1 is dedicated to the imprints of the plasma on the divertor target: At first the level of cross-field transport which is consistent with experimental results is estimated. Afterwards a direct comparison to experimental observations is given. 3D volume effects are then investigated in section 5.3.2 with particular focus on helical magnetic lobes and short magnetic flux tubes. The results presented in this section have been published in [135].

#### 5.3.1 Particle and heat flux pattern on the divertor target

##### Estimation of cross-field transport

Three independent transport simulations with  $D_{\perp,1} = 1.0 \text{ m}^2 \text{ s}^{-1}$ ,  $D_{\perp,2} = 0.25 \text{ m}^2 \text{ s}^{-1}$  and  $D_{\perp,3} = 0.1 \text{ m}^2 \text{ s}^{-1}$  are performed with  $\chi_{\perp} = 3 D_{\perp}$  in each case. These calculations are based on the magnetic configuration of DIII-D discharge 122342 with a simplified wall geometry: the wall is approximated by a horizontal plane (i.e. neglecting the 45 deg tile at the high field side). The magnetic footprint in the presence of RMP fields splits into a characteristic striation pattern, as discussed above. Both, particle and heat fluxes to the wall are guided by the underlying magnetic topology and hence, a similar striation pattern is expected also for the particle and heat flux. Simulation results of particle and heat flux onto the divertor target  $\Gamma_{\text{target}}$  and  $q_{\text{target}}$ , respectively, are presented in figure 5.5. Both,  $\Gamma_{\text{target}}$  and  $q_{\text{target}}$  show a clear helical pattern for all transport levels. However, a sharp striation pattern is present only for low enough cross-field transport ( $D_{\perp} \lesssim 0.25 \text{ m}^2 \text{ s}^{-1}$ ). Such a sharp striation pattern is indeed observed in the experiment for the particle flux [127, 128], distinctly different from the more blurred pattern which emerges with transport model  $D_{\perp,1}$ , where  $\Gamma_{\text{target}}$  is spread over 15 cm along the wall. Hence,  $D_{\perp,2}$  provides a rough upper limit for the free model parameter for cross-field diffusion. At TEXTOR, however, simulations with EMC3-EIRENE have shown that a pronounced pattern prevails for much higher values of  $D_{\perp}$ . In particular, sub-structures in the target particle and heat fluxes there have still been visible at a cross-field transport level of  $D = 1.4 \text{ m}^2 \text{ s}^{-1}$  and  $\chi_{\perp} = 4.1 \text{ m}^2 \text{ s}^{-1}$  [97]. The reason for this is related to the shorter connection length at TEXTOR, allowing for higher  $D_{\perp}, \chi_{\perp}$  for still sufficiently low overall cross-field losses as compared to parallel losses.

Remarkably, only very weak striation patterns are observed for the heat flux in low density RMP experiments such as DIII-D discharges 122342 and 132731 [136] while

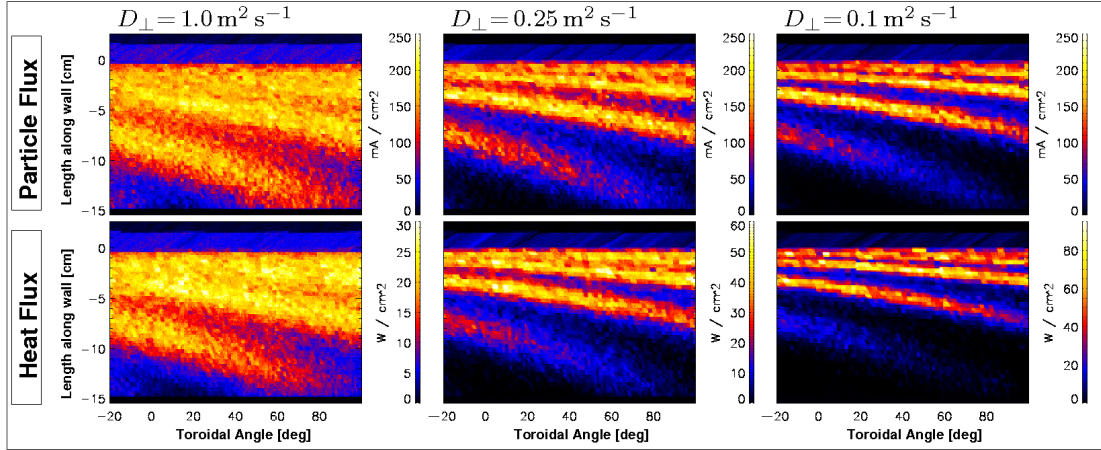


Figure 5.5: Particle (upper row) and heat flux (lower row) footprints  $\Gamma_{\text{target}}$  and  $q_{\text{target}}$  at the outer strike point for three levels of cross-field transport.

heat flux splitting is observed in high density DIII-D RMP experiments [137]. In the former, the main peak heat flux is located just at the strike point, which is closer to the low  $\chi_{\perp}$  case in figure 5.5. The presence of a clear striation pattern in the corresponding simulation results, however, indicates that some physical processes may be missing in the present transport model when considering the difference between high and low density plasmas<sup>1</sup>. A more detailed discussion is given in the next paragraph. However, the same qualitative behavior was also found in earlier heat transport simulations with the E3D code [138]. These simulations now demonstrate that this mismatch cannot be explained by the additional accounting for self-consistent particle and momentum transport nor by the self-consistent recycling neutrals, which both are included in the present model but not in [138].

### Analysis of target particle and heat fluxes

For a direct comparison to experimental observations, the magnetic configuration of the more recent DIII-D discharge 132731 (from figure 5.3) is considered again. Now the complete wall geometry is included in the simulations. Here, transport coefficients of  $D_{\perp} = 0.2 \text{ m}^2 \text{ s}^{-1}$  and  $\chi_{\perp} = 0.6 \text{ m}^2 \text{ s}^{-1}$  are used, which are slightly below the upper limit estimated above. The input power is set to  $P_{\text{in}} = 6.3 \text{ MW}$ , which corresponds to the experimental value during the H-mode phase of this discharge.

Profiles of the resulting target particle and heat fluxes at the inner strike point are shown in figure 5.6 (blue solid lines), where  $n_{\text{in}} = 1.2 \cdot 10^{19} \text{ m}^{-3}$ . Both profiles are

<sup>1</sup>Further analysis of the experimental results, which have become available only after completion of this present thesis, do now indicate also heat flux striation pattern similar to those found in the code application. It should be noted that in particular inferring target heat fluxes experimentally is a highly indirect and very subtle issue in itself.



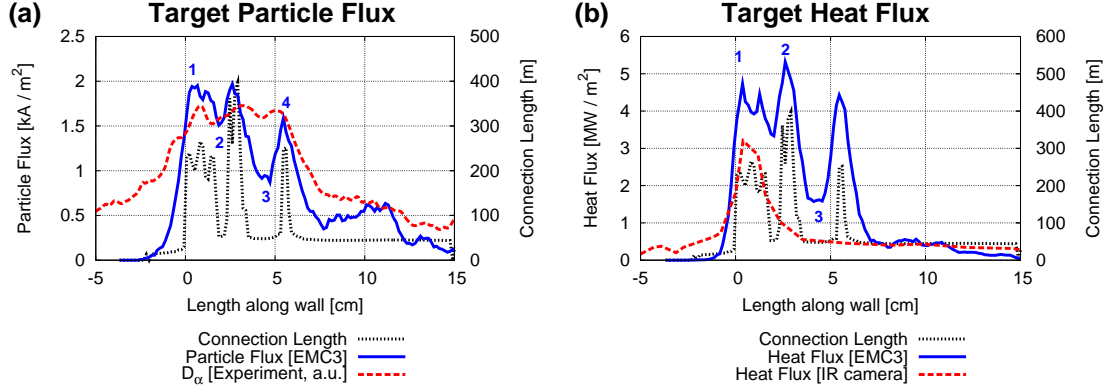


Figure 5.6: Profiles of (a) target particle flux  $\Gamma_{\text{target}}$  and (b) heat flux  $q_{\text{target}}$  (blue solid lines) in comparison to experimental observations (red dashed lines) and the local connection length  $L_c$  (black dotted lines). The blue numbers in the figure indicate the positions of  $\Gamma_1, \dots, \Gamma_4$  and  $q_1, \dots, q_3$  which are mentioned in the text.

well aligned to the magnetic topology (black dotted lines). The modeled particle flux is compared to the observed  $D_\alpha$  emission (red dashed line) which is correlated to the experimental particle flux (with an additional dependence on edge plasma parameters which is, however, not considered here in detail. See section 6.4.1 for this issue). Both profiles show a clear splitting and are in qualitative agreement. The slight shifts in the two outer peaks are probably due to error fields (e.g. misalignments of the field coils) which are neglected in these simulations. The peak particle flux of  $\Gamma_1 = 1.95 \text{ kA m}^{-2}$  is reduced to  $\Gamma_2 = 1.50 \text{ kA m}^{-2}$  at the first and  $\Gamma_3 = 0.90 \text{ kA m}^{-2}$  at the second minimum. The outer peak is with  $\Gamma_4 = 1.55 \text{ kA m}^{-2}$  at 80 % of  $\Gamma_1$ . A similar splitting is found for the modeled heat flux (figure 5.6.b) which prevails after including the complete wall geometry. The experimental peak heat flux of  $q_{1,\text{exp}} = 3.2 \text{ MW m}^{-2}$  drops to  $q_{3,\text{exp}} = 0.5 \text{ MW m}^{-2}$  without any significant splitting. Furthermore, the modeled heat flux is with  $q_1 = 4.7 \text{ MW m}^{-2}$  and  $q_2 = 5.3 \text{ MW m}^{-2}$  significantly larger than the observed one. Even the ratio of the second minimum  $q_3 = 1.6 \text{ MW m}^{-2}$  to  $q_1$  is significantly larger (35 %) than the experimentally observed one of only  $q_{3,\text{exp}}/q_{1,\text{exp}} = 16 \%$ .

Kinetic corrections to the parallel heat conduction in the fluid model, which have recently been investigated in context with modeling of RMP scenarios at the TEXTOR tokamak [47], might be necessary to improve agreement. It has been found in simulations for RMP scenarios at TEXTOR that  $T_e$  in front of the target is reduced when these kinetic corrections are applied, but not in the axisymmetric reference case. How this relates to the target heat flux pattern at DIII-D, however, has still to be determined. In addition, the treatment of cross-field transport in the present model needs to be advanced to include effects of an edge transport barrier in H-mode plasmas. This is investigated in section 5.4. Both types of corrections have already been taken into account in other approaches [28, 29], there, however, without the full 3D magnetic topology.



### 5.3.2 3D structure of the edge plasma

The complex magnetic field structure in figure 5.3 already suggests that a 3D spatial modulation is also present in the entire edge plasma. That there is indeed a complex 3D structure in the edge plasma is demonstrated in this section. The inner boundary of the simulation domain for the edge plasma is located at  $\psi^* \approx 0.77$ , where boundary conditions are set to  $n_{\text{in}} = 1.2 \cdot 10^{19} \text{ m}^{-3}$  and  $P_{\text{in}} = 0.9 \text{ MW}$ . This corresponds to experimental values observed during the L-mode phase in DIII-D discharge 132731. The resulting strong spatial modulation of the edge plasma is demonstrated in figure 5.7 (a) and (b) for the electron density  $n_e$  and electron temperature  $T_e$  by 2D cuts at a toroidal reference plane  $\varphi = 0$  deg. Clearly, the structure of the magnetic field is reflected in the edge plasma as well. In particular, the parallel plasma flow pattern in figure 5.7 (c) demonstrates the 3D character of the plasma edge layer. The 3D modulation is now investigated in more detail, in particular the effects of helical magnetic lobes and short magnetic flux tubes in the X-point region.

#### Helical magnetic lobes

In the presence of RMPs an intermediate layer between confined plasma and the regular SOL exists. In this layer field lines have an intermediate connection length of the order  $L_c \approx 400 \text{ m}$  (green regions in figure 5.3), which is smaller than that of ergodic field lines further inside but larger than field lines in the regular SOL and in the short flux tubes. This layer is bounded by the separatrix manifolds in the form of helical magnetic lobes which extend into the SOL. The helical nature of this boundary is most pronounced in the X-point region (figure 5.3.c), but also clearly visible on the high field side (HFS) midplane (figure 5.3.b). With the EMC3-EIRENE code it is possible to investigate the detailed effects of this structure on the edge plasma. It is demonstrated in figure 5.8 and 5.9 that the structure of these magnetic lobes also emerges in the modeled  $n_e$  and  $T_e$  profiles. These figures show 3D visualizations of  $n_e$  and  $T_e$  by means of selected 2D cuts (rainbow colored) and iso-parametric surfaces (blue shaded). In particular the  $n_{e,1} = 4.5 \cdot 10^{18} \text{ m}^{-3}$  and  $T_{e,1} = 60 \text{ eV}$  surfaces reflect very well the structure of the helical magnetic lobes at  $R \approx 108 \text{ cm}$ . But also further inside in the ergodic domain the  $n_{e,2} = 8.5 \cdot 10^{18} \text{ m}^{-3}$  and  $T_{e,2} = 120 \text{ eV}$  surfaces in figure 5.8 and 5.9 show a clear 3D pattern.

It can be expected from these figures that radial profiles of  $n_e$  and  $T_e$  depend strongly on the toroidal and poloidal position, inside the former separatrix as well as outside. Radial profiles located at the midplane ( $Z = 0 \text{ cm}$ ) are of particular interest, as these are usually measured in the experiment. Such midplane profiles are extracted from figure 5.8 at  $\varphi_1 = -10$  deg (red line, position B) and  $\varphi_2 = 50$  deg (blue line, position A) and compared to the corresponding connection length in figure 5.10. In particular it can be seen in parts (c) and (d) of figure 5.10 that  $n_e$  and  $T_e$  in the magnetic lobe (index A) at  $R = 108 \text{ cm}$ , i.e. just outside the former separatrix, is increased with respect to a

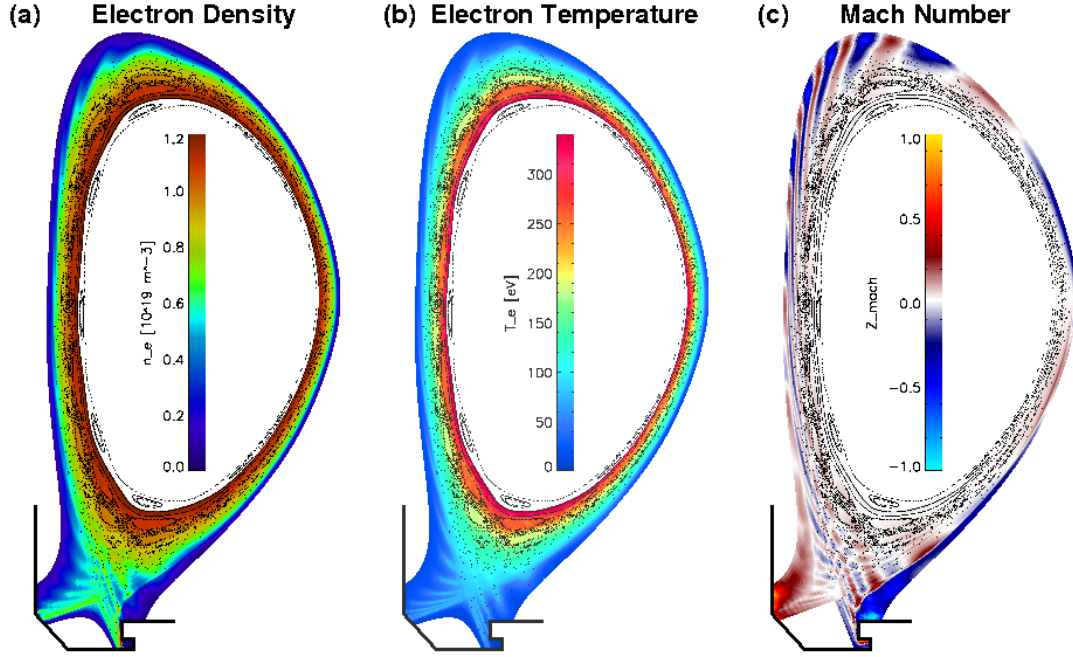


Figure 5.7: 2D cuts at the reference plane  $\varphi = 0$  deg of (a) electron density  $n_e$ , (b) electron temperature  $T_e$  and (c) Mach number. All figures are combined with a Poincaré-plot (black dots).

toroidal position where no such lobe is present (index  $B$ ):

$$\begin{aligned} n_{e,A} &= 4.2 \cdot 10^{18} \text{ m}^{-3} \\ n_{e,B} &= 2.9 \cdot 10^{18} \text{ m}^{-3} \\ T_{e,A} &= 68 \text{ eV} \\ T_{e,B} &= 37 \text{ eV} \end{aligned}$$

which is an increase by 45 % for  $n_e$  and 84 % for  $T_e$ . This behavior is in agreement with findings from simulations of limiter RMP scenarios at TEXTOR and DIII-D with similar magnetic field structures, also performed with the EMC3-EIRENE code [139]. As the toroidal position of diagnostic equipment in the experiment is fixed, direct comparison to experimental observations remains challenging. However, with a new RMP coil set planned for DIII-D, it will be possible to rotate the RMP field and hence, to move the magnetic field structure in front of the diagnostics. Furthermore, such a toroidal dependence is indicated experimentally by  $q$ -scans (i.e. by ramping up the plasma current) [140].

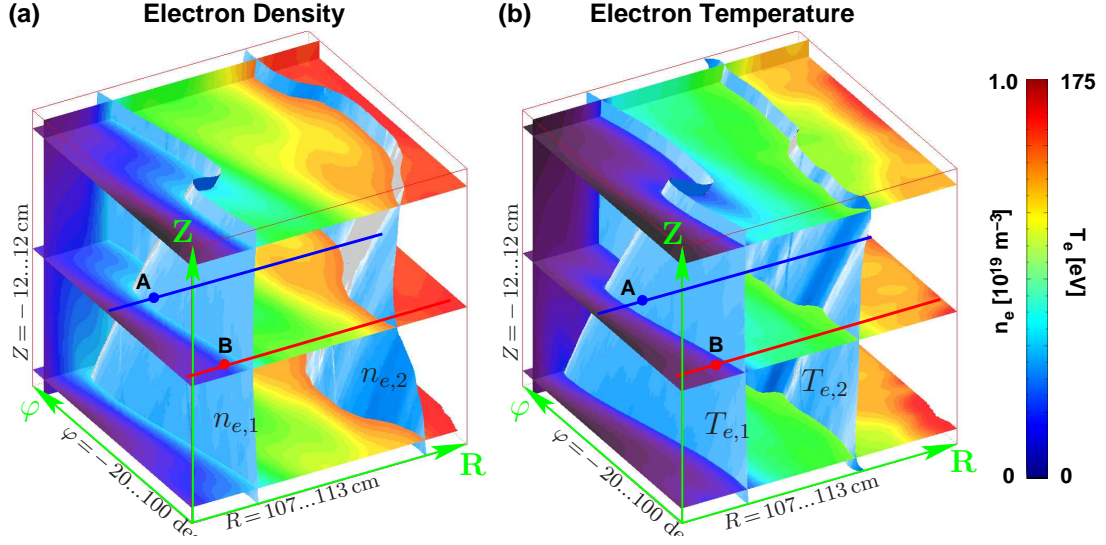


Figure 5.8: 3D visualization of (a) electron density  $n_e$  and (b) electron temperature  $T_e$  in the region of the HFS midplane by 2D cuts (rainbow colored) and iso-parametric surfaces (blue shaded) for  $n_{e,1} = 4.5 \cdot 10^{18} \text{ m}^{-3}$ ,  $n_{e,2} = 8.5 \cdot 10^{18} \text{ m}^{-3}$  and  $T_{e,1} = 60 \text{ eV}$ ,  $T_{e,2} = 120 \text{ eV}$ , respectively. Red and blue lines mark the positions of the profiles shown in figure 5.10

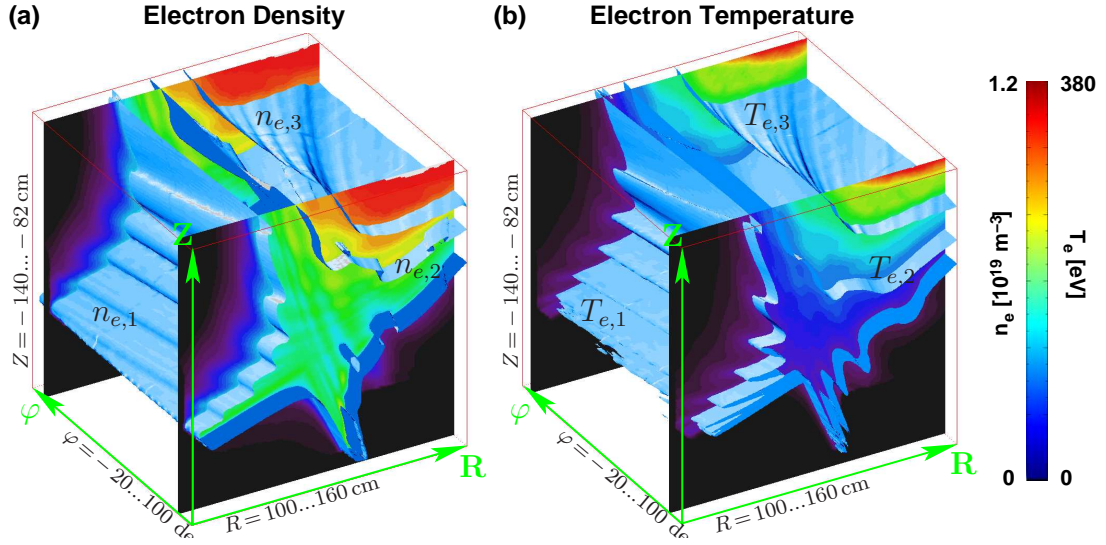


Figure 5.9: 3D visualization of (a) electron density  $n_e$  and (b) electron temperature  $T_e$  (right) in the X-point region by 2D cuts (rainbow colored) and iso-parametric surfaces (blue shaded) for  $n_{e,1} = 4.5 \cdot 10^{18} \text{ m}^{-3}$ ,  $n_{e,2} = 8.5 \cdot 10^{18} \text{ m}^{-3}$ ,  $n_{e,3} = 1.0 \cdot 10^{19} \text{ m}^{-3}$  and  $T_{e,1} = 60 \text{ eV}$ ,  $T_{e,2} = 120 \text{ eV}$ ,  $T_{e,3} = 200 \text{ eV}$ , respectively.

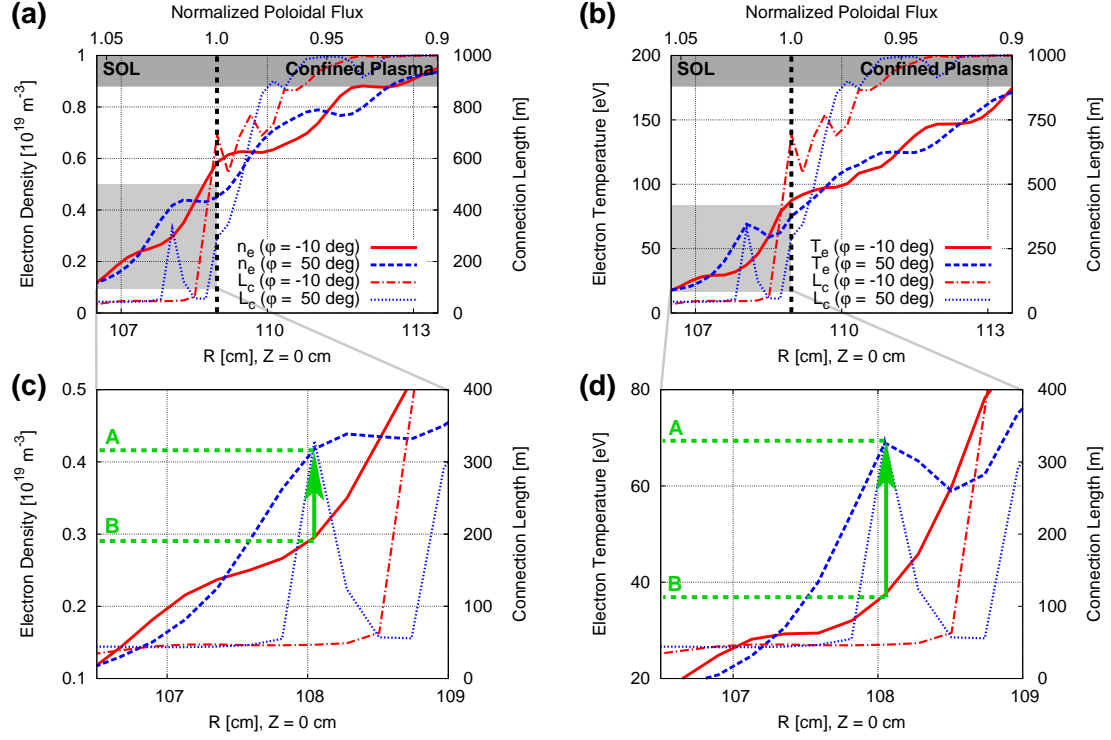


Figure 5.10: Solid and dashed lines: midplane profiles of (a,c) electron density  $n_e$  and (b,d) electron temperature  $T_e$ , dash-dotted and dotted lines: connection length  $L_c$ . Profiles are taken at  $\varphi_1 = -10$  deg (red) and  $\varphi_2 = 50$  deg (blue). Parts (c) and (d) are magnifications of the region where a helical magnetic lobe extends to the outside of the former separatrix. Green arrows indicate the increase of plasma parameter from position B to A in figure 5.8.

### Short magnetic flux tubes

Short magnetic flux tubes, i.e. field line bundles with short connection length  $L_c \approx 100$  m (blue regions in figure 5.3), exist in the domain inside the former separatrix [130]. These short flux tubes are suspected to act as an inward extension of the usually axisymmetric scrape-off layer (SOL). In figure 5.11 profiles of  $n_e$  and  $T_e$  on the  $\psi^* = 0.99$ -surface in the X-point region are shown and compared to the connection length of field lines. On this surface short flux tubes alternate with partially ergodic regions with long connection length of field lines. A strong modulation of  $n_e$  and  $T_e$  between short flux tubes (index  $F$ ) and long field lines (index  $L$ ) is found. Average peak and minimum values are:

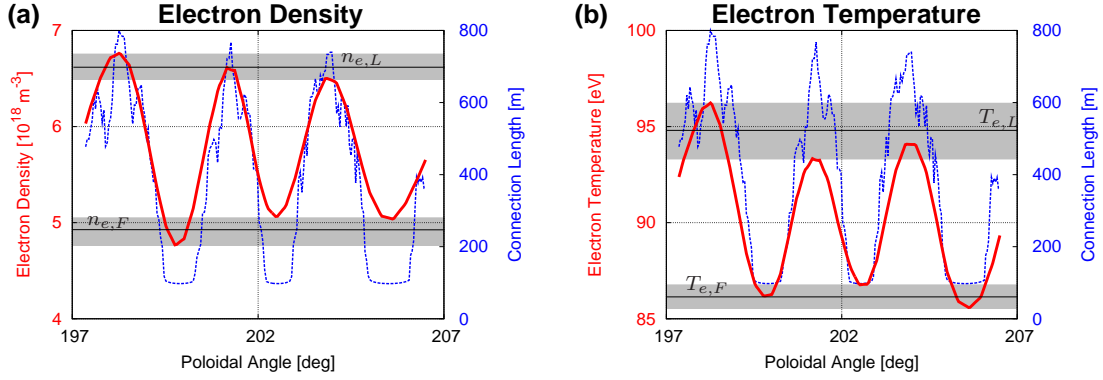


Figure 5.11: (a) Electron density  $n_e$  and (b) electron temperature  $T_e$  on the  $\psi^* = 0.99$  - surface in the X-point region (along the profile marked in figure 5.3.c). The corresponding connection length  $L_c$  is given as blue dashed line.

$$\begin{aligned}
 n_{e,F} &= (4.96 \pm 0.13) \cdot 10^{18} \text{ m}^{-3} \\
 n_{e,L} &= (6.62 \pm 0.11) \cdot 10^{18} \text{ m}^{-3} \\
 T_{e,F} &= (86.2 \pm 0.4) \text{ eV} \\
 T_{e,L} &= (94.5 \pm 1.2) \text{ eV}
 \end{aligned}$$

which corresponds to a density reduction of 25 % and a temperature reduction of 9 % in the short flux tubes. This is in qualitative agreement with earlier experimental observations and modeling (also with the EMC3-EIRENE code) at the TEXTOR tokamak [72, 97], even the more pronounced effect on  $n_e$ . These findings suggests that short flux tubes either act like an additional strong SOL sink or are not filled efficiently by cross-field diffusion from neighboring longer field lines.

From figure 5.3.c it seems that these short flux tubes have a well-defined (non-fractal) cross-section of about  $1 \text{ cm} \times 1 \text{ cm}$  and thus can be discussed within a 1D SOL model. However, when tracing this cross-section along the flux tube from the upstream position (near the X-point) to the divertor plates (figure 5.12), a strong deformation of the shape occurs just after one toroidal turn. The flux tube gets stretched in one direction to more than 30 cm while in the other direction it is compressed to less than 1 mm (see magnification in the upper left inset in figure 5.12), which results from a conservation of toroidal flux in the tube as it connects to different radial positions. After a few toroidal turns, completing a full poloidal turn, the stretching relaxes again, but then the flux tube is folded into U-shape. This is demonstrated in figure 5.12 by the blue contours (especially by the magnifications in the right inset) which show the shape of the flux tube after trace steps of  $\Delta\varphi = 120 \text{ deg}$ . In the end this U-shape is stretched again so that the flux tube creates an expanded footprint of  $\Delta\vartheta = 120 \text{ deg}$  in toroidal direction on the inner strike point. The footprint of the flux tube is displayed in red in figure

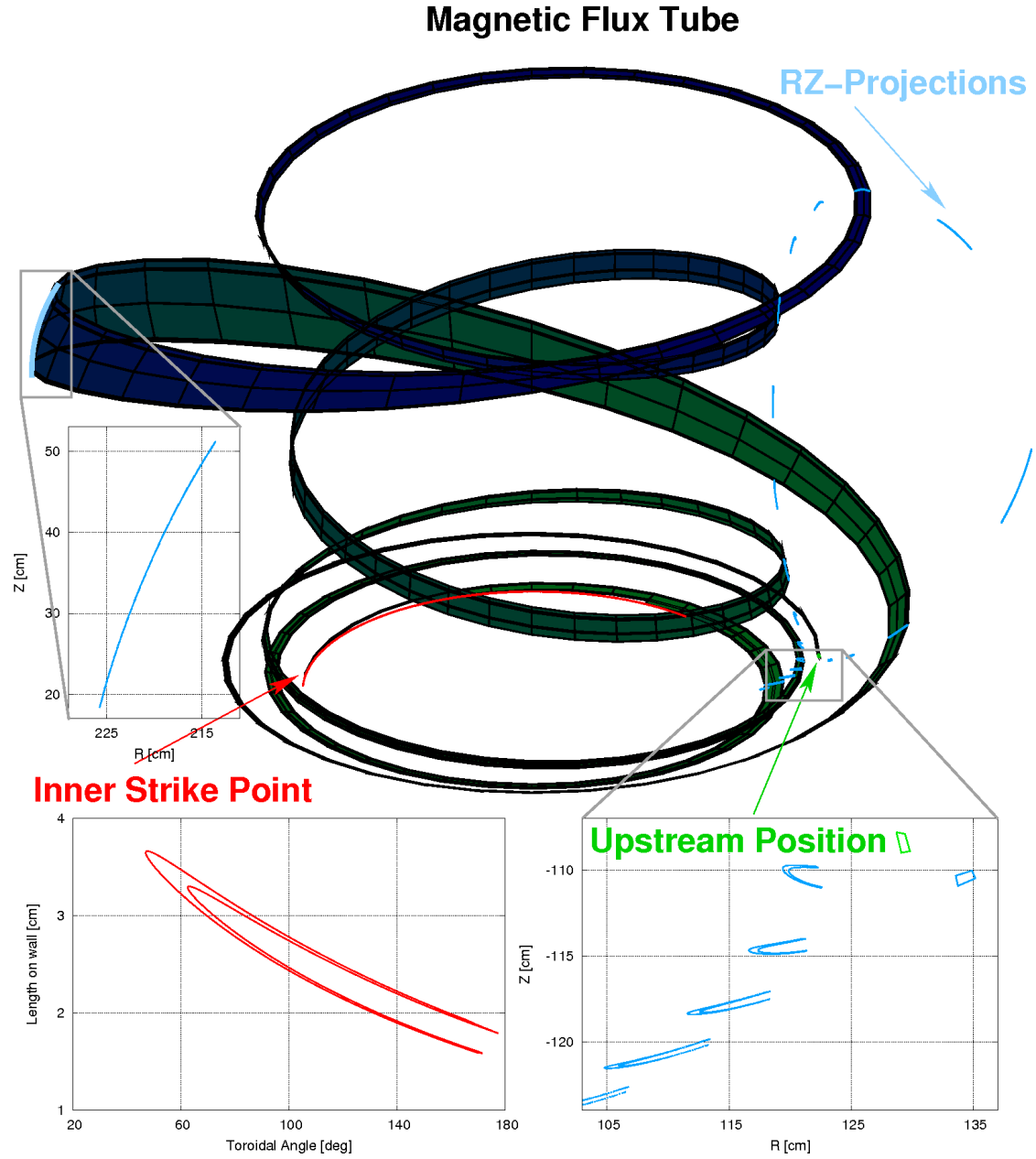


Figure 5.12: Visualization of a magnetic flux tube from its upstream position near the X-point (green) to the inner strike point (red). The blue contours are the shape of the flux tube in the  $R - Z$  plane after steps of  $\Delta\varphi = 120$  deg. The upper left and right insets are magnifications of the  $R - Z$  contours, where the positions are marked by gray boxes. The lower left inset displays the shape of the footprint of the flux tube on the wall.

5.12, where the lower left inset displays the shape of the flux tube on the wall. A similar behavior is also observed for the other part of the flux tube from its upstream position to the outer strike point.

This space shape-analysis already suggests that it would be over-simplistic to formulate a 1D transport model in these 3D flux tubes. This fact is now revealed in very detail for the first time by comparing profiles of  $n_e$ ,  $T_e$  and Mach number  $M$  along this selected flux tube to a 1D sheath-limited SOL (isothermal fluid) model [7]. Such a model was used at TEXTOR to describe plasma transport in similar short flux tubes there. Let  $x \in [-L, L]$  denote the coordinate along the flux tube with connection length  $2L$ , then the isothermal fluid model is:

$$n(x) = \frac{n_0}{1 + M^2(x)} \quad (5.11)$$

$$M(x) = \frac{1}{\hat{y}} \left[ 1 - \sqrt{1 - \hat{y}^2} \right], \quad \hat{y} = \frac{x}{L} \quad (5.12)$$

$$T(x) = T_0 \quad (5.13)$$

with free model parameters  $n_0$ ,  $T_0$  at the upstream position and uniformly distributed sources. Figure 5.13 (a)-(c) shows averaged profiles (blue solid lines) for  $n_e$ ,  $T_e$  and  $M$  calculated from 4 selected field lines within the flux tube and corresponding profiles from a simple 1D isothermal model (red dashed lines). Obviously, the 1D isothermal fluid model does not reproduce the plasma parameters in this strongly distorted magnetic flux tube. In particular  $T_e = \text{const}$  along the flux tube is not observed: the upstream value of  $T_e = 85 \text{ eV}$  drops to  $T_e = 51$  at the target. The density, on the other hand, increases from an upstream value of  $n_e = 0.5 \cdot 10^{19} \text{ m}^{-3}$  to  $n_e \approx 1.0 \cdot 10^{19} \text{ m}^{-3}$  at the outer strike point, while it is only slightly increased at the inner strike point. The qualitative behavior of  $n_e$  and  $T_e$  is more similar to that in a “high-recycling flux tube” (see section 5.2), however, the pronounced pattern in  $M$  confirms that 3D transport effects are important. In any case, sources are not uniformly distributed along the flux tube. These are due to diffusion from long field lines into the flux tube, but also due to ionization of neutrals. To account for particle sources, let us assume for simplicity that the former are proportional to the flux tube surface per toroidal angle  $A(\varphi)$ , then  $n_e$  and  $M$  in the isothermal fluid model are still determined by (5.11)-(5.12), however with  $\hat{y}$  replaced by

$$\hat{y}(x) = \frac{1}{Y} \int_0^x dl A(\varphi(l)), \quad Y = \int_0^{\varphi(L)} dl A(\varphi(l)). \quad (5.14)$$

The modified Mach number profile is shown in figure 5.13.c by a red dotted line. This correction slightly changes the  $M$  profile, however, it can not explain the results from 3D modeling. Certainly, the source distribution is far more complex when considering 3D



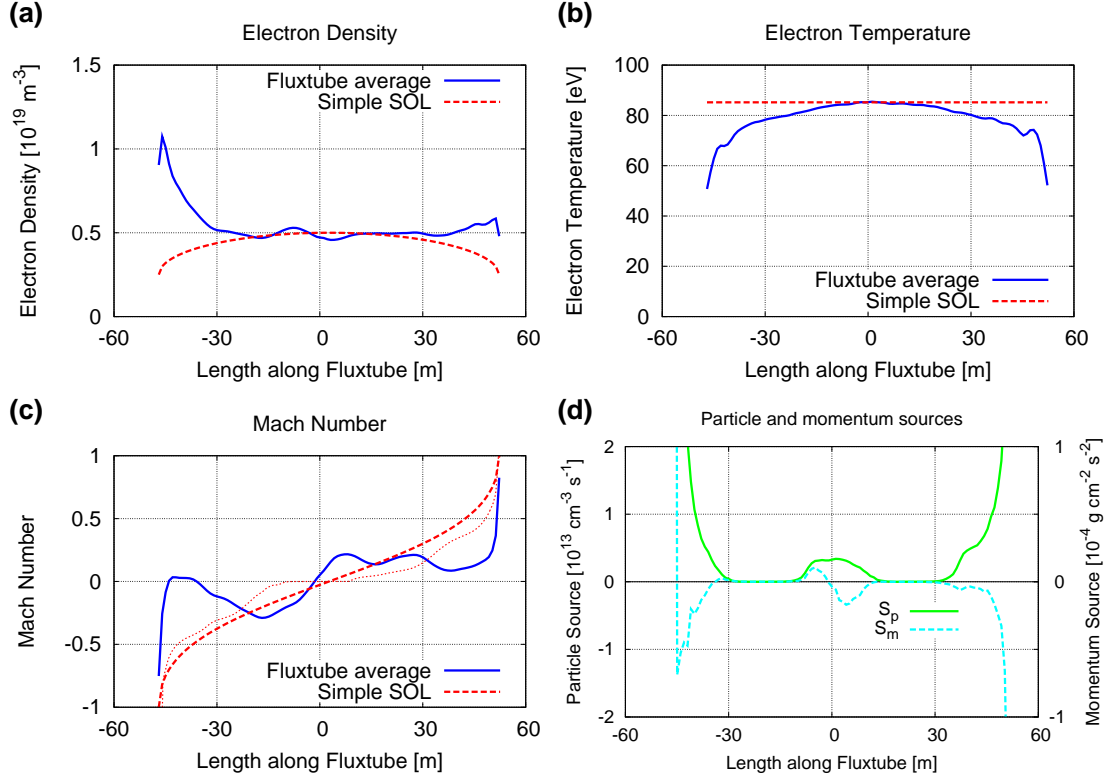


Figure 5.13: Profiles of (a)  $n_e$ , (b)  $T_e$  and (c)  $M$  along the flux tube from figure 5.12. The flux tube average (blue solid lines) is calculated from 4 field lines within the flux tube and compared to a 1D isothermal fluid model (red dashed lines). The red dotted line in (c) is from an extended model (eq. 5.14) with local sources adapted to the flux tube surface. (d) Parallel profiles of particle and momentum sources  $S_p$  and  $S_m$  due to interaction with neutral particles.

transport effects, in particular when ionization sources  $S_p$  are included. Furthermore, momentum sources  $S_m$  need to be included as well, as is demonstrated in figure 5.13 (d). Without  $S_p$  and  $S_m$  it is not possible to obtain a flow reversal and an increase of  $n_e$  in front of the target as observed for the modeled profiles in figure 5.13. The 3D edge model in the EMC3-EIRENE code includes transport and ionization of neutrals. The resulting effects on the plasma are included in the balance equations (3.35), (3.36), (3.41) and (3.42) by particle, momentum and energy sources  $S_p$ ,  $S_m$  and  $S_{ee}$ ,  $S_{ei}$ , respectively.  $S_p$  and  $S_m$  along the flux tube are shown in figure 5.13.d. Clearly, neutral particles penetrate into the upstream region of the flux tube and contribute to particle and momentum sources for the plasma. The penetration of neutrals depends on local plasma parameter, and hence, it is an intrinsic 3D transport problem. In conclusion, it is apparently not possible to use an isolated 1D transport model on top of a 3D magnetic geometry, not even for rather simple short magnetic flux tubes. Nevertheless, earlier research is based on such a procedure [132, 20].



## 5.4 Edge transport modeling for H-mode plasmas

Realistic simulations of H-mode plasma require an advancement of the cross-field transport model in the EMC3-EIRENE code. This advancement is necessary to include the effects of an edge transport barrier, which is thought to be responsible for the increase of confinement in H-mode plasmas. A numerical scheme has been developed in section 4.1.3 which allows for the implementation of spatially varying cross-field diffusion coefficients without the explicit calculation of the arising cross-field gradients in the transport equation. Although cross-field diffusion coefficients can now be specified as an arbitrary 3D function in EMC3, only a one parametric dependency is investigated in the following. In particular  $D_{\perp} = D_{\perp}(\psi^*)$ ,  $\chi_{\perp} = \chi_{\perp}(\psi^*)$  is assumed, which makes  $D_{\perp}$  and  $\chi_{\perp}$  a “radial” function only.

The remaining part of this chapter is dedicated to the effects resulting from a transport barrier on the edge plasma. At first, different models for  $D_{\perp}$ ,  $\chi_{\perp}$  are presented in section 5.4.1 and are then analyzed within an axisymmetric scenario in section 5.4.2. Then findings from this first analysis are applied to an RMP scenario in section 5.4.3. This section is intended as motivation for subsequent work, a detailed analysis cannot be performed in this thesis.

### 5.4.1 Ad hoc modeling of an edge transport barrier

An analysis of detailed edge transport barrier physics is out of the scope of this thesis. Therefore only ad hoc models for  $D_{\perp}$  and  $\chi_{\perp}$  are presented and discussed in the following. These models are then applied to an axisymmetric H-mode plasma and compared to experimental observations in order to find a reasonable model which can later be applied to RMP scenarios. This approach is similar to that in 2D modeling with SOLPS5 (B2-EIRENE) [141]. Throughout this section  $\chi_{\perp}(\psi^*) = 3 D_{\perp}(\psi^*)$  is assumed.

The first model under investigation is based on a tanh-like transition to the transport barrier, similar to the ansatz presented in [29] for 1D transport modeling, but here extended into the regular SOL:

$$D_{\perp}^{(1)}(\psi^*) = D_B + (D_0 - D_B) \cdot \left[ \alpha_1 - \alpha_2 \tanh\left(\frac{\psi^* - \psi_B}{\delta_B}\right) + \alpha_3 \tanh\left(\frac{\psi^* - \psi_1}{\delta_B}\right) \right]. \quad (5.15)$$

The basic parameters for this model are the transport levels inside and outside the barrier  $D_0$  and  $D_B$ , the inner and outer barrier position being  $\psi_B$  and  $\psi_1$ , respectively, and smoothness of the barrier transition  $\delta_B$ . This model can be fine tuned by the parameters  $\alpha_1, \alpha_2$  and  $\alpha_3$ , e.g. to allow for different transport levels in the core plasma and in the SOL. The following sub-models are considered:

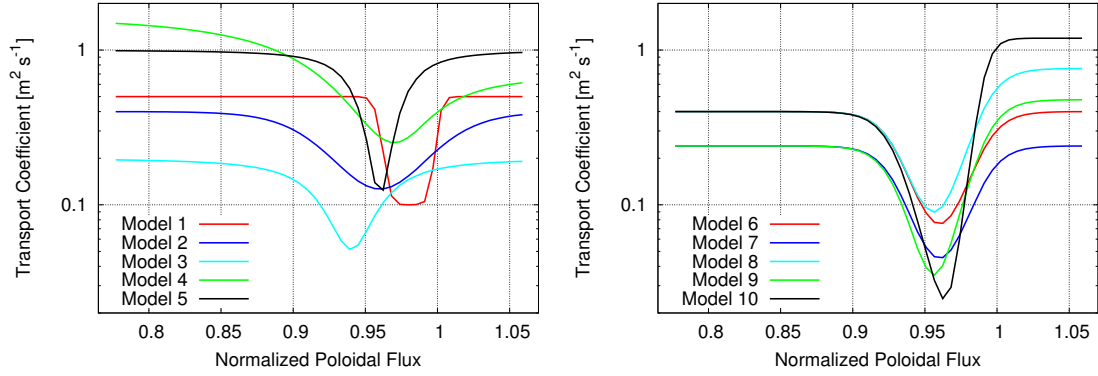


Figure 5.14: Comparison of various models considered for anomalous cross-field diffusion.

Model #	$\alpha_1$	$\alpha_2$	$\alpha_3$
1.1	1	1/2	1/2
1.2	3/2	1/2	1
1.3	2	1/2	3/2

This already allows for a wide variety of realizations. However, a second model type with similar properties is introduced in addition. This is to reflect the general uncertainty of the transport barrier physics. The second model type is based on the parametrization:

$$D_{\perp}^{(2)}(\psi^*) = D_0 + \frac{D_B - D_0}{1 + \left(\frac{\psi^* - \psi_B}{\delta_B}\right)^2}. \quad (5.16)$$

The parameters of this model are the transport levels inside and outside the barrier  $D_0$  and  $D_B$ , the center position of the barrier  $\psi_B$  and the barrier width  $\delta_B$ . The following parameter sets are investigated this chapter, where  $D_0$  and  $D_B$  are given in units of  $\text{m}^2 \text{s}^{-1}$ :

Label	1	2	3	4	5	6	7	8	9	10
Model #	1.1	1.1	2	2	2	1.1	1.1	1.2	1.2	1.3
$D_0$	0.5	0.4	0.2	$\psi < 0.97$ 1.7 $\psi > 0.97$ 0.7	1.0	0.4	0.24	0.4	0.24	0.4
$D_B$	0.1	0.04	0.05	0.25	0.1	0.04	0.024	0.04	0.002	0.004
$\psi_B$	0.96	0.92	0.94	0.97	0.96	0.93	0.93	0.93	0.93	0.93
$\psi_1$	1	1	-	-	-	0.99	0.99	0.99	0.99	0.99
$\delta_B$	0.005	0.04	0.03	0.08 0.043	0.02	0.02	0.02	0.02	0.02	0.02

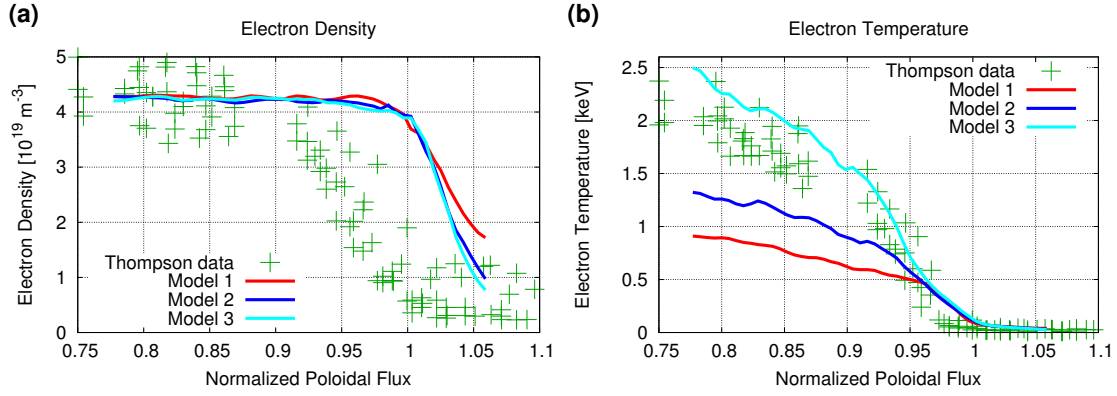


Figure 5.15: Radial profiles of (a) electron density and (b) electron temperature at the outboard midplane. Simulations have been performed for transport models 1-3.

### 5.4.2 Modeling of axisymmetric H-mode plasmas

The cross-field transport models presented in the previous section are now applied to plasma transport simulations for an axisymmetric scenario. Comparing simulation results with experimental observation allows to evaluate these models. The intention is to find the best matching model and then apply it to the corresponding RMP scenario.

The following simulations have been performed for models 1-3 with boundary conditions of  $n_{\text{in}} = 4.3 \cdot 10^{19} \text{ m}^{-3}$  and  $P_{\text{in}} = 6.3 \text{ MW}$ , which are taken from experimental observations for DIII-D discharge 132731 at  $t = 2200 \text{ ms}$ . Radial profiles at the outboard midplane are extracted from the simulation results and displayed in figure 5.15 in comparison to data from the Thompson scattering system. The most striking feature of the modeled data is that  $n_e = \text{const}$  throughout the confined region up to the separatrix. The shape of the  $T_e$  profiles on the other hand is reasonable. In particular, the  $T_e$  profile for model 3 is in good agreement with experimental observations. The flat  $n_e$  profiles in the simulations can be explained as follows: All neutrals are ionized directly in front of the divertor target and cannot penetrate into the confined plasma for the given  $n_{\text{in}}$  and  $P_{\text{in}}$ . In particular no neutrals can penetrate to the inner simulation boundary. This results in  $S_p = 0$  throughout the confined region and  $\Gamma_{\text{in}}^{(p)} = 0$ . Under these conditions it is easy to see from (3.35) that no cross-field gradients can arise.

A reason for the mismatch might be that recycling of the particle flux associated with the  $\lambda_p$  boundary condition (see section 4.3.1) has been neglected. This main chamber recycling would probably result in  $S_p \neq 0$  in the confined region. Similarly, a gas-puff in the main chamber, currently also not included in the model, could contribute to particle sources in the confined region.

### Hydrogen pumping and re-fueling

So far, re-fueling of the plasma by neutral beam injection (i.e. gas-puffing as it occurs in the experiment) has been neglected. This would result in additional sources within the confined region, and therefore should be taken into account regarding the observations presented above. Also pumping of neutral hydrogen from the outer divertor has been neglected so far. Both are now taken into account, however in a simplified manner to realize a steady state condition. Re-fueling by neutral beam injection is approximated by an additional in-flux  $\Gamma_{\text{fuel}}$  into the simulation domain. The approximation is that all neutrals (from the beam) penetrate into the very core plasma, are ionized there and enter the edge plasma as poloidally uniform particle flux  $\Gamma_{\text{fuel}}$ . To realize a steady state, the amount of in-flux is taken from the pumped hydrogen flux  $\Gamma_{\text{pump}}$  at the divertor target. The numerical realization of  $\Gamma_{\text{pump}}$  in the EIRENE code is accomplished by introducing an additional surface at which all particles are absorbed (or, more generally, with a prescribed sticking probability).

The realization of neutral hydrogen pumping by an absorbing surface is an approximation to the real pumping process. Therefore, to estimate the related effect, three different combinations of regular walls and pumping surfaces are analyzed (see figure 5.16 (a)). The resulting impact on the neutral hydrogen density  $n_H$  and the corresponding plasma source  $S_p$  is demonstrated in figure 5.16 (b) by radial profiles at the outer strike point for simulations within transport model 2. The self-consistent target (plasma) particle fluxes and (neutral) pump fluxes are summarized below and compared to the reference case without pumping:

	Reference	Model P1	Model P2	Model P3
$\Gamma_{\text{target}}$ [kA]	18.3	1.85	1.61	1.61
$\Gamma_{\text{pump}}$ [kA]	-	0.15	0.16	0.16

From figure 5.16 (b) it can be seen that the neutral hydrogen density is reduced by one order of magnitude, and even stronger in the pump duct region. Right at the separatrix  $n_H$  is reduced from  $n_{H,\text{Reference}} = 2.51 \cdot 10^{18} \text{ m}^{-3}$  to  $n_{H,\text{Model P1}} = 6.53 \cdot 10^{17} \text{ m}^{-3}$  for pump model 1 and  $n_{H,\text{Model P2}} = 5.62 \cdot 10^{17} \text{ m}^{-3}$ ,  $n_{H,\text{Model P3}} = 5.54 \cdot 10^{17} \text{ m}^{-3}$  for pump model 2 and 3, respectively. Correspondingly, also the plasma sources  $S_p$  are reduced by one order of magnitude when pumping is switched on. Clearly, pumping has a very strong effect on the neutral particle distribution. The impact on the edge plasma is investigated in the following for pump model P1.

### Impact on the edge plasma

Self-consistent simulations with neutral hydrogen pumping and re-fueling have been performed for the cross-field transport models in figure 5.14. Radial profiles of  $n_e$  and  $T_e$  at the outboard midplane are presented in figure 5.17. It can be seen clearly that  $n_e$  profiles are in much better agreement with experimental observation when pumping

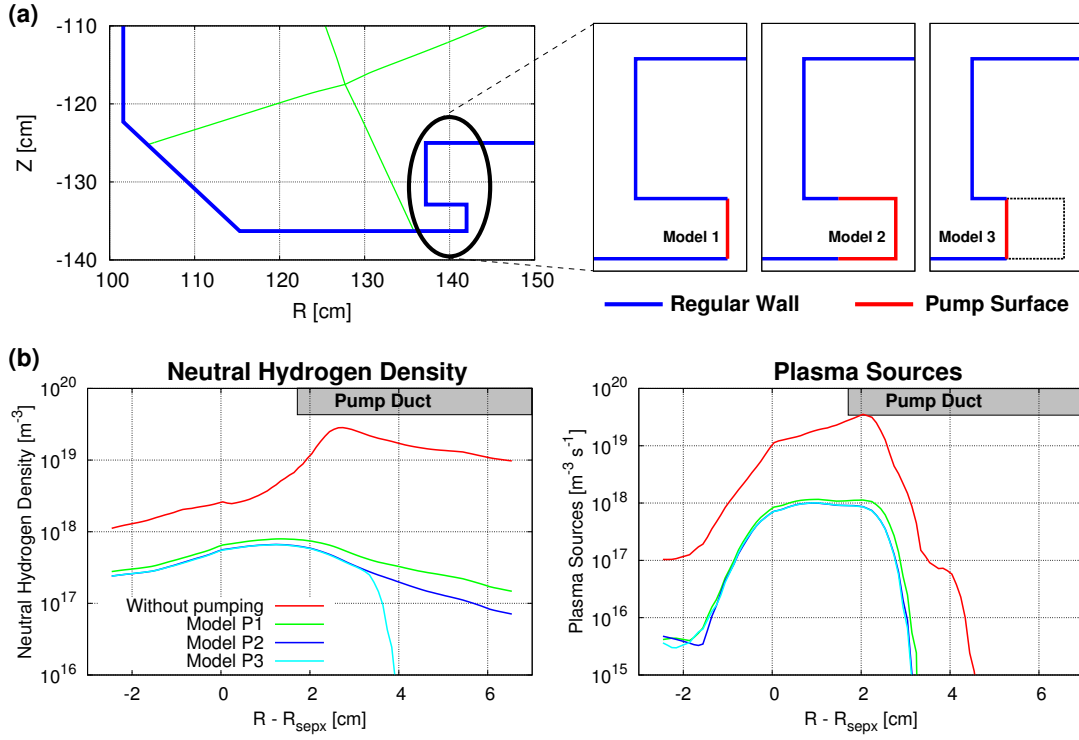


Figure 5.16: (a) Different realizations of pumping surfaces in the pump duct region of the DIII-D tokamak. The unperturbed separatrix of the present plasma scenario is marked in green to guide the eye. (b) Radial profiles of the neutral hydrogen density  $n_H$  and the plasma sources at the outer strike point at  $Z = -135.5$  cm. The radial coordinate is normalized to the position  $R_{\text{sepx}}$  of the separatrix.

is switched on. However, the good agreement of the  $T_e$  profile from model 3 without pumping does not prevail.  $T_e$  is increased throughout the simulation domain, which is, however, consistent with a decrease of  $n_e$  while  $P_{\text{in}}$  is fixed. In particular at the separatrix:  $T_{e, \text{Model 3}}^1 \approx 550$  eV, which is much too large. The other models result in a large discrepancy as well, e.g.  $T_{e, \text{Model 2}}^1 \approx 280$  eV or  $T_{e, \text{Model 7}}^1 \approx 640$  eV. The best match for  $T_e$  at the separatrix is obtained from model 5:  $T_{e, \text{Model 5}}^1 \approx 100$  eV, however the corresponding density is too large:  $n_{e, \text{Model 5}}^1 \approx 1.5 \cdot 10^{19} \text{ m}^{-3} \text{ s}^{-1}$ . Also  $T_e$  at the ISB from model 5 is with  $T_{e, \text{Model 5}}^{\text{ISB}} \approx 600$  eV much lower than the experimental value. Much better agreement for  $T_e$  at the ISB is found for model 10:  $T_{e, \text{Model 10}}^{\text{ISB}} \approx 2.1$  keV, however the slope up to the barrier is too small.

As demonstrated, either  $n_e$  or  $T_e$  are in agreement to experimental observation with or without pumping. However, (5.15) and (5.16) still leave much freedom for exploration and fine tuning, but this is beyond the scope of this thesis. Also the implementation

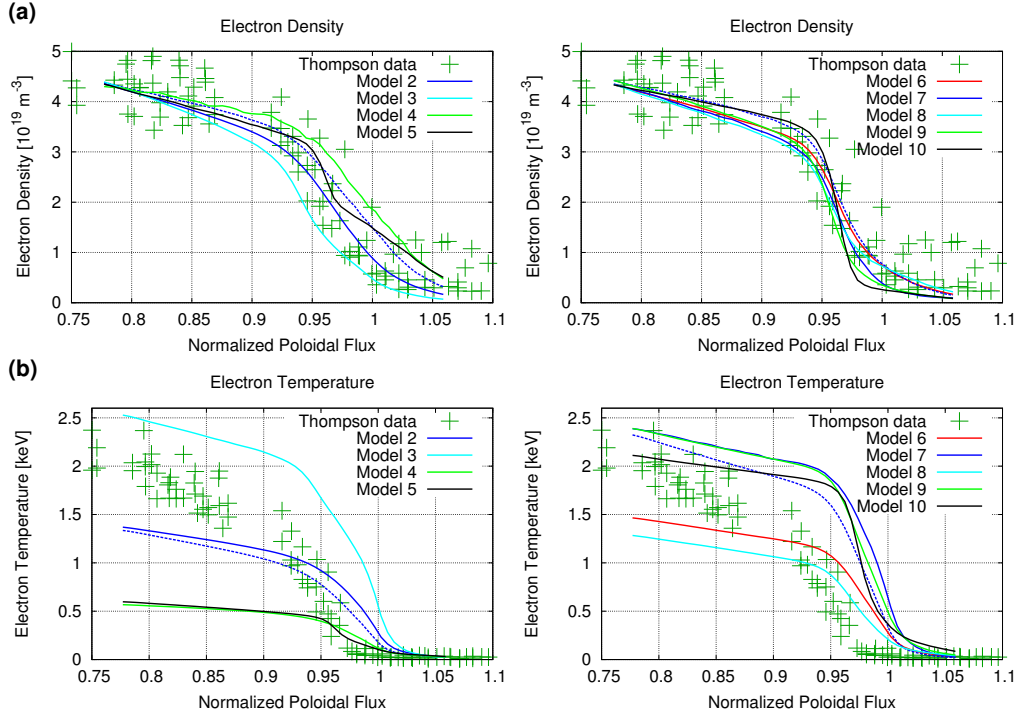


Figure 5.17: Radial profiles of (a) electron density and (b) electron temperature at the outboard midplane. Simulations have been performed for pumping model 1 and transport models 1-10. The blue dashed lines are for transport models 2 and 7 with a reduced pumping efficiency of 30 %.

of pumping by absorbing surfaces might overestimate the actual effect. This can be accounted for by an additional parameter: the pumping efficiency  $\varepsilon_P$  (i.e. sticking probability), which is an input parameter that specifies the fraction of absorbed (and consequently pumped) particles at pumping surfaces. Reducing  $\varepsilon_P$  to 30 % (this value is in 2D SOLPS5 modeling [142] for transport model 2 results in an increase of  $n_e$  and a corresponding decrease of  $T_e$ : at the separatrix  $T_e$  is reduced to  $T_{e, \text{Model 2}^*}^1 \approx 180 \text{ eV}$ , while  $n_e$  is increased from  $n_{e, \text{Model 2}}^1 \approx 0.89 \cdot 10^{19} \text{ m}^{-3}$  to  $n_{e, \text{Model 2}^*}^1 \approx 1.5 \cdot 10^{19} \text{ m}^{-3}$ . A similar effect is observed for model 7, for which the modified  $n_e$  profile is still in very good agreement with experimental observations while  $T_e$  is reduced (but not enough to match experimental observations).

Possible reasons for this mismatch are that on the one hand ELMy H-mode plasmas are not stationary: plasma conditions are significantly different during and between ELMs. The present transport model, however, accounts only for steady state conditions and therefore should be considered with caution for the inter-ELM phase. On the other hand, error fields due to coil misalignments already introduce a small perturbation of the edge plasma. In fact, modeling of the magnetic field structure with the TRIP3D code has shown that magnetic flux surfaces are destroyed within 2 % poloidal flux inside

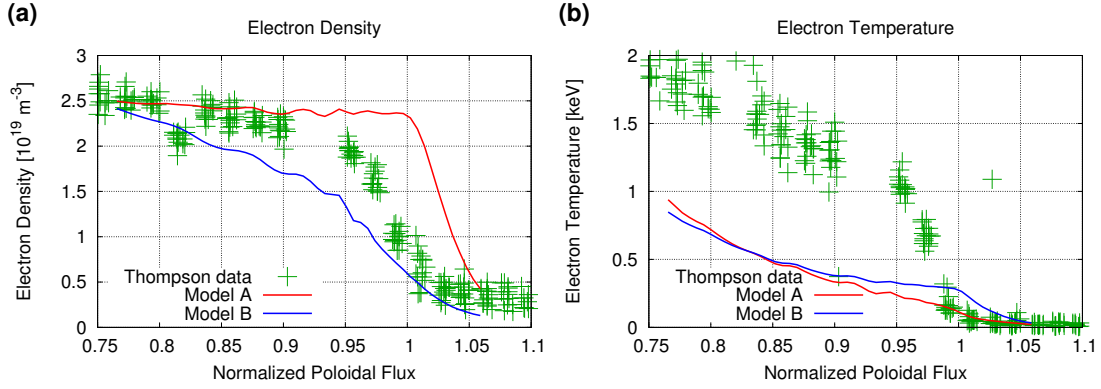


Figure 5.18: Radial profiles of (a) electron density and (b) electron temperature at the outboard midplane. Simulations have been performed with transport model A and B for an RMP H-mode plasma.

the separatrix [143]. This is exactly the region where  $T_e$  in all simulations is too large.

### 5.4.3 Modeling of RMP H-mode plasmas

As the preceding analysis failed to provide a single cross-field transport model that matches both  $n_e$  and  $T_e$  profiles, two of the above models are selected to investigate RMP H-mode plasmas: A = model 3 without pumping (which gives good agreement to the experimental  $T_e$  profiles) and B = model 7 with 30 % pumping (which gives good agreement to the experimental  $n_e$  profiles).

In figure 5.19 it can be seen that the structure of the edge plasma induced by RMPs remains under H-mode conditions. Boundary conditions are set to  $n_{in} = 2.3 \cdot 10^{19} \text{ m}^{-3}$  and  $P_{in} = 6.3 \text{ MW}$  which corresponds to experimental conditions of this scenario. Radial profiles at the outboard midplane are extracted in figure 5.18 and compared to experimental observations. Without pumping (model A) the  $n_e$  profile turns out to be flat when  $n_{in}$  is raised to H-mode like values. This is similar to the results for the axisymmetric reference case. Model A has been selected because of its good agreement with experimental  $T_e$  profiles. However, as can be seen in figure 5.18 (b), the same model does not provide good agreement for  $T_e$  in the RMP case. The temperature collapses in the complete simulation domain, e.g.  $T_{e, \text{Model A}}^{ISB} \approx 940 \text{ eV}$  at the ISB.

In model B, which includes pumping, radial profiles of  $n_e$  and  $T_e$  are significantly different from model A. Pumping decreases  $n_e$  at the separatrix, resulting in a local increase of  $T_e$ . At the separatrix:  $T_{e, \text{Model B}}^1 \approx 270 \text{ eV}$ , which is much larger than observed experimentally. However, no pedestal-like structure is present in the  $T_e$  profiles in both cases, so that  $T_e$  is too low further inside.

Comparing the  $n_e$  profiles from model A and B suggest that the correct model is some-

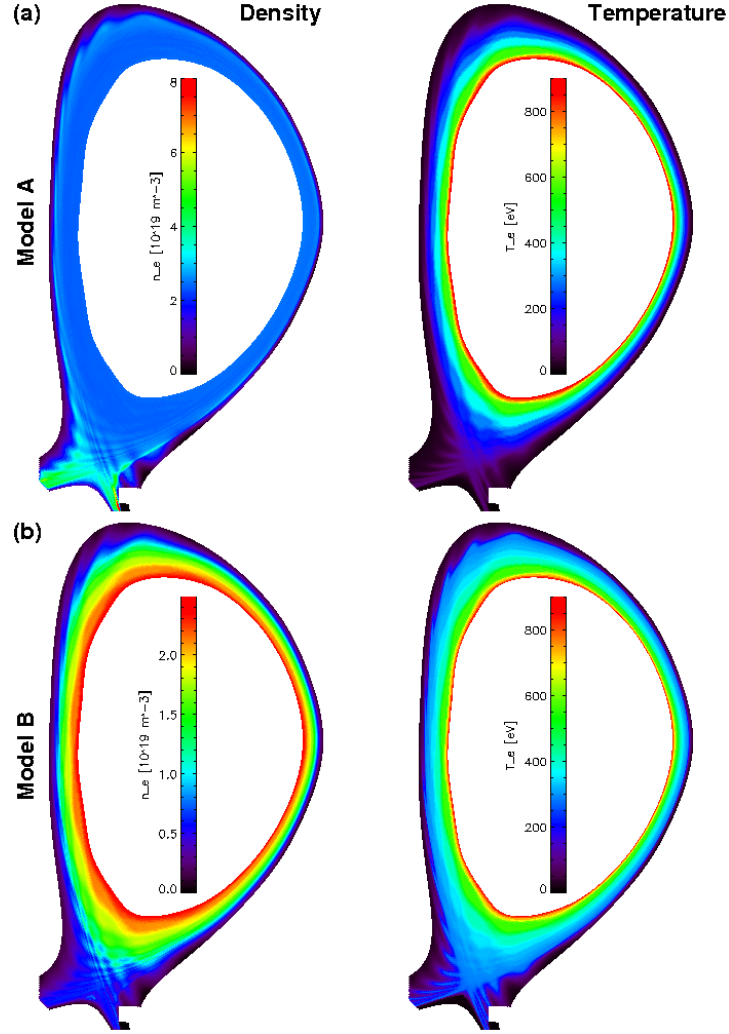


Figure 5.19: 2D cuts of  $n_e$  and  $T_e$  for model A and B.

where in between. One might obtain the correct  $n_e$  behavior by adjusting the pumping efficiency  $\varepsilon_P$ , however, the more credible approach would be to estimate the pumped flux and re-fueling from experimental observation. This still leaves the  $D_\perp$  and  $\chi_\perp$  profiles as unknown parameters. Additionally one should consider kinetic corrections to the parallel electron heat flux, which are here left for future analysis. Furthermore, screening of the perturbation field might be important. A first step to include this effect is to consider a homogeneous screening of all modes, i.e. simply by reduction of the perturbation current. All this and a detailed analysis of the plasma footprint pattern in comparison to the results from section 5.3 are left for subsequent work.



## 6 Plasma transport in the helical divertor at TEXTOR

Helical divertor scenarios (by application of RMPs) are investigated at the TEXTOR tokamak in order to control plasma edge transport and the resulting particle and heat fluxes to the divertor target [65]. These scenarios are investigated both experimentally [144, 145, 72, 146, 96, 73, 97] and numerically [132, 46, 117, 99, 47, 77]. Of particular interest is a specific plasma state called *detachment*, with reduced particle and heat fluxes to the material surfaces bounding the system. In this chapter, numerical studies are performed to investigate whether the helical divertor at TEXTOR allows to control particle and heat fluxes in such a way that plasma detachment can be achieved. Beginning with a brief summary of the phenomenology of plasma detachment in section 6.1, this chapter continues with an overview of the magnetic field structure and the resulting plasma structure in section 6.2. The inherent complex 3D magnetic field structure - and consequently the demand for 3D plasma transport simulations - is demonstrated by applying the visualization procedures presented in section 2.4. It will be shown that in the present 3D magnetic field configuration it is not possible to speak of phenomena such as *high-recycling* or *detachment* in the sense of the typical upstream-downstream balances (2-point model) for poloidal divertors [7].

The typical conditions at the plasma edge allow to apply a fluid transport model (presented in chapter 3), which is implemented in the EMC3-EIRENE code (presented in chapter 4), to perform plasma transport studies. The main part of this chapter begins in section 6.3, where at first characteristic parameters are established to allow an analysis of global transport phenomena which is then performed. Afterwards, in section 6.4, a detailed study of spatially resolved transport characteristics is given in order to investigate the relevance of different domains within the chaotic magnetic edge layer and to demonstrate that the helical divertor physics at TEXTOR is significantly different from that in axisymmetric configurations such as poloidal divertors or toroidal limiters. The edge plasma may be affected by the presence of impurities (e.g. carbon which is released by plasma-wall interaction). The major effect of impurities is a cooling of electrons due to line radiation. Therefore this chapter closes with a short analysis of the impact of carbon impurities on the edge plasma. A more detailed analysis of impurity transport (boundary conditions, reaction rates, source distribution) is given in appendix D.

## 6.1 Brief summary of plasma detachment

The reduction of divertor heat loads is a crucial issue for designing a fusion reactor, which motivated the investigation of so called *detached plasmas*. In particular these plasmas are considered for ITER [147, 56]. The basic idea is to extinguish the plasma exhausts (target particle and heat loads  $\Gamma_{\text{target}}$ ,  $q_{\text{target}}$ ) in a neutral gas cloud in a remote divertor chamber. Quite different definitions of “detachment” are in use, and also quite different physical phenomena are today referred to as “detachment” (see [148, 149, 150, 7, 151]). For the sake of clarity, the definition of plasma detachment in poloidal divertors given in [150] shall be noted here: *state in which large pressure gradients are observed parallel to the magnetic field with consequently low plasma power and ion fluxes to the material surfaces bounding the system*. The concept to achieve plasma detachment is to increase the plasma density at the separatrix and/or to increase the power in the SOL, e.g. by impurity radiation. This results in a localization of plasma sources in the divertor region and, after an initial increase, a roll-over and then a decrease in parallel plasma flow with increasing upstream density. Parallel heat flux is essentially determined by conduction, which leads to a drop of the temperature in front of the target and allows the buildup of a neutral gas cloud. The pressure drop is then caused by parallel momentum losses.

The wide variety of fusion devices and particle exhaust configurations (limiter tokamaks, poloidal divertor tokamaks, stellarators with island or helical divertors, see section 2.1) allows a wide variety of plasma recycling regimes. A detailed characterization of various fusion devices is beyond the scope of this thesis, and only a brief description is given here. In poloidal divertor tokamaks three different regimes are observed with increasing upstream density  $n_u$  (where upstream refers to the stagnation point in the axisymmetric SOL):

- the linear regime:  $\Gamma_{\text{target}} \sim n_u$ , which corresponds to the so called *Sheath-Limited regime* where the temperature on field lines in the SOL is constant,
- the high-recycling regime, where  $\Gamma_{\text{target}}$  increases non-linearly with  $n_u$ , which corresponds to the so called *Conduction-Limited regime* with large temperature gradients (but plasma pressure being constant along field lines), and
- the detachment regime with a roll-over in  $\Gamma_{\text{target}}$  without a corresponding decrease in the  $H_\alpha$  emission ( $\lambda = 656.2 \text{ nm}$  line emission) in the divertor (instead:  $H_\alpha$  emission continues to increase).

In stellarators, particularly in W7-AS and LHD, a roll-over of  $\Gamma_{\text{target}}$  is observed as well, both experimentally and in simulations with the EMC3-EIRENE code [152, 133]. At these machines, however, without the intermediate high-recycling regime before detachment. This suppression of the high recycling regime suggests that additional momentum losses, other than plasma-gas friction, are present, and it has been found that these are due to cross-field transport on open field lines with long wall-to-wall connection length.

The detachment regime in limiter tokamaks is fundamentally distinct from poloidal

divertor tokamaks. In the former it is observed that the ionization front (measured by  $H_\alpha$  emission) moves radially inward (across the  $\mathbf{B}$ -field) from the target. Hence, in the definition of [150], this is not regarded as detachment at all. The underlying physics is fundamentally different as well: while recycled neutral particles in limiter tokamaks penetrate basically in radial (i.e. cross-field) direction, they penetrate basically in parallel (to  $\mathbf{B}$ ) direction in poloidal divertor tokamaks. As will be shown below, in tokamaks with a 3D chaotic magnetic edge layer such as TEXTOR in the helical divertor configuration (see section 2.2.2 and figure 6.1) it is neither of both exclusively, but rather a complex combination of both. Hence, no direct correspondence to the phenomena in poloidal divertors can be expected and therefore a different nomenclature should be applied.

## 6.2 Characteristics of the TEXTOR helical divertor

The TEXTOR helical divertor is a scenario where the DED coils are used for a resonant magnetic perturbation of the edge plasma (see section 2.2.2). The intent of this section is to give a short overview of the magnetic field and plasma structure of the helical divertor configuration at the TEXTOR tokamak. A more detailed structure analysis is given in [145, 97, 77]. The selected plasma scenario is based on the MHD equilibrium of TEXTOR discharge #95896 with superimposed RMP field of toroidal/poloidal base mode number  $m/n = 6/2$ , powered by  $I_{\text{DED}} = 6.75$  A. This type of equilibrium configuration has been used at TEXTOR in several discharges of various RMP field configurations and currents. Characteristic values for this discharge are:

$\mathbf{B}_{\text{tor}}(R = 175 \text{ cm})$	$= 1.88 \text{ T}$
$I_p$	$= 350 \text{ kA}$
$q(r_{\text{min}} = 47.7 \text{ cm})$	$= 3.72$

### 6.2.1 Structure of the magnetic field

The application of RMPs results in a heterogeneous magnetic field structure at the plasma edge with magnetic islands, short magnetic flux tubes and partially ergodic domains with field lines in a wide spectrum of connection length  $L_c$ . This magnetic field structure is displayed in figure 6.1 (a). In figure 6.1 (b) it is shown that as a result a helical magnetic strike point - or better strike line pattern - on the DED target is formed. Particle and heat fluxes are guided by the magnetic field to this helical target pattern, therefore this configuration can be regarded as helical divertor. A feature of this open chaotic system (see section 2.4) is the formation of short magnetic flux tubes which connect within one poloidal turn from one strike point on the DED to the other. The shape of such a flux tube is indicated in white in figure 6.1 (a) by its contour in the  $RZ$ -plane at  $\varphi = 0$  deg and in figure 6.1 (b) by its footprints on the DED target. This magnetic topology has been chosen because of its helical SOL-like features with a

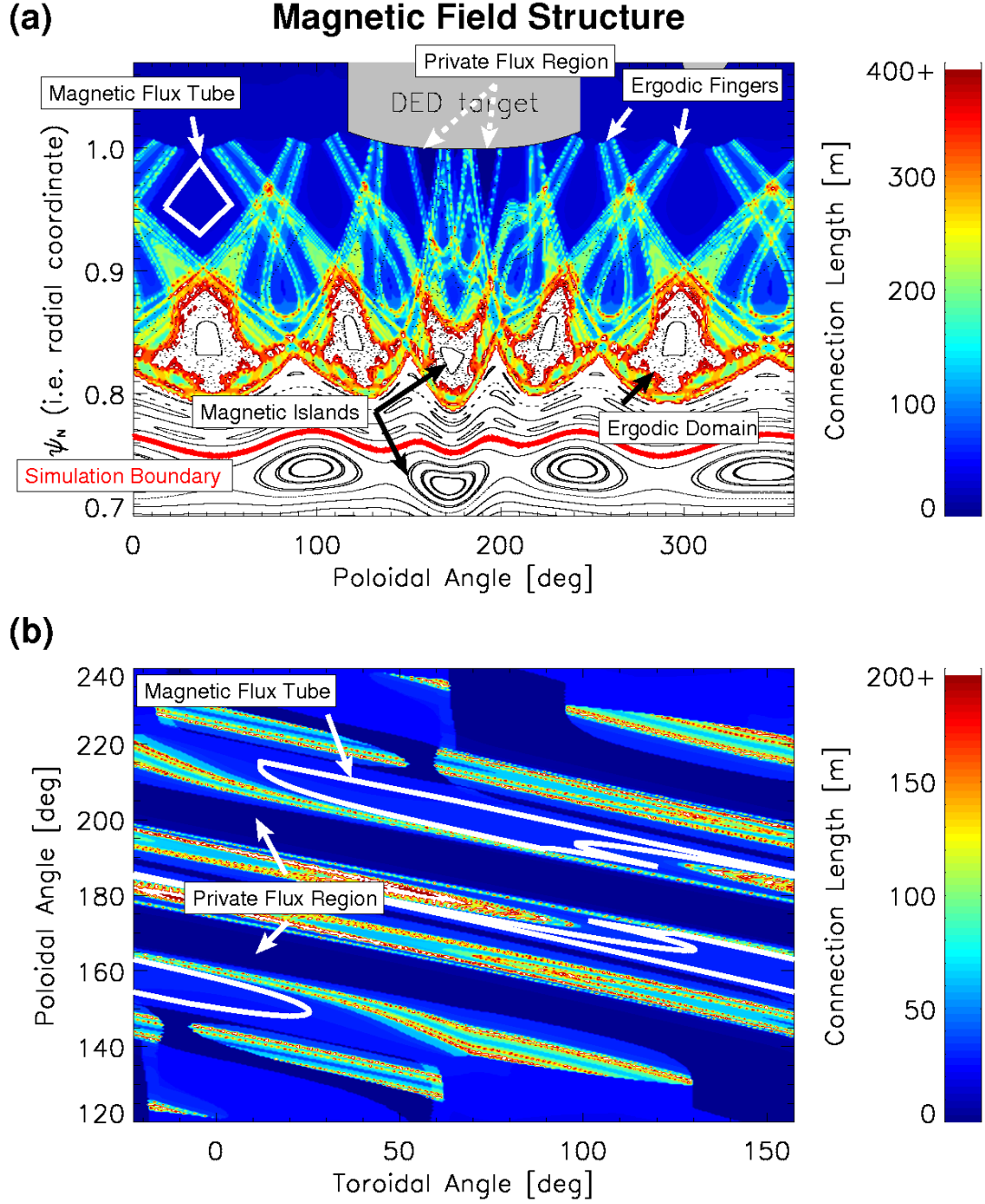


Figure 6.1: Magnetic field structure of a TEXTOR helical divertor scenario in  $m/n = 6/2$  configuration of the DED field: (a) Combined Poincaré and connection length plot at the toroidal position  $\varphi = 0$  deg, (b) magnetic footprint on the DED target. White contours indicate the shape of a short magnetic flux tube.

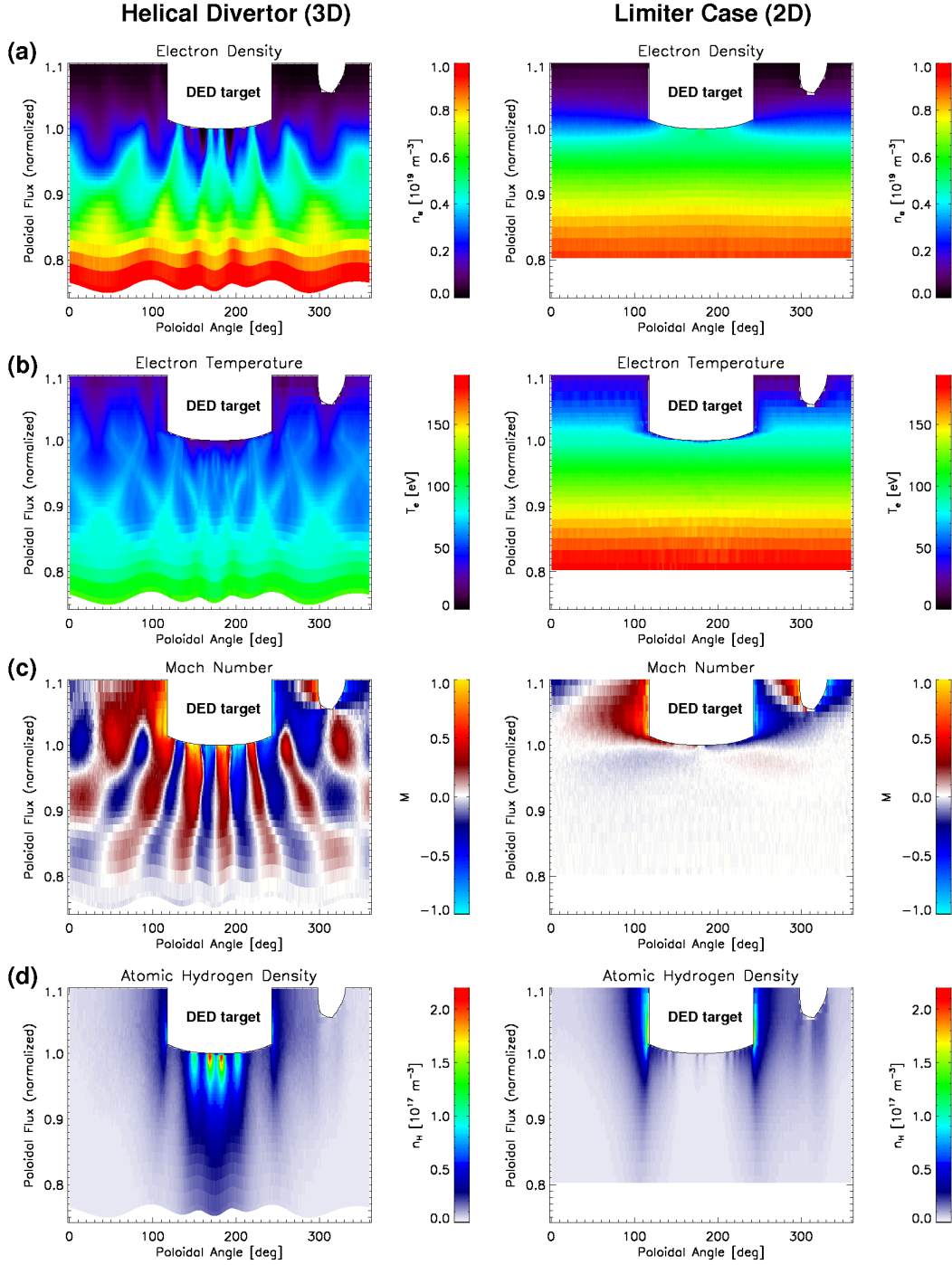


Figure 6.2: Plasma parameters for the helical divertor scenario with magnetic topology shown in figure 6.1 (left column) compared to the axisymmetric reference case (right column). 2D cuts at  $\varphi = 0$  deg of (a) electron density  $n_e$ , (b) electron temperature  $T_e$ , (c) Mach number  $M$  and (d) atomic hydrogen density  $n_H$ . The color bars for  $T_e$  and  $n_H$  are adapted to the respective maximum values.

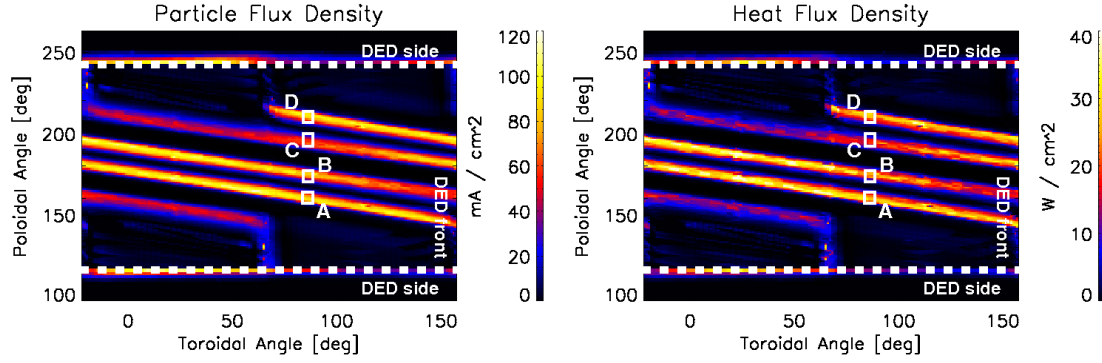


Figure 6.3: Particle and heat fluxes to the DED-target. The side parts of the DED target are mapped to an artificial poloidal coordinate for better visualization ( $\vartheta < 120$  deg and  $\vartheta > 240$  deg). The white boxes marked A,B,C,D indicate the positions used for the detailed analysis later in this chapter.

wide region of plasma flow in front of the DED target [97]. Embedded in this flux tube region are domains with field lines of long  $L_c$ , the so called *ergodic fingers*. These ergodic fingers have a fractal structure [89], which is demonstrated in figure C.1, and connect the inner ergodic domain ( $\psi^* \approx 0.8$ ) to the wall.

### 6.2.2 Structure of the edge plasma

The magnetic field structure induced by RMPs has a pronounced effect on the edge plasma. Simulation results are shown in figure 6.2 (left column) for the boundary conditions  $n_{in} = 1.0 \cdot 10^{19} \text{ m}^{-3}$  and  $P_{in} = 600 \text{ kW}$  and cross-field transport parameters  $D_{\perp} = 1.0 \text{ m}^2 \text{ s}^{-1}$  and  $\chi_{e,\perp} = \chi_{i,\perp} = 3.0 \text{ m}^2 \text{ s}^{-1}$  and compared to the unperturbed (axisymmetric) reference case (right column). As a consequence of the modified edge plasma (density  $n_e$ , temperature  $T_e$  and parallel flow characterized by the Mach number  $M$ , displayed in parts (a),(b) and (c) of figure 6.2), the atomic hydrogen density  $n_H$  is also modified (part (d) of figure 6.2). Neutral particles penetrate (radially) much deeper into the plasma, to about  $\psi^* \approx 0.90$  compared to  $\psi^* \approx 0.97$  in the axisymmetric reference case. This seems - at first sight - opposite to what one would have hoped: to keep neutral particles out of the core plasma, i.e. strong multiple recycling within the divertor volume, etc... However, as a result of RMPs, the last closed magnetic surface is shifted inward as well, from  $\psi^* = 1$  to  $\psi^* \approx 0.8$  (see figure 6.1 (a)), and so neutral particles are indeed kept outside the actual confined plasma and are still ionized mostly within the helical divertor SOL.

The open chaotic region between  $\psi^* \approx 0.8$  and  $\psi^* = 1.0$  with its ergodic domains and short flux tubes acts as a divertor volume, which guides particle and heat flux in a helical pattern onto the DED target (figure 6.3) as has already been suggested by the magnetic footprint in figure 6.1 (b). The detailed structure of the plasma footprint strongly

depends on the interplay between ergodic field lines and short flux tubes and the level of cross-field transport (see also chapter 7 in [145]). The issue of high recycling in the divertor or even of plasma detachment is closely related to the exhaust of particle and heat flux. However, detachment is a very complex state involving delicate balances and complex chemistry and it is still not fully understood quantitatively which mechanisms are important in different fusion devices and divertor configurations, not even in the axisymmetric case. At the TEXTOR tokamak it is (among other things) investigated whether the helical divertor configuration can provide a plasma detachment similar to the common detachment observed in poloidal divertor machines (dominated by neutral-plasma friction). The EMC3-EIRENE code allows to quantify the various effects in context in this inherent 3D problem.

### 6.3 Averaged transport analysis

As mentioned in the introduction, it is not straightforward to analyze the existence or quality of high recycling conditions or even plasma detachment within a complex 3D magnetic field structure. Therefore a global study is performed at first in this section to analyze the general functionality of the TEXTOR helical divertor configuration. Here the integrated target particle and heat fluxes  $\Gamma_{\text{target}}$ ,  $P_{\text{target}}$  are analyzed with respect to the plasma parameters  $n_{\text{in}}$ ,  $T_{\text{in}}$  at the inner simulation boundary, which can be regarded (roughly) as a separatrix between the confined region and the chaotic magnetic edge layer (see figure 6.1 (a)). In the following  $n_{\text{sepx}}$  and  $T_{\text{sepx}}$  are used synonymously with  $n_{\text{in}}$  and  $T_{\text{in}}$ . The target parameters are related (in a very complex way) to upstream conditions, where upstream denotes a stagnation point of plasma flow from which a continuous 1D, parallel flow to the target is built up. However, *upstream* in the present 3D scenario is not well-defined for the global configuration: upstream can be at different radial and poloidal positions for different field lines, which is why  $n_{\text{sepx}}$  and  $T_{\text{sepx}}$  are used for the analysis of the general functionality. Therefore: no direct correspondence to so called 2-point poloidal divertor models (relating “true” upstream to downstream) can be expected. Detailed transport studies follow later in section 6.4.

#### 6.3.1 Integrated particle flux

The integrated particle flux is analyzed at first, because in poloidal divertor tokamaks and in stellarators the most pronounced effect is seen there [150, 133]. For this, a density scan is performed, i.e. a sequence of simulations starting from  $n_{\text{sepx}} = 0.7 \cdot 10^{19} \text{ m}^{-3}$  to  $n_{\text{sepx}} = 4.8 \cdot 10^{19} \text{ m}^{-3}$ , while  $P_{\text{in}} = 600 \text{ kW}$  is kept fixed. Note that consequently  $T_{\text{sepx}}$  then varies; in particular a “temperature dilution” at increasing density will result. Coefficients for anomalous cross-field transport are set to  $D_{\perp} = 1.0 \text{ m}^2 \text{ s}^{-1}$  and  $\chi_{\perp} = 3 D_{\perp}$ . An overview of the edge plasma distribution for increasing  $n_{\text{sepx}}$  is given in figures C.2 and C.3 in appendix C by 2D cuts of electron density  $n_e$ , electron temperature  $T_e$  and atomic hydrogen density  $n_H$ . The resulting target particle flux  $\Gamma_{\text{target}}$  is shown in

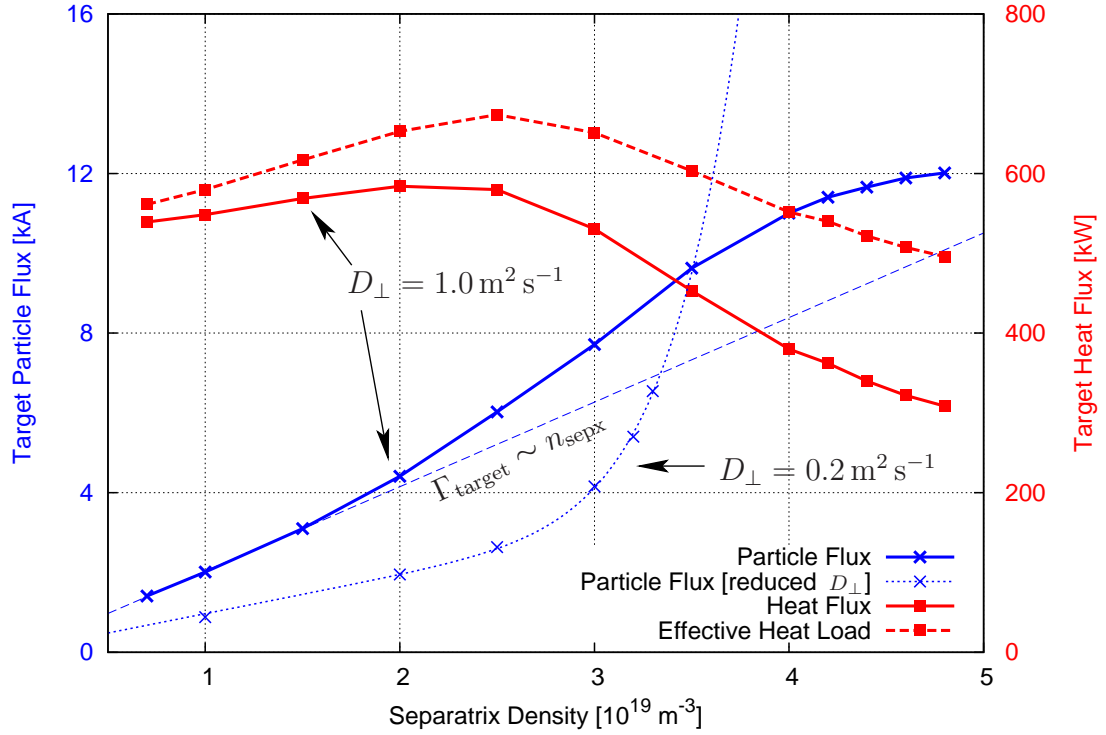


Figure 6.4: Integrated particle and heat fluxes to the DED target (solid lines) for a cross-field transport level of  $D_{\perp} = 1.0 \text{ m}^2 \text{ s}^{-1}$  and  $\chi_{\perp} = 3 D_{\perp}$ . The target particle flux  $\Gamma_{\text{target}}$  (blue solid line) is compared to  $\Gamma_{\text{target}}$  from another simulation series with reduced  $D_{\perp}$ ,  $\chi_{\perp}$  (blue dotted line). The target heat flux (red solid line) is compared to the effective target heat load (red dashed line) which includes the recombination energy of the incident ion flux. The corresponding  $T_{\text{sepx}}$  is shown in figure 6.6, black line.

figure 6.4 by a blue solid line. It can be seen that  $\Gamma_{\text{target}}$  increases monotonically from 1.4 kA at  $n_{\text{sepx}} = 0.7 \cdot 10^{19} \text{ m}^{-3}$  to 12.0 kA at  $n_{\text{sepx}} = 4.8 \cdot 10^{19} \text{ m}^{-3}$ . For low densities this increase is linear (indicated by the blue dashed line), which is still roughly the case for intermediate densities  $2.0 \cdot 10^{19} \text{ m}^{-3} \leq n_{\text{sepx}} \leq 3.5 \cdot 10^{19} \text{ m}^{-3}$ . A closer analysis yields  $\Gamma_{\text{target}} \sim n_{\text{sepx}}^{\beta}$  with  $\beta = 1.37 \pm 0.02$  for this intermediate regime. Another regime is found for  $n_{\text{sepx}} > 3.5 \cdot 10^{19} \text{ m}^{-3}$ , where the particle flux  $\Gamma_{\text{target}}$  begins to saturate, but does not quite reach a maximum value before simulations turn unstable at  $n_{\text{sepx}} = 5.0 \cdot 10^{19} \text{ m}^{-3}$ . The transition to this regime corresponds to the onset of momentum losses due to plasma-neutral interaction (friction). This can be seen by the blue line in figure 6.12 (c), which is discussed later in section 6.5.

This general behavior is similar to the EMC3-EIRENE simulations for pure hydrogen plasmas at the W7-AS stellarator presented in [133]. It has been found at this machine



[152] that the absence of a high-recycling regime is due to cross-field transport processes, which causes a damping of parallel counter-flows. The impact of cross-field particle and momentum losses is now investigated for the TEXTOR helical divertor configuration as well. Another sequence of simulations is performed with strongly reduced cross-field transport:  $D_{\perp} = 0.2 \text{ m}^2 \text{ s}^{-1}$  and  $\chi_{\perp} = 3 D_{\perp}$ . The corresponding particle flux  $\Gamma_{\text{target}}$  is shown by the blue “+” symbols in figure 6.4, which displays a strong non-linear behavior like in the high-recycling regime in poloidal divertors. However, whereas in the poloidal divertor high-recycling regime  $\Gamma_{\text{target}} \sim n_u^2$  is expected according to the standard 2-point model [7], the non-linearity of  $\Gamma_{\text{target}}(n_{\text{sepx}})$  in figure 6.4 is much stronger. A direct power law scaling is not found for  $\Gamma_{\text{target}}$ , but rather a dependency of the form

$$\Gamma_{\text{target}} = a_1 n_{\text{sepx}} + a_2 n_{\text{sepx}}^{\beta_{\text{HR}}}. \quad (6.1)$$

This is indicated in figure 6.4 by the blue dotted line, for which the power coefficient  $\beta_{\text{HR}} = 10.5 \pm 0.9$  has been found. Coming back to the simulations performed with the more realistic value of  $D_{\perp} = 1.0 \text{ m}^2 \text{ s}^{-1}$  and considering the restrictions of this analysis with respect to the  $n_{\text{sepx}}$  vs.  $n_u$  issue mentioned above, one can conclude that for this magnetic field configuration at TEXTOR a high-recycling-like regime is (almost completely) suppressed, similar to observations at W7-AS. However, no detachment-like regime with a sudden drop in  $\Gamma_{\text{target}}$  is observed in the present simulations. Nevertheless, the existence of a third regime for  $n_{\text{sepx}} \geq 3.5 \cdot 10^{19} \text{ m}^{-3}$  with a weaker than linear scaling of  $\Gamma_{\text{target}}$  may indicate the beginning of a detachment-like regime, which can only be called beyond-high-recycling-like at this point.

### 6.3.2 Integrated heat flux

In the following the functionality of the TEXTOR helical divertor with respect to the integrated target heat flux is investigated. For this, the simulations with  $D_{\perp} = 1.0 \text{ m}^2 \text{ s}^{-1}$  are considered again. As seen by the red solid line in figure 6.4, the target heat flux increases from  $P_{\text{target}} = 541 \text{ kW}$  at  $n_{\text{sepx}} = 0.7 \cdot 10^{19} \text{ m}^{-3}$  to a maximum value of  $P_{\text{target}} = 593 \text{ kW}$  at  $n_{\text{sepx}} = 2.0 \cdot 10^{19} \text{ m}^{-3}$  and then decreases continuously to  $P_{\text{target}} = 308 \text{ kW}$  at  $n_{\text{sepx}} = 4.8 \cdot 10^{19} \text{ m}^{-3}$ . The strong decrease of  $P_{\text{target}}$  for  $n_{\text{sepx}} > 2.0 \cdot 10^{19} \text{ m}^{-3}$  is caused by an increasing fraction of  $P_{\text{in}}$  that is lost to plasma - neutral hydrogen interaction. At  $n_{\text{sepx}} = 2.0 \cdot 10^{19} \text{ m}^{-3}$  only 1 % is lost to neutral gas, but this fraction increases significantly to 45 % at  $n_{\text{sepx}} = 4.8 \cdot 10^{19} \text{ m}^{-3}$ .

Of great importance for the design of a fusion reactor is the effective target heat load  $H_{\text{target}}$ , which is composed of the target heat flux  $P_{\text{target}}$  and the potential energy (atomic + molecular recombination energy)  $E_{\text{pot}} = (13.6 + 2) \text{ eV}$  of the incident ion flux  $\Gamma_{\text{target}}$ :

$$H_{\text{target}} = P_{\text{target}} + E_{\text{pot}} \Gamma_{\text{target}}. \quad (6.2)$$

As can be seen by the red dashed line in figure 6.4, decrease of  $P_{\text{target}}$  is large enough to result in a decreasing effective target load  $H_{\text{target}}$  as well. This feature is exactly what one intended to achieve with detached plasmas. However, in the present case also the separatrix temperature decreases with increasing  $n_{\text{sepx}}$ , which will be demonstrated later in figure 6.6.

## 6.4 Detailed transport analysis

After this global transport analysis which considered only the integrated particle and heat fluxes, now a more detailed, spatially resolved analysis is given. In particular it is investigated whether the third regime with a weaker than linear scaling of  $\Gamma_{\text{target}}$  is due to a full detachment at some strike points, but without detachment at some other strike points, generally referred to as *partial detachment* in poloidal divertor physics. To conduct this study, 4 strike location with distinct magnetic field structure are selected on the DED target (see white boxes in figure 6.3). Local particle and heat fluxes at these strike locations are investigated in section 6.4.1. Experimentally, particle target loads are investigated by so called Langmuir probes (see e.g. [73] or section 7.2 in [145]). However, measurements with these probes are possible only at very few and very localized positions and presently no conclusive data is available. Much better accessible is the  $H_{\alpha}$  emission in front of the DED target, e.g. by cameras equipped with interference filter (with a transmitted central wave length of  $\lambda = 656.2 \text{ nm}$  and a full width at half maximum of  $\Delta\lambda = 2.0 \text{ nm}$  [153]). The relation between the target  $H_{\alpha}$  emission and the particle target fluxes is analyzed in section 6.4.1 as well. The volume distribution of the  $H_{\alpha}$  emission and the particle sources  $S_p$  due to ionization of neutrals are then investigated in section 6.4.2 and compared to the features of limiter detachment [150]: an ionization front which moves radially away from the target. Distinct from the axisymmetric limiter scenario, where radial transport is due to cross-field transport only, the very complex magnetic field structure (figure 6.1) in the helical divertor scenario introduces an additional radial component by parallel transport along inclined ergodic field lines and short magnetic flux tubes. A detailed analysis of the geometry and plasma parameters on one such ergodic field line is presented in section 6.4.3 in comparison to a field line within a short magnetic flux tube.

### 6.4.1 Analysis of selected strike points

The local particle fluxes to the DED target are averaged at the 4 strike point-areas marked in figure 6.3 (referred to as strike points A,B,C and D in the following) and displayed in figure 6.5 (a). The two outer strike points are selected at locations where only ergodic field lines intersect the target surface. These field lines guide a large particle flux to the wall. This particle flux increases from  $\Gamma_{A,D} = 3.5 \text{ A}$  at both strike points A and D at  $n_{\text{sepx}} = 0.7 \cdot 10^{19} \text{ m}^{-3}$  to  $\Gamma_A = 26.0 \text{ A}$  and  $\Gamma_D = 27.4 \text{ A}$  at  $n_{\text{sepx}} = 4.0 \cdot 10^{19} \text{ m}^{-3}$  and saturates at a level of  $\Gamma_A \approx 27 \text{ A}$  and  $\Gamma_D \approx 28 \text{ A}$ , respectively. At strike point C only

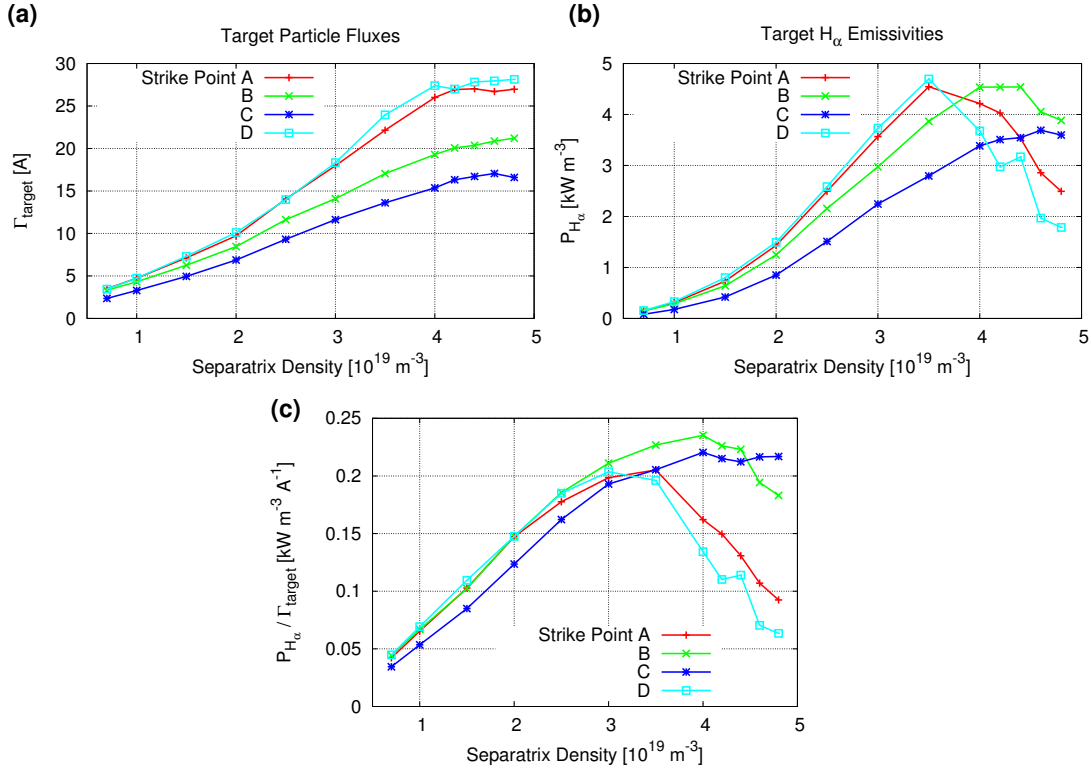


Figure 6.5: (a) Particle target fluxes  $\Gamma_{\text{target}}$  and (b)  $H_\alpha$  emissivities at the 4 strike points marked in figure 6.3. The ratio  $P_{H_\alpha} / \Gamma_{\text{target}}$  is given in part (c).

field lines from within a short magnetic flux tube intersect the target surface, whereas strike point B represents a mixture of both, short and long field lines (compare figures 6.1 (b) and 6.3). It can be seen that the target particle flux from short magnetic flux tubes is considerably smaller than that from long, ergodic field lines, which penetrate much deeper into the plasma (see e.g. figure 6.8 (a)). The particle flux at strike point C increases from  $\Gamma_C = 2.4 \text{ A}$  to  $\Gamma_C = 17.0 \text{ A}$  at  $n_{\text{sepx}} = 4.6 \cdot 10^{19} \text{ m}^{-3}$  where it saturates.

Plasma recycling is assumed at target plates (see section 4.3.1), that is  $\Gamma_{\text{target}}$  results in surface recombination of the incident ion and electron flux and consequently re-emission of neutral particles. Therefore  $\Gamma_{\text{target}}$  is correlated to the  $H_\alpha$  emission in front of the target. This relation, however, is strongly dependent on the magnetic field structure and the corresponding plasma properties in the divertor region. There is in fact no linear relation between the local  $\Gamma_{\text{target}}$  and the  $H_\alpha$  emissivity  $P_{H_\alpha}$ . To see this,  $P_{H_\alpha}$  at the four strike points A, B, C and D is averaged radially over 1 cm inwards from the DED target. No qualitative difference is found if  $P_{H_\alpha}$  is averaged over 0.5 cm or 2 cm instead.

The density dependence of this *divertor*  $H_\alpha$  radiation is shown in figure 6.5 (b). The average  $H_\alpha$  emissivity from strike point C (the one with the short magnetic flux tube) in-

creases continuously from a very low level of  $P_C = 0.08 \text{ kW m}^{-3}$  at  $n_{\text{sepx}} = 0.7 \cdot 10^{19} \text{ m}^{-3}$  and saturates at a level of  $P_C = 3.6 \text{ kW m}^{-3}$  at high densities.  $P_{H_\alpha}$  at the two outer strike points A and D is quite different: it increases from  $P_{A,D} = 0.15 \text{ kW m}^{-3}$  to a maximum value of  $P_A = 4.5 \text{ kW m}^{-3}$  and  $P_D = 4.7 \text{ kW m}^{-3}$ , respectively, at  $n_{\text{sepx}} = 3.5 \cdot 10^{19} \text{ m}^{-3}$  and then significantly decreases again. The qualitative behavior of  $P_{H_\alpha}$  at strike point B is in between that of strike point C and strike points A and D, respectively. The ratio  $P_{H_\alpha}/\Gamma_{\text{target}}$  is given in part (c) of figure 6.5 and clarifies that there is indeed no linear relation between the local  $\Gamma_{\text{target}}$  and the  $H_\alpha$  emissivity, except for low densities  $n_{\text{sepx}} \leq 2.5 \cdot 10^{19} \text{ m}^{-3}$ .

The cause for this roll-over in the target  $H_\alpha$  emission is a strong decrease of the target electron temperature  $T_{e,\text{target}}$ . The basic two-point model for the divertor SOL (presented in chapter 5.2 in [7]) suggest a  $T_{e,\text{target}} \sim n_{\text{sepx}}^{-2}$  scaling, if both are on the same field line. From figure 6.6 it can be seen that also in the present 3D case  $T_{e,\text{target}}$  can be described by a power law

$$T_{e,\text{target}} = T_0 \left( \frac{n_0}{n_{\text{sepx}}} \right)^\alpha, \quad (6.3)$$

however, with two significantly different coefficients for low and high densities. A threshold density of  $n_{\text{thresh}} \approx 2.4 \cdot 10^{19} \text{ m}^{-3}$  can be determined from figure 6.6, such that for  $n_{\text{sepx}} < n_{\text{thresh}}$  the target temperature at strike point D is well described by a power law with exponent

$$\alpha_1 = 0.78 \pm 0.03 (3.9 \%). \quad (6.4)$$

Compared to the temperature at the separatrix  $T_{\text{sepx}}$  (black line) this is roughly a linear scaling  $T_{e,\text{target}} \sim T_{\text{sepx}}$ . Furthermore, this coefficient  $\alpha_1$  is close to the value  $2/3$  from an idealized simple (low recycling) model:  $T \sim n_{\text{sepx}}^{-2/3}$ , indicating the energy dilution effect (see section 4.10.2 in [7]) at constant power into the SOL with increasing density. For  $n_{\text{sepx}} > n_{\text{thresh}}$  on the other hand, it can be seen that  $T_{e,\text{target}}$  scales according to a power law with much larger coefficient  $\alpha_2 > \alpha_1$ :

$$\alpha_2 = 3.40 \pm 0.12 (3.4 \%). \quad (6.5)$$

The threshold density of  $n_{\text{thresh}} \approx 2.4 \cdot 10^{19} \text{ m}^{-3}$  corresponds to the onset of power losses by plasma-neutral interaction. It has already been shown in figure 6.4 that  $P_{\text{target}}$  significantly decreases for  $n_{\text{sepx}} > n_{\text{thresh}}$ , which is associated with a larger fraction of  $P_{\text{in}}$  that is lost by plasma-neutral particle interactions. The value of  $T_{e,\text{target}} \approx 20 \text{ eV}$  at  $n_{\text{thresh}}$  is consistent with figure 1.25 in [7], which shows that for  $T \lesssim 20 \text{ eV}$  the ionization rate significantly drops. Hence, the lifetime of neutral particles is increased, and consequently also the radiation potential  $E_{\text{rad, pot}}$ , i.e. the total amount of energy radiated by a single particle during its lifetime.

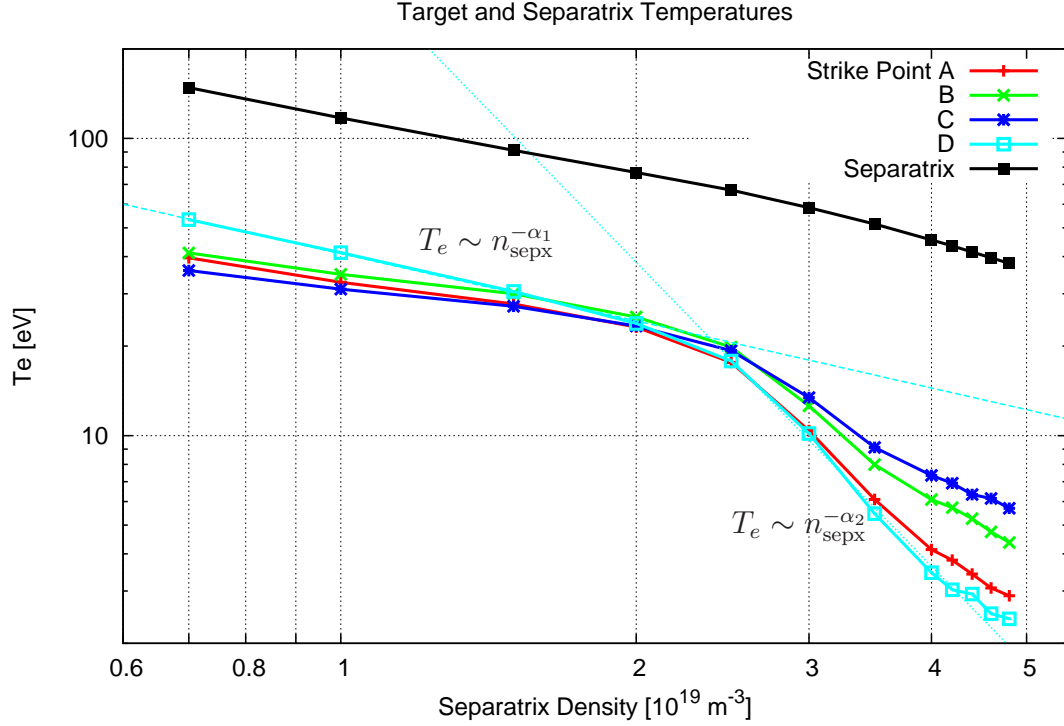


Figure 6.6: Target electron temperatures  $T_{e,\text{target}}$  at the strike points A,B,C and D from figure 6.3 compared to the separatrix temperature  $T_{\text{sepx}}$ .

The  $T_{e,\text{target}}$  values at the other strike points obey a similar power law with a transition between small and large exponents at the same threshold density  $n_{\text{thresh}}$ . Note again that a direct comparison to the basic two-point model is not possible, because this model is based on the upstream density  $n_u$  in the SOL, while here  $n_{\text{sepx}}$ , the density at the inner simulation boundary, is used. The mean upstream density  $\bar{n}_u$ , averaged over the upstream densities of many field lines connected with each strike point region, might depend non-linearly on  $n_{\text{sepx}}$ , because of the complex magnetic field structure and non-linear transport effects. Nevertheless,  $n_{\text{in}}$  and  $P_{\text{in}}$  are prescribed as boundary conditions in the present simulations, which is as similar as one can probably get compared to the control parameters  $n_u$ ,  $q_u$  in the basic 2-point model.

The decrease of  $T_{e,\text{target}}$  is much stronger at the two outer strike points:  $T_{e,\text{target}}$  decreases below 5 eV at  $n_{\text{sepx}} = 3.6 - 3.7 \cdot 10^{19} \text{ m}^{-3}$ , which corresponds to the drop in  $P_{H_\alpha}$  shown in figure 6.5 (b). This is because the rate coefficient for  $H_\alpha$  emission significantly decreases for  $T_e \lesssim 5 \text{ eV}$  (see figure 3.31 in [7]). At even higher densities  $n_{\text{sepx}} \approx 4.5 \cdot 10^{19} \text{ m}^{-3}$ , also  $T_{e,\text{target}}$  at strike point B decreases below 5 eV. This corresponds to a local drop in  $P_B$  as well.  $T_{e,\text{target}}$  at strike point C does not decrease below, but almost reaches the level of 5 eV. This is consistent with the absence of a clear drop in the local  $H_\alpha$  emission  $P_C$ .

### 6.4.2 Distribution of hydrogen radiation and ionization sources

In the previous section it has been demonstrated that the local  $H_\alpha$  emission in front of the target, which can be attributed to a specific strike point, is non-linearly related to the local target particle flux  $\Gamma_{\text{target}}$ . The local - as well as the global - particle fluxes increase and saturate at high  $n_{\text{sepx}}$ . A drop at high densities is only observed for the target  $H_\alpha$  emission. This is quite opposite to observations in poloidal divertor detachment scenarios, where a roll-over is observed in  $\Gamma_{\text{target}}$  without a decrease (even an increase) in the divertor  $H_\alpha$  emission. The difference is that in the present TEXTOR study only the  $H_\alpha$  emission directly in front of target has been considered, whereas the full divertor  $H_\alpha$  emission would correspond to the volume integrated  $H_\alpha$  emission up to the last closed flux surface, i.e. roughly the entire simulation domain. The integrated  $H_\alpha$  emission indeed increases with  $n_{\text{sepx}}$ . This can be seen by analyzing the distribution of the  $H_\alpha$  emission, which is now done by 2D cuts perpendicular to the DED target (i.e. at a fixed toroidal position). 2D cuts of the distribution of the ionization sources  $S_p$  are given in comparison as well.

Both  $P_{H_\alpha}$  and  $S_p$  distributions are displayed in figure 6.7 for a low density ( $n_{\text{sepx}} = 2.0 \cdot 10^{19} \text{ m}^{-3}$ , before the drop of target  $H_\alpha$ ) and a high density ( $n_{\text{sepx}} = 4.8 \cdot 10^{19} \text{ m}^{-3}$ , after this drop of target  $H_\alpha$ ). The  $H_\alpha$  distribution in the low density case (6.7 (a)) is localized radially in the region 2 cm in front of the target and is distributed poloidally in 4 separate radial stripes. These stripes are clearly related to the position of the strike points. The ionization front is even more localized with a radial width of about 1 cm. In the high density case (figure 6.7 (b)), the peaks of the  $P_{H_\alpha}$  and  $S_p$  distributions move radially inward from the DED target, resulting in stripes of about 6 cm length. It can be seen that the two outer stripes slightly move away from the target surface, which corresponds to the drop in  $H_\alpha$  observed in figure 6.5 (b).

To quantify this observation, radial profiles are extracted from the 2D cuts at the poloidal position of strike point D and displayed in figure 6.7 (c). The black curves mark the maximum values of  $P_{H_\alpha}$  and  $S_p$  with increasing  $n_{\text{sepx}}$ . At low densities ( $n_{\text{sepx}} = 1.0 \cdot 10^{19} \text{ m}^{-3}$ ) the maximum value of  $P_{H_\alpha}$  is  $0.38 \text{ kW m}^{-3}$  which is located at  $r_{\text{min}} = 46.9 \text{ cm}$ . With increasing  $n_{\text{sepx}}$  the maximum value increases to  $P_{H_\alpha} = 4.50 \text{ kW m}^{-3}$  at  $n_{\text{sepx}} = 3.0 \cdot 10^{19} \text{ m}^{-3}$  which is located at  $r_{\text{min}} = 47.3 \text{ cm}$ . Then the maximum value is increased further to  $P_{H_\alpha} = 6.15 \text{ kW m}^{-3}$  at  $n_{\text{sepx}} = 4.0 \cdot 10^{19} \text{ m}^{-3}$ , but shifted radially inwards to  $r_{\text{min}} = 46.5 \text{ cm}$ . At even higher densities ( $n_{\text{sepx}} = 4.8 \cdot 10^{19} \text{ m}^{-3}$ ), the maximum value decreases to  $P_{H_\alpha} = 3.44 \text{ kW m}^{-3}$  which is shifted even further inward to  $r_{\text{min}} = 45.1 \text{ cm}$ , i.e. 2.6 cm away from the DED target. The profiles of the ionization source  $S_p$  display a similar behavior. The patterns of the 2D distributions of  $H_\alpha$  and  $S_p$  are not significantly modified if simulated camera pictures are considered (see appendix E.4), only a slight smoothing can be observed. This smoothing is because of the tangential view of the camera on the helical strike points.

These observations are phenomenologically similar to the limiter detachment described in [150]. However, the physical mechanism behind it is different, because due to field

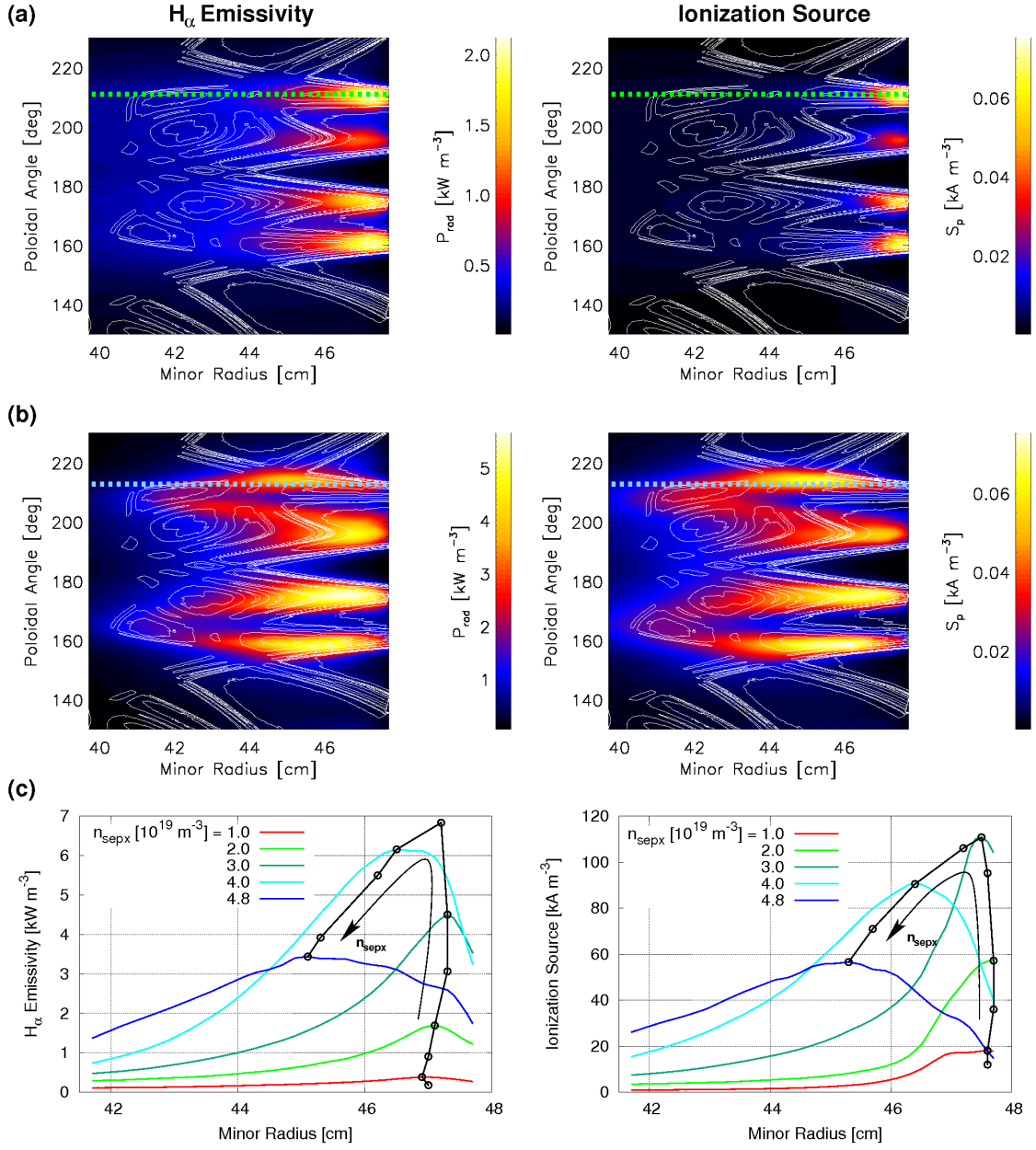


Figure 6.7: Distribution of  $H_\alpha$  emissivity (left column) and ionization source  $S_p$  (right column) in front of the DED target at  $\varphi = 86^\circ$ : (a) for  $n_{\text{sepx}} = 2.0 \cdot 10^{19} \text{ m}^{-3}$  and (b) for  $n_{\text{sepx}} = 4.8 \cdot 10^{19} \text{ m}^{-3}$ . Contour lines of the connection length  $L_c$  are superimposed in white. (c) Radial profiles extracted at the poloidal position of strike point D, which is indicated by the dotted, horizontal lines in (a) and (b). The black curves mark the maximum values of  $P_{H_\alpha}$  and  $S_p$  with increasing  $n_{\text{sepx}}$ .

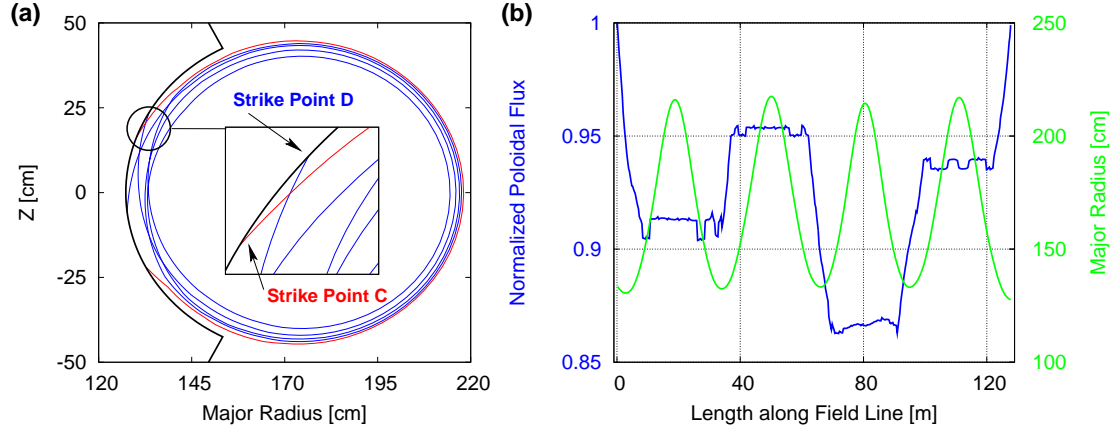


Figure 6.8: (a) Projection of field lines  $F_1$  (red) and  $F_2$  (blue) into the  $R - Z$  plane. (b) Radial excursion of the ergodic field line  $F_2$  depicted by the normalized poloidal flux  $\psi^*$ , which is compared to the local major radius.

line inclination in the present case a radially inward shifted ionization front corresponds to an upward shift of particle sources along field lines. This mixes the radial and parallel transport and complicates interpretation. How this affects plasma transport on field lines is investigated in the next section.

### 6.4.3 Field line profiles

In this section a detailed analysis of plasma parameter on selected field lines is given to address the important topic of upstream and downstream regions in the TEXTOR helical divertor configuration. Two field lines are selected for comparison: field line  $F_1$ , which is located inside a short magnetic flux tube and connects to the target at strike point C with a connection length of  $L_{c,F_1} = 29$  m, and field line  $F_2$ , an ergodic field line that connects to the target at strike point D with a connection length of  $L_{c,F_2} = 128$  m.

#### Field line geometry

An overview of the field line geometry of  $F_1$  and  $F_2$  is given in figure 6.8 (a) by a projection into the  $R - Z$  plane. The geometry of the short field line  $F_1$  is rather simple, it performs (almost) one poloidal turn until it intersects the DED target again. The ergodic field line  $F_2$  on the other hand, performs 4 poloidal turns until it strikes the DED target again. This is also demonstrated in figure 6.8 (b) by the local major radius  $R(L)$  (green), where  $L$  is the position along the field line. Each time the field line is in front of the DED target it is “pushed” either inwards or outwards by the perturbation field, which is displayed in figure 6.8 (b) by the local normalized poloidal flux  $\psi^*(L)$  (blue). Starting at  $\psi^* = 1$ , it is immediately pushed inwards to  $\psi^* \approx 0.91$ . After one



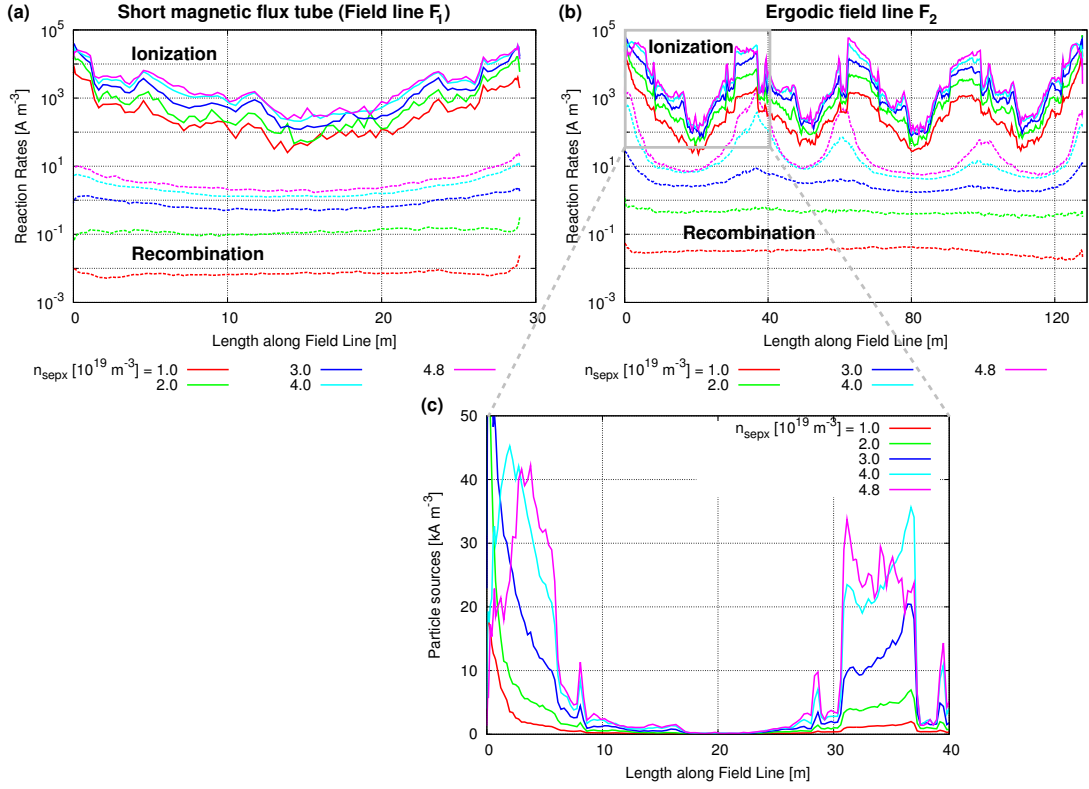


Figure 6.9: Ionization rates (solid lines) and recombination rates (dashed lines) for a field line inside a short magnetic flux tube (a) and for an ergodic field line (b). Ionization rates (i.e. particle sources  $S_p$ ) along the first poloidal turn of the ergodic field line are magnified in part (c).

poloidal turn it is pushed back outwards to  $\psi^* \approx 0.95$ , only to be pushed inwards again to  $\psi^* \approx 0.87$  after another poloidal turn. After the third poloidal turn it is pushed outwards to  $\psi^* \approx 0.94$  and intersects the wall one poloidal turn later.

### Ionization and recombination

As demonstrated in figure 6.8 (b), the field line  $F_2$  performs 4 poloidal turns and therefore passes 3 times the vicinity of the DED target. This is directly reflected in the modulation of plasma particle sources (ionization rates)  $S_p$  along  $F_2$ , which are shown in figure 6.9 (b). Comparing this to figure 6.8 (b) one finds that plasma sources are always present when the field line is in the vicinity of the DED target, hence the 3 maxima of  $S_p$  along  $F_2$  in figure 6.9 (b). As field line  $F_1$  performs only one poloidal turn, no intermediate maxima of  $S_p$  can be found in figure 6.9 (a). Whether the intermediate maxima along  $F_2$  correspond to upstream sources along this field line is investigated in the next paragraph after the issue of volume recombination has been discussed.

A closer look at the ionization rates in figure 6.9 (c) reveals that  $S_p$  is indeed pushed upwards along the field line as suggested by the radially inward shift observed in the previous section. The maximum value of  $S_p$  for  $n_{\text{sepx}} = 1.0 \cdot 10^{19} \text{ m}^{-3}$  is  $18 \text{ kA m}^{-3}$  which is located almost directly at the target strike point ( $L = 0.06 \text{ m}$ ). This increases significantly to  $S_p = 61 \text{ kA m}^{-3}$  for  $n_{\text{sepx}} = 3.0 \cdot 10^{19} \text{ m}^{-3}$ , still located directly at the strike point. When  $n_{\text{sepx}}$  is increased to  $4.0 \cdot 10^{19} \text{ m}^{-3}$ , the maximum value of  $S_p$  reduces to  $45 \text{ kA m}^{-3}$  which is now pushed upward to  $L \approx 2 \text{ m}$ . When  $n_{\text{sepx}}$  is further increased to  $4.8 \cdot 10^{19} \text{ m}^{-3}$ ,  $S_p$  reduces to  $42 \text{ kA m}^{-3}$  at  $L \approx 4 \text{ m}$ .

A more pronounced feature is that the sources further along the ergodic field lines are significantly influenced by increasing  $n_{\text{sepx}}$ . E.g. averaged peak values  $S_{p,P1}$  (between  $L = 31 \text{ m}$  and  $L = 38 \text{ m}$ ) at the first peak after one poloidal turn significantly increase with increasing  $n_{\text{sepx}}$ . This is summarized in the following table:

$n_{\text{sepx}} [10^{19} \text{ m}^{-3}]$	1.0	2.0	3.0	4.0	4.8
$S_{p,P1} [\text{kA m}^{-3}]$	1.3	4.7	13.0	24.8	25.4

From the target temperature in figure 6.6 it might be expected that the volumetric recombination process



becomes relevant. This process is so far neglected in the EMC3-EIRENE code, where the effective particle source  $S_p$  in (3.35) is given by ionization rates  $R_{\text{ion}}$  alone. Post processed recombination rates  $R_{\text{rec}}$  for the two selected field lines are displayed in figure 6.9 by dashed lines. Clearly, local volume recombination rates are by more than 2 orders of magnitude lower than ionization rates along the short field line, even for high separatrix densities. Also along the long field line  $R_{\text{rec}}$  is much lower than  $R_{\text{ion}}$ ; at high  $n_{\text{sepx}}$  still by 1 order of magnitude. This analysis shows that it is justified to neglect volume recombination in the present simulations (that is as long as  $T_e$  does not drop further).

### Density, temperature and Mach number

The strong increase of  $S_p$  along the ergodic field line  $F_2$  results in the formation of peaks in the density, which can be seen in figure 6.10 (a). Consequently, the temperature is reduced, in particular at the location of the  $S_p$  and  $n_e$  peaks (see figure 6.10 (b)). Peak densities  $n_{e,P1}$  and the corresponding temperatures  $T_{e,P1}$  at  $L = 37 \text{ cm}$  are summarized in the table below:

$n_{\text{sepx}} [10^{19} \text{ m}^{-3}]$	1.0	2.0	3.0	4.0	4.8
$n_{e,P1} [10^{19} \text{ m}^{-3}]$	0.4	1.3	3.5	11.8	17.8
$T_{e,P1} [\text{eV}]$	62.4	32.2	15.5	4.4	2.7

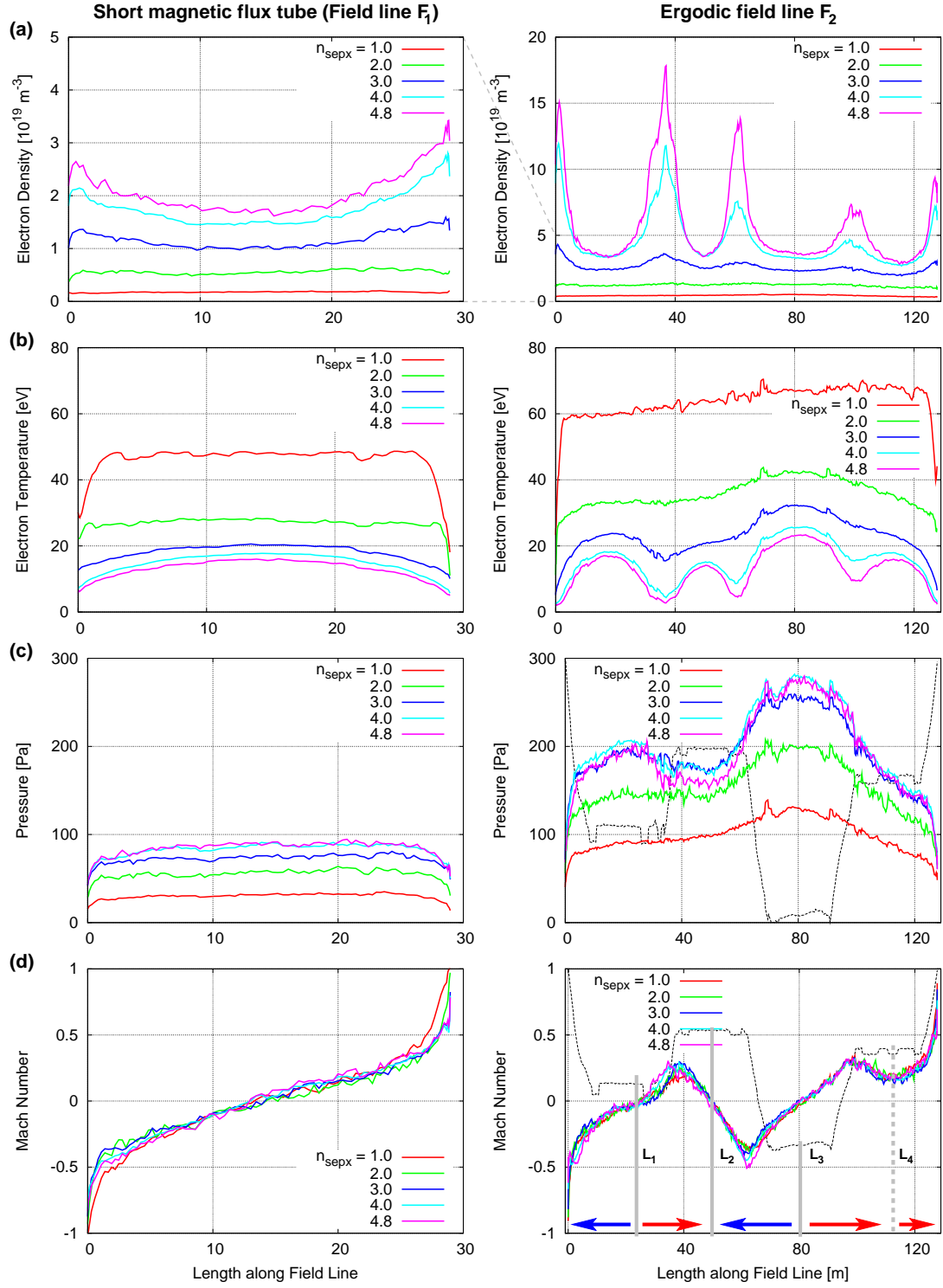


Figure 6.10: Field line profiles of (a) electron density  $n_e$ , (b) electron temperature  $T_e$ , (c) pressure  $P$  and (d) Mach number  $M$  for field line  $F_1$  (left column) and  $F_2$  (right column).

The peak density  $n_{e,P1}$  already exceeds the separatrix density for  $n_{\text{sepx}} = 3.0 \cdot 10^{19} \text{ m}^{-3}$  and continues to increase significantly for even higher  $n_{\text{sepx}}$ . Peak values on the short field line  $F_1$ , on the other hand, are located in front of the target only and stay well below  $n_{\text{sepx}}$ . For low  $n_{\text{sepx}}$ , both the short field line  $F_1$  and the ergodic field line  $F_2$  are isothermal (except for the very last part in front of the target). With increasing  $n_{\text{sepx}}$ , heat conduction becomes relevant, which is reflected by the presence of temperature gradients all along the field line. The Mach number  $M$  along the selected field lines is shown in figure 6.10 (d). It can be seen that  $M$  does not change significantly with increasing  $n_{\text{sepx}}$ , however, the effective plasma flow velocity  $u_{\parallel} = M c_s$  decreases. This is because  $c_s \propto \sqrt{T_e + T_i}$  and  $T_e, T_i$  decrease with increasing  $n_{\text{sepx}}$  and constant  $P_{\text{in}}$ .

The  $M$  profile along the short field line  $F_1$ , with a single stagnation point halfway between targets, allows a clear distinction between upstream and downstream regions. However, on the ergodic field line  $F_2$  there is no unique upstream position, but there are three stagnation points along the field line: at  $L_1 = 25 \text{ m}$ ,  $L_2 = 50 \text{ m}$  and  $L_3 = 80 \text{ m}$  which are marked in figure 6.10 (d) by gray, vertical bars. Furthermore, there is a point of almost stagnation at  $L_4 = 110 \text{ m}$ . All these stagnation points are located on the low field side after  $\frac{2k-1}{2}, k = 1, \dots, 4$  poloidal turns, which can be seen by a comparison with figure 6.8 (b). To analyze the difference between  $L_4$  and the other points, stagnation points are classified in two categories: one where the flow direction changes (type 1) and one where the flow direction does not change on both sides (type 2). Given the boundary condition of sonic flow to the wall, it can be seen easily that there must always be an odd number of type 1 stagnation points on a field line. The existence, type and position of several stagnation points can be understood by the following analysis: As can be seen in figure 6.10 (c), the plasma pressure  $P$  is almost constant on parts of the field line with  $\psi^* = \text{const}$ .  $P$  only changes when the field line is pushed inwards or outwards, which happens always at the HFS. These pressure gradients give rise to a plasma flow which is directed outwards, because  $P$  increases in direction towards the core plasma. Therefore type 1 stagnation points must exist at  $L_1, L_2$  and  $L_3$ . Type 2 stagnation points on the other hand, can arise when plasma flow is damped, e.g. due to viscous effects of counter-flows on neighboring field lines (see figure 6.2 (c)) or friction with neutrals. If, however, parallel transport is strong, damping is only partial such as for  $L_4$ .

#### 6.4.4 Conclusions of the detailed transport analysis

Obviously, the definition of upstream and downstream regions in a chaotic magnetic edge layer is challenging, even for selected field lines. The present analysis has shown that there are two upstream positions on the ergodic field line  $F_2$ , one for each strike point:  $L_1$  for the left strike point ( $L = 0 \text{ m}$ ) and  $L_3$  for the right strike point ( $L = 128 \text{ m}$ ). This leaves the region between  $L_1$  and  $L_3$  with an additional stagnation point, but where plasma flow occurs as well. This flow is not directed to the target, however, it has been shown that it is directed outward, at least in the present case. Hence, it would be an over-simplification to define the upstream region by geometric properties, e.g. by

$L_{c,s} < 1/2 p.t.$ , where  $L_{c,s}$  is the connection length in shortest direction to the wall.

Beside the analysis of upstream and downstream regions in the previous section, it has been shown in section 6.4.1 that at high densities  $n_{\text{sepx}}$  a sudden drop of the  $H_\alpha$  emission at some strike points can be observed without a drop of the corresponding local particle flux  $\Gamma_{\text{target}}$ . This is quite opposite to observations in poloidal divertor detachment scenarios. In particular, it has been found that a linear relation between  $\Gamma_{\text{target}}$  and  $P_{H_\alpha}$  is valid only for low densities  $n_{\text{sepx}} \leq 2.5 \cdot 10^{19} \text{ m}^{-3}$ . The strong drop of  $P_{H_\alpha}$  in the present TEXTOR configuration has been connected to a drop of  $T_{e,\text{target}}$  below 5 eV. Studies of the  $H_\alpha$  radiation distribution in section 6.4.2 have shown a radially inward shift of  $P_{H_\alpha}$  with increasing  $n_{\text{sepx}}$ , which is phenomenologically similar to limiter detachment, however, with a different physical mechanism behind it. It has to be concluded, therefore, that simple 2-point models are not generally applicable, nor are the resulting concepts of (parallel) divertor detachment or high-recycling regime.

## 6.5 Impact of impurity radiation

While impurities play a significant role in certain limiter-detachment scenarios (where they are introduced on purpose) [149, 154], intrinsic impurities such as carbon released by plasma-surface interaction might have an impact on the edge plasma as well. E.g. in simulations of detachment scenarios at W7-AS [40] and LHD [44] a significant impact of carbon radiation has been found. Therefore the simulations of the TEXTOR helical divertor configuration presented in the previous sections have been repeated including carbon impurities. In the present model the impact of impurities is considered by an energy sink  $\mathcal{S}_{e,\text{cool}}$  for electrons due to ionization and line radiation of impurities (see section 3.3.2). Friction forces on the main plasma are neglected.

A detailed study of various model parameters for impurity transport is presented in appendix D. Here only the resulting impact of carbon impurities on the edge plasma is investigated. In the present analysis impurity sources are given by a sputter yield  $Y = 2\%$  of the recycling flux  $\Gamma_{\text{target}}$  with a  $\delta$ -distributed energy of  $E_{\text{sput}} = 0.1 \text{ eV}$ , which corresponds to chemical sputtering. The chosen sputter yield  $Y$  is the same as that used in edge plasma simulations for W7-AS [152], LHD [44] and W7-X [133]. An overview of the  $\mathcal{S}_{e,\text{cool}}$  distribution for  $n_{\text{sepx}} = 2.0 \cdot 10^{19} \text{ m}^{-3}$  and  $n_{\text{sepx}} = 4.0 \cdot 10^{19} \text{ m}^{-3}$  is given in figure 6.11 (a) and for more densities in the appendix in figure C.4. The volume integrated value  $P_{\text{cool}}$  is given in figure 6.12 (a). Starting from  $P_{\text{cool}} = 32 \text{ kW}$  at  $n_{\text{sepx}} = 1.0 \cdot 10^{19} \text{ m}^{-3}$  the carbon radiation increases slowly to  $P_{\text{cool}} = 76 \text{ kW}$  at  $n_{\text{sepx}} = 2.5 \cdot 10^{19} \text{ m}^{-3}$ , then suddenly increases significantly to  $P_{\text{cool}} = 168 \text{ kW}$  at  $n_{\text{sepx}} = 3.0 \cdot 10^{19} \text{ m}^{-3}$  and continues to increase to  $P_{\text{cool}} = 300 \text{ kW}$  and further at  $n_{\text{sepx}} = 4.3 \cdot 10^{19} \text{ m}^{-3}$ . The latter value is 50 % of the total input power.

The high level of impurity radiation at high  $n_{\text{sepx}}$  has a significant impact on the edge plasma. The primary effect is a cooling of the edge plasma, which is shown in figure 6.11 (b). This is also reflected in the separatrix temperature in figure 6.12 (b). At

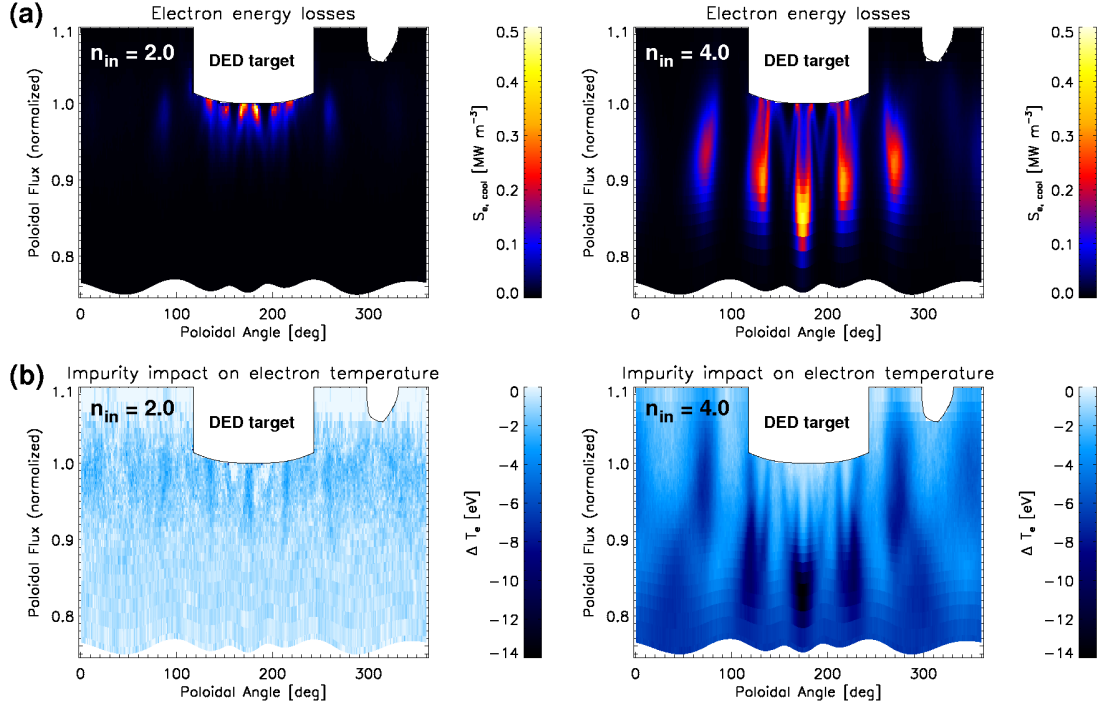


Figure 6.11: (a) 2D cuts of the electron cooling rate  $\mathcal{S}_{e,\text{cool}}$  due to ionization and line radiation of carbon impurities. (b) Resulting modification of the electron temperature.

$n_{\text{sepx}} = 2.0 \cdot 10^{19} \text{ m}^{-3}$  and  $T_{\text{sepx}} = 77 \text{ eV}$  the modification  $\Delta T_{\text{sepx}}$  is negligible, and only a weak reduction of  $T_e$  by  $\Delta T_e \approx -2 \text{ eV}$  is observed in front of the DED target. However, at  $n_{\text{sepx}} = 4.0 \cdot 10^{19} \text{ m}^{-3}$ , the separatrix temperature is significantly reduced, from  $T_{\text{sepx}} = 46 \text{ eV}$  by  $\Delta T_{\text{sepx}} = -7 \text{ eV}$ . Within the edge region, right at the position of the peak radiation,  $T_e$  is reduced by  $\Delta T_e = -14 \text{ eV}$ . As a result of the modified edge plasma, momentum losses due to plasma-neutral interaction (e.g. by charge exchange) significantly increase, because the lifetime of neutral particles increases due to reduced ionization rate coefficients. This is demonstrated in figure 6.12 (c) by the (dimensionless) momentum loss factor

$$f_M = \frac{\int dV \frac{S_m}{m_p c_s}}{\Gamma_{\text{target}}}. \quad (6.7)$$

At  $n_{\text{sepx}} = 2.5 \cdot 10^{19} \text{ m}^{-3}$  (i.e. the onset of strong impurity radiation) the momentum losses start to increase significantly from  $f_M = 0.23$  to  $f_M = 0.7$  at  $n_{\text{sepx}} = 4.0 \cdot 10^{19} \text{ m}^{-3}$ , much faster than in the reference case without impurities. As a result, the target particle flux is reduced at high  $n_{\text{sepx}}$ . A peak value of  $\Gamma_{\text{target}} = 7.2 \text{ kA}$  is found at  $n_{\text{sepx}} = 3.5 \cdot 10^{19} \text{ m}^{-3}$  compared to  $\Gamma_{\text{target}} = 9.6 \text{ kA}$  in the reference case without impurities (see

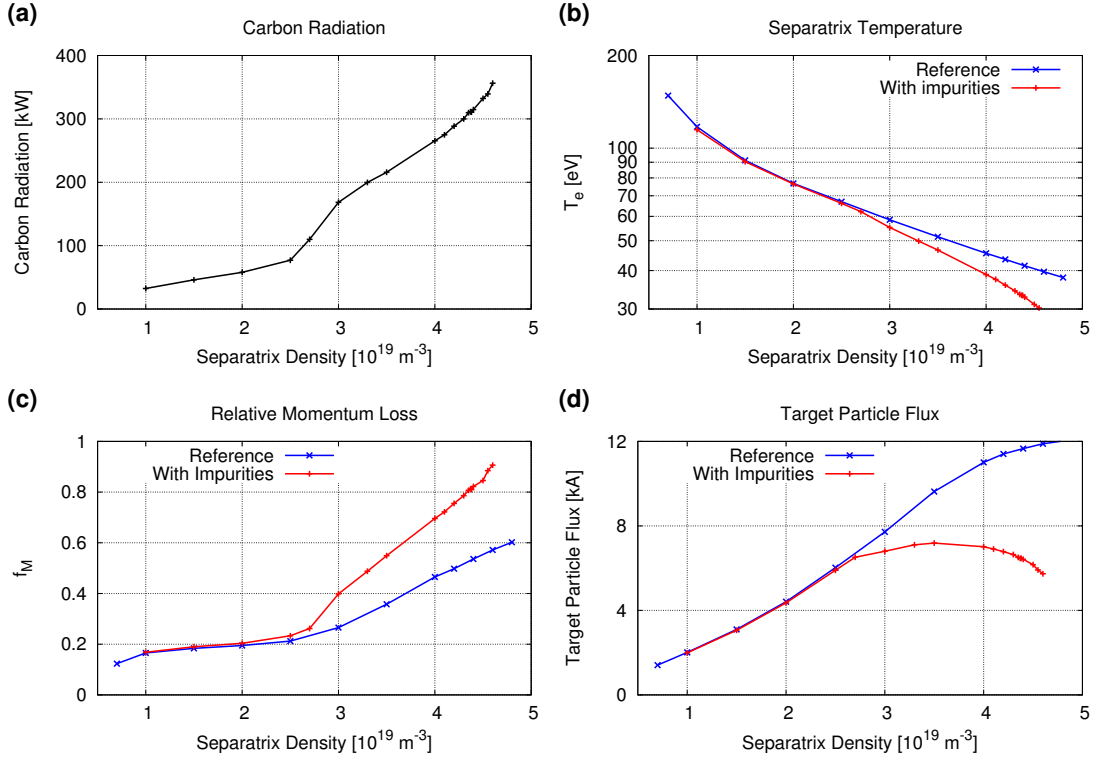


Figure 6.12: (a) Total carbon radiation as a function of  $n_{\text{sepx}}$ , (b) resulting separatrix temperature  $T_{\text{sepx}}$ , (c) relative momentum losses due to plasma-neutral interaction and (d) resulting target particle flux  $\Gamma_{\text{target}}$  compared to the reference case without impurities.

figure 6.12 (d)). For even higher densities, the target particle flux drops to a level of  $\Gamma_{\text{target}} = 5.8 \text{ kA}$  at  $n_{\text{sepx}} = 4.6 \cdot 10^{19} \text{ m}^{-3}$ .

In conclusion, impurities can be neglected only in the low density and high temperature cases, while it is found that at higher densities their impact can be significant. The drop of  $\Gamma_{\text{target}}$  is phenomenologically similar to the roll-over observed in poloidal divertor detachment, while the radial inward shift of the  $H_\alpha$  emission - and in particular that of the impurity radiation in figure 6.11 (a) - is phenomenologically more similar to the features of limiter detachment. Hence, although one might speak of detachment in the present TEXTOR helical divertor configuration as well, this would be very confusing: it has been shown in this chapter that the physical mechanisms behind it are neither that of poloidal divertor nor limiter detachment alone, and that this plasma state belongs into a new, its own, category. However, as this state is significantly affected by plasma impurities, one should improve the model for impurity production and transport first before this plasma state can be fully established as helical divertor operational regime. This has to be done in a future analysis.





## 7 Conclusions

Resonant magnetic perturbations (RMPs) are applied at several fusion devices in order to modify edge plasma transport and to control particle and energy exhausts. In particular, a recent experimental finding was that RMPs provide a promising tool to control ELMs, an instability at the plasma edge. However, the detailed effects of RMPs on the edge plasma are not fully understood. Therefore, the motivation for this thesis has been to perform 3D numerical simulations in order to analyze these effects. This is a necessary step in order to provide a reliable modeling tool to allow predictions for the next step fusion device ITER.

The concept of magnetic confinement and plasma exhaust has been briefly introduced, concluding with an introduction to open chaotic magnetic edge layers in tokamaks. Such chaotic layers are created by RMPs, which is currently investigated e.g. at the TEXTOR and DIII-D tokamaks. Modeling of the resulting magnetic field structure is a first step to understanding the impact on the edge plasma. In this thesis the so called vacuum approach has been applied where the vacuum perturbation field is superimposed to an axisymmetric equilibrium field. The process of visualizing the magnetic field structure by Poincaré and connection length plots involves field line integration, for which an Adams-Bashforth method is applied. The accuracy and performance of this method has been compared to other, more routinely applied methods. It has been found that the Adams-Bashforth method yields better accuracy than the Euler and Heun methods and is comparable to the 4th order Runge-Kutta method. The multi-step nature of the Adams-Bashforth method allows computation times similar to the Euler method, which is faster than the Heun and Runge-Kutta methods. Therefore the Adams-Bashforth method is the most suitable one for field line tracing, which is also the basis for edge plasma transport simulations by generating magnetic field aligned grids.

Presently, the most promising application of RMP induced chaotic magnetic edge layers is the control of ELMs in ITER relevant plasma scenarios, such as under investigation at the DIII-D tokamak. The generalization of the EMC3-EIRENE code to block-structured grids has allowed for the first time to perform self-consistent 3D fluid plasma transport simulations including kinetic neutral particle transport, applied to RMP scenarios at the poloidal divertor machine DIII-D. It has been shown that the magnetic field structure is reflected in the edge plasma as well, emphasizing the necessity for 3D transport simulations. In particular, the footprint of target particle and heat fluxes has been analyzed and it has been found that a certain low level  $D_{\perp} \lesssim 0.25 \text{ m}^2 \text{ s}^{-1}$  of anomalous cross-field transport is necessary to observe a distinct striation pattern. Such a pattern is indeed observed experimentally, at least for the particle flux. This low level of  $D_{\perp}$  is

much smaller than that found in simulations for TEXTOR, where a pronounced helical strike point pattern prevails for much larger  $D_{\perp}$ . This is related to the different connection length of field lines at TEXTOR and DIII-D. The striation pattern of the modeled particle flux has been found to be in qualitative agreement to experimental observations which suggests the applicability of the vacuum approach for the magnetic field structure. The modeled heat flux, however, also shows a clear striation pattern in the simulations, distinct from the experiment. But: see also footnote on page 71 regarding revised experimental results. This mismatch indicates the necessity to include, at least, kinetic corrections of the parallel electron heat flux as well as probably an advancement of the cross-field transport model to include effects of an edge transport barrier in H-mode plasmas. Only then the full validity of the vacuum approach can either be verified or disproved.

The strong 3D volumetric effects of RMPs on the edge plasma have been demonstrated as well, and in particular that the structure of helical magnetic lobes is very well reflected in the plasma parameters  $n_e$  and  $T_e$ . This includes a very strong, toroidally and poloidally localized increase of  $n_e$  (45 %) and  $T_e$  (85 %) outside the separatrix in the magnetic lobes. By means of a short magnetic flux tube it has been demonstrated that it is not justified to formulate a 1D transport model for selected flux tubes on top of a 3D magnetic geometry, but it is necessary to include the full 3D plasma and neutral transport. The poloidal modulation found in the region of short flux tubes is in qualitative agreement to observations and 3D modeling for RMP scenarios at the TEXTOR tokamak, even the more pronounced effect on  $n_e$ .

The set of model equations for the edge plasma is solved in the EMC3-EIRENE code by simulation of fluid parcels that are representatives either for particles, parallel (to  $\mathbf{B}$ ) momentum or energy. A two-step method for tracing fluid parcels which allows to account for spatially inhomogeneous transport coefficients without an explicit calculation of cross-field derivatives has been presented. Such a two-step method is implemented in the EMC3-EIRENE code to account for the density dependence of the cross-field heat conductivity  $\kappa_{\perp} = n\chi$ . This implementation has been further generalized to include spatially inhomogeneous  $\chi_e$  and  $\chi_i$  as well. Furthermore, this two-step method has also been implemented in the particle and momentum transport part of the code, which now allows spatially inhomogeneous  $D_{\perp}$  as well. The correct performance of this code improvement has been analyzed. It now allows a more realistic modeling of H-mode plasmas by including the effects of an intrinsic transport barrier at the edge. Several ad hoc models for these transport coefficients have been compared and applied to simulations of axisymmetric H-mode plasmas at DIII-D. Hydrogen pumping and re-fueling has been implemented in the present model and it has been shown that the corresponding redistribution of particle sources is necessary to obtain agreement between experimental and modeled density profiles, however, at the expense of losing agreement between experimental and modeled temperature profiles. In the present studies the pumping efficiency remains an ad hoc model parameter. However, the pumped hydrogen flux can be obtained experimentally and can be used in a later analysis as additional boundary condition. Simulations of RMP H-mode plasmas have shown a collapse of the electron

---

temperature at the plasma edge in comparison to experimental observations. This collapse indicates that the parallel electron heat flux may be overestimated in the current fluid model and that kinetic corrections (“flux-limiters”) may be necessary. This is also supported by the analysis of plasma footprints mentioned above.

Of particular interest is also the reduction of steady state heat fluxes, even in absence of the transient ones caused by ELMs. Such plasma states are e.g. investigated at the TEXTOR tokamak in helical divertor configuration. Simulations with the EMC3-EIRENE code have shown that the RMP induced magnetic field structure has a significant impact on the edge plasma, which is essentially distinct to the axisymmetric reference case. The general functionality of the TEXTOR helical divertor has been investigated by means of integrated target particle and heat fluxes. It has been demonstrated that for the present scenario a high-recycling-like regime is almost completely suppressed, similar to the results for W7-AS in [133]. The absence of such a regime has been found to be caused by cross-field diffusion and consequently damping of parallel counter-flows. The same mechanism has also earlier been found in W7-AS simulations. Therefore the present findings are a generalization of these results and show the similarities of the TEXTOR helical divertor configuration and the island divertor configuration at W7-AS. A third recycling regime has been found for high densities, where the target particle flux  $\Gamma_{\text{target}}$  begins to saturate with increasing separatrix density  $n_{\text{sepx}}$ . This has been connected to the onset momentum losses due to plasma-neutral interaction. Furthermore it is shown that the effective target heat load is significantly reduced, e.g. at high  $n_{\text{sepx}}$  up to 45 % of the input power is lost to plasma-neutral interaction instead of deposition on the DED target.

A more detailed analysis of selected strike point locations has demonstrated that the local target particle fluxes show the same qualitative behavior as the integrated flux  $\Gamma_{\text{target}}$ . A striking feature of the TEXTOR helical divertor is that the target  $H_{\alpha}$  emission suddenly drops at the strike points with ergodic field lines, with a peak value at  $n_{\text{sepx}} = 3.5 \cdot 10^{19} \text{ m}^{-3}$ . This drop is quite opposite to the features of detachment in poloidal divertor tokamaks, however, it is indeed observed experimentally at TEXTOR. Furthermore, it has been shown that no unique upstream position (stagnation point) exists in the helical divertor scenario, not even on selected field lines. Therefore, it has to be concluded that simple 2-point models are not generally applicable, nor are the resulting concepts of (parallel) divertor detachment or high-recycling regime.

The effects of intrinsic carbon impurities have been investigated. It has been found that impurity radiation and ionization losses significantly increase with increasing  $n_{\text{sepx}}$ , which leads to an additional cooling of the edge plasma. This cooling can be neglected for low densities but is important for intermediate and high densities. As a result, plasma-neutral interaction is modified and momentum losses for the plasma increase. These momentum losses results in a reduction of the target particle flux  $\Gamma_{\text{target}}$  with a weak drop at high densities. A peak value of  $\Gamma_{\text{target}} = 7.2 \text{ kA}$  is found at  $n_{\text{sepx}} = 3.5 \cdot 10^{19} \text{ m}^{-3}$  which is 75 % of the value observed in the reference case without impurities. The drop of  $\Gamma_{\text{target}}$  is phenomenologically similar to the roll-over observed in poloidal divertor

detachment, while for the  $H_\alpha$  emission and impurity radiation a radial inward shift is observed, which is phenomenologically more similar to the features of limiter detachment. In conclusion, it has been shown by the detailed transport analysis in this chapter that this plasma state falls into a different kind of detachment category and should therefore be referred to by a different name. As this state is significantly affected by plasma impurities, one should improve the model for impurity production and transport in a later analysis.

Because of the inherent 3D nature of plasma transport in the presence of RMPs, the computational effort for simulations is very large. However, the numerical scheme implemented in the EMC3-EIRENE code is ideally suited for parallelization on multi-processor computing architectures, and therefore allows to reduce the effective computation time. The scalability depends on many details of the selected plasma scenario and no general limit can be given. Nevertheless, it has been shown for one specific scenario that the speedup is almost linear up to 512 processors. Execution times have been investigated for several TEXTOR and DIII-D scenarios, which are of about one order of magnitude larger for the latter, because of the larger simulation volume. This indicates that the direct application of the code to ITER might be problematic (although it is in principle possible from a point of view of the magnetic configuration and edge transport barrier), even with present supercomputers. Further investigations have been suggested - in particular of the particle tracing strategy - but have to be left for future work.

## A Random numbers and related issues

Often probabilistic events are analyzed by an ensemble of numerical outcomes of many test runs. The generation of numerical values for a random variable  $X$  requires knowledge of its statistical distribution  $F_X : \mathbb{R} \rightarrow [0, 1]$ . A formal definition of random variables can e.g. be found in [112, 155, 111], here only univariate random variables  $X$  on a subset of real numbers  $I \subseteq \mathbb{R}^1$  are considered where  $F_X$  is differentiable and  $F'_X(x) = p(x)$  is the probability density.

### Example 1

Uniformly distributed random variable  $X$  in the finite interval  $[a, b]$ . The distribution function  $F_X$  and the corresponding probability density  $p$  are given by

$$F_X(x) = \begin{cases} 0 & , x < a \\ \frac{x-a}{b-a} & , a \leq x \leq b \\ 1 & , x > b \end{cases} \quad p(x) = \begin{cases} 0 & , x \notin [a, b] \\ \frac{1}{b-a} & , x \in [a, b] \end{cases} \quad (\text{A.1})$$

### Example 2

Exponential distribution with decay parameter  $\lambda$ :

$$F_X(x) = \begin{cases} 0 & , x < 0 \\ 1 - \exp(-\lambda x) & , x \geq 0 \end{cases}; \quad p(x) = \begin{cases} 0 & , x < 0 \\ \lambda \exp(-\lambda x) & , x \geq 0 \end{cases} \quad (\text{A.2})$$

### Example 3

Gaussian distribution:

$$F_X(x) = \frac{1}{2} \left[ 1 + \operatorname{erf} \left( \frac{x}{\sqrt{2}} \right) \right]; \quad p(x) = \frac{1}{\sqrt{2\pi}} \exp \left( -\frac{1}{2} x^2 \right) \quad (\text{A.3})$$

No algebraic form of  $F_X$  is known. Instead it is related to the so called error function which is defined by  $\operatorname{erf}(x) = \frac{2}{\sqrt{\pi}} \int_0^x dt e^{-t^2}$ .

## A.1 Random number generators

In computer simulations of a probabilistic model a large number of random numbers have to be generated. For this purpose algorithms have been developed to generate random numbers. These algorithms, however, are deterministic, i.e. they cannot generate true random numbers, and hence are called *pseudo random number generators* (PRNGs). A review on PRNGs used for Monte Carlos calculations can be found in [156]. The most common PRNGs are a linear congruential generators (LCGs), which are of the recursive form

$$X_{n+1} = (a X_n + b) \mod c \quad (\text{A.4})$$

for an integer initial value  $X_0$  (called *seed*). The parameter  $a$  and  $c$  are positive integers and  $b$  a non-negative integer. The properties of LCGs have been studied extensively and are well-known [157], a list of LCGs can be found in [158]. (A.4) can be used to generate uniformly distributed pseudo random numbers in the unit interval:

$$U_n = X_n/c. \quad (\text{A.5})$$

One particular drawback of LCGs is that  $d$ -tuples of such numbers which represent points in a  $d$ -dimensional space fall on a certain number of hyperplanes [159] which decreases with increasing  $d$ . This can be a problem e.g. for Monte Carlo simulations of high dimensional integrals, but not necessarily for simulations in 3D space. Several tests to check the statistical properties have been described in [157] and implemented in the “*Diehard Battery of Tests of Randomness*” [160]. Based on this, “*Dieharder: A Random Number Test Suite*” has been developed to provide an open source (GPL) [161] test suite. This test suite additionally includes some of the test described in [162] which have been developed for cryptographic applications by the National Institute for Standards and Technology (NIST).

## A.2 Generation of non-uniformly distributed random numbers

Random variables with a non-uniform distribution  $X$  can be related to a uniformly distributed random variable, if the corresponding distribution function  $F_X$  is invertible. Let  $U$  be uniformly distributed, then  $x(U)$  is defined by  $U = F_X(x(U))$  so that  $x(U) = F_X^{-1}(U)$ . This *inverse transform method* can e.g. be used for exponential random variables (A.2)

$$x(U) = -\frac{\ln(1-U)}{\lambda} = -\frac{\ln U'}{\lambda}, \quad (\text{A.6})$$

where  $U' = 1 - U$  is also uniformly distributed. If  $F_X$  cannot be inverted easily, then other methods are more appropriate. E.g. for Gaussian random variables the *Box-Muller method* [163] provides an efficient way to generate Gaussian random numbers: Let  $U_1$  and  $U_2$  be two independent, uniformly distributed random variables then  $G_1$  and  $G_2$  defined by

$$G_1 = \sqrt{-2 \ln U_1} \cos(2\pi U_2) \quad (\text{A.7})$$

$$G_2 = \sqrt{-2 \ln U_1} \sin(2\pi U_2) \quad (\text{A.8})$$

are two independent standard Gaussian random variables. A detailed review on Gaussian random number generators is given in [164], where various algorithms are described and benchmarked.

### A.3 Application in the EMC3-EIRENE code

Over the last years a lot of Monte Carlo computer programs, such as the EMC3-EIRENE code, have been advanced for high-performance computing, i.e. by running in parallel on a multitude of processors. To deal with the issues in parallel random number generation the *Scalable Library for Pseudorandom Number Generation* (SPRNG) [165] has been developed. The EMC3-EIRENE code, however, comes with its own PRNG, a 48 bit multiplicative LCG with

$$\begin{aligned} a &= 44485709377909 \\ b &= 0 \\ c &= 2^{48}. \end{aligned} \quad (\text{A.9})$$

This PRNG is initialized with the seed

$$X_0 = i_{\text{CPU}} \cdot S, \quad i_{\text{CPU}} = 1, \dots, N_{\text{CPU}}, \quad (\text{A.10})$$

where  $i_{\text{CPU}}$  is the process number and  $S$  is some user defined input number.

The EMC3-EIRENE code turns out to be robust against the choice of the PRNG. This is demonstrated in figure A.1 for a selected TEXTOR simulation. A converged solution of  $T_e$  is shown in figure A.1 (a) which is taken as reference data. Based on this  $T_e$  one ENERGY iteration is performed with the EMC3-EIRENE code with 160 k MC particles on 32 CPUs each for several PRNGS. For this the EMC3-EIRENE code is coupled to the SPRNG library which provides easy access to various PRNGS. The default PRNG in the EMC3 code is labeled PRNG0 in figure A.1 which is compared to

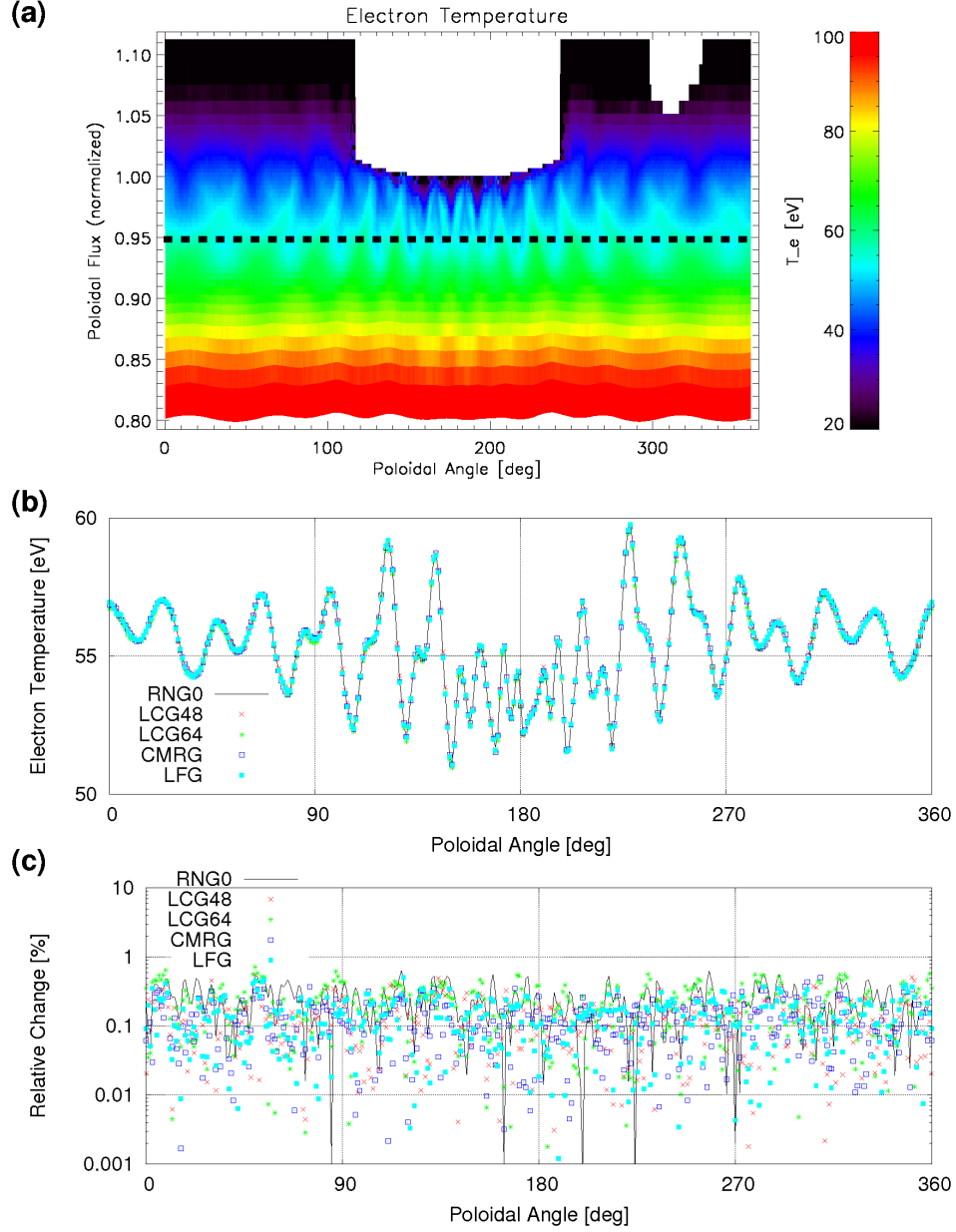


Figure A.1: Test of several PRNGs applied in simulations with the EMC3-EIRENE code. (a) Converged  $T_e$  distribution at  $\varphi = 0$  deg, (b) poloidal  $T_e$  profiles obtained with different PRNGs after one ENERGY-iteration with EMC3-EIRENE with 160k MC particles on 32 CPUs each, (c) relative differences  $\Delta T_e^*$  to the converged solution from (a).



- another 48-bit LCG with different parameters (LCG48),
- a 64-bit LCG (LCG64),
- a combined multiple recursive generator (CMRG)
- and an additive Lagged Fibonacci Generator (LFG).

Poloidal profiles of  $T_e$  obtained from these PRNGs are shown in figure A.1 (b). The profiles show no obvious deviation from a calculation with the default PRNG. This is supported by figure A.1 (c) which shows the relative differences

$$\Delta T_e^* = \left| 2 \frac{T_e^{(0)} - T_e^{(\text{PRNG})}}{T_e^{(0)} + T_e^{(\text{PRNG})}} \right| \quad (\text{A.11})$$

between the converged solution  $T_e^{(0)}$  and  $T_e^{(\text{PRNG})}$  from an additional calculation for the PRNG-test. In all cases, with the default PRNG and the PRNGs from the SPRNG library,  $\Delta T_e^*$  is at the same level well below 1 %. This demonstrates the robustness of the EMC3-EIRENE code with respect to the applied PRNG.

## A.4 Relaxation of noisy iterations

The iterative procedure described in chapter 4 to obtain a self-consistent solution of the edge plasma involves a relaxation scheme in order to suppress numerical instabilities. Applying a specific relaxation scheme allows to further reduce the noise level without the need to increase the number of Monte Carlo particles per iteration step. The idea is to subsequently increase the relaxation factor  $\alpha$  to smooth out the noise in each iteration step. The general relaxation scheme is given by

$$x_{n+1}^* = \alpha_{n+1} x_n^* + (1 - \alpha_{n+1}) x_{n+1}, \quad (\text{A.12})$$

where  $*$  denotes the relaxed quantity. Starting from a converged solution  $x_1$  (up to some noise level),  $\alpha_n$  is increased with each iteration step  $n \geq 2$ :

$$\alpha_n = \frac{n-1}{n}. \quad (\text{A.13})$$

Using  $x_1^* = x_1$  as initial condition it is easily found that

$$x_2^* = \frac{1}{2} (x_1 + x_2) \quad \text{and} \quad x_3^* = \frac{1}{3} (x_1 + x_2 + x_3). \quad (\text{A.14})$$

Now it is easy to prove the general case as well:

$$x_n^* = \frac{1}{n} \sum_{i=1}^n x_i. \quad (\text{A.15})$$

Assume that (A.15) is valid for some  $n \in \mathbb{N}$ , then

$$\begin{aligned} x_{n+1}^* &= \alpha_{n+1} x_n^* + (1 - \alpha_{n+1}) x_{n+1} \\ &= \frac{n}{n+1} \frac{1}{n} \sum_{i=1}^n x_i + \frac{1}{n+1} x_{n+1} \\ &= \frac{1}{n+1} \sum_{i=1}^{n+1} x_{n+1}. \end{aligned} \quad (\text{A.16})$$

As the iteration scheme (A.12) with (A.13) is started from a converged solution, it can be assumed that the standard error  $\sigma_n = \sigma$  of each calculation  $x_n$  is constant. Hence, the standard error of  $x_n^*$  is given by  $\sigma_n^* = \frac{1}{\sqrt{n}} \sigma$ . Now it can be shown that the difference between iterations

$$\begin{aligned} \Delta_{n+1} &= x_{n+1}^* - x_n^* \\ &= \frac{1}{n+1} x_{n+1} - \frac{1}{n+1} x_n^* \end{aligned} \quad (\text{A.17})$$

is distributed with variance given by (note that  $x_{n+1}$  and  $x_n^*$  are statistically independent while  $x_{n+1}^*$  and  $x_n^*$  are not)

$$\begin{aligned} s_{n+1}^2 &= \frac{1}{(n+1)^2} \sigma^2 + \frac{1}{(n+1)^2} \sigma_n^{*2} \\ &= \frac{1}{(n+1)n} \sigma^2. \end{aligned} \quad (\text{A.18})$$

Hence, for large enough  $n$ , the standard error of  $\Delta_n$  is given by

$$s_n \approx \frac{1}{n} \sigma. \quad (\text{A.19})$$

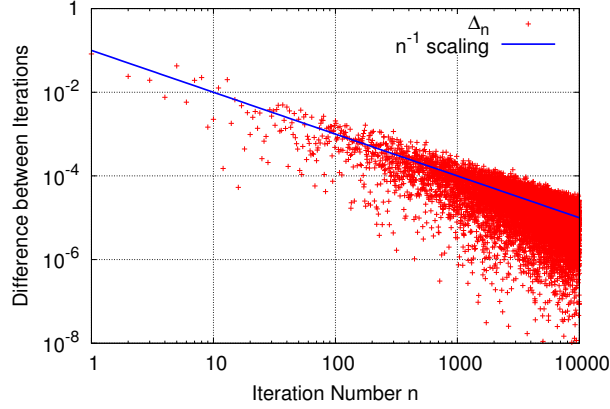


Figure A.2: Differences between iterations of (A.20) with relaxation factor from (A.13).

### Example

Consider the noisy iteration scheme

$$x_n = 1 + d \xi_n \quad (\text{A.20})$$

with normal distributed  $\xi_n$  and  $d = 0.1$ . Then the relaxation scheme (A.12) with (A.13) results in the differences  $\Delta_n$  in (A.17) which are shown in figure A.2. Clearly, these differences decrease according to the  $n^{-1}$  scaling expected from (A.19).

### Application to multi-dimensional functions

The iterative application of the EMC3-EIRENE core can be regarded as a fixed point iteration of a multi-dimensional function  $\mathcal{F}$  in (4.56) where the mean relative change  $\Delta\mathcal{F}$  in (4.57) is used to study convergence. The latter quantity is of the general form

$$\Delta^2 = \frac{\sum_i w_i \Delta_i^2}{\sum_i w_i} \quad (\text{A.21})$$

where  $i$  denotes the cell number and  $w_i$  the corresponding weight. Provided that expectation values are  $E(\Delta_i) = 0$  and  $E(\Delta_i^2) = s_i^2$  then the expected global quantity is

$$\overline{\Delta^2} = E(\Delta^2) = \frac{\sum_i w_i E(\Delta_i^2)}{\sum_i w_i} = \frac{\sum_i w_i s_i^2}{\sum_i w_i}. \quad (\text{A.22})$$

For iteration number  $n$ :  $s_i(n) \sim n^{-1}$  according to (A.19), and therefore also  $\overline{\Delta} \sim n^{-1}$ .



## B Verification of the generalized EMC3-EIRENE code

The field line reconstruction method in the EMC3-EIRENE code has been supplemented by a cell surface mapping technique in order to allow computational grids with arbitrary connectivity (see section 4.2). For convenience, grids are block-structured in this present work. Details of the coordinate transformation between blocks and test for the correct performance of this code generalization are presented in section B.1. A second generalization of the EMC3-EIRENE code is the implementation of local coefficients for cross-field transport (see section 4.1.3). The correct performance is investigated in section B.2.

### B.1 Block-structured grid decomposition

The transformation of coordinates at the boundary between adjacent blocks according to (4.44) involves the transformation matrices given in (4.45),(4.46).  $\underline{\mathbf{M}}_{\xi\eta}$ , which relates the coordinates  $(\xi', \eta')$  to  $(\xi, \eta)$ , can be derived from figure 4.5 by introducing intermediate coordinates: a surface coordinate  $s_c$  and a perpendicular coordinate  $p_c$ .  $s_c$  is fixed at the cell interface while  $p_c$  is transformed to  $-p_c$ , because  $(\xi, \eta), (\xi', \eta') \in [-1, 1]^2$ . The relation of these intermediate coordinates to field line coordinates depends on the orientation  $(i_{\text{surf}}, i'_{\text{surf}})$  of the cells and is basically a rotation of the coordinate system:

$$\underline{\mathbf{R}}(\varphi) = \begin{pmatrix} \cos \varphi & \sin \varphi \\ -\sin \varphi & \cos \varphi \end{pmatrix}, \quad (\text{B.1})$$

one for the old field line coordinates

$$\begin{pmatrix} s_c \\ p_c \end{pmatrix} = \underline{\mathbf{A}}_{i_{\text{surf}}} \begin{pmatrix} \xi \\ \eta \end{pmatrix} \quad (\text{B.2})$$

and one for the new field line coordinates

$$\begin{pmatrix} \xi' \\ \eta' \end{pmatrix} = \underline{\mathbf{B}}_{i'_{\text{surf}}} \begin{pmatrix} s_c \\ -p_c \end{pmatrix}. \quad (\text{B.3})$$

$\underline{\mathbf{A}}_{i_{\text{surf}}} = \underline{\mathbf{R}}(\varphi_A)$  and  $\underline{\mathbf{B}}_{i'_{\text{surf}}} = \underline{\mathbf{R}}(\varphi_B)$  are determined by (B.1) with the corresponding angles given by

$$\varphi_A = (i_{\text{surf}} - 3) \cdot \frac{\pi}{2} \quad (\text{B.4})$$

$$\varphi_B = (-i'_{\text{surf}} + 1) \cdot \frac{\pi}{2}. \quad (\text{B.5})$$

(B.2) and (B.3) can be combined to determine the transformation matrix  $\underline{\mathbf{M}}_{\xi\eta}$ :

$$\underline{\mathbf{M}}_{\xi\eta} = \underline{\mathbf{B}}_{i'_{\text{surf}}} \begin{pmatrix} 1 & 0 \\ 0 & -1 \end{pmatrix} \underline{\mathbf{A}}_{i_{\text{surf}}}. \quad (\text{B.6})$$

Inserting (B.1) gives

$$\underline{\mathbf{M}}_{\xi\eta} = \begin{pmatrix} \cos(\varphi_A - \varphi_B) & \sin(\varphi_A - \varphi_B) \\ \sin(\varphi_A - \varphi_B) & -\cos(\varphi_A - \varphi_B) \end{pmatrix}, \quad (\text{B.7})$$

which reduces with (B.4), (B.5) and  $m = i_{\text{surf}} + i'_{\text{surf}}$  to

$$\underline{\mathbf{M}}_{\xi\eta} = \begin{cases} (-1)^{\frac{m}{2}} \cdot \underline{\mathbf{M}}_0, & m \text{ even} \\ (-1)^{\frac{m-1}{2}} \cdot \underline{\mathbf{M}}_1, & m \text{ odd} \end{cases} \quad (\text{B.8})$$

with  $\underline{\mathbf{M}}_0$ ,  $\underline{\mathbf{M}}_1$  from (4.46).

The correct performance of this newly implemented method is investigated in the following. At first, a well-established simulation scenario at the TEXTOR tokamak is considered. Then the application to poloidal divertor tokamaks investigated by an example simulation for the DIII-D tokamak.

### B.1.1 Comparison to established simulations

The reference case for the first benchmark of the newly implemented cell surface mapping technique is a TEXTOR scenario with  $m/n = 12/4$  perturbation field, which has been extensively investigated in the past [99, 96, 97, 77]. Two toroidal blocks of  $\Delta\varphi = 45$  deg are used (see sketch in figure B.1 (a)). The regular grid structure in the radial and poloidal direction is translated into a  $4 \times 4$  block structure (see sketch in figure B.1 (b)). These blocks are re-connected by introducing a cell surface mapping ( $M_{\text{neigh}}, \underline{\mathbf{M}}_{\xi\eta}$ ) (see section 4.2.3).

Before performing actual plasma and neutral gas transport calculations, the correct representation of the magnetic field structure is demonstrated, because the plasma transport part in the code is based on a magnetic coordinate system. Here only the correct performance of a block-structured decomposition is demonstrated, the interpolation error of the field line approximation (4.35) is not discussed. This was already investigated in [46, 49]. If the cell surface mapping technique (4.43),(4.44) required for a block-structured decomposition was not correctly implemented, then this would result in a

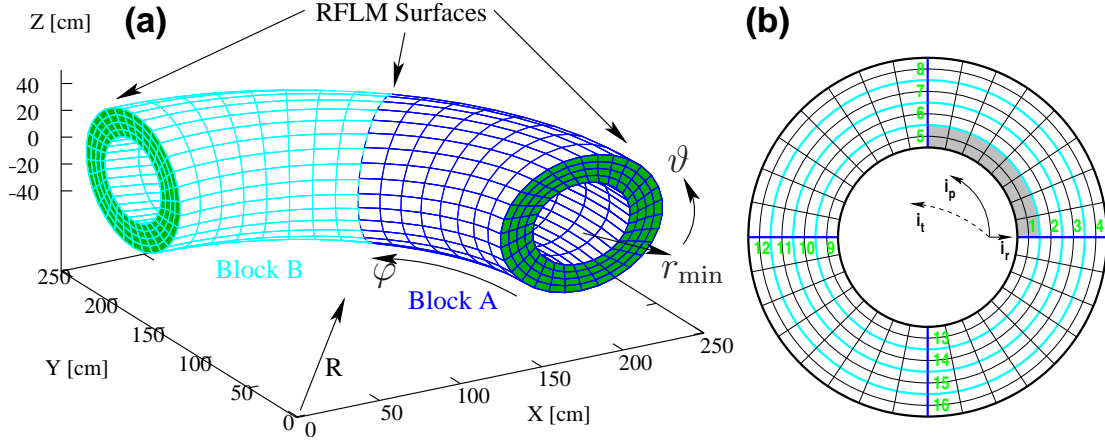


Figure B.1: (a) Field aligned grid for a TEXTOR reference scenario with  $m/n = 12/4$  perturbation field. (b) Schematic view of a  $4 \times 4$  block structured decomposition in the radial and poloidal direction. Block boundaries (dark and light blue) are connected by a cell surface mapping ( $M_{\text{neigh}}$ ,  $\underline{M}_{\xi\eta}$ ) for block number  $i_b$  (green), cell indices  $i_r, i_p, i_t$  and local coordinates  $\xi, \eta, \tau$ .

very different reconstructed magnetic field and plasma structure. Hence, the following analysis can indicate the correct performance's of the generalized code.

The reconstructed magnetic field structure is visualized in figure B.2 by means of the wall-to-wall connection length  $L_c$  of magnetic field lines. Radial profiles at  $\vartheta_1 = 12$  deg and  $\vartheta_2 = 34$  deg, as well as poloidal profiles at  $r_{\min,1} = 42$  cm and  $r_{\min,2} = 46$  cm are selected. It is shown in figure B.2 that they exactly match the reference profiles from a regular structured grid (see figure B.1 (a) for definitions of toroidal coordinates  $\varphi, \vartheta, r_{\min}$ ). The physics of such an open chaotic system and its impact on plasma transport is not part of this paper and is investigated elsewhere (e.g. in [88, 89, 97]).

Transport calculation within a  $4 \times 4$  block decomposition give - as expected - the same results as obtained from a regular grid. This is illustrated in figure B.3, again by selected radial and poloidal profiles of the electron temperature  $T_e$  and density  $n_e$ . The same tests have also been performed for the neutral transport part EIRENE. Hence, these numerical tests exemplify the correct performance of the generalized code.

### B.1.2 Application to poloidal divertor tokamaks

Now the enhanced applicability of the EMC3-EIRENE code is presented by an example of a simulation for the DIII-D tokamak. The computational domain and the topology of the grid has already be introduced in section 4.2.1.

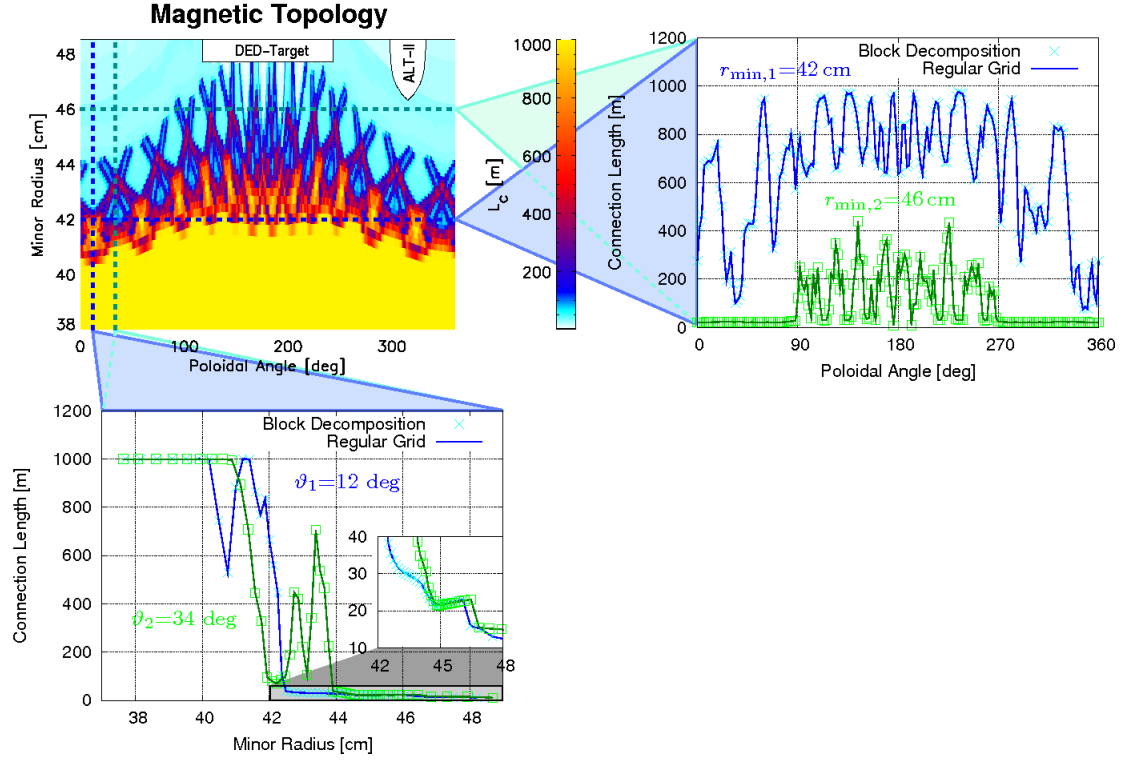


Figure B.2: Magnetic Topology of an RMP scenario at the TEXTOR tokamak, depicted by the wall-to-wall connection length  $L_c$  of magnetic field lines. The center part shows a 2D cut at  $\varphi = 0$  deg, giving an overview of the magnetic topology. Bottom: radial profiles at  $\vartheta_1 = 12$  deg (blue) and  $\vartheta_2 = 34$  deg (green), right: poloidal profiles at  $r_{\min,1} = 42$  cm (blue) and  $r_{\min,2} = 46$  cm (green). Data from calculations within a  $4 \times 4$  block-structured grid is presented as symbols, while reference data within a regular grid is presented as solid lines.



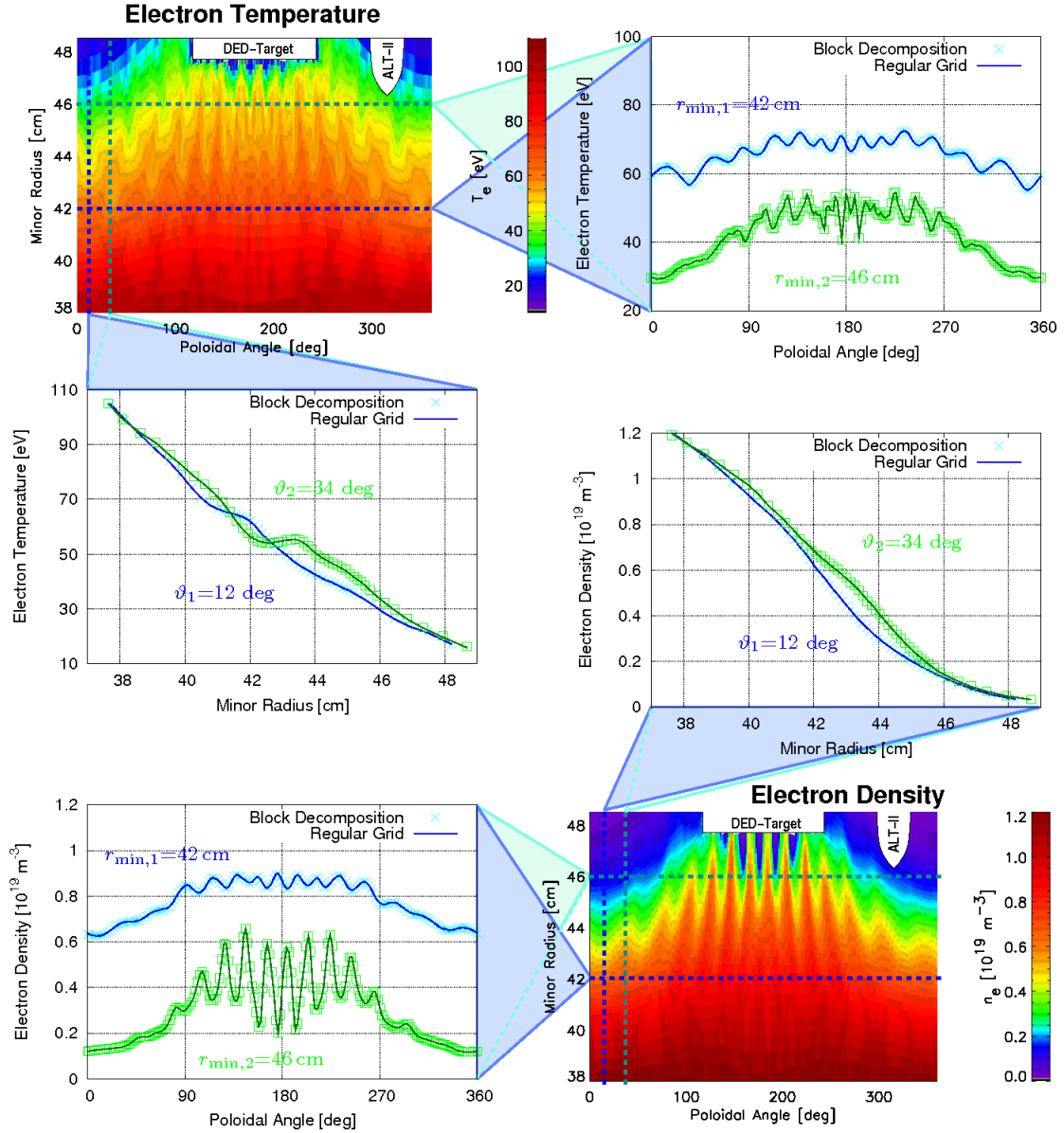


Figure B.3: Electron temperature  $T_e$  and density  $n_e$  for the magnetic topology from figure B.2. The upper left and lower right parts are 2D cuts at  $\varphi = 0 \text{ deg}$ . Middle row: radial profiles at  $\vartheta_1 = 12 \text{ deg}$  (blue) and  $\vartheta_2 = 34 \text{ deg}$  (green), upper right and lower left parts: poloidal profiles at  $r_{\min,1} = 42 \text{ cm}$  (blue) and  $r_{\min,2} = 46 \text{ cm}$  (green). Data from calculations within a  $4 \times 4$  block-structured grid is presented as symbols, while reference data within a regular grid is presented as solid lines.

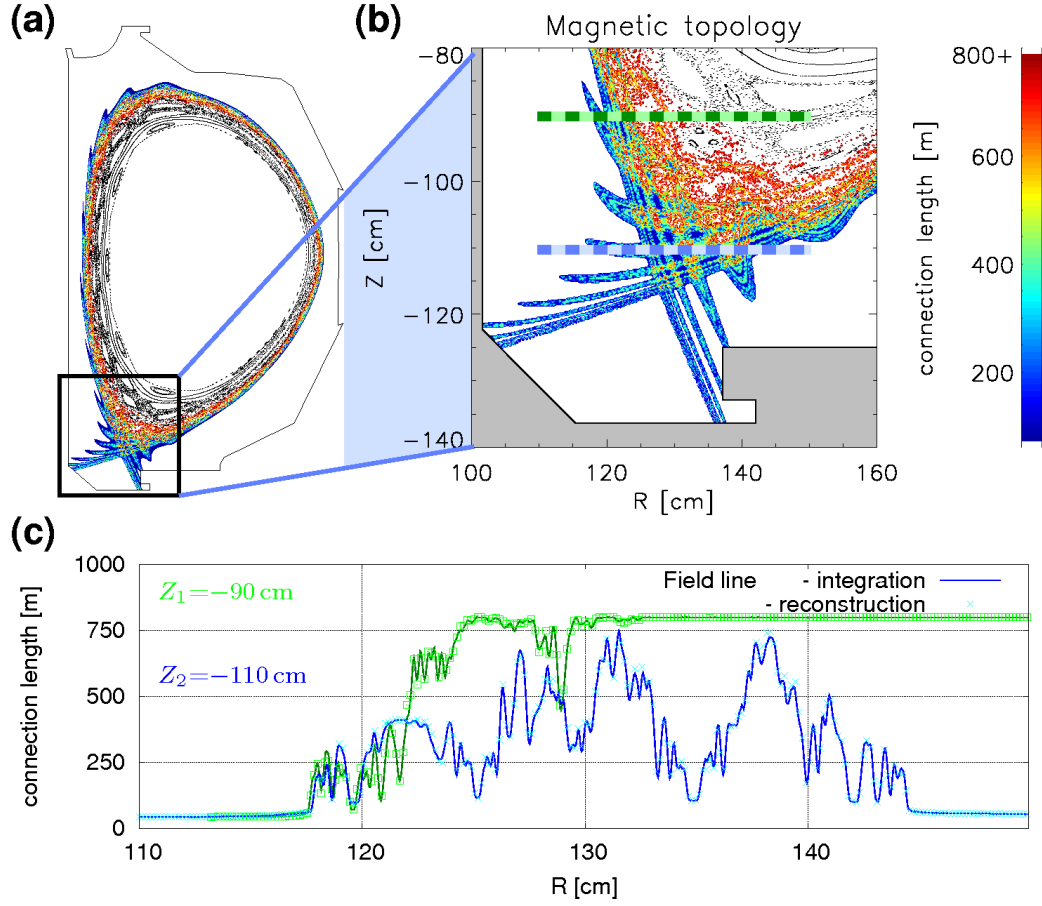


Figure B.4: (a,b) 2D cuts of the connection length  $L_c$  of magnetic field lines and (c) radial profiles at  $Z_1 = -90$  cm (green) and  $Z_2 = -110$  cm (blue) comparing the reconstructed  $L_c$  (symbols) to the original  $L_c$  from field line integration (lines).

### Field line reconstruction

The magnetic field structure is depicted in figure B.4 (a),(b) by 2D cuts of the wall-to-wall connection length  $L_c$  of magnetic field lines. It is shown in figure B.4 (c) that the reconstructed field structure is in good agreement with the original one obtained from direct field line integration.

### Plasma transport verification

Now the correct treatment of plasma transport in a poloidal divertor configuration is investigated. For this an axisymmetric magnetic configuration, i.e. a configuration

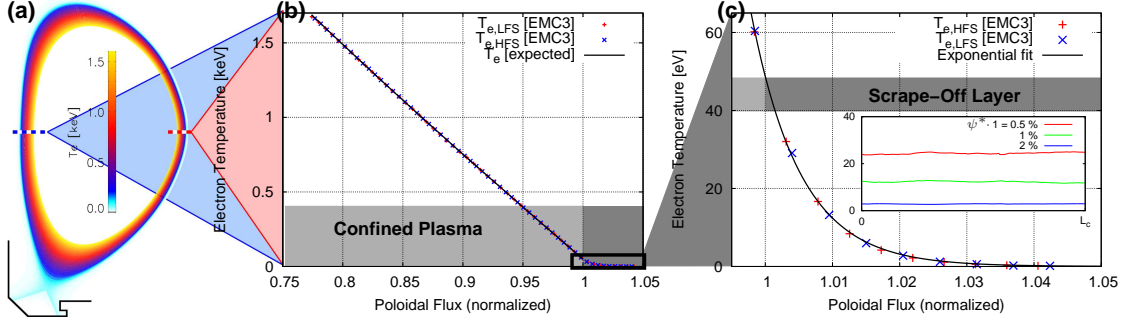


Figure B.5: (a) 2D cut of the electron temperature  $T_e$  at  $\varphi = 0$  deg and (b,c) radial  $T_e$  profiles extracted at the inner (High Field Side, HFS) and outer (Low Field Side, LFS) midplane. The inset in (c) shows  $T_e$  profiles along field lines located at  $\psi^* = 1.005$  (red),  $\psi^* = 1.01$  (green) and  $\psi^* = 1.02$  (blue).

without RMP field, is considered, because in this case analytic solutions are known. A separatrix exists with closed magnetic surfaces inside. Plasma parameters on these surfaces are constant (see e.g.  $T_e$  in figure B.5 (a)), because of the fast parallel transport. Hence, the normalized poloidal magnetic flux  $\psi^*$  from (2.15) can be used as radial coordinate so that  $n_e = n_e(\psi^*)$  and  $T_e = T_e(\psi^*)$ . Inside the separatrix ( $\psi^* \leq 1$ ) and for a preset constant plasma background, the 3D transport equations then reduce to a 1D balance, e.g. for the electron temperature:

$$\frac{\partial T_e}{\partial \psi^*} = -\frac{P_{in}}{A_{\psi^*} |\nabla \psi^*| n_e \chi_{\perp}}, \quad \psi^* \leq 1. \quad (\text{B.9})$$

The total input power for electrons  $P_{in}$ , the electron density  $n_e$  and the cross-field diffusion coefficient  $\chi_{\perp}$  are set to the following values for this test case:

$$\begin{aligned} P_{in} &= 3.2 \text{ MW} \\ n_e &= 2 \cdot 10^{19} \text{ m}^{-3} \\ \chi_{\perp} &= 1.2 \text{ m}^2 \text{ s}^{-1} \end{aligned}$$

while the area  $A_{\psi^*}$  of flux surface  $\psi^*$  as well as the flux surface averaged gradient  $|\nabla \psi^*|$  are determined by the given magnetic configuration:

$$A_{\psi^*} |\nabla \psi^*| = \oint_{A_{\psi^*}} dA \mathbf{e}_{\psi^*} \cdot \nabla \psi^*. \quad (\text{B.10})$$

Outside the separatrix ( $\psi^* > 1$ ), in the so called *Scrape-Off Layer* (SOL), exponential decay

$$T_e(\psi^*) = T_{e,\text{LCFS}} \exp \left[ -\frac{\psi^* - 1}{\lambda_{T_e}^*} \right], \quad (\text{B.11})$$

with an e-folding length  $\lambda_{T_e}^*$  is expected, because of nearly constant parallel loss rates, i.e. sink action in parallel direction due to free streaming along  $\mathbf{B}$  and plasma recombination at divertor targets. Any SOL sources, e.g. due to divertor recycling, are turned off in this test. Exponential decay is recovered very accurately with the EMC3-code (see figure B.5 (c)):

$$T_{e,\text{LCFS}} = (48.7 \pm 0.2) \text{ eV} \quad (\text{B.12})$$

$$\lambda_{T_e}^* = (7.32 \pm 0.05) \cdot 10^{-3} \quad (\text{B.13})$$

$\lambda_{T_e}^*$  is an e-folding length with respect to  $\psi^*$ , but it can be related to an average e-folding length in real space:

$$\lambda_{T_e} = \lambda_{T_e}^* \cdot \overline{|\nabla \psi^*|}_{\text{LCFS}}^{-1} = (3.35 \pm 0.02) \text{ mm} \quad (\text{B.14})$$

where  $\overline{|\nabla \psi^*|}_{\text{LCFS}}$  is the average gradient of the normalized poloidal flux  $\psi^*$  at the separatrix. In the present test case heat conduction parallel to  $\mathbf{B}$  plays no role, the plasma temperature is essentially constant along the magnetic field (isothermal flow in the parallel direction, see inset in figure B.5 (c)). The cross field decay length  $\lambda_{T_e}$  can therefore simply be estimated from target sheath losses vs. cross field conduction gains in each flux-tube (sheath limited SOL regime). The analytic estimate for  $\lambda_{T_e}$  is given in [7], which reduces for the present case to

$$\lambda_{T_e} = \sqrt{\frac{\chi_{\perp} L_{c,\text{eff}}}{2 \gamma_e c_s}} \approx 3.2 \text{ mm} \quad (\text{B.15})$$

with sheath heat-transmission factor  $\gamma_e = 4.5$  and ion sound speed  $c_s = 4.4 \cdot 10^5 \frac{\text{m}}{\text{s}}$ .  $L_{c,\text{eff}} \approx 34 \text{ m}$  is the average effective length of SOL field lines, i.e. the contact-length with the confined plasma, taken at the first decay length (B.14) outside the separatrix. This estimate is within 5 % of the calculated value, which is a good agreement regarding the very crude approximations made here. Using  $T_{e,\text{LCFS}}$  from (B.12),  $T_e$  can be integrated from the separatrix inwards using (B.9). Figure B.5 (b) shows that the EMC3 data very accurately agree with this prediction.  $T_e$  at the inner simulation boundary is predicted to  $T_e = 1.68 \text{ keV}$ , while  $T_e$  from EMC3 is  $T_e = 1.67 \text{ keV}$ , computed on 32 CPUs with 1000 Monte Carlo particles each.

## B.2 Spatially varying coefficients for cross-field transport

Distinct from finite volume or finite element implementations, the generalization to spatially varying transport coefficients is non-trivial for the Lagrangian Monte Carlo approach in EMC3, as it affects the basic random walk generation. The implemented procedure (see section 4.1.3) is therefore verified explicitly in this section. The generalized code is applied to a scenario which resembles a 1D radial transport case on a given plasma background. In this case plasma transport equations are of the form:

$$-\frac{1}{r} \frac{d}{dr} r \mathcal{D} \frac{d}{dr} \mathcal{F} = \mathcal{S}. \quad (\text{B.16})$$

The radial domain for the present study is given by  $[R_A, R_B]$ , which is fitted to the edge plasma region at the LFS midplane in DIII-D for the scenario discussed in chapter 5. In the present study only surface sources are considered at the radial boundaries:

$$\mathcal{S} = \mathcal{S}_A \delta(r - R_A) - \mathcal{S}_B \delta(r - R_B), \quad (\text{B.17})$$

where the surface sources  $\mathcal{S}_A = \Gamma/F_A$  and  $\mathcal{S}_B = \Gamma/F_B$  are determined by the total in and out flux  $\Gamma$  and the respective surface areas  $F_A(\sim R_A)$  and  $F_B(\sim R_B)$ . Integrating (B.16) from  $r$  to  $R_B$  yields

$$\frac{d\mathcal{F}}{dr} = \frac{R_B \mathcal{D}_B}{r \mathcal{D}} \frac{d\mathcal{F}}{dr} \Big|_{R_B} \quad \text{and} \quad \mathcal{D}_B = \mathcal{D}(R_B), \quad (\text{B.18})$$

where  $\frac{d\mathcal{F}}{dr} \Big|_{R_B}$  is determined by (B.17) to

$$\frac{d\mathcal{F}}{dr} \Big|_{R_B} = -\frac{\mathcal{S}_B}{\mathcal{D}_B}, \quad (\text{B.19})$$

or by an alternative formulation for the boundary condition

$$\frac{d\mathcal{F}}{dr} \Big|_{R_B} = \frac{\mathcal{F}_B}{\lambda}. \quad (\text{B.20})$$

Hence, by prescribing  $\Gamma$  and  $\lambda$ , the boundary value  $\mathcal{F}_B$  can be determined to

$$\mathcal{F}_B = -\lambda \frac{\Gamma}{F_B \mathcal{D}_B} \quad (\text{B.21})$$

and (B.18) can then be transformed to the following form:

$$\frac{d\mathcal{F}}{dr} = -\frac{\Gamma}{F_B} \frac{1}{\mathcal{D}} \frac{R_B}{r}. \quad (\text{B.22})$$

(B.22) is now integrated analytically

$$\mathcal{F}_B - \mathcal{F}(R) = \int_R^{R_B} dr \frac{d\mathcal{F}}{dr}, \quad (\text{B.23})$$

where the right hand side is evaluated according to one of the following models for  $\mathcal{D}$  and solved for  $\mathcal{F}(R)$ :

1.  $\mathcal{D}(R) = \mathcal{D}_0 = \text{constant}$

$$\mathcal{F}(R) = \mathcal{F}_B + \frac{\Gamma R_B}{F_B \mathcal{D}_0} \log\left(\frac{R_B}{R}\right) \quad (\text{B.24})$$

2. linearly varying  $\mathcal{D}$ :  $\mathcal{D}(R) = \mathcal{A}R + \mathcal{B}$  with  $\mathcal{A} = \frac{\mathcal{D}_B - \mathcal{D}_A}{R_B - R_A}$  and  $\mathcal{B} = \mathcal{D}_A - R_A \frac{\mathcal{D}_B - \mathcal{D}_A}{R_B - R_A}$

$$\mathcal{F}(R) = \mathcal{F}_B + \frac{\Gamma R_B}{F_B \mathcal{B}} \log\left(\frac{R_B}{R} \frac{\mathcal{A}R + \mathcal{B}}{\mathcal{D}_B}\right) \quad (\text{B.25})$$

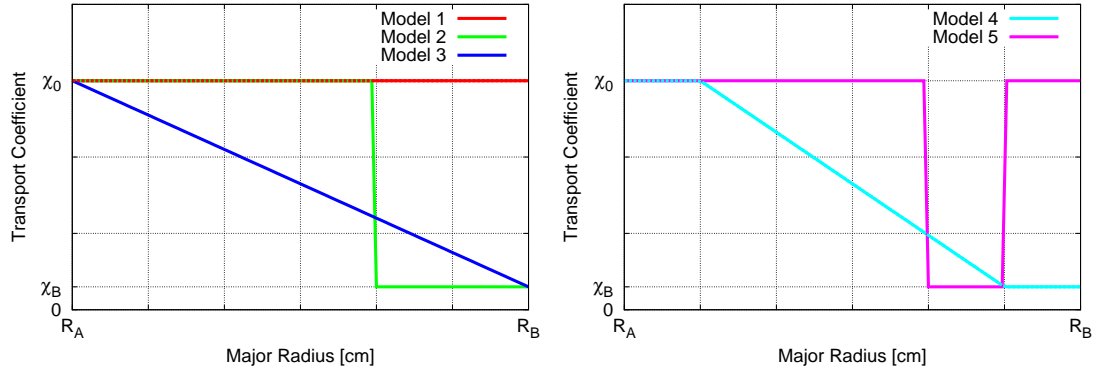
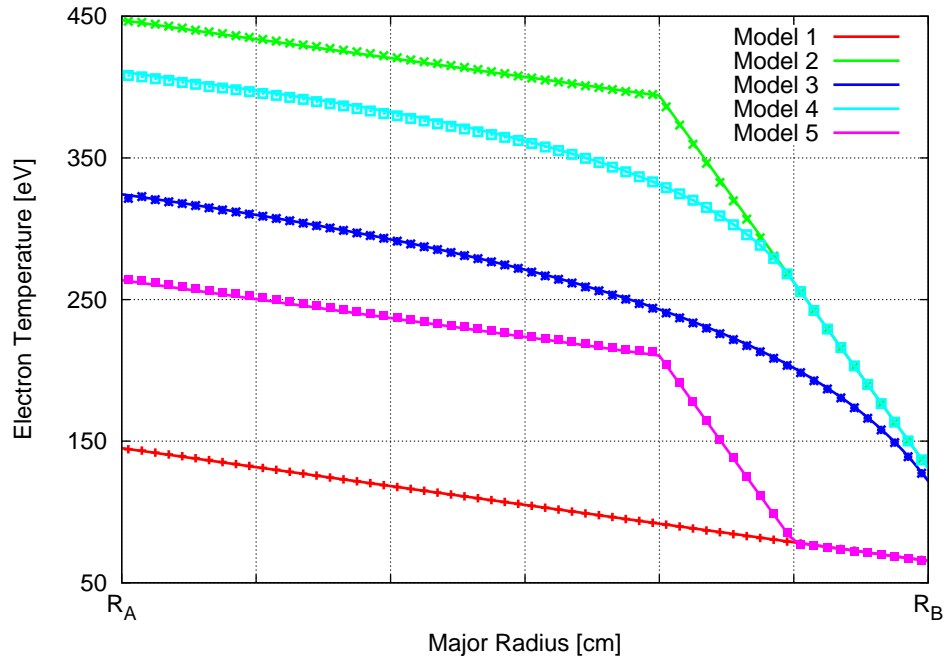
3. Segmented  $\mathcal{D}$  (stepwise constant or linear):

$$\mathcal{D}(R) = \begin{cases} \mathcal{D}_1(R) & R \in [R_0 = R_A, R_1] \\ \vdots \\ \mathcal{D}_n(R) & R \in [R_{n-1}, R_n = R_B] \end{cases} \quad (\text{B.26})$$

where each segment is described by one of the above models. Then  $\mathcal{F}(R)$  is segmented as well and each segment can be determined iteratively from (B.24) or (B.25) by starting with  $\mathcal{F}_n(R)$  and replacing  $\mathcal{F}_B$  by  $\mathcal{F}_{B,i} = \mathcal{F}_{i+1}(R_i)$ ,  $i < n$ .

Five realizations of these models with different parameter values are now applied to check the correct treatment of local cross-field diffusion  $\chi_\perp$  in the energy transport equation:  $\mathcal{F} = T$ ,  $\mathcal{D} = n \chi_\perp$ ,  $\Gamma = P_{\text{in}}$ . The explicit test models are summarized in figure B.6, where  $\chi_0 = 3.0 \text{ m}^2 \text{ s}^{-1}$  and  $\chi_B = 0.3 \text{ m}^2 \text{ s}^{-1}$ .

Transport simulations with the EMC3-EIRENE code are preformed with these models with the boundary condition  $\lambda = -5 \text{ cm}$  for models 1 and 5 and  $\lambda = -1 \text{ cm}$  for models 2, 3 and 4. Results are shown in figure B.7 and compared to the analytical solutions given above. Excellent agreement is found, indicating the correct implementation of local transport coefficients in the EMC3-EIRENE code. Similar tests have been performed for particle transport simulations with the same result.


 Figure B.6: Test models for the energy cross-field transport coefficient  $\chi_{\perp}$ .

 Figure B.7: Radial profiles of  $T_e$  for different  $\chi_{\perp}$  models, obtained with the EMC3-EIRENE code (symbols) and from analytic integration of the transport equation (B.22).





## C Visualization of the magnetic field and plasma structures in the TEXTOR helical divertor

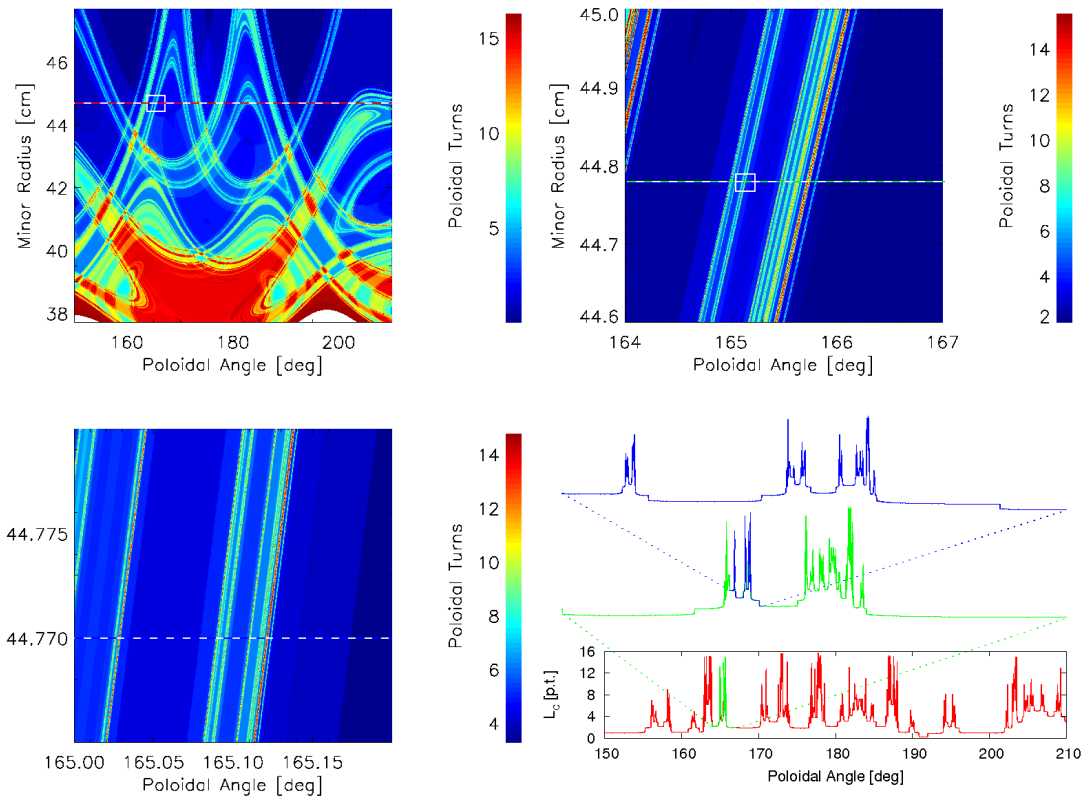


Figure C.1: Demonstration of the fractal structure of the magnetic field in the poloidal plane at  $\varphi = 0$  deg. The connection length of field lines is given in poloidal turns. White boxes indicate the subsequent zoom regions. The position of the poloidal profiles is marked by dashed lines in the respective color.

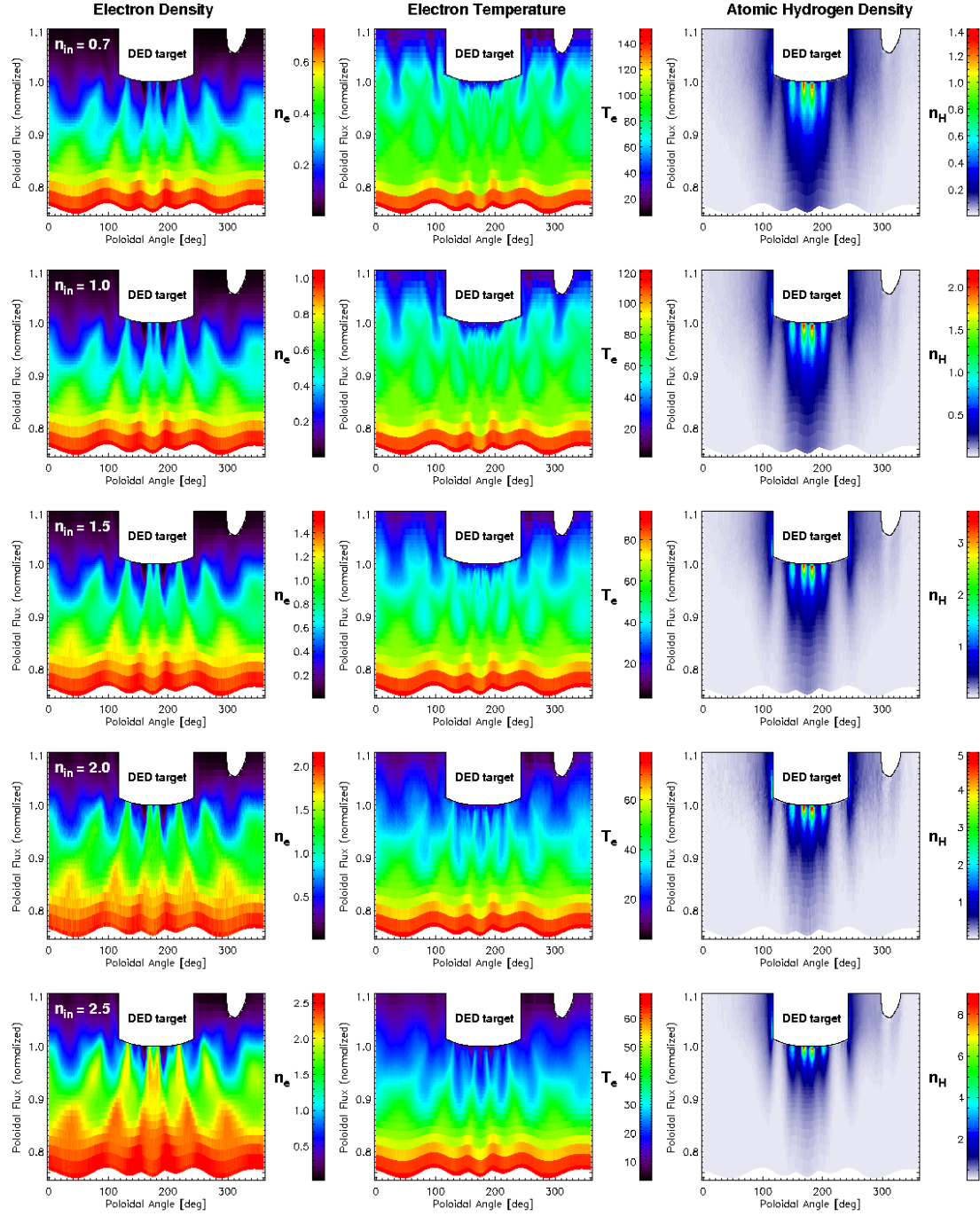


Figure C.2: 2D cuts at  $\varphi = 0$  deg of the electron density  $n_e [10^{19} \text{ m}^{-3}]$ , electron temperature  $T_e [\text{eV}]$  and atomic hydrogen density  $n_H [10^{17} \text{ m}^{-3}]$  for separatrix densities  $n_{in} = 0.7 \cdot 10^{19} \text{ m}^{-3}$  to  $n_{in} = 2.5 \cdot 10^{19} \text{ m}^{-3}$ . Color bars are adjusted to the respective maximum values.

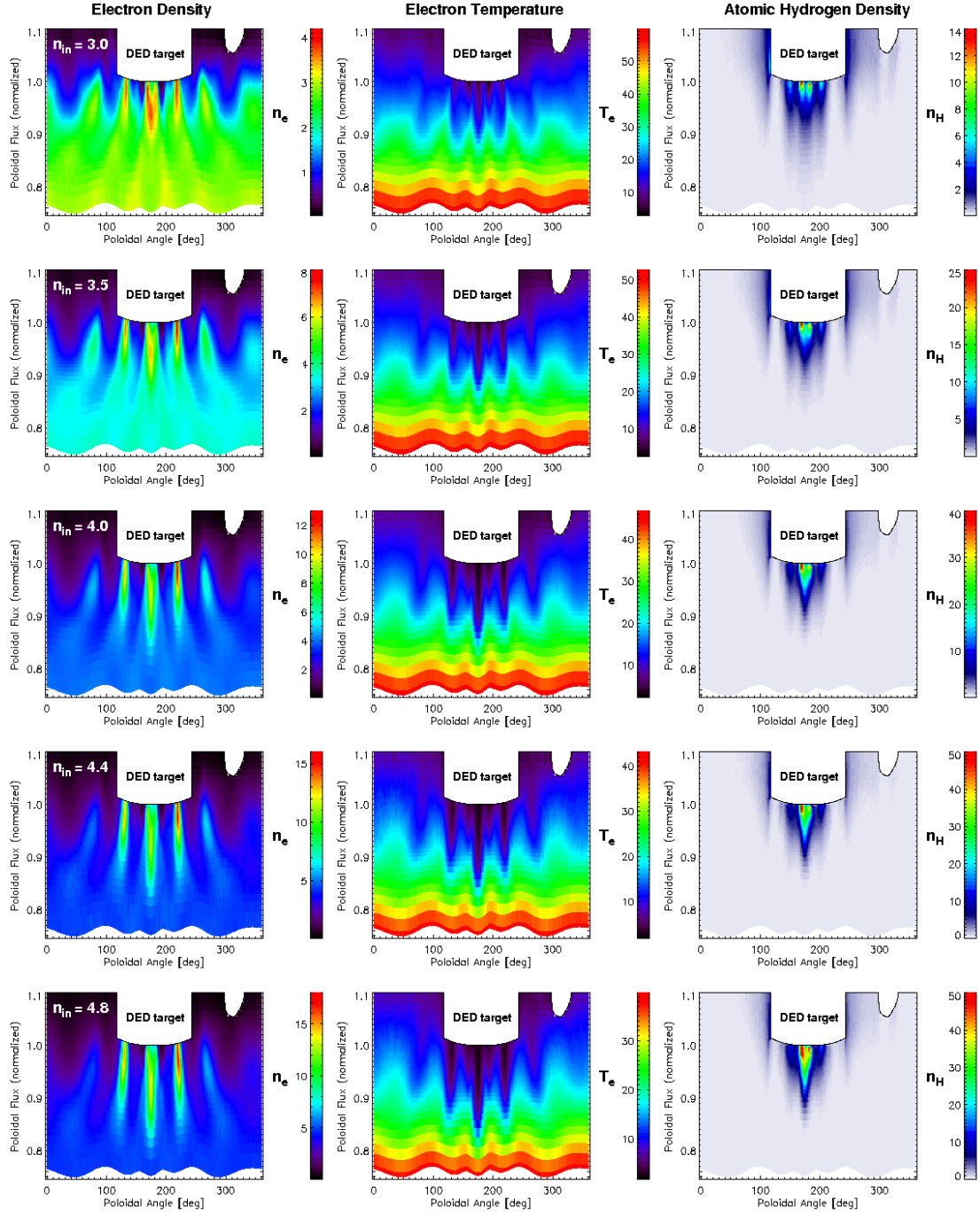


Figure C.3: 2D cuts at  $\varphi = 0$  deg of the electron density  $n_e$  [ $10^{19} \text{ m}^{-3}$ ], electron temperature  $T_e$  [eV] and atomic hydrogen density  $n_H$  [ $10^{17} \text{ m}^{-3}$ ] for separatrix densities  $n_{in} = 3.0 \cdot 10^{19} \text{ m}^{-3}$  to  $n_{in} = 4.8 \cdot 10^{19} \text{ m}^{-3}$ . Color bars are adjusted to the respective maximum values.

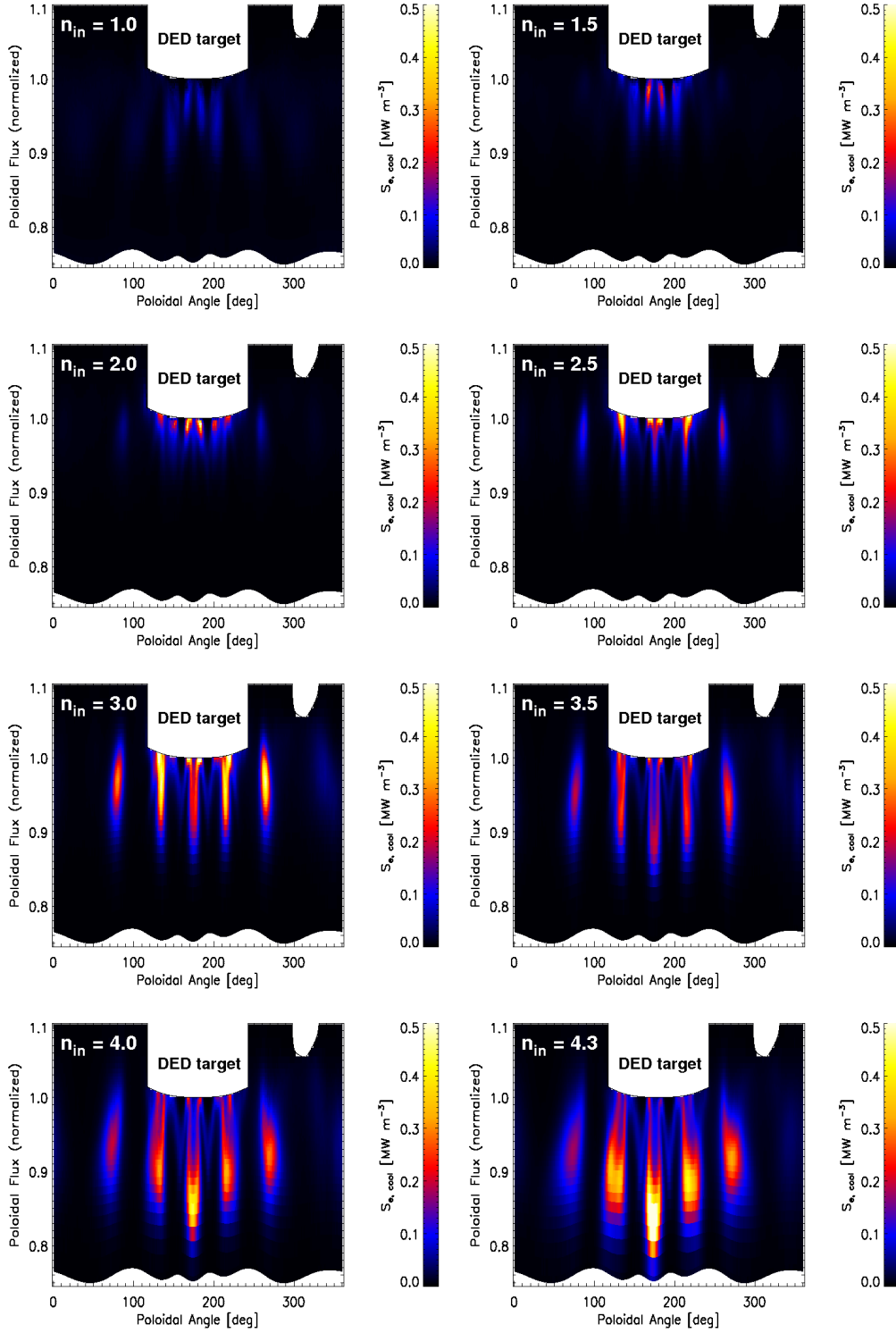


Figure C.4: 2D cuts at  $\varphi = 0$  deg of the electron cooling rate  $\mathcal{S}_{e,\text{cool}}$  due to carbon radiation and ionization. The separatrix density  $n_{\text{in}}$  is given in  $10^{19} \text{ m}^{-3}$ .

## D Impurity transport

The impurity transport option in EMC3 and applications to TEXTOR have been extensively studied in [99]. Here only a brief summary of the main results is given. Impurities are naturally present in fusion devices because of plasma-wall interactions. The intrinsic impurity species in the TEXTOR tokamak is carbon, which is sputtered from the graphite plates at the DED target. The effect of RMPs on production and transport of carbon is analyzed in this section for the same plasma equilibrium used in the previous section, however with an  $m/n = 12/4$  perturbation field. In particular the capability to shield the core plasma from impurities by application of RMPs is of great interest. Indications for this have been found in the experiment [144, 166]. The influence of certain model parameters is investigated here: the boundary condition at the inner simulation boundary (see section 4.3.1), the model for atomic processes (corona or non-corona) and the model for impurity production.

### D.1 Distribution of carbon ions

Before discussing the details of impurity shielding, an overview of the distribution of carbon ions is given in this paragraph. The input parameters for the following simulation are:

$n_{\text{in}}$	$= 1.2 \cdot 10^{19} \text{ m}^{-3}$
$P_{\text{in}}$	$= 600 \text{ kW}$
$D_{\perp}$	$= D_{\perp}^{(\text{carbon})} = 1.4 \text{ m}^2 \text{ s}^{-1}$
$\chi_{\perp}$	$= 4.1 \text{ m}^2 \text{ s}^{-1}$

In particular the same cross-field diffusion coefficient  $D_{\perp}$  is used for hydrogen and carbon ions. 2D cuts of the carbon ion densities  $n_{\text{C}^{Z+}}$ ,  $Z = 1, \dots, 6$  are given in figure D.1. A strong spatial modulation is clearly visible in all carbon densities, which is a result from the modified magnetic field structure due to application of RMPs. The distribution of  $\text{C}^{1+}$ ,  $\text{C}^{2+}$  and  $\text{C}^{3+}$  ions is mainly localized in front of the DED target, with an increasing penetration depth with increasing charge number. This is because in the relevant parameter range for given  $n_e$  and  $T_e$ , ionization rates for carbon ions decrease with increasing charge number (see figure 3.1). The absolute values indicate that carbon is basically present as  $\text{C}^{4+}$ . The clear distinction between ionization rates for  $Z \geq 4$  and  $Z < 4$  (which is related to the atomic structure of the  $\text{C}^{4+}$  ion) is obviously reflected in the density distribution in the present TEXTOR case. Once carbon is ionized to  $\text{C}^{4+}$

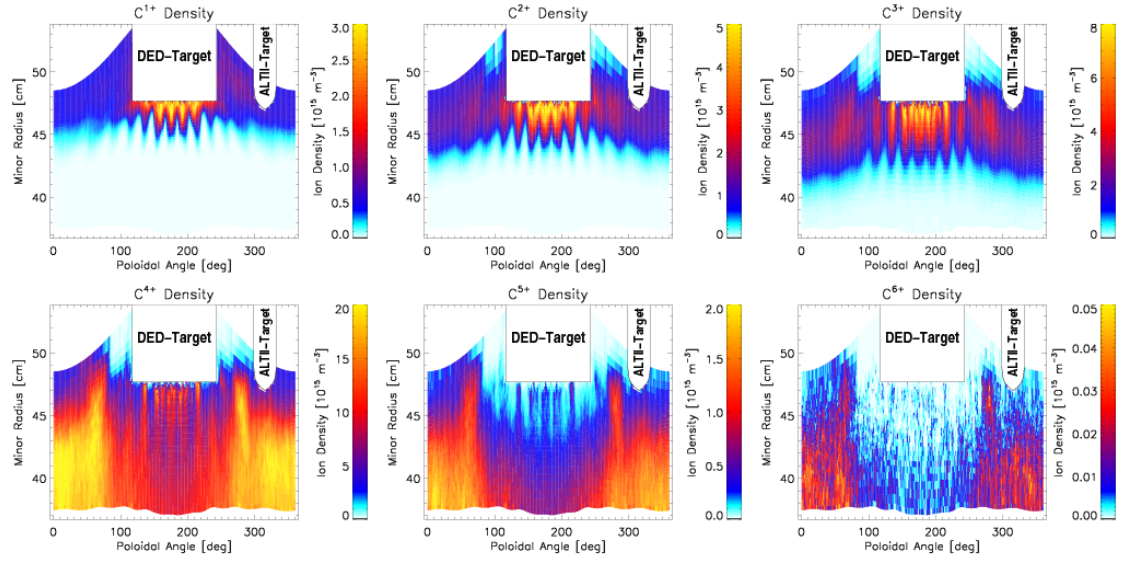


Figure D.1: 2D cuts of carbon densities at  $\varphi = 0$  deg. Color bars are adjusted to the respective peak values in each picture.

further ionization is balanced with recombination so that  $C^{5+}$  and  $C^{6+}$  densities are much smaller than the  $C^{4+}$  density.

As can be seen in figure D.1, carbon ions penetrate into the core plasma up to the inner simulation boundary. To study the effect of RMPs on impurity penetration it is therefore necessary to apply reasonable boundary conditions.

## D.2 Boundary conditions

As already stated in section 4.3.1, no mass accumulation of impurities in the core plasma is assumed for a steady state condition, i.e.

$$\sum_{a=0}^Z \Gamma_{\text{in}}^{(\text{imp},a)} = 0. \quad (\text{D.1})$$

This is implemented as reflection of Monte Carlo fluid parcels at the inner simulation boundary. The charge stage after reflection  $Z_{\text{reflect}}$  is determined by one of the following models:

- **Model ZCFL:** No change of charge stage. This implies zero charge flux of impurity ions into the core plasma.

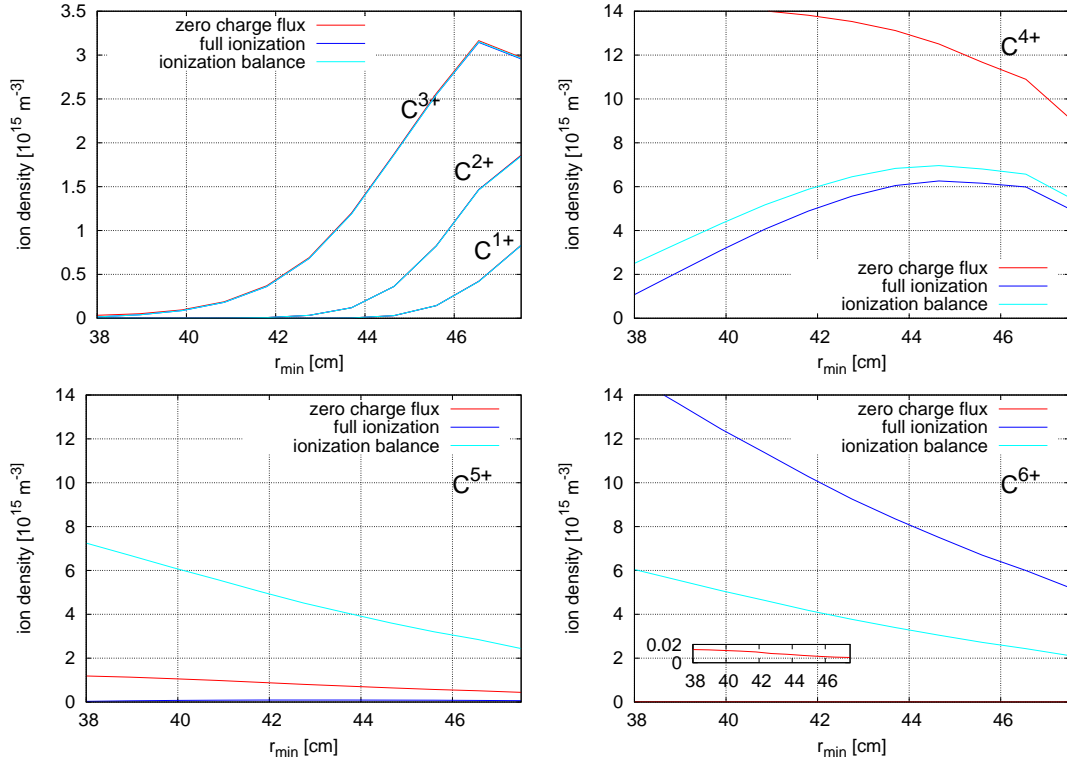


Figure D.2: Radial profiles of carbon densities obtained from simulations with different core-boundary conditions. Profiles are averaged on unperturbed flux surfaces for the given minor radius at the HFS.

- **Model FION:**  $Z_{\text{reflect}} = Z_{\text{max}} (= 6)$ . This corresponds to full ionization of C in the core plasma.
- **Model IBAL:** Simple ionization balance where transport is neglected (see also section 5.1.3 in [99]).  $Z_{\text{reflect}}$  is sampled according to a probability distribution  $p_Z$ , which is obtained from the local balances at the inner simulation boundary

$$n_{C^{Z+1+}} = \frac{R_Z^{(\text{ion})}}{R_{Z+1}^{(\text{rec})}} n_{C^{Z+}} \quad (\text{D.2})$$

by normalization

$$p_Z = \frac{n_{C^{Z+}}}{\sum_{j=0}^{Z_{\text{max}}} n_{C^{j+}}}, \text{ i.e. } \sum_{Z=0}^{Z_{\text{max}}} p_Z = 1. \quad (\text{D.3})$$

The impact of the boundary condition on impurity transport is summarized in figure

D.2 by averaged radial profiles. Obviously, the densities of  $C^{1+}$ ,  $C^{2+}$  and  $C^{3+}$  are not affected by the choice of boundary condition. Values at the DED target are:

Boundary condition	$n_{C^{1+}}^{(\text{target})} [10^{15} \text{ m}^{-3}]$	$n_{C^{2+}}^{(\text{target})} [10^{15} \text{ m}^{-3}]$	$n_{C^{3+}}^{(\text{target})} [10^{15} \text{ m}^{-3}]$
ZCFL	0.834	1.860	2.974
FION	0.830	1.852	2.956
IBAL	0.831	1.848	2.964

The deviations are smaller than 1% and well within the noise level of the Monte Carlo procedure (see section 4.3.4). This robustness against the choice of boundary condition results because these low charge stage ions do not reach the inner simulation boundary at all. Also the impact of recombination from higher charge stages is weak, because the recombination times are (under TEXTOR conditions) much larger than the average life time of impurity ions in the plasma. However, it can be seen that for  $C^{4+}$ ,  $C^{5+}$  and  $C^{6+}$  the choice of boundary condition is essential. The dominant ion species in simulations with the ZCFL boundary condition is  $C^{4+}$  (red curves in figure D.2), which has already been found in figure D.1. This is because further ionization is suppressed, because of low ionization rates. However, further ionization can occur in the much hotter core plasma, and therefore the charge distribution of impurity ions leaving the core plasma is expected to be shifted towards higher charge stages.

The application of the FION boundary condition leads to a completely different distribution of high charge stage ions. Now  $C^{6+}$  is the dominant ion species, with a density maximum at the inner simulation boundary (ISB). Densities of  $C^{4+}$ ,  $C^{5+}$  and  $C^{6+}$  ions at the ISB are summarized in the following table for all three boundary conditions:

Boundary condition	$n_{C^{4+}}^{(\text{ISB})} [10^{15} \text{ m}^{-3}]$	$n_{C^{5+}}^{(\text{ISB})} [10^{15} \text{ m}^{-3}]$	$n_{C^{6+}}^{(\text{ISB})} [10^{15} \text{ m}^{-3}]$
ZCFL	14.26	1.19	0.01
FION	1.08	0.03	14.78
IBAL	2.50	7.25	6.04

However, the FION boundary condition might overestimate the effect of impurity ionization in the core plasma. Temperatures in the intermediate region between the very deep core and the edge may not be high enough for full ionization of carbon ions. Consequently, a third type of boundary condition is introduced: the local ionization balance (IBAL). The charge distribution is obtained from the balance (D.2) with normalization (D.3), evaluated for densities and temperatures at the inner simulation boundary. For  $n_e \approx 1.2 \cdot 10^{19} \text{ m}^{-3}$  and  $T_e \approx 100 \text{ eV}$  the relative distribution of  $C^{4+}:C^{5+}:C^{6+}$  is about 10 : 50 : 40, where the contribution of low charge stages can be neglected (see figure 3.16 in [7]). The self consistent ratio of densities at the inner simulation boundary (see table above), however, is shifted to lower charge stages (about 16 : 46 : 38), because this balance is influenced by transport processes in the edge plasma. This boundary condition can be improved by using some average values for  $n_e$  and  $T_e$  in the core plasma, but some uncertainty in the charge distribution still remains. Hence, comparisons to experimental observation of high charge stage ions are impossible without a realistic boundary condition. This might be obtained in the future by a coupling of the 3D edge



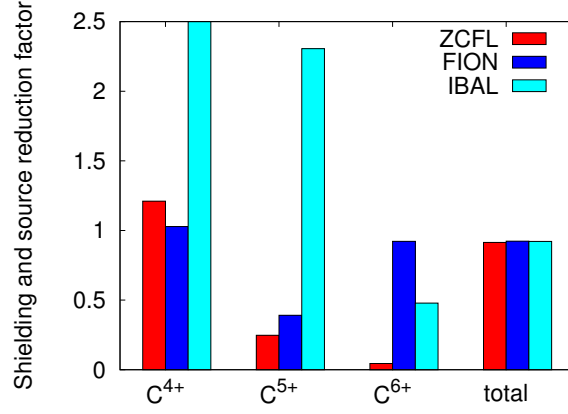


Figure D.3: Impact of the boundary condition on the shielding and source reduction factors  $f_{\text{RMP}}$ , evaluated separately for  $\text{C}^{4+}$  to  $\text{C}^{6+}$  and for the total impurity density according to (D.5).

transport code EMC3-EIRENE to some 1D core transport model for impurities, e.g. the STRAHL code [102, 167].

Nevertheless, core contamination by impurities can be investigated numerically by means of the total impurity density at the ISB:

$$n_{\text{imp}} = \sum_{i=1}^6 n_{\text{C}^{i+}}^{(\text{ISB})}, \quad (\text{D.4})$$

This is because, within the trace impurity model used, there is no significant change in the underlying transport characteristics between high charge state ions. Therefore  $n_{\text{imp}}$  remains robust against the choice of boundary condition:

Boundary condition	$n_{\text{imp}} [10^{15} \text{ m}^{-3}]$
ZCFL	15.46
FION	15.89
IBAL	15.79

and can be used as a parameter to study core contamination.

The RMP effect on core contamination can now be investigated under the assumption that transport within the core plasma is not affected by RMPs. The shielding and source reduction factor

$$f_{\text{RMP}} = \frac{n_{\text{imp}}^{(\text{RMP})}}{n_{\text{imp}}^{(0)}}, \quad (\text{D.5})$$

is defined as the ratio between impurity densities at the ISB with and without RMP field. As the radial profiles in figure (D.2) already suggest,  $f_{\text{RMP}}^{(Z)}$  evaluated for each charge stage  $Z$  depends significantly on the boundary condition. This is demonstrated in figure D.3. Depending on the boundary condition  $n_{\text{C}^{4+}}^{(\text{ISB})}$  is either not reduced at all (FION) or even increased by a factor of 3.2 (IBAL).  $n_{\text{C}^{6+}}^{(\text{ISB})}$  is reduced in any case, but resulting in  $f_{\text{RMP}}^{(6)} = 0.04$  (ZCFL) or  $f_{\text{RMP}}^{(6)} = 0.92$  (FION). However, (D.5) provides a robust parameter with respect to the boundary condition:  $f_{\text{RMP}} \approx 0.92$  in all cases. Hence, this parameter is used for the following analysis.

The change in core contamination can be caused by two effects, a change in impurity source and transport (= shielding). To separate one from the other,  $n_{\text{imp}}$  is normalized to the respective total impurity source strength  $S_{\text{imp}}$ , so that a separate transport factor  $f_{\text{shield}}$  and a source factor can be defined:

$$f_{\text{shield}} = \frac{n_{\text{imp}}^{(\text{RMP})}/S_{\text{imp}}^{(\text{RMP})}}{n_{\text{imp}}^{(0)}/S_{\text{imp}}^{(0)}}, \quad f_{\text{src}} = \frac{S_{\text{imp}}^{(\text{RMP})}}{S_{\text{imp}}^{(0)}}. \quad (\text{D.6})$$

Now  $f_{\text{RMP}}$  can be split into the respective contributions from source and transport effects:

$$f_{\text{RMP}} = f_{\text{src}} \cdot f_{\text{shield}}. \quad (\text{D.7})$$

Impurity sources are obtained from the hydrogen recycling flux (see next section for a detailed discussion of the impurity source model) and increase by 14 % due to application of the RMP field. This yield the source factor  $f_{\text{src}} = 1.14$  and consequently the transport factor  $f_{\text{shield}} = 0.81$ . The transport effects are caused by main plasma flow in front of the DED target (see figure 6.2<sup>1</sup>), which can push impurity ions back to the DED target due to friction forces. The fractions  $F_{\text{RMP}}$ ,  $F_{\text{w/o RMP}}$  of impurity ions within such a downstream region (i.e. where the Mach number  $|M| \geq 0.2$ ) are given in the following table:

Ion type	$F_{\text{w/o RMP}}$	$F_{\text{RMP}}$
C <sup>1+</sup>	47 %	64 %
C <sup>2+</sup>	38 %	52 %
C <sup>3+</sup>	27 %	36 %
C <sup>4+</sup>	8 %	12 %

Clearly, a larger fraction of impurity ions is pushed back to the DED target in the RMP scenario, leading to a reduction of core contamination of  $f_{\text{shield}} = 0.81$ . This transport effect compensates the effect of increased impurity sources and results in an overall RMP effect of  $f_{\text{shield}} = 0.92$ .

---

<sup>1</sup> Although this figure is for a  $m/n = 6/2$  configuration, a similar flow field is present in the  $m/n = 12/4$  configuration as well.

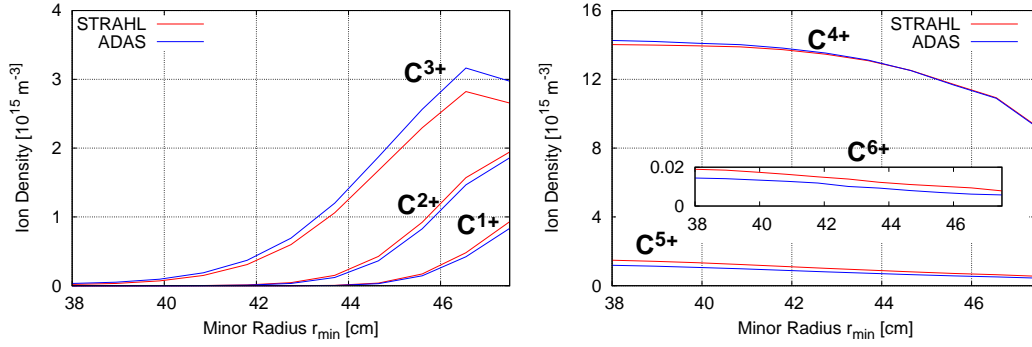


Figure D.4: Impact of the model for atomic processes on averaged radial density profiles in the presence of an  $m/n = 12/4$  RMP field.

### D.3 Reaction Rates

Reaction rates for ionization, recombination and radiation have been updated from a simple corona model taken from the STRAHL [102] code to an advanced collisional radiative model (ADAS) [103]. The impact of the model for atomic processes on averaged radial density profiles is displayed in figure D.4 for the  $m/n = 12/4$  RMP scenario. Here the ZCFL boundary condition has been used to study the differences obtained from the STRAHL model to the ADAS model. The latter has also been used in the previous section. Ionization from excited states is included in the ADAS model, which leads to higher ionization rates of low charge stage ions (see chapter 2 in [99] for a detailed discussion of the models). Consequently,  $n_{C1+}$  and  $n_{C2+}$  obtained with the ADAS model are lower than the respective densities obtained with the STRAHL model, while  $n_{C3+}$  and  $n_{C4+}$  are larger. The densities in front of the DED target are summarized below for  $C1+$ ,  $C2+$  and  $C3+$  ions:

Model	$n_{C1+}^{(\text{target})} [10^{15} \text{ m}^{-3}]$	$n_{C2+}^{(\text{target})} [10^{15} \text{ m}^{-3}]$	$n_{C3+}^{(\text{target})} [10^{15} \text{ m}^{-3}]$
STRAHL	0.93	1.94	2.66
ADAS	0.83 (−10 %)	1.86 (−4 %)	2.97 (+12 %)

The ADAS model also includes three-body recombination, which leads to higher recombination rates for high charge stage ions. Consequently,  $n_{C5+}$  and  $n_{C6+}$  obtained with the ADAS model are lower than the respective densities obtained with the STRAHL model. The densities at the ISB are summarized below for  $C4+$ ,  $C5+$  and  $C6+$  ions:

Model	$n_{C4+}^{(\text{target})} [10^{15} \text{ m}^{-3}]$	$n_{C5+}^{(\text{target})} [10^{15} \text{ m}^{-3}]$	$n_{C6+}^{(\text{target})} [10^{15} \text{ m}^{-3}]$
STRAHL	14.02	1.48	0.019
ADAS	14.26 (+2 %)	1.19 (−20 %)	0.014 (−24 %)

Nevertheless, the total impurity density at the ISB remains essentially unchanged at  $n_{\text{imp}}^{(\text{RMP})} = 15.5 [10^{15} \text{ m}^{-3}]$ . Also  $n_{\text{imp}}^{(0)} = 16.9 [10^{15} \text{ m}^{-3}]$  remains unchanged, resulting in

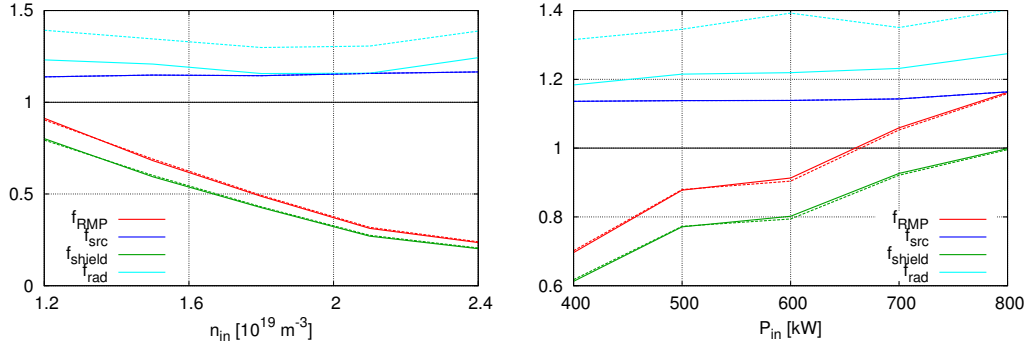


Figure D.5: Scan of the control parameters  $n_{\text{in}}$  and  $P_{\text{in}}$  for the RMP factor  $f_{\text{RMP}}$  (red), its parts due to change in sources  $f_{\text{src}}$  (blue) and transport  $f_{\text{shield}}$  (green) and the fraction of the radiated power  $f_{\text{rad}}$  (light blue). Left: scan of  $n_{\text{in}}$  at constant  $P_{\text{in}} = 600 \text{ kW}$ , right: scan of  $P_{\text{in}}$  at constant  $n_{\text{in}} = 1.2 \cdot 10^{19} \text{ m}^{-3}$ .

the same RMP effect  $f_{\text{RMP}}$  for both models.

However, the radiated power is quite sensitive to the applied model for atomic processes, in particular the integrated radiated power by  $\text{C}^{2+}$  ions  $P_{\text{rad},2}$ . Often specific line emissions, e.g. from the so called CIII-line ( $\lambda = 465.0 \text{ nm}$  by  $\text{C}^{2+}$ ), are used in the experiment to deduce the impurity source strength. As using the condensed the STRAHL data does not allow to resolve this line, the complete emission by  $\text{C}^{2+}$  ions is used in the following for a comparison between the two models. In analogy to (D.5) the radiated power ratio is defined by

$$f_{\text{rad}} = \frac{P_{\text{rad},2}^{(\text{RMP})}}{P_{\text{rad},2}^{(0)}}. \quad (\text{D.8})$$

## D.4 Parameter studies of separatrix density and input power

A scan of the control parameters  $n_{\text{in}}$  and  $P_{\text{in}}$  shows a reduction in core contamination with RMPs for high  $n_{\text{in}}$  and low  $P_{\text{in}}$  (see figure D.5). This reduction is basically caused by a change in transport ( $f_{\text{shield}}$ , green curves), while the ratio of sources remains roughly unchanged at  $f_{\text{src}} = 1.14 - 1.16$  (blue curves). Reducing  $P_{\text{in}}$  to 400 kW results in a stronger shielding effect, which is reflected in a reduction of  $f_{\text{RMP}}$  to 0.70. Increasing  $P_{\text{in}}$  to 800 kW on the other hand, results in a weaker shielding effect which cannot compensate the increase in impurity sources. This reflects in an increase of  $f_{\text{RMP}}$  to 1.16. The cause for this  $P_{\text{in}}$  dependence is that with  $P_{\text{in}}$  also  $T_i$  increases, which leads to a reduction of friction forces ( $F_{\text{fr}} \sim n_i T_i^{-3/2}$ , compare (3.27) and (3.26)) and consequently a reduction of the drag on impurity ions.

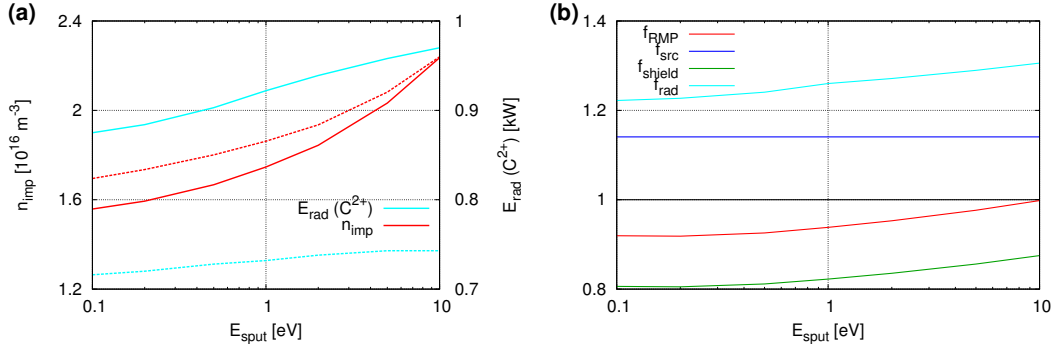


Figure D.6: Left: Dependence of  $n_{\text{imp}}$  (red) and  $E_{\text{rad}}$  (light blue) on the energy of sputtered particles  $E_{\text{sput}}$  with RMP field (solid lines) and without (dashed lines). Right: Related RMP effect factors  $f_{\text{rad}}$  and  $f_{\text{RMP}}$  and its contributions  $f_{\text{src}}$ ,  $f_{\text{shield}}$ . Input parameters are  $n_{\text{in}} = 1.2 \cdot 10^{19} \text{ m}^{-3}$  and  $P_{\text{in}} = 600 \text{ kW}$ .

Furthermore, increasing  $n_{\text{in}}$  to  $2.4 \cdot 10^{19} \text{ m}^{-3}$  causes an even stronger shielding effect which is reflected in a reduction of  $f_{\text{RMP}}$  to 0.24. This effect originates from an amplification of frictional forces: On the one hand  $F_{\text{fr}}$  linearly increases with  $n_i$ , and on the other hand  $T_i$  decreases with  $n_{\text{in}}$  (at constant  $P_{\text{in}}$ ) which leads to an additional increase of  $F_{\text{fr}}$ . In conclusion, effective shielding (incl. source effects) of the core plasma from impurities ( $f_{\text{RMP}} < 1$ ) can be observed numerically for a wide range of values of the control parameters, except for high  $P_{\text{in}}$  at low  $n_{\text{in}}$ . This prediction is robust with respect to the model for atomic processes, as can be deduced from figure D.5 by comparing the solid (ADAS) and dashed (STRAHL) lines. Experimentally, a weak impurity screening is observed in the 12/4 configuration. This is consistent with the presented numerical results for typical values of  $n_{\text{in}} = 1.2 \cdot 10^{19} \text{ m}^{-3}$  and  $P_{\text{in}} = 600 \text{ kW}$ . A more pronounced screening effect is observed in the 6/2 configuration [166]. If this is reflected in the simulations as well remains to be investigated in the future.

## D.5 Impurity sources

The source strength for impurities in the original EMC3 model is given by a constant sputter yield  $Y$  of the hydrogen influx on target  $\Gamma_{\text{target}}$ :

$$S_{\text{imp}} = Y \cdot \Gamma_{\text{target}}. \quad (\text{D.9})$$

Sputtered impurity particles have a  $\delta$ -distributed energy of  $E_{\text{sput}}$  (see section 4.2.2 in [99] for numerical details of impurity production and transport). Source effects of the shielding factor are, as a consequence of (D.9), determined by the main plasma alone (compare (D.6):

$$f_{\text{src}} = \frac{\Gamma_{\text{target}}^{(\text{RMP})}}{\Gamma_{\text{target}}^{(0)}}. \quad (\text{D.10})$$

The parameter  $E_{\text{sput}}$  on the other hand does not affect  $f_{\text{src}}$  at all. It only affects the penetration depth of impurities and, related to that,  $f_{\text{shield}}$ . As can be seen in figure D.6.a, a parameter scan of  $E_{\text{sput}}$  reveals that  $n_{\text{imp}}$  increases for higher  $E_{\text{sput}}$ . This is because of a deeper penetration of impurities with increasing  $E_{\text{sput}}$ . In addition figure D.6.a reveals that this effect is stronger in the RMP scenario, which results in a weaker shielding (red curve in figure D.6.b). At a fictitious value of  $E_{\text{sput}} = 10\text{eV}$  transport effects would just compensate the source effects with no overall RMP effect ( $f_{\text{RMP}} = 1$ ).

The shielding of low energy particles (typical from chemical sputtering) is more efficient than shielding of high energy particles (typical from physical sputtering). This is because of the localized downstream region in front of the target which fast particles can penetrate. The next step would be to analyze the impact of realistic sputter models, such as a Thompson distribution of  $E_{\text{sput}}$  for physical sputtering with a sputter yield given by the Bohdanský formula [168], or its revised version including an angular dependence [169]. This has been preliminary analyzed in [99] and confirms the above tendencies.

## E Trilinear hexahedral elements and their application in toroidal configurations

The particular field line reconstruction method presented in section 4.2 introduces hexahedral grid cells that are curved in Cartesian coordinates but straight in cylindrical coordinates. Following the isoparametric concept, which is commonly used in finite element methods, these hexahedral cells can be used for a continuous description of some data  $F_i$  defined on the grid nodes  $i = 1, \dots, n_{\text{nodes}}$  (section E.2), e.g. the magnetic field  $\mathbf{B}$ . Such a continuous description is e.g. necessary for a kinetic treatment of ions in the trace ion module (TIM), which is currently being implemented and verified in the EIRENE code [170]. Another application is the visualization or post-processing of plasma data. This method has e.g. been applied for the generation of figures 6.7 and 5.9. At the end of this chapter (section E.4) an additional application is presented: the evaluation of line of sight integrals, e.g. for the simulation of camera pictures.

The formulation the special kind of hexahedral element (i.e. curved element with planar end-faces in the  $R - Z$  plane, see figures 4.3 and 4.4) involves three different coordinate systems. The following notation is used for coordinates:

$$\begin{aligned} \mathbf{x} &\equiv (x, y, z) && : \text{Cartesian coordinates} \\ \mathbf{R} &\equiv (R, Z, \varphi) && : \text{cylindrical coordinates} \\ \boldsymbol{\xi} &\equiv (\xi, \eta, \zeta) && : \text{natural coordinates} \end{aligned}$$

The advantage of the special kind of hexahedral element presented here is that curvilinear coordinate lines allow an accurate representation of magnetic field lines while planar end-faces allow an algebraic formulation of the inverse of the coordinate mapping. For bilinear quadrilaterals (see figure E.1) it is well-known that the coordinate mapping (E.1-E.2) is invertible if and only if the Jacobian at the four corners is positive. However, in [115] it is shown that the condition of a positive Jacobian at the 8 corners is not sufficient to guarantee invertability. No algebraic expression is known so far and one has to resort to alternative tests, e.g. an algorithmic method is presented in [171] to check for the local positivity of the Jacobian. In [172] an infinite power series is derived for the inverse mapping, which is based on the theory of geodesics in differential geometry. However, due to the planar end-faces of the special hexahedron discussed here, the issue of invertability is reduced to that of a bilinear quadrilateral and an algebraic expression can be given for the inverse mapping. Therefore this chapter starts with an overview on bilinear quadrilaterals before turning to trilinear hexahedra.

## E.1 Bilinear quadrilateral

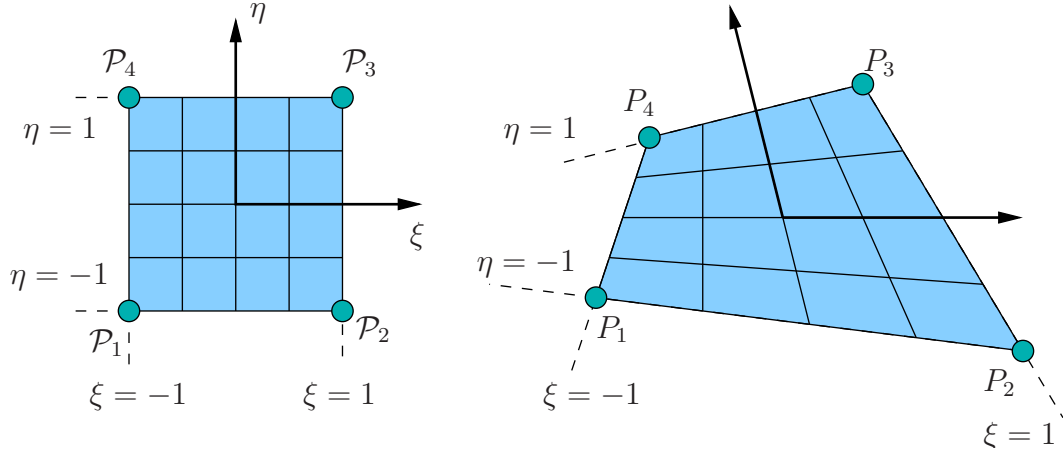


Figure E.1: Bilinear quadrilateral in its reference plane (left) and in the real plane (right)

The bilinear quadrilateral (Q4) is defined by assuming a bilinear expansion of  $x, y$  in the natural coordinates  $\xi, \eta$ :

$$x(\xi, \eta) = \alpha_0 + \alpha_1 \xi + \alpha_2 \eta + \alpha_3 \xi \eta \quad (\text{E.1})$$

$$y(\xi, \eta) = \beta_0 + \beta_1 \xi + \beta_2 \eta + \beta_3 \xi \eta. \quad (\text{E.2})$$

The parameters  $\alpha_i$  and  $\beta_i, i = 1 \dots 4$  are determined by the four nodes  $(x_i, y_i)$  and the corresponding natural coordinates  $(\xi_i, \eta_i)$ :

$$x(\xi_i, \eta_i) = x_i, \quad y(\xi_i, \eta_i) = y_i. \quad (\text{E.3})$$

A different representation of  $x(\xi, \eta)$  and  $y(\xi, \eta)$  is obtained by the use of shape functions  $N_i(\xi, \eta)$  which are commonly used in finite element methods (for an introduction to isoparametric elements and shape functions see [108, chap. 3], [109, chap. 16-18]):

$$x(\xi, \eta) = \sum_{i=1}^4 N_i(\xi, \eta) x_i, \quad y(\xi, \eta) = \sum_{i=1}^4 N_i(\xi, \eta) y_i \quad (\text{E.4})$$

$$N_i(\xi, \eta) = \frac{1}{4} (1 + \xi_i \xi) (1 + \eta_i \eta) \quad (\text{E.5})$$

For the bilinear quadrilateral considered here,  $\xi_i$  and  $\eta_i$  are defined in figure E.1 and in the table below:



$i$	1	2	3	4
$\xi_i$	-1	1	1	-1
$\eta_i$	-1	-1	1	1

The inverse transformation  $\xi = \xi(x, y)$ ,  $\eta = \eta(x, y)$  exists and is unique for convex quadrilaterals [115]. A stable numerical algorithm to calculate the natural coordinates  $\xi_P, \eta_P$  for a given point  $x_P, y_P$  is presented in [109, chap. 23]:

$$\begin{aligned}
 x_b &= x_1 - x_2 + x_3 - x_4, & y_b &= y_1 - y_2 + y_3 - y_4, & x_{cx} &= x_1 + x_2 - x_3 - x_4, & y_{cx} &= y_1 + y_2 - y_3 - y_4, \\
 x_{ce} &= x_1 - x_2 - x_3 + x_4, & y_{ce} &= y_1 - y_2 - y_3 + y_4, & x_0 &= \frac{1}{4} \sum_{i=1}^4 x_i, & y_0 &= \frac{1}{4} \sum_{i=1}^4 y_i, \\
 A &= \frac{1}{2} ((x_3 - x_1)(y_4 - y_2) - (x_4 - x_2)(y_3 - y_1)), & x_{P0} &= x_P - x_0, & y_{P0} &= y_P - y_0, \\
 J_1 &= (x_3 - x_4)(y_1 - y_2) - (x_1 - x_2)(y_3 - y_4), & J_2 &= (x_2 - x_3)(y_1 - y_4) - (x_1 - x_4)(y_2 - y_3), \\
 b_\xi &= A - x_{P0}y_b + y_{P0}x_b, & b_\eta &= -A - x_{P0}y_b + y_{P0}x_b, & c_\xi &= x_{P0}y_{cx} - y_{P0}x_{cx}, & c_\eta &= x_{P0}y_{ce} - y_{P0}x_{ce}, \\
 \xi_P &= \frac{2c_\xi}{-\sqrt{b_\xi^2 - 2J_1c_\xi - b_\xi}}, & \eta_P &= \frac{2c_\eta}{\sqrt{b_\eta^2 + 2J_2c_\eta - b_\eta}}
 \end{aligned} \tag{E.6}$$

Following the isoparametric concept, data values  $F_i$  given at the node positions  $P_i$  can be interpolated smoothly into the interior in analogy to E.4:

$$F(\xi_p, \eta_p) = \sum_{i=1}^4 N_i(\xi_p, \eta_p) F_i. \tag{E.7}$$

This can be used to obtain an interpolated value of  $F$  at  $(x_P, y_P)$  by applying (E.6) for the natural coordinates  $(\xi_p, \chi_p)$ .

## E.2 Trilinear, cylindrical hexahedra

In three dimensions an 8-point hexahedral element with straight edges is defined by the trilinear expansion

$$\mathbf{x} = \boldsymbol{\alpha}_0 + \xi \boldsymbol{\alpha}_1 + \eta \boldsymbol{\alpha}_2 + \zeta \boldsymbol{\alpha}_3 + \xi \eta \boldsymbol{\alpha}_4 + \eta \zeta \boldsymbol{\alpha}_5 + \xi \zeta \boldsymbol{\alpha}_6 + \xi \eta \zeta \boldsymbol{\alpha}_7, \tag{E.8}$$

where the vectorial coefficients  $\boldsymbol{\alpha}_0, \dots, \boldsymbol{\alpha}_7$  are determined by the conditions

$$\mathbf{x}(\boldsymbol{\xi}_a) = \mathbf{x}_a, \quad a = 1, \dots, 8 \tag{E.9}$$

at the 8 nodes  $\mathbf{x}_a$ . For reasons to become clear later, the coordinate  $\zeta$  is chosen to be in  $[0, 1]$ , while the coordinates  $\xi, \eta \in [-1, 1]$  in analogy to the bilinear quadrilateral. This leads to the following definition of node coordinates  $\xi_a, \eta_a, \zeta_a$  (see also figure E.2):

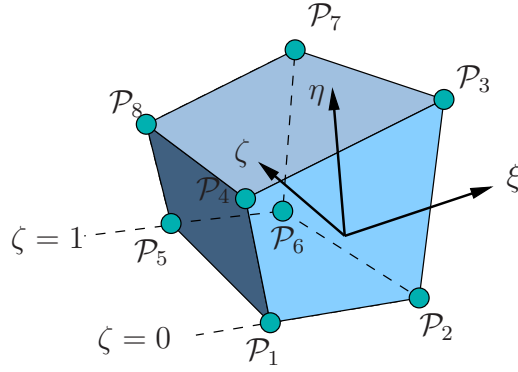


Figure E.2: Node setup in a trilinear hexahedron.

a	1	2	3	4	5	6	7	8
$\xi_a$	-1	1	1	-1	-1	1	1	-1
$\eta_a$	-1	-1	1	1	-1	-1	1	1
$\zeta_a$	0	0	0	0	1	1	1	1

and consequently for the vectorial coefficients  $\alpha_0, \dots, \alpha_7$  in (E.8):

$$\begin{aligned}
 \alpha_0 &= 1/4 (\mathbf{x}_1 + \mathbf{x}_2 + \mathbf{x}_3 + \mathbf{x}_4) \\
 \alpha_1 &= 1/4 (-\mathbf{x}_1 - \mathbf{x}_2 + \mathbf{x}_3 + \mathbf{x}_4) \\
 \alpha_2 &= 1/4 (-\mathbf{x}_1 + \mathbf{x}_2 + \mathbf{x}_3 - \mathbf{x}_4) \\
 \alpha_3 &= 1/4 ((\mathbf{x}_5 - \mathbf{x}_1) + (\mathbf{x}_6 - \mathbf{x}_2) + (\mathbf{x}_7 - \mathbf{x}_3) + (\mathbf{x}_8 - \mathbf{x}_4)) \\
 \alpha_4 &= 1/4 (\mathbf{x}_1 - \mathbf{x}_2 + \mathbf{x}_3 - \mathbf{x}_4) \\
 \alpha_5 &= 1/4 ((\mathbf{x}_6 - \mathbf{x}_2) - (\mathbf{x}_5 - \mathbf{x}_1) + (\mathbf{x}_7 - \mathbf{x}_3) - (\mathbf{x}_8 - \mathbf{x}_4)) \\
 \alpha_6 &= 1/4 ((\mathbf{x}_8 - \mathbf{x}_4) - (\mathbf{x}_5 - \mathbf{x}_1) + (\mathbf{x}_7 - \mathbf{x}_3) - (\mathbf{x}_6 - \mathbf{x}_2)) \\
 \alpha_7 &= 1/4 ((\mathbf{x}_5 - \mathbf{x}_1) - (\mathbf{x}_6 - \mathbf{x}_2) + (\mathbf{x}_7 - \mathbf{x}_3) - (\mathbf{x}_8 - \mathbf{x}_4)) \quad (\text{E.10})
 \end{aligned}$$

Now it is again convenient to write (E.8) with (E.10) by introducing shape functions:

$$\mathbf{x}(\boldsymbol{\xi}) = \sum_{a=1}^8 N_a(\boldsymbol{\xi}) \mathbf{x}_a \quad (\text{E.11})$$

$$N_a(\boldsymbol{\xi}) = \frac{1}{4} (1 + \xi_a \xi) (1 + \eta_a \eta) \frac{1}{2} (1 + (2\zeta_a - 1)(2\zeta - 1)) \quad (\text{E.12})$$

$$\equiv N_i^{Q4}(\xi, \eta) \cdot N_j^{L2}(\zeta), \quad a = i + 4j, \quad i = 1, 2, 3, 4, \quad j = 0, 1 \quad (\text{E.13})$$

where  $N_i^{Q4}$  are the shape functions of the bilinear quadrilateral in (E.5) and  $N_j^{L2}$  are the shape function of a linear element:

$$N_0^{L_2}(\zeta) = 1 - \zeta, \quad N_1^{L_2}(\zeta) = \zeta. \quad (\text{E.14})$$

So far, the edges of the hexahedral element given by (E.11) are straight and not curved. Curvature can be introduced by going to a higher polynomial expansion by introducing additional points on the edges. This procedure leads to 20-node (serendipity) or 27-node hexahedral elements (see e.g. [110, chap. 18]).

A different approach to obtain a special class of curved elements is the here presented *cylindrical hexahedral* element. The trilinear mapping (E.11) between Cartesian and natural coordinates is replaced by the same kind of mapping, but now between cylindrical and natural coordinates:

$$\mathbf{R}(\boldsymbol{\xi}) = \sum_{a=1}^8 N_a(\boldsymbol{\xi}) \mathbf{R}_a \quad (\text{E.15})$$

with the same shape functions  $N_a(\boldsymbol{\xi})$  from (E.12). A special version of this cylindrical hexahedron is considered in the following, namely one in which the end-faces are planar, i.e.

$$\varphi_1 = \varphi_2 = \varphi_3 = \varphi_4 \equiv \varphi_A, \quad \varphi_5 = \varphi_6 = \varphi_7 = \varphi_8 \equiv \varphi_B. \quad (\text{E.16})$$

This condition simplifies the  $\varphi$ -component of (E.10) to

$$\begin{aligned} \alpha_{\varphi 0} &= \varphi_A \\ \alpha_{\varphi 1} &= \alpha_{\varphi 2} = \alpha_{\varphi 4} = \alpha_{\varphi 5} = \alpha_{\varphi 6} = \alpha_{\varphi 7} = 0, \\ \alpha_{\varphi 3} &= \varphi_B - \varphi_A, \end{aligned} \quad (\text{E.17})$$

thus reducing the  $\varphi$ -component of (E.15) to

$$\varphi(\boldsymbol{\xi}) = \varphi_A + \zeta(\varphi_B - \varphi_A) = \varphi(\zeta). \quad (\text{E.18})$$

Using (E.13), the other two components of (E.15) can be written in the following form:

$$\begin{pmatrix} R(\boldsymbol{\xi}) \\ Z(\boldsymbol{\xi}) \end{pmatrix} = \sum_{i=1}^4 N_i^{Q_4}(\xi, \eta) \left[ N_0^{L_2}(\zeta) \begin{pmatrix} R_i \\ Z_i \end{pmatrix} + N_1^{L_2}(\zeta) \begin{pmatrix} R_{i+4} \\ Z_{i+4} \end{pmatrix} \right] \quad (\text{E.19})$$

$$= \sum_{i=1}^4 N_i^{Q_4}(\xi, \eta) \begin{pmatrix} R_i^*(\zeta) \\ Z_i^*(\zeta) \end{pmatrix} \quad (\text{E.20})$$

This is the familiar equation for a bilinear quadrilateral at the position  $\varphi$  from (E.18) with the intermediate nodes  $R_i^*, Z_i^*$ . The inverse mapping of (E.15) can now be obtained in two steps. First,  $\zeta$  is obtained from (E.18):

$$\zeta(\varphi) = \frac{\varphi - \varphi_A}{\varphi_B - \varphi_A}, \quad (\text{E.21})$$

which fixes  $R_i^*, Z_i^*$  in (E.20). Then (E.6) for a bilinear quadrilateral can be applied to obtain  $\xi(R_i^*, Z_i^*), \eta(R_i^*, Z_i^*)$ .

Now the isoparametric concept can be applied to interpolate data values  $F_a$  from the hexahedral nodes into the interior:

$$F(\boldsymbol{\xi}) = \sum_{a=1}^8 N_a^{H_8}(\boldsymbol{\xi}) F_a, \quad (\text{E.22})$$

where  $N_a^{H_8}(\boldsymbol{\xi})$  are the shape functions of the trilinear hexahedra presented in (E.12).

### E.3 Data interpolation

The concept of isoparametric elements allows to interpolate data at any point within a grid cell. While  $\mathbf{B}$  is usually known at the cell nodes and can therefore be applied directly in (E.22), plasma parameters from the transport calculations performed in this thesis - such as  $n_e$  - are given as cell averaged values. Therefore it is necessary to setup a mapping *cell2node* to distribute  $F_i, i = 1, \dots, n_{\text{cell}}$  cell averaged values to  $G_j, j = 1, \dots, n_{\text{nodes}}$  values at the cell corners. Naturally this mapping is ambiguous, because  $n_{\text{nodes}} > n_{\text{cell}}$ . The ambiguity can be reduced by periodic boundary conditions, e.g. in toroidal and poloidal direction. However, no such conditions exist at the radial boundaries or at the divertor plates and some freedom remains.

When preparing the mapping *cell2node* it makes a difference whether the  $F_i$  are defined on the magnetic grid (which is used for data interpolation) or on the much coarser plasma grid (which is defined by joining several magnetic grid cells to a plasma grid cell). Here only plasma cells created by combining magnetic cells in toroidal direction are considered. In the following the mapping *pc2mc* is presented which distributes data from a plasma cell to its sub-cells, afterwards the mapping *cell2node* is presented.

#### Plasma cell to magnetic cell

Although one can just distribute the value  $F_i$  in plasma cell  $i$  to all its sub-cells, this is not recommended, because this results in some kind of numerical artifact when sampling data values in toroidal direction: toroidal profiles will be flat in all sub-cells except the

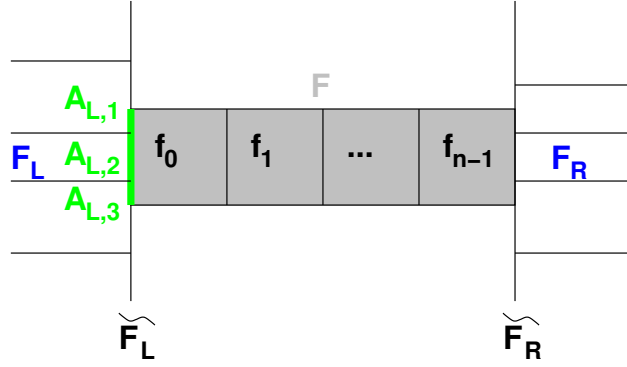


Figure E.3: Sketch of a plasma cell with data  $F$ , which is distributed to  $f_0, \dots, f_{n-1}$  in its sub-cells (magnetic cells). The left and right cell neighbors are used to obtain intermediate values  $S_L, S_R$  at the toroidal cell boundaries, where the overlap areas  $A_{L,i}, A_{R,j}, i = 1, \dots, n_L, j = 1, \dots, n_R$  are used to obtain a left and right average values  $F_L, F_R$ .

very first and last in toroidal direction. The following procedure is performed for each plasma cell  $i$  with data  $F_i, i = 1, \dots, n_{\text{plas}}$  to smoothly distribute data from plasma cells to magnetic cells:

- First the left and right cell neighbors have to be determined. Note that there can be several partial cell neighbors at toroidal mapping surfaces (see section 4.2.3 and figure E.3). Let there be  $n_L, n_R$  left and right cell neighbors with plasma cell number  $m_{L,j}, m_{R,k}$  and overlap area  $A_{L,j}, A_{R,k}, j = 1, \dots, n_L, k = 1, \dots, n_R$ .
- Calculate left and right overlap area weighted average values  $F_L, F_R$ , e.g.:

$$F_L = \frac{1}{W} \sum_{j=1}^{n_L} A_{L,j} F_{m_{L,j}}, \quad W = \sum_{j=1}^{n_L} A_{L,j}, \quad (\text{E.23})$$

The average cell lengths  $l_L, l_R$  of the left and right neighbor are calculated in the same way.

- Intermediate values  $\tilde{F}_L, \tilde{F}_R$  at the toroidal cell boundaries are now calculated, e.g.:

$$\tilde{F}_L = \alpha \cdot F_L + (1 - \alpha) \cdot F_i, \quad \alpha = \frac{l_i}{l_i + l_L}, \quad (\text{E.24})$$

where  $l_i$  is the length of cell  $i$ .

- Finally, data can now be distributed to the  $n$  sub-cells:

$$f_a = \beta_a \tilde{F}_L + (1 - \beta_a) \tilde{F}_R, \quad \beta_a = \frac{a + 0.5}{n}, a = 0, \dots, n - 1 \quad (\text{E.25})$$

### Magnetic cell to nodes

Now that data values are defined in each magnetic cell, these values are mapped to the grid nodes. Each node value  $G_b, b = 1, \dots, n_{\text{nodes}}$  is defined as the weighted average

$$G_b = \frac{1}{W_b} \sum_{a \in A_b} w_a f_a, \quad W_b = \sum_{a \in A_b} w_a, \quad (\text{E.26})$$

where  $A_b$  is the set of magnetic cells that share node  $b$  and  $w_a = 1/V_a$  is the weight for cell  $a$  (and  $V_a$  is the volume of cell  $a$ ).

## E.4 Example: Simulation of camera pictures

This example describes the simulation of a camera at the TEXTOR tokamak which is used to observe the DED target, e.g. the  $H_\alpha$  emission. The setup of the camera is sketched in figure E.4 for a tangential view on the target region at  $\varphi_t = 67.5 \text{ deg}$ <sup>1</sup>. The camera position is denoted by  $\mathbf{x}_{\text{cam}}$  in the following. Grid points  $\mathbf{x}_{ij}$  are defined in a poloidal plane at  $\varphi_t$  (the projection plane) which are later used to plot the line-of-sight integrated values. The same radial and poloidal range  $r_{\min} \in [39.7, 47.7]$  and  $\vartheta \in [130, 230]$  as for the 2D cuts in figure 6.7 is used to provide equidistant grid points  $\mathbf{x}_{ij}, i = 1, \dots, n_r, j = 1, \dots, n_p$ . This defines  $i \cdot j$  lines of sight, all fixed at  $\mathbf{x}_{\text{cam}}$  with direction  $\mathbf{d}_{ij}$

$$\mathbf{l}_{ij}(t) = \mathbf{x}_{\text{cam}} + t \cdot \mathbf{d}_{ij}, \quad \mathbf{d}_{ij} = \mathbf{x}_{ij} - \mathbf{x}_{\text{cam}}, \quad t \in \mathbb{R} \quad (\text{E.27})$$

For the purpose of integrating line-of-sight values,  $2n_l + 1$  data points are selected for each line:

$$\mathbf{l}_{ijk} = \mathbf{l}_{ij}(t_k), \quad t_k = k/n_l, \quad k = 0, \dots, 2n_l \quad (\text{E.28})$$

to cover the complete volume in the vessel which is observed by the model camera. Then the line-of-sight integrated values of  $P_{H_\alpha}(i, j)$  are approximated by

$$\mathfrak{P}_{ij} = \sum_{k=0}^{2n_l} \Delta l P_{H_\alpha}(\mathbf{l}_{ijk}), \quad (\text{E.29})$$

where  $\Delta l = |\mathbf{d}_{ij}|/n_l$ . To obtain the actual photon flux, an additional weight  $w_k$  has to be introduced which accounts for a finite observation angle of the camera and for

---

<sup>1</sup>Note that  $\varphi_t = 67.5 \text{ deg}$  in the present simulation corresponds to  $\varphi_t = 157.5 \text{ deg}$  using the TEXTOR convention for the toroidal angle.

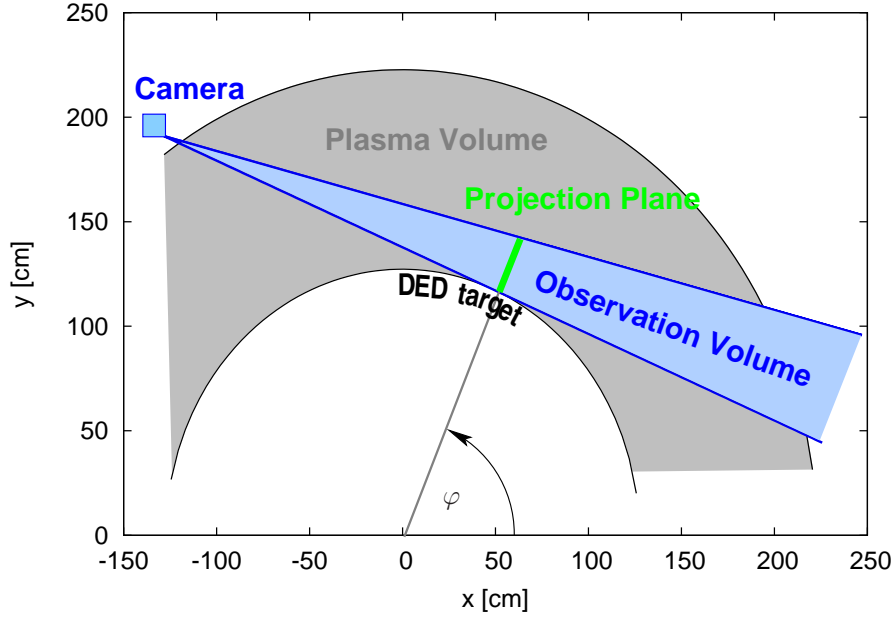


Figure E.4: Geometric setup of a camera to observe the DED target region at  $\varphi_t = 67.5$  deg.

the fraction of emitted photons that reach the camera. This weight, however, is just a constant factor which only depends on the resolution  $n_r \cdot n_p$ , i.e. the amount of the sample lines, and the aperture of the camera. Hence,  $\mathfrak{P}_{ij}$  is proportional to the expected photon flux.

Two examples of the so obtained camera picture are presented in figure E.5 and compared to 2D cuts at the projection plane. As can be seen, there is no significant difference in the general structure. Only the structures are smoother in the simulated camera picture, which is reasonable, because of the helical nature of the strike points and the toroidal view direction. However, details of the distribution are indeed different between the simulated picture and the 2D cut, but are left here for future analysis.

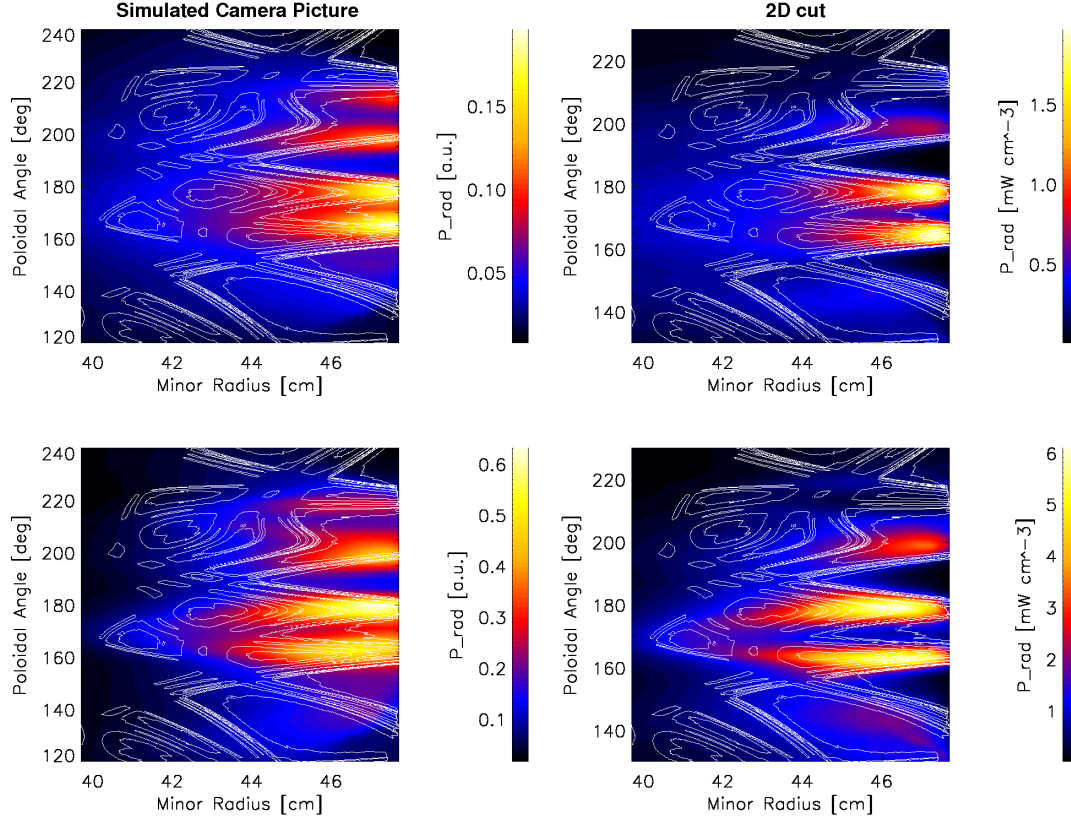


Figure E.5:  $H_\alpha$  distribution observed by the model camera (left) and 2D cut of the  $H_\alpha$  distribution at  $\varphi = 67.5$  deg (right) for  $n_{\text{sepx}} = 2.0 \cdot 10^{19} \text{ m}^{-3}$  (upper row) and  $n_{\text{sepx}} = 4.8 \cdot 10^{19} \text{ m}^{-3}$ .



# Bibliography

- [1] FREIDBERG, J. Plasma Physics and Fusion Energy. Cambridge University Press (2007).
- [2] KADOMTSEV, B. Tokamak Plasma; A Complex Physical System. Institute of Physics Publishing, Bristol and Philadelphia (1992).
- [3] WESSON, J. Tokamaks. Oxford: Clarendon Press (2004).
- [4] SPITZER, L. The Stellarator Concept. *Phys. Fluids*, **1** (1958), 253. doi:10.1063/1.1705883.
- [5] ITER - The way to new energy.  
URL <http://www.iter.org>
- [6] Progress in the ITER Physics Basis, volume 47 (2007). doi:10.1088/0029-5515/47/6/E01.
- [7] STANGEBY, P. The Plasma Boundary of Magnetic Fusion Devices. Institute of Physics Publishing Bristol and Philadelphia (2000).
- [8] WAGNER, F. ET AL. Regime of Improved Confinement and High Beta in Neutral-Beam-Heated Divertor Discharges of the ASDEX Tokamak. *Phys. Rev. Lett.*, **49** (1982), 1408. doi:10.1103/PhysRevLett.49.1408.
- [9] KEILHACKER, M. H-Mode confinement in tokamaks. *Plasma Phys. Control. Fusion*, **29** (1987), 10A, 1401. doi:10.1088/0741-3335/29/10A/320.
- [10] ZOHM, H. Edge localized modes (ELMs). *Plasma Phys. Control. Fusion*, **38** (1996), 105–128. doi:10.1088/0741-3335/38/2/001.
- [11] HUYSMANS, G. ELMs: MHD instabilities at the transport barrier. *Plasma Phys. Control. Fusion*, **47** (2005), B165–B178. doi:10.1088/0741-3335/47/12B/S13.
- [12] LOARTE, A. ET AL. Characteristics and scaling of energy and particle losses during Type I ELMs in JET H-modes. *Plasma Phys. Control. Fusion*, **44** (2002), 1815. doi:10.1088/0741-3335/44/9/303.
- [13] FEDERICI, G. ET AL. Key ITER plasma edge and plasma-material interaction issues. *Journal of Nuclear Materials*, **313-316** (2003), 11–22. doi:10.1016/S0022-3115(02)01327-2.

- [14] ENGELHARDT, W. AND FENEBERG, W. Influence of an ergodic magnetic limiter on the impurity content in a tokamak. *J. Nucl. Mater.*, **76-77** (1978), 518–520. doi:10.1016/0022-3115(78)90198-8.
- [15] FENEBERG, W. AND WOLF, G. H. A helical magnetic limiter for boundary layer control in large tokamaks. *Nuclear Fusion*, **21** (1981), 669–675.
- [16] EVANS, T. E. ET AL. Experiments to test an intra-island scoop limiter on TEXT. *J. Nucl. Mater.*, **145-147** (1987), 812–818. doi:10.1016/0022-3115(87)90451-X.
- [17] TAKAMURA, S.; YAMADA, H. AND OKUDA, T. Control of the Tokamak Edge Plasma by Static and Rotating Helical Magnetic Limiters. *Nuclear Fusion*, **27** (1988), 2, 183–191.
- [18] EVANS, T. E. ET AL. Resonant Helical Divertor Experiments in Ohmic and Auxiliary heated JIPP T-IIU Plasmas. *J. Nucl. Mater.*, **162-164** (1989), 636–642. doi:10.1016/0022-3115(89)90340-1.
- [19] GHENDRIH, P.; GROSMAN, A. AND CAPES, H. Theoretical and experimental investigations of stochastic boundaries in tokamaks. *Plasma Phys. Control. Fusion*, **38** (1996), 1653. doi:10.1088/0741-3335/38/10/002.
- [20] GHENDRIH, P. ET AL. Progress in ergodic divertor operation on Tore Supra. *Nuclear Fusion*, **42** (2002), 10, 1221–1250. doi:10.1088/0029-5515/42/10/308.
- [21] EVANS, T. E. ET AL. Suppression of Large Edge-Localized Modes in High-Confinement DIII-D Plasmas with a Stochastic Magnetic Boundary. *Phys. Rev. Lett.*, **92** (2004), 23, 235003. doi:10.1103/PhysRevLett.92.235003.
- [22] EVANS, T. E. ET AL. Edge stability and transport control with resonant magnetic perturbations in collisionless tokamak plasmas. *Nature Physics*, **2** (2006), 419–423. doi:10.1038/nphys312.
- [23] LIANG, Y. ET AL. Active Control of Type-I Edge-Localized Modes with  $n=1$  Perturbation Fields in the JET Tokamak. *Phys. Rev. Lett.*, **98** (2007), 265004, 1–5. doi:10.1103/PhysRevLett.98.265004.
- [24] BÉCOULET, M. ET AL. Numerical study of the resonant magnetic perturbations for Type I edge localized modes control in ITER. *Nuclear Fusion*, **48** (2008), 024003. doi:10.1088/0029-5515/48/2/024003.
- [25] SCHAFFER, M. J. ET AL. Study of in-vessel nonaxisymmetric ELM suppression coil concepts for ITER. *Nuclear Fusion*, **48** (2008), 024004. doi:10.1088/0029-5515/48/2/024004.
- [26] RECHESTER, A. B. AND ROSENBLUTH, M. N. Electron Heat Transport in a Tokamak with Destroyed Magnetic Surfaces. *Phys. Rev. Lett.*, **40** (1978), 38. doi:10.1103/PhysRevLett.40.38.

- 
- [27] GHENDRIH, P. ET AL. Comparison of ergodic and axisymmetric divertors. *J. Nucl. Mater.*, **266-269** (1999), 189–196. doi:10.1016/S0022-3115(98)00525-X.
- [28] TOKAR, M. Z. ET AL. Mechanisms of Edge-Localized-Mode Mitigation by External-Magnetic-Field Perturbations. *Phys. Rev. Lett.*, **98** (2007), 095001. doi:10.1103/PhysRevLett.98.095001.
- [29] TOKAR, M. Z. ET AL. Modelling of pedestal transport during ELM suppression by external magnetic field perturbations. *Nuclear Fusion*, **48** (2008), 024006. doi:10.1088/0029-5515/48/2/024006.
- [30] REITER, D. Progress in two-dimensional plasma edge modeling. *Journal of Nuclear Materials*, **196-198** (1992), 80–89. doi:10.1016/S0022-3115(06)80014-0.
- [31] REITER, D.; BAELEMAN, M. AND BOERNER, P. The EIRENE and B2-EIRENE codes. *Fusion Science and Technology*, **47** (2005), 2, 172.
- [32] SCHNEIDER, R. ET AL. Plasma Edge Physics with B2-Eirene. *Contrib. Plasma Phys.*, **46** (2006), 1-2, 3–191.
- [33] TARONI, A. ET AL. The Multi-Fluid codes EDGE1D and EDGE2D: Models and Results. *Contrib. Plasma Phys.*, **32** (1992), 3-4, 438–443. doi:10.1002/ctpp.2150320339.
- [34] SIMONINI, R. ET AL. Models and Numerics in the Multi-Fluid 2-D Edge Plasma Code EDGE2D/U. *Contrib. Plasma Phys.*, **34** (1994), 2-3, 368–373. doi:10.1002/ctpp.2150340242.
- [35] KAWASHIMA, H. ET AL. Development of Integrated SOL/Divertor Code and Simulation Study in JAEA. *Plasma Fusion Res.*, **1** (2006), 31. doi:10.1585/pfr.1.031.
- [36] KAWASHIMA, H. ET AL. Design study of JT-60SA divertor for high heat and particle controllability. *Fusion Engineering and Design*, **83** (2008), 1643–1647. doi:10.1016/j.fusengdes.2008.07.009.
- [37] FENG, Y. ET AL. A 3D Monte Carlo code for plasma transport in island divertors. *Journal of Nuclear Materials*, **241-243** (1997), 930–934. doi:10.1016/S0022-3115(97)80168-7.
- [38] FENG, Y.; SARDEI, F. AND KISSLINGER, J. 3D fluid modelling of the edge plasma by means of a Monte Carlo technique. *Journal of Nuclear Materials*, **266-269** (1999), 812–818. doi:10.1016/S0022-3115(98)00844-7.
- [39] FENG, Y.; KISSLINGER, J. AND SARDEI, F. Formulation of a Monte Carlo model for edge plasma transport. In 27th EPS Conference on Contr. Fusion and Plasma Phys., volume 24B, pages 1188–1191. Budapest (12-16 June 2000).
- [40] FENG, Y. ET AL. Transport in island divertors: physics, 3D modelling and comparison to first experiments on W7-AS\*. *Plasma Phys. Control. Fusion*, **44** (2002), 611–625.
-

- [41] FENG, Y. ET AL. 3D Edge Modeling and Island Divertor Physics. *Contrib. Plasma Phys.*, **44** (2004), 1-3, 57–69. doi:10.1002/ctpp.200410009.
- [42] SHARMA, D. ET AL. Three-dimensional Monte Carlo simulations of W7-X plasma transport: density control and particle balance in steady-state operations. *Nuclear Fusion*, **45** (2005), 825–836. doi:10.1088/0029-5515/45/8/008.
- [43] KOBAYASHI, M. ET AL. Divertor transport study in the large helical device. *Journal of Nuclear Materials*, **363-365** (2007), 294–300. doi:10.1016/j.jnucmat.2007.01.038.
- [44] FENG, Y. ET AL. Fluid features of the stochastic layer transport in LHD. *Nuclear Fusion*, **48** (2008), 024012. doi:10.1088/0029-5515/48/2/024012.
- [45] KOBAYASHI, M. ET AL. Implementation of the EMC3-EIRENE code on TEXTOR-DED: accuracy and convergence study. *Contrib. Plasma Phys.*, **44** (2004), 1-3, 25–30. doi:10.1002/ctpp.200410003.
- [46] KOBAYASHI, M. ET AL. 3D numerical transport study of the edge ergodized plasma in TEXTOR-DED. *Nuclear Fusion*, **44** (2004), S64–S73. doi:10.1088/0029-5515/44/6/S07.
- [47] HARTING, D. ET AL. 3D edge transport studies with EMC3-EIRENE for the Dynamic Ergodic Divertor (DED) at TEXTOR. *Contrib. Plasma Phys.*, **48** (2008), 1-3, 99–105. doi:10.1002/ctpp.200810017.
- [48] KOBAYASHI, M. ET AL. 3D edge transport analysis of ITER start-up configuration for limiter power load assessment. *Nuclear Fusion*, **47** (2007), 61–73. doi:10.1088/0029-5515/47/2/001.
- [49] FENG, Y.; SARDEI, F. AND KISSLINGER, J. A simple highly accurate field-line mapping technique for three-dimensional Monte Carlo modeling of plasma edge transport. *Phys. Plasmas*, **12** (2005), 052505, 1–7. doi:10.1063/1.1888959.
- [50] WESSON, J. A. Hydromagnetic stability of tokamaks. *Nuclear Fusion*, **18** (1978), 87.
- [51] CONNOR, J. W. ET AL. Magnetohydrodynamic stability of tokamak edge plasmas. *Phys. Plasmas*, **7** (1998), 2687. doi:10.1063/1.872956.
- [52] SNYDER, P. ET AL. Edge localized modes and the pedestal: A model based on coupled peeling-ballooning modes. *Phys. Plasmas*, **9** (2002), 2037. doi:10.1063/1.1449463.
- [53] EFDA - JET: Image Gallery.  
URL <http://www.jet.efda.org/pages/multimedia/gallery/graphics.html>
- [54] SHAFRANOV, V. D. Plasma equilibrium in a magnetic field. In *Reviews of Plasma Physics*, volume Vol. 2, page p. 103. New York: Consultants Bureau (1966).

- [55] KRUSKAL, M. D. AND KULSRUD, R. M. Equilibrium of a Magnetically Confined Plasma in a Toroid. *Phys. Fluids*, **1** (1958), 265–274. doi:10.1063/1.1705884.
- [56] LOARTE, A. ET AL. Chapter 4: Power and particle control. *Nuclear Fusion*, **47** (2007), S203–S263. doi:10.1088/0029-5515/47/6/S04.
- [57] GUCKENHEIMER, J. AND HOLMES, P. Nonlinear Oscillations, Dynamical Systems, and Bifurcations of Vector Fields. Applied Mathematical Science (1983).
- [58] RASBAND, S. N. Chaotic dynamics of nonlinear systems. New York: Wiley (1990).
- [59] LICHTENBERG, A. J. AND LIEBERMAN, M. A. Regular and chaotic dynamics. Applied mathematical sciences 38 (1992).
- [60] GLEICK, J. Chaos : making a new science. Penguin Books (1987).
- [61] CHIRIKOV, B. V. Resonance Processes in Magnetic Traps. *J. Nucl. Energy Part C: Plasma Phys.*, **1** (1960), 253. doi:10.1088/0368-3281/1/4/311.
- [62] GHENDRIH, P. ET AL. Control of the Edge Transport with the Ergodic Divertor. *Contrib. Plasma Phys.*, **32** (1992), 179. doi:10.1002/ctpp.2150320303.
- [63] LUXON, J. L. A design retrospective of the DIII-D tokamak. *Nuclear Fusion*, **42** (2002), 614–633. doi:10.1088/0029-5515/42/5/313.
- [64] NEUBAUER, O. ET AL. Design features of the Tokamak TEXTOR. *Fusion Engineering and Design*, **47** (2005), 76–86.
- [65] FINKEN, K. AND WOLF, G. Background, motivation, concept and scientific aims for building a dynamic ergodic divertor. *Fusion Engineering and Design*, **37** (1997), 337–340.
- [66] FINKEN, K. ET AL. The structure of magnetic field in the TEXTOR-DED, volume 45 of *Reihe Energietechnik*. Schriften des Forschungszentrums Jülich (2005).
- [67] PARK, J. K. Control of Asymmetric Magnetic Perturbations in Tokamaks. *Phys. Rev. Lett.*, **99** (2007), 195003. doi:10.1103/PhysRevLett.99.195003.
- [68] KOBAYASHI, M. ET AL. Frequency dependence of tokamak plasma response to the externally applied rotating helical field. *Phys. Plasmas*, **7** (2000), 8, 3288. doi:10.1063/1.874194.
- [69] KIKUCHI, Y. ET AL. Forced Magnetic Reconnection and Field Penetration of an Externally Applied Rotating Helical Magnetic Field in the TEXTOR Tokamak. *Phys. Rev. Lett.*, **97** (2006), 085003. doi:10.1103/PhysRevLett.97.085003.
- [70] MILITELLO, F. AND WAELEBROECK, F. L. Error field penetration in the presence of diamagnetic effects. *Nuclear Fusion*, **49** (2009), 065018. doi:10.1088/0029-5515/49/6/065018.

- [71] REISER, D. AND CHANDRA, D. Plasma currents induced by resonant magnetic field perturbations in tokamaks. *Phys. Plasmas*, **16** (2009), 042317. doi:10.1063/1.3126548.
- [72] JAKUBOWSKI, M. ET AL. Change of the Magnetic-Field Topology by an Ergodic Divertor and the Effect on the Plasma Structure and Transport. *Phys. Rev. Lett.*, **96** (2006), 035004. doi:10.1103/PhysRevLett.96.035004.
- [73] LEHNEN, M. ET AL. The DED at TEXTOR: Transport and Topological Properties of a Helical Divertor. *Plasma and Fusion Research*, **3** (2008), S1039. doi:10.1585/pfr.3.S1039.
- [74] ABDULLAEV, S. S.; FINKEN, K. H. AND SPATCHEK, K. H. Asymptotical and mapping methods in study of ergodic divertor magnetic field in a toroidal system. *Phys. Plasmas*, **6** (1999), 153. doi:10.1063/1.873270.
- [75] ABDULLAEV, S. S. The Hamilton-Jacobi method and Hamiltonian maps. *Journal of Physics A*, **35** (2002), 2811. doi:10.1088/0305-4470/35/12/307.
- [76] ABDULLAEV, S. S. On mapping models of field lines in a stochastic magnetic field. *Nuclear Fusion*, **44** (2004), S12. doi:10.1088/0029-5515/44/6/S02.
- [77] HARTING, D. 3-dimensionale Plasmarandschicht-Simulationen in unvollständig ergodisierten Magnetfeldern. Ph.D. thesis, Heinrich-Heine-Universität Düsseldorf (2008).
- [78] ZHENG, S. B.; WOOTTON, A. J. AND SOLANO, E. R. Analytical tokamak equilibrium for shaped plasmas. *Phys. Plasmas*, **3** (1996), 3, 1176–1178. doi:10.1063/1.871772.
- [79] ATANASIU, C. V. ET AL. Analytical solutions to the Grad-Shafranov equation. *Phys. Plasmas*, **11** (2004), 3510. doi:10.1063/1.1756167.
- [80] HABERSCHIEDT, T. MHD-Gleichgewichte im TEXTOR Tokamak. Diplomarbeit, Heinrich-Heine Universität Düsseldorf, Germany (2002).
- [81] LAO, L. ET AL. Reconstruction of current profile parameters and plasma shapes in tokamaks. *Nuclear Fusion*, **25** (1985), 1611–1622.
- [82] ZWINGMANN, W. Equilibrium analysis of steady state tokamak discharges. *Nuclear Fusion*, **43** (2003), 842–850. doi:10.1088/0029-5515/43/9/308.
- [83] DE BOOR, C. A Practical Guide to Splines. Applied Mathematical Sciences 27 (1978).
- [84] FARIN, G. Curves and Surfaces for CAGD: A Practical Guide. The Morgan Kaufmann Series in Computer Graphics (2002).
- [85] POINCARÉ, H. New Methods of Celestial Mechanics, volume 1-3. AIP, History of Modern Physics and Astronomy (1992).

- 
- [86] LODGE, G.; WALSH, J. AND KRAMER, M. A trilinear three-body problem. *International Journal of Bifurcation and Chaos*, **13** (2003), 8, 2141–2155.
- [87] FINKEN, K.; EICH, T. AND KALECK, A. First modelling of the TEXTOR DED near field divertor. *Nuclear Fusion*, **38** (1998), 515–530. doi:10.1088/0029-5515/38/4/304.
- [88] FINKEN, K. ET AL. Operation space of the Dynamic Ergodic Divertor for TEXTOR-94. *Nuclear Fusion*, **39** (1999), 5, 637–662.
- [89] ABDULLAEV, S.; EICH, T. AND FINKEN, K. Fractal structure of the magnetic field in the laminar zone of the Dynamic Ergodic Divertor of the Torus Experiment for Technology-Oriented Research (TEXTOR-94). *Phys. Plasmas*, **8** (2001), 6, 2739–2749.
- [90] BRAGINSKII, S. Transport processes in a plasma. *Review of Plasma Physics*, **1** (1965), 205–311.
- [91] ZHDANOV, V. M. Transport Processes in Multicomponent Plasmas. *Plasma Phys. Control. Fusion*, **44** (2002), 10, 2283. doi:10.1088/0741-3335/44/10/701.
- [92] CHAPMAN, S. AND COWLING, T. G. Mathematical Theory of Nonuniform Gases. Cambridge University Press (1953).
- [93] HUBA, J. D. NRL Plasma Formulary. Naval Research Laboratory, Washington DC (2007).
- [94] CONNOR, J. AND WILSON, H. Survey of theories of anomalous transport. *Plasma Phys. Control. Fusion*, **36** (1994), 719–795.
- [95] COSTER, D. ET AL. Benchmarking Tokamak edge modelling codes. *J. Nucl. Mater.*, **337-339** (2005), 336–370. doi:10.1016/j.jnucmat.2004.10.013.
- [96] SCHMITZ, O. ET AL. Characterization of transport in the stochastic edge layer of TEXTOR by analysis of the radial and poloidal distribution of electron density and temperature. *Journal of Nuclear Materials*, **363-365** (2007), 680–685. doi:10.1016/j.jnucmat.2007.01.067.
- [97] SCHMITZ, O. ET AL. Identification and analysis of transport domains in the stochastic boundary of TEXTOR-DED for different mode spectra. *Nuclear Fusion*, **48** (2008), 024009. doi:10.1088/0029-5515/48/2/024009.
- [98] RADFORD, G. The Application of Moment Equations to Scrape-Off Layer Plasmas. *Contrib. Plasma Phys.*, **32** (1992), 297–302. doi:10.1002/ctpp.2150320319.
- [99] FRERICH, H. 3D numerische Parameterstudien zum Verunreinigungstransport in TEXTOR-DED. Diplomarbeit, RWTH-Aachen / IEF-4, FZJ (2006).  
URL [http://www.eirene.de/frerichs\\_diplomarbeit.pdf](http://www.eirene.de/frerichs_diplomarbeit.pdf)
- [100] CHAPMAN, S. Thermal Diffusion in Ionized Gases. *Proc. Phys. Soc.*, **72** (1958), 353. doi:10.1088/0370-1328/72/3/305.
-

- [101] GOLDSTON, R. J. AND RUTHERFORD, P. H. Introduction to Plasma Physics. Institute of Physics Publishing, Bristol and Philadelphia (1995).
- [102] BEHRINGER, K. Description of the Impurity Transport Code *STRAHL*. Technical Report 08, JET-R (1987).
- [103] SUMMERS, H. P. ET AL. Ionization state, excited populations and emission of impurities in dynamic finite density plasmas: I. The generalized collisional-radiative model for light elements. *Plasma Phys. Control. Fusion*, **48** (2006), 263–293. doi:10.1088/0741-3335/48/2/007.
- [104] ADAS - Atomic Data and Analysis Structure.  
URL <http://www.adas.ac.uk/about.php>
- [105] RISKEN, H. The Fokker-Planck equation. Springer-Verlag, Berlin, 2nd edition (1989).
- [106] MACKEOWN, P. K. Stochastic Simulation in Physics. Springer-Verlag Singapore (1997).
- [107] FRERICHs, H. ET AL. Block-structured grids in Lagrangian 3D edge plasma transport simulations. *Comp. Phys. Commun.*, **181** (2010), 61–70. doi:10.1016/j.cpc.2009.08.016.
- [108] HUGHES, T. J. R. The Finite element method : linear static and dynamic finite element analysis. Prentice-Hall (1987).
- [109] Department of Aerospace Engineering Sciences, University of Colorado at Boulder. Introduction to Finite Element Methods (2009).  
URL <http://www.colorado.edu/engineering/CAS/courses.d/IFEM.d/>
- [110] Aerospace Engineering Sciences, University of Colorado at Boulde. Advanced Finite Element Methods (2009).  
URL <http://www.colorado.edu/engineering/CAS/courses.d/AFEM.d/>
- [111] KLOEDEN, P. AND PLATEN, E. Numerical solution of Stochastic Differential Equations. Springer-Verlag (1999).
- [112] MINIER, J.-P. AND PEIRANO, E. The pdf approach to turbulent polydispersed two-phase flows. *Physics Reports*, **352** (2001), 1–214. doi:10.1016/S0370-1573(01)00011-4.
- [113] MARUYAMA, G. Continuous markov processes and stochastic equations. *Rend. Circ. Mat. Palermo*, **4** (1955), 48–93.
- [114] RUNOV, A. ET AL. Monte Carlo study of heat conductivity in stochastic boundaries: Application to the TEXTOR ergodic divertor. *Phys. Plasmas*, **8** (2001), 3, 916–930. doi:10.1063/1.1344921.
- [115] KNUPP, P. M. On the Invertibility of the Isoparametric Map. *Comput. Methods Appl. Mech. Eng.*, **78** (1990), 313–329.



- [116] REITER, D. EIRENE - A Monte Carlo linear transport solver.  
URL <http://www.eirene.de>
- [117] HARTING, D. AND REITER, D. 3D Monte-Carlo-Simulation der ergodisierten Randschicht von TEXTOR. Berichte des Forschungszentrum Jülich (Jül-4173), Institut für Plasmaphysik (2005).
- [118] MPI: A Message-Passing Interface standard.  
URL <http://www.mpi-forum.org>
- [119] JUMP - Jülich Multi Processor.  
URL <http://www.fz-juelich.de/jsc/jump>
- [120] JuRoPA - Jülich Research on Petaflop Architectures.  
URL <http://www.fz-juelich.de/jsc/juropa>
- [121] VIP - The IBM Power6 System at Rechenzentrum Garching.  
URL <http://www.rzg.mpg.de/computing/hardware/Power6/the-ibm-power6-system>
- [122] AMDAHL, G. M. Validity of the single processor approach to achieving large scale computing capabilities. In AFIPS spring joint computer conference (1967).  
URL <http://www-inst.eecs.berkeley.edu/~n252/paper/Amdahl.pdf>
- [123] Gnuplot - An Interactive Plotting Program.  
URL <http://www.gnuplot.info>
- [124] MAY, R. M. Simple mathematical models with very complicated dynamics. *Nature*, **261** (1976), 459. doi:10.1038/261459a0.
- [125] STROGATZ, S. H. Nonlinear dynamics and chaos : with applications to physics, biology, chemistry and engineering. Cambridge, Mass.: Perseus Book Publ. (1994).
- [126] EVANS, T. E. ET AL. Experimental signatures of homoclinic tangles in poloidally diverted tokamaks. *J. Phys. Conf. Ser.*, **7** (2005), 174. doi:10.1088/1742-6596/7/1/015.
- [127] SCHMITZ, O. ET AL. Aspects of three dimensional transport for ELM control experiments in ITER-similar shape plasmas at low collisionality in DIII-D. *Plasma Phys. Control. Fusion*, **50** (2008), 124029. doi:10.1088/0741-3335/50/12/124029.
- [128] EVANS, T. E. Chaos, Complexity and Transport: Theory and Applications. World Scientific Press (2008).
- [129] WINGEN, A.; EVANS, T. E. AND SPATSCHEK, K. H. Footprint structures due to resonant magnetic perturbations in DIII-D. *Phys. Plasmas*, **16** (2009), 042504. doi:10.1063/1.3099053.
- [130] WINGEN, A.; EVANS, T. E. AND SPATSCHEK, K. H. High resolution numerical studies of separatrix splitting due to non-axisymmetric perturbation in DIII-D. *Nuclear Fusion*, **49** (2009), 055027. doi:10.1088/0029-5515/49/5/055027.

- [131] NGUYEN, F.; GHENDRIH, P. AND GROSMAN, A. Interaction of stochastic boundary layer with plasma facing components. *Nuclear Fusion*, **37** (1997), 6, 743–757. doi:10.1088/0029-5515/37/6/I03.
- [132] EICH, T.; REISER, D. AND FINKEN, K. Two dimensional modelling approach to transport properties of the TEXTOR-DED laminar zone. *Nuclear Fusion*, **40** (2000), 10, 1757–1772. doi:10.1088/0029-5515/40/10/307.
- [133] FENG, Y. ET AL. Comparative divertor-transport study for helical devices. *Nuclear Fusion*, **49** (2009), 095002. doi:10.1088/0029-5515/49/9/095002.
- [134] HARTING, D. ET AL. Application Of The 3D Edge Code EMC3-EIRENE To JET Single Null Configurations By Validating Against 2D Simulations With EDGE2D-EIRENE. *J. Nucl. Mater.*, (submitted).
- [135] FRERICHs, H. ET AL. Three-dimensional edge transport simulations for DIII-D plasmas with resonant magnetic perturbations. *Nuclear Fusion*, **50** (2010), 034004. doi:10.1088/0029-5515/50/3/034004.
- [136] JAKUBOWSKI, M. ET AL. Overview of the results on divertor heat loads in RMP controlled H-mode plasmas on DIII-D. *Nuclear Fusion*, **49** (2009), 095013. doi:10.1088/0029-5515/49/9/095013.
- [137] EVANS, T. E. ET AL. Experimental and numerical studies of separatrix splitting and magnetic footprints in DIII-D. *J. Nucl. Mater.*, **363-365** (2007), 570. doi:10.1016/j.jnucmat.2006.12.064.
- [138] JOSEPH, I. ET AL. Calculation of stochastic thermal transport due to resonant magnetic perturbations in DIII-D. *Nuclear Fusion*, **48** (2008), 045009. doi:10.1088/0029-5515/48/4/045009.
- [139] FRERICHs, H. ET AL. 3D numerical analysis of magnetic topology and edge transport for RMP limiter scenarios at TEXTOR and DIII-D. In Proc. 35th EPS Conf. Plasma Phys. Hersonissos, volume 32 (2008).
- [140] SCHMITZ, O. ET AL. Resonant Pedestal Pressure Reduction Induced by a Thermal Transport Enhancement due to Stochastic Magnetic Boundary Layers in High Temperature Plasmas. *Phys. Rev. Lett.*, **103** (2009), 165005. doi:10.1103/PhysRevLett.103.165005.
- [141] MORDIJCk, S. ET AL. Fluid modeling of an ELMing H-mode and a RMP H-mode. *J. Nucl. Mater.*, **390-391** (2009), 299–302. doi:10.1016/j.jnucmat.2009.01.130.
- [142] MORDIJCk, S. ET AL. Modeling of particle transport in ELMing and RMP H-modes (2009). 4th International Workshop on Stochasticity in Fusion Plasmas.
- [143] SCHMITZ, O. Private Communication (September 2009).
- [144] LEHNEN, M. ET AL. First results from the dynamic ergodic divertor at TEXTOR. *J. Nucl. Mater.*, **337-339** (2005), 171–175. doi:10.1016/j.jnucmat.2004.10.100.

- [145] SCHMITZ, O. Experimentelle Untersuchung der Plasmastruktur und Charakterisierung des Transportverhaltens in der laminaren Zone einer stochastisierten Plasmarandschicht. Berichte des Forschungszentrum Jülich (Jül-4220), Institut für Plasmaphysik (2006).
- [146] LEHNEN, M. ET AL. The effect of the magnetic topology on particle recycling in the ergodic divertor of TEXTOR. *Journal of Nuclear Materials*, **363-365** (2007), 377–381. doi:10.1016/j.jnucmat.2007.01.125.
- [147] JANESCHITZ, G. ET AL. The ITER divertor concept. *J. Nucl. Mater.*, **220-222** (1995), 73–88. doi:10.1016/0022-3115(94)00447-1.
- [148] STRACHAN, J. D. ET AL. Experimental results from detached plasmas in TFTR. *J. Nucl. Mater.*, **145-147** (1987), 186–190. doi:10.1016/0022-3115(87)90324-2.
- [149] TOKAR, M. Z. Non-Linear Phenomena in Textor Plasmas Caused by Impurity Radiation. *Phys. Scr.*, **51** (1995), 665–672. doi:10.1088/0031-8949/51/5/020.
- [150] MATTHEWS, G. F. Plasma detachment from divertor targets and limiters. *J. Nucl. Mater.*, **220-222** (1995), 104–116. doi:10.1016/0022-3115(94)00450-1.
- [151] THOMSEN, H. ET AL. Radiative condensation and detachment in Wendelstein 7-AS stellarator. *Nuclear Fusion*, **44** (2004), 820–826. doi:10.1088/0029-5515/44/8/002.
- [152] FENG, Y. ET AL. Physics of island divertors as highlighted by the example of W7-AS. *Nuclear Fusion*, **46** (2006), 807–819. doi:10.1088/0029-5515/46/8/006.
- [153] STOSCHUS, H. Private Communication (September 2009).
- [154] MESSIAEN, A. M. ET AL. Transport and improved confinement in high power edge radiation cooling experiments on TEXTOR. *Nuclear Fusion*, **36** (1996), 39–53. doi:10.1088/0029-5515/36/1/I03.
- [155] PAUL, W. AND BASCHNAGEL, J. Stochastic Processes - From Physics to Finance. Springer (1999).
- [156] JAMES, F. A review of pseudorandom number generators. *Comp. Phys. Commun.*, **60** (1990), 329–344. doi:10.1016/0010-4655(90)90032-V.
- [157] KNUTH, D. The art of computer programming, volume 2: Seminumerical algorithms. Addison-Wesley, 3rd ed. edition (1998).
- [158] L’ECUYER, P. Tables of linear congruential generators of different sizes and good lattice structure. *Math. Comput.*, **68** (1999), 225, 249–260. doi:10.1090/S0025-5718-99-00996-5.
- [159] MARSAGLIA, G. Random numbers fall mainly in the planes. *Proc Natl Acad Sci U.S.A.*, **61** (1968), 25–28.
- [160] MARSAGLIA, G. Diehard Battery of Tests of Randomness.  
URL <http://stat.fsu.edu/pub/diehard/>

- [161] GNU General Public License.  
URL <http://www.gnu.org/licenses/gpl.html>
- [162] NIST SPECIAL PUBLICATION 800-22REV1. A Statistical Test Suite for Random and Pseudorandom Number Generators for Cryptographic Applications (August 2008).  
URL <http://csrc.nist.gov/publications/nistpubs/800-22-rev1/SP800-22rev1.pdf>
- [163] BOX, G. AND MULLER, M. A note on the generation of random normal deviates. *Annals Math. Stat.*, **29** (1958), 610–611. doi:10.1214/aoms/1177706645.
- [164] THOMAS, D. B. ET AL. Gaussian Random Number Generators. *ACM Comput. Surv.*, **39** (2007), 4, 11. doi:10.1145/1287620.1287622.
- [165] MASCAGNI, M. AND SRINIVASAN, A. SPRNG: A Scalable Library for Pseudorandom Number Generation. *ACM Transactions on Mathematical Software*, **26** (2000), 3, 436–461.  
URL <http://sprng.cs.fsu.edu>
- [166] TELESKA, G. ET AL. Screening of intrinsic carbon with a stochastic magnetic boundary on TEXTOR-DED. *34th EPS Conference on Plasma Phys. Warsaw, 2 - 6 July 2007 ECA*, **31F** (2007), P-1.045.  
URL [http://epsppd.epfl.ch/Warsaw/pdf/P1\\_045.pdf](http://epsppd.epfl.ch/Warsaw/pdf/P1_045.pdf)
- [167] GREICHE, A. ET AL. Transport of argon and iron during a resonant magnetic perturbation at TEXTOR-DED. *Plasma Phys. Control. Fusion*, **51** (2009), 032001. doi:10.1088/0741-3335/51/3/032001.
- [168] BOHDANSKY, J. A universal relation for the sputtering yield of monatomic solids at normal ion incidence. *Nucl. Instr. and Meth.*, **2** (1984), 587. doi:10.1016/0168-583X(84)90271-4.
- [169] GARCIA-ROSALES, C.; ECKSTEIN, W. AND ROTH, J. Revised formulae for sputtering data. *Journal of Nuclear Materials*, **218** (1994), 8–17. doi:10.1016/0022-3115(94)00376-9.
- [170] SEEBACHER, J. Consistent kinetic trace-impurity transport and chemistry modelling in fusion plasmas. Ph.D. thesis, Department of Mathematics, Computer Science and Physics of the University of Innsbruck (2009).
- [171] KNABNER, P.; KOROTOV, S. AND SUMM, G. Conditions for the invertibility of the isoparametric mapping for hexahedral finite elements. *Finite Elements in Analysis and Design*, **40** (2003), 159–172.
- [172] YUAN, K. Y. ET AL. The inverse mapping and distortion measures for 8-node hexahedral isoparametric elements. *Computational Mechanics*, **14** (1994), 189–199. doi:10.1007/BF00350284.

# Symbols and Acronyms

## Magnetic configuration

$L_c$	Connection length . . . . .	20
$\psi^*$	Normalized poloidal flux . . . . .	20
$\vartheta$	Poloidal angle . . . . .	20
$\mathbf{B}_{\text{pol}}$	Poloidal magnetic field . . . . .	6
$q$	Safety factor . . . . .	6
$\varphi$	Toroidal angle . . . . .	6
$\mathbf{B}_{\text{tor}}$	Toroidal magnetic field . . . . .	6

## Plasma parameters

$D_{\perp}$	Anomalous cross-field diffusion coefficient . . . . .	27
$\chi_{e,i}$	Anomalous cross-field heat conductivity . . . . .	27
$n_{\text{in}}$	Density at the inner simulation boundary . . . . .	52
$n_{\text{C}^{Z+}}$	Density of carbon ions with charge stage $Z$ . . . . .	141
$q_a$	Electric charge of a particle from species $a$ . . . . .	24
$\mathcal{S}_{e,\text{cool}}$	Electron cooling rate . . . . .	34
$\mathbf{u}_a$	Fluid velocity of species $a$ . . . . .	24
$P_{\text{in}}$	Heat flux into simulation domain . . . . .	51
$\mathbf{h}_a$	Heat flux of species $a$ . . . . .	25
$c_s$	Ion sound velocity . . . . .	52
$n_a$	Particle density of species $a$ . . . . .	24
$I_p$	Plasma current . . . . .	6
$p_a$	Pressure of species $a$ . . . . .	25
$n_{\text{sepx}}$	Separatrix density . . . . .	95
$T_{\text{sepx}}$	Separatrix temperature . . . . .	95
$\gamma_e$	Sheath heat transmission coefficient for electrons . . . . .	52
$\gamma_e$	Sheath heat transmission coefficient for ions . . . . .	52
$q_{\text{target}}$	Target heat flux . . . . .	70, 90
$\Gamma_{\text{target}}$	Target particle flux . . . . .	70, 90
$T_a$	Temperature of species $a$ . . . . .	24
$T_{\text{in}}$	Temperature at the inner simulation boundary . . . . .	95
$P_{\text{target}}$	Total power losses at the target plates . . . . .	68, 95
$P_{\text{vol}}$	Total volumetric power losses . . . . .	68

**Simulation parameters**

$N_{\text{CPU}}$	Number of CPUs used in a simulation.....	53
$N_{\text{cell}}$	Number of grid cells .....	39
$N_{\text{MC}}$	Number of Monte Carlo particles in a simulation .....	39
$\alpha_{\text{relax}}$	Relaxation factor .....	57

**Acronyms**

<b>DED</b>	Dynamic Ergodic Divertor .....	11
<b>ELM</b>	Edge localized mode .....	2
<b>FION</b>	Full ionization - boundary condition.....	143
<b>FPE</b>	Fokker-Planck equation .....	36
<b>HFS</b>	High Field Side .....	11
<b>IBAL</b>	Ionization balance - boundary condition.....	143
<b>ISB</b>	Inner simulation boundary .....	144
<b>ISP</b>	Inner Strike Point .....	66
<b>LFS</b>	Low Field Side .....	10
<b>MC</b>	Monte Carlo .....	39
<b>MHD</b>	Magnetohydrodynamics .....	6
<b>RFLM</b>	Reversible field line mapping .....	3
<b>RMP</b>	Resonant magnetic perturbation.....	2
<b>SDE</b>	Stochastic differential equation.....	37
<b>SOL</b>	Scrape-Off Layer .....	7
<b>ZCFL</b>	Zero charge flux - boundary condition.....	142

# Index

## A

Anomalous cross-field transport ..... 26

## C

Chaotic magnetic edge layer ..... 9

Connection length ..... 22

Cylindrical coordinate system ..... 6

## D

DED target ..... 11

Density ..... 24

Detachment ..... 90

DIID-D tokamak ..... 10

Divertor plates ..... 8

## E

Edge localized mode ..... 2

Edge plasma ..... 8

Ergodic

domain ..... 20

field line ..... 9, 20

finger ..... 22, 94

## F

Field aligned grid ..... 42

Fluid velocity ..... 24

Fokker-Planck equation ..... 37

Friction force ..... 28

## H

H-mode ..... 2, 8

Heat flux ..... 25

Helical divertor ..... 12, 91

High Field Side ..... 11

High-recycling ..... 90

## I

Inner strike point ..... 66

## L

Low Field Side ..... 10

## M

Magnetic

flux tube ..... 22

footprint ..... 22

grid ..... 50

separatrix ..... *see* Separatrix

Major Radius ..... 10 f

Markov process ..... 37

Minor Radius ..... 10

## N

Normalized poloidal flux ..... 20

## O

Open chaotic system ..... 9, 20

## P

Plasma current ..... 6

Plasma grid ..... 50

Poincaré plot ..... 19

Poloidal

angle ..... 20

divertor ..... 8

magnetic field ..... 6

Pressure.....25

## **R**

Recycling.....23, 52

Resonant magnetic perturbations.....9

## **S**

Safety factor.....6

Scrape-Off Layer.....7, 65

Separatrix.....8

Stochastic region.....9

## **T**

Target..... *see* Divertor plates

Temperature.....24

TEXTOR tokamak.....11

Thermal force.....28

Toroidal  
    angle.....6  
    magnetic field.....6

## **U**

Upstream.....90, 95

## **V**

Vacuum approach.....12

Viscosity.....25

## **X**

X-point.....64



# Curriculum vitae

## Personal Details

Name:	Heinke Gerd Frerichs
Date of birth:	30 <sup>th</sup> Sept. 1980
Place of birth:	Jülich, Germany
Nationality:	German

## Education

(Since 06/2008)	Member of the German Research School for Simulation Sciences
12/2006 - 02/2010	Graduate studies at RWTH Aachen University and Forschungszentrum Jülich
10/2005 - 10/2006	Diploma thesis at Forschungszentrum Jülich, Institute for Energy Research - Plasma Physics: "3D numerische Parameterstudien zum Verunreinigungstransport in TEXTOR-DED"
10/2001 - 11/2006	Studies of physics at RWTH Aachen University
06/2000	Abitur, Gymnasium Zitadelle Jülich



# Acknowledgments

On this final page of the present thesis I would like to thank my colleagues, my friends and my family for their support during the last three years of research and thesis writing. In particular:

I would like to express my sincere gratitude to my advisor Prof. Dr. Detlev Reiter at the Institute for Energy Research - Plasma Physics at the Research Centre Jülich. He has offered me to work on this very exciting topic, and his guidance provided a solid basis for the present thesis.

I am also very grateful to my supervisor Prof. Dr. Hans-Jörg Kull at the Institute for Theoretical Physics A at the RWTH-Aachen University. He facilitated the collaborative scope of this thesis between the Research Centre Jülich and RWTH-Aachen University.

I wish to thank Dr. Oliver Schmitz for his valuable advice on experimental observations and for many helpful discussions. Furthermore, I would like to thank him for the detailed review and constructive criticism during the preparation of this thesis.

I am also grateful to Dr. Yühe Feng and Dr. Derek Harting for their introduction to the EMC3-EIRENE code. They offered me valuable insight into the detailed mechanisms of the code.

I also wish to thank Dipl.-Phys. Benjamin Berberich and Dipl.-Phys. Henning Stoschus for their helpful comments during the preparation of this thesis.

Furthermore, I am thankful to General Atomics, in particular to Dr. Todd Evans, for three very exciting and productive research trips to San Diego.

Finally, I would like to thank the German Research School for Simulation Sciences for their financial support of this thesis.

Jülich, Germany, November 2009  
Heinke Gerd Frerichs



Jül-4321  
April 2010  
ISSN 0944-2952